VAPOR

Conceptual Design of an Atmospheric UAV Powered by a Compact 500N Liquid Bipropellant Propulsion System

Final Report, Group 01
AE3200 Design Synthesis

Delft University of Technology

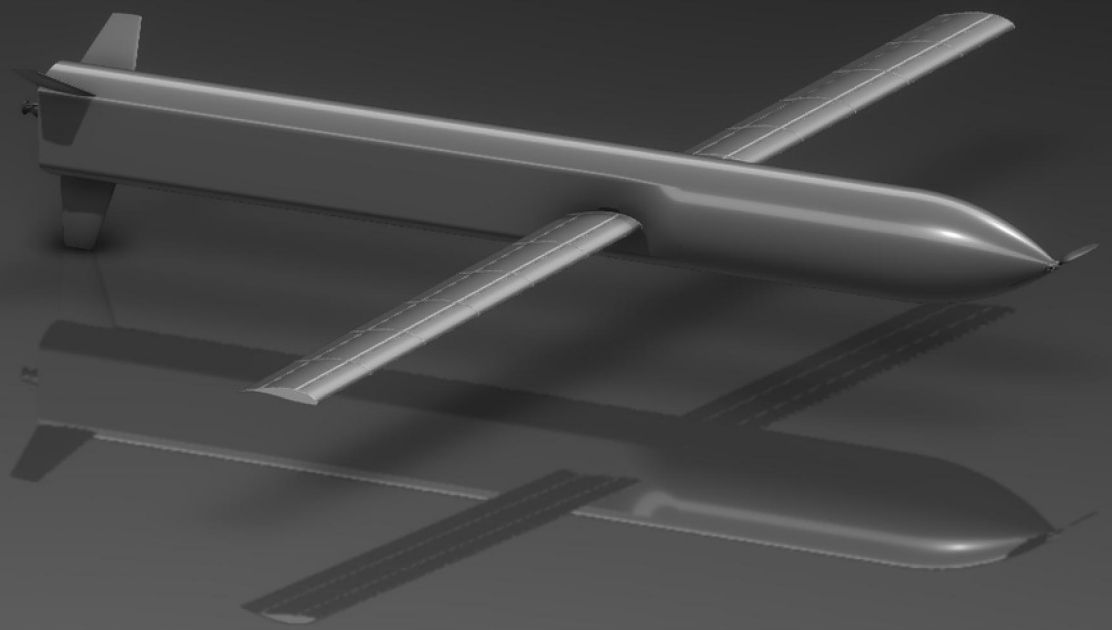

TU Delft

This page is intentionally left blank.

VAPOR
Final Report

by

Group 01

Student Name	Student Number
Marco Armeli	5985730
Kaj Breeman	5982510
Ivan Ezcurra Masip	5728711
Mario Larrondo Pérez-Izaguirre	5903939
Noah Lievens	5915449
Duco Lindhout	5748348
Victor Plugaru	5906121
Paul Vander Stichele	5720281
Vladimir Voineag	5959322
Kyle Zantboer	5780551

Principal Tutor: B.V.S. Jyoti
Project Duration: April, 2026 - June, 2026
Faculty: Faculty of Aerospace Engineering, Delft

TU Delft

Executive Overview

Author(s): Kaj, Marco, Paul, Kyle

VTOL Atmospheric Peroxide-Oxidised Reconnaissance (VAPOR) is a rapid-response surveillance Unmanned Aerial Vehicle (UAV) combining vertical take-off and landing with a sea-level optimised pressure-fed bi-propellant engine running on 98% hydrogen peroxide. With a 34 kg Maximum Take-Off Mass (MTOM), 3 kg payload, and 500 N thrust-class engine, it is sized to reach high altitudes significantly faster than any comparable platform and to sustain a 1-hour mission. A foldable airframe and net-based recovery to keep the deployment footprint compact, allowing transport in a small ground vehicle and readiness within minutes. Building on the midterm [1], which identified a clear design concept, this report aims to perform a detailed analysis and sizing of the design, highlighting its competitiveness in the market.

Market Position and Future Outlook

The market analysis identified rapid-response surveillance as the primary application for VAPOR. While conventional electric UAVs offer strong endurance and operational maturity, they are limited in their ability to rapidly reach operational altitude. By combining a liquid atmospheric bi-propellant propulsion system with efficient electric cruise flight, VAPOR addresses this gap and offers a unique capability within the current UAV market.

Compared to competing platforms, VAPOR distinguishes itself through its exceptionally short time-to-altitude while maintaining competitive endurance, range, and payload capability. This positions the vehicle as a complementary first-response asset, capable of providing valuable information during the critical first minutes of an incident before longer-endurance systems assume sustained monitoring tasks.

The future market outlook further strengthens the relevance of the proposed concept. The global UAV market continues to grow rapidly, driven by increasing demand for autonomous aerial systems across both civilian and governmental sectors. In particular, the surveillance drone market is expected to experience strong growth over the coming decade due to rising requirements for public safety, infrastructure monitoring, environmental protection, and emergency response. These trends indicate a growing demand for systems capable of delivering immediate aerial situational awareness, supporting the long-term commercial potential of the VAPOR mission.

Propulsion Design

The VAPOR mission employs an hybrid propulsion system composed of a liquid bi-propellant engine for take-off and ascent, and an electric propeller for cruise.

The bi-propellant propulsion system is composed of many different subsystems, these include the feeding subsystem, the catalyst, the injector, and the thrust chamber. The engine is overall designed for the driving requirement of 500 thrust at sea-level, from this starting point the key design variables are identified and optimised, these comprehend the Oxidizer-to-fuel ratio (O/F), the chamber pressure and the contraction ratio.

The optimization is carried out while fulfilling the driving engine cooling requirements, regenerative cooling with peroxide is identified as the best solution both in terms of performance and sustainability. Results of the optimization are reported in Table 1.

Subsequently, the injector subsystem is designed, a pintle injector is chosen as the best solution for its simplicity, mixing capability and combustion stability properties. Furthermore, the catalyst is responsible for full decomposition of the peroxide from liquid to gaseous state; the manganese dioxide catalyst bed is chosen for its affordability and high melting point. A render of the engine is shown in Figure 1.

Table 1: Overview of Engine Performance Parameters

Parameter	Value	Parameter	Value	Parameter	Value
p_c	2 MPa	t_b	25.49 s	D_e	2.89 cm
O/F	4	$\dot{m}$	0.244 kg/s	D_t	1.53 cm
CR	10	A_e/A_t	3.58	p_c/p_e	19.7
T_c	2321 K	I_{sp}	208.8 s		
T_{sl}	500 N	L^*	0.8 m		

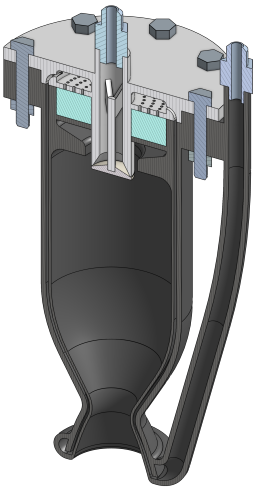

Figure 1: Rendering of the VAPOR main engine

Secondly, the electric propulsion system is designed, a variety of propellers and motors is analysed based on power required requirements, an optimization is performed minimizing the total system's mass. Results showed that the best solution is the APC 20x15E foldable spinner propeller and the T-Motor AT 5330 Fixed Wing motor.

Airframe Design

The airframe is defined by four main components: aerodynamics, tail, folding, and structure. The wing employs a custom optimised airfoil based on the WORTMANN FX 63-137 shape. The 3D wing shape has been optimised for mission endurance; however, this has been done under constraints imposed by structural limits and the folding mechanism.

The tail was sized for both the rocket and cruise phases. Ensuring stability in the rocket phase and ensuring both controllability and static stability in the cruise phase. The tail is also responsible for the transition from take-off to cruise. This transition was modelled, and a controller has been developed to supply the appropriate control signals to the tail to successfully transition the UAV.

Performance and Operations

VAPOR is optimized for rapid climb performance, endurance during cruise, and range during glide. The propulsion system, aerodynamics, and structures have been optimized accordingly. The fast-response characteristics are what truly make VAPOR competitive in the market. Range and endurance figures are also comparable with conventional electric UAVs; the most important performance figures are tabulated in Table 2.

These figures are a strong indication of where VAPOR stands in the market, capable of achieving exceptionally fast response times while maintaining a sustainable and efficient flight profile. Reaching the operational altitude in only 39 seconds enables mission execution almost immediately after launch, making the vehicle particularly attractive for time-critical applications. At the same time, the achieved range and endurance demonstrate that this rapid deployment capability does not come at the expense of mission effectiveness.

Table 2: Mission Performance Summary

Performance Metric	Value	Unit
Time to Target Altitude	39	s
Total Range	85.2	km
Total Endurance	68.16	min

The combination of rocket-assisted vertical ascent, efficient electric cruise, and high lift-over-drag glide flight allows VAPOR to cover large operational areas from a single launch location. Furthermore, the vertical launch capability eliminates the need for runways or dedicated launch infrastructure, increasing deployment flexibility and allowing operation from remote or constrained environments. As a result, VAPOR is

well suited for applications such as emergency response, environmental monitoring, infrastructure inspection, surveillance, and other missions where rapid access to the operational area is of critical importance.

Overall, the performance characteristics of VAPOR demonstrate a successful balance between responsiveness, range, endurance, and operational flexibility, providing a competitive solution for next-generation unmanned aerial systems.

Manufacturing and Sustainability

The UAV is built mostly from aluminium and a thermoplastic carbon-fibre composite, with the engine laser-printed in Inconel as a single consolidated part and the electric propulsion and avionics bought off the shelf. Components are produced in parallel and brought together into sub-assemblies, of which the propulsion module is designed to be removed and refitted as a unit.

Sustainability shapes these choices throughout. By favouring aluminium and a reprocessable thermoplastic composite over thermoset materials, and by selecting low-waste, near-net-shape processes, the design keeps the large majority of the structure recyclable and easy to disassemble at end of life. The 98% hydrogen peroxide oxidiser reinforces this, as it is non-cryogenic, low in toxicity, and releases mainly oxygen and water rather than hydrocarbon emissions. Together these decisions give VAPOR a competitive environmental footprint, with mission emissions far below an air-breathing UAV and resource and end-of-life impacts well below an electric one, meeting its objective of sustainable competitiveness.

Cost

The academic-scale prototype is delivered within the €30,000 budget set by the stakeholders, split between a modest testing campaign and the UAV itself, with design and labour treated as free, given the student-built nature of the project. This confirms that a working proof of concept is achievable at low cost.

Beyond the prototype, the same design is projected to be profitable once taken to commercial production. Assuming an €18 million up-front investment and a production run of 300 units per year, the recurring cost settles below €45,000 per unit while a value-based selling price of €95,000 keeps VAPOR above conventional electric drones yet below high-end military systems. On these assumptions the programme returns a five-year Net Present Value of around €8 million and an opportunity cost of capital near 30%, comfortably above its cost of capital. The case is therefore financially attractive and cost-competitive with electric rivals, though it remains sensitive to sustaining both the production volume and the selling price.

Discussions and Recommendations

The conceptual design of VAPOR shows the feasibility of utilizing a novel liquid atmospheric bi-propellant propulsion system and a cruise concept powered by electric propellers. Through the successful combination of these two very different propulsion systems, the strengths of each propulsion technology is used. On one hand, the rocket propulsion system allows for extremely fast vertical lift-off and very good response times, and on the other hand, the electric propulsion system allows for efficient cruise operation and increased endurance.

In addition, the conceptual design fulfils an obvious gap in the current UAV market, in which products typically specialize either in long endurance operations or fast deployment capabilities.

Despite the promising results obtained from the conceptual design, there are a number of aspects that could be further explored as part of future design phases. First, there is the need for iterative designs between all the subsystems in order to arrive at a fully converged design. Second, more accurate aerodynamic modelling needs to be considered through higher fidelity methods, e.g., CFD analysis.

An extensive testing campaign is also recommended. This should include validation of all models used for simulations. Ultimately, a full flight test campaign should be conducted to demonstrate the complete mission profile and verify the integrated performance of the vehicle. These activities will provide the confidence required to transition VAPOR from a conceptual design to a mature and operationally viable system.

Contents

Nomenclature

List Of Symbols

a	Speed Of Sound	m/s
A	Area	m^2
A	Propeller Disk Area	m^2
A^*	Throat Area	m^2
A_{ref}	Aerodynamic Reference Area	m^2
A_{cc}	Combustion Chamber Area	m^2
A_e	Exit Area	m^2
a_f	Frame Spacing	m
B	Spalding Transfer Number	–
b_s	Stringer Pitch	m
c^*	Characteristic Velocity	m/s
c_e	Control-Surface Mean Chord	m
c_p	Specific Heat At Constant Pressure	J/(kg·K)
c_{ref}	Reference Diameter	m
CR	Contraction Ratio	–
C_{h_δ}	Hinge-Moment Deflection Derivative	rad^{-1}
C_{h_e}	Hinge-Moment Coefficient	–
$C_{L_{\text{opt}}}$	Optimal Lift Coefficient	–
C_{m_δ}	Pitching-Moment Control-Deflection Derivative	rad^{-1}
C_{mq}	Pitch Aerodynamic Damping Moment Coefficient	–
C_n	Normal Aerodynamic Force Coefficient	–
C_t	Tangential Aerodynamic Force Coefficient	–
d	Slant Range	km
D	Propeller Diameter	m
D^*	Throat Diameter	m
D_{32}	Sauter Mean Droplet Diameter	m
D_c	Thrust Chamber Diameter	m
D_{pt}	Pintle Diameter	m
d_h	Hydraulic Diameter	m
E	Endurance	min
E	Mission Energy	Wh
f	Carrier Frequency	MHz
F_n	Normal Aerodynamic Force Component	N
F_t	Tangential Aerodynamic Force Component	N
F_T	Thrust	N
Fo	Fourier Number	–
G_p	Acoustic Pressure Power Spectral Density	Pa^2·s
G_r	Receive Antenna Gain	dBi
G_t	Transmit Antenna Gain	dBi
Gr	Grashof Number	–
h_{chan}	Coolant Channel Height	m
h_f	Frame Web Height	m
h_g	Gas Heat Transfer Coefficient	W/(m^2·K)
h_l	Coolant-Side Heat Transfer Coefficient	W/(m^2·K)
H_e	Control-Surface Hinge Moment	N·m
i	Motor Current	A
i_0	Motor No-Load Current	A
I_{sp}	Specific Impulse	s
I_{xx}	Second Moment Of Area About x-Axis	m^4
I_{xz}	Product Moment Of Area	m^4
I_{yy}	Moment Of Inertia About Body y-Axis	kg·m^2
I_{zz}	Second Moment Of Area About z-Axis	m^4
J	Advance Ratio	–
k	Buckling Coefficient	–
K_1	Outer-Loop (Pitch-Angle) Controller Gain	–
K_2	Inner-Loop (Pitch-Rate) Controller Gain	–
K_Q	Motor Torque Constant	A/(N·m)
K_V	Motor Speed Constant	rpm/V
L^*	Characteristic Length	m
L_{conv}	Convergent Section Length	m
L_{div}	Divergent Section Length	m
L_{fs}	Free-Space Path Loss	dB
L_{cc}	Combustion Chamber Length	m
L_ℓ	Cable And Implementation Losses	dB
M	Link Margin	dB
M	Mach Number	–
M_∞	Freestream Mach Number	–
M_p	Propellant Mass	kg
M_q	Pitch Damping Moment	N·m
M_{control}	Control Pitching Moment	N·m
M_{tip}	Propeller Tip Mach Number	–
M_w	Molecular Mass	kg/mol
M_x	Bending Moment About x-Axis	N·m
M_z	Bending Moment About z-Axis	N·m
N_{chan}	Number Of Coolant Channels	–
p	Pressure	Pa
p_c	Chamber Pressure	Pa
p_e	Exit Pressure	Pa
P	Power	W
P_{batt}	Battery Power	W
P_{ESC}	ESC Power	W
P_{Heat}	Heated Perimeter	m
P_{shaft}	Motor Shaft Power	W
P_{wire}	Wire Power Loss	W

P_r	Received Power (Link Budget)	dBm
P_t	Transmit Power	dBm
Pr	Prandtl Number	–
q	Pitch Rate	rad/s
q_b	Variable Shear Flow	N/m
q_{s_0}	Base (Constant) Shear Flow	N/m
q_{mes}	Measured Pitch Rate	rad/s
q_{ref}	Reference (Commanded) Pitch Rate	rad/s
Q_m	Motor Shaft Torque	N·m
r_c	Radius Of Curvature	m
R	Motor Internal Resistance	Ω
R	Range	km
R	Specific Gas Constant	J/(mol·K)
R_h	Maximum Horizontal Range	km
R_{wire}	Wire Resistance	Ω
R_u	Universal Gas Constant	J/(mol·K)
Ra	Rayleigh Number	–
Re	Reynolds Number	–
S_{FF}	Force Power Spectral Density	N^2/Hz
S_{XX}	Displacement Response Power Spectral Density	m^2/Hz
S_e	Control-Surface Area	m^2
S_r	Receiver Sensitivity	dBm
SF	Safety Factor	–
t_b	Burn Time	s
T	Temperature	K
T	Thrust	N
T_c	Chamber Temperature	K
u_{d0}	Initial Droplet Velocity	m/s
v	Motor Terminal Voltage	V
v_{cool}	Coolant Velocity	m/s
v_e	Nozzle Exhaust Velocity	m/s
v_m	Motor Back-EMF Voltage	V
V_{batt}	Battery Voltage	V
V_{cruise}	Cruise Velocity	m/s
V_{opt}	Optimal Velocity	m/s
V_{cc}	Combustion Chamber Volume	m^3
V_{X_e}	Inertial-Frame Velocity Component, x	m/s
V_{Z_e}	Inertial-Frame Velocity Component, z	m/s
V_x	Internal Shear Force, x	N
V_z	Internal Shear Force, z	N
w_{chan}	Coolant Channel Width	m
w_f	Frame Flange Width	m
x^*	Vaporisation Distance	m
x_e	Inertial-Frame Position Coordinate, x	m
x_{cp}	Centre-Of-Pressure Location	m
z_e	Inertial-Frame Position Coordinate, z	m
α	Angle Of Attack	rad
α	Thermal Diffusivity	m^2/s
β	Volumetric Thermal Expansion Coefficient	K^{-1}
γ	Flight-Path Angle	rad
γ	Specific Heat Ratio	–
Γ	Dihedral Angle	rad
δ	Control-Surface Deflection Angle	rad
ζ	Modal Damping Ratio	–
η	Propulsive Efficiency	–
η_{all}	Overall Propulsion-Chain Efficiency	–
η_{bat}	Battery Discharge Efficiency	–
η_{ESC}	ESC Efficiency	–
η_{fold}	Folding-Mechanism Efficiency	–
η_m	Motor Efficiency	–
η_p	Propeller Efficiency	–
θ	Pitch Angle	rad
θ_{mes}	Measured Pitch Angle	rad
θ_{ref}	Reference (Commanded) Pitch Angle	rad
κ	Thermal Conductivity	W/(m·K)
λ_{conv}	Convergent Half Angle	Rad.
λ_{div}	Divergent Half Angle	Rad.
λ_r	Eigenvalue Of Mode r	rad^2/s^2
μ	Dynamic Viscosity	Pa·s
ν	Kinematic Viscosity	m^2/s
ϕ_r	Mode Shape Vector Of Mode r	–
ρ	Density	kg/m^3
σ	Bartz Boundary-Layer Property Correction Factor	–
σ_{cr}	Critical (Buckling) Stress	MPa
σ_{max}	Maximum Stress	MPa
σ_y	Yield Stress	MPa
τ	Shear Stress / Shear Yield Strength	MPa
ω	Bartz Transport-Property Temperature Exponent	–
$\omega_{n,r}$	Natural Frequency Of Mode r	rad/s
Ω	Motor Rotation Rate	rad/s
Δt	Time Interval Between Two Instants	s
Δx	Displacement in x-direction	m
Δz	Displacement in z-direction	m

List Of Abbreviations

AC Aerodynamic Centre
AI Artificial Intelligence
BVLOS Beyond Visual Line of Sight
CAD Computer-Aided Design
CAM Computer-Aided Manufacturing
CAN Controller Area Network
CEA Chemical Equilibrium with Applications
CF/PEEK Carbon-Fibre-Reinforced PEEK
CFD Computational Fluid Dynamics

CFL Courant- Friedrichs–Lewy
cg Centre Of Gravity
CNC Computer Numerical Control
ConOps Concept of Operations
COTS Commercial Off-The-Shelf
C.P. Centre of Pressure
DHBD Data-Handling Block Diagram
DoF Degrees of Freedom
DSE Design Synthesis Exercise
DVR Design Verification Report
EASA European Union Aviation Safety Agency
EBD Electrical Block Diagram
EO/IR Electro-Optical/Infrared
EPS Electrical Power System
ESC Electronic Speed Controller
eVTOL Electric Vertical Take-Off and Landing
FBD Free Body Diagram
FBS Functional Breakdown Structure
FEM Finite Element Method
FFD Functional Flow Diagram
FRF Frequency Response Function
GCS Ground Control Station
GFRP Glass-Fibre-Reinforced Polymer
GPS Global Positioning System
HIP Hot Isostatic Pressing
HTP High Test Peroxide
ICAO International Civil Aviation Organisation
IMU Inertial Measurement Unit
IRR Internal Rate of Return
ISA International Standard Atmosphere
ISO International Organisation for Standardisation
L/D Lift-to-Drag ratio
LCA Life Cycle Assessment
LE Leading Edge
MOPSO Multi-Objective Particle Swarm Optimisation
MS Margin of Safety
MTOM Maximum Take-Off Mass
MTOW Maximum Take-Off Weight
NAA National Aviation Authority
NLR Netherlands Aerospace Centre
NPV Net Present Value
NRSPL Normalised Relative Sound Power per unit core Length
NRSPSL Normalised Relative Sound-Power-Spectrum Level
OASPL Overall Sound Pressure Level
OCC Opportunity Cost of Capital
O/F Oxidizer-to-fuel ratio
PDU Power Distribution Unit
PPE Personal Protective Equipment
PSD Power Spectral Density
RAMS Reliability, Availability, Maintainability and Safety
RF Radio Frequency
RMS Root Mean Square
RP-1 Rocket Propellant-1
RPA Rocket Propulsion Analysis
RPM Revolutions Per Minute
SAIL Specific Assurance Integrity Level
SDG Sustainable Development Goal
SeR Search and Rescue
SLS Selective Laser Sintering
SORA Specific Operations Risk Assessment
SWOT Strengths, Weaknesses, Opportunities, Threats
T/W Thrust-to-Weight Ratio
TAM Thermal Analysis Model
TIG Tungsten Inert Gas
UAS Unmanned Aircraft System
UAV Unmanned Aerial Vehicle
VAPOR VTOL Atmospheric Peroxide-Oxidised Reconnaissance
V&V Verification and Validation
VTOL Vertical Take-Off and Landing

1 | Introduction *Author(s): Kyle*

Over the past couple of decades, Unmanned Aerial Vehicles have become one of the most relevant pieces of engineering in both commercial and government-run sectors. The current UAV market relies on small electric or propeller-driven fixed-wing aircraft, none of which offer a high rate of climb. This limits their operational flexibility and delays their time before deployment. During emergencies, this can create a significant disadvantage for maintaining control of the situation. However, this also creates a clear market opportunity for a novel UAV design that achieves both high climb rates and optimal cruise performance. With this objective, VAPOR is created, utilising an innovative propulsion system that closes this gap. The 3D model can be seen in Figure 1.1.

This report aims to justify the decisions made in the conceptual design of VAPOR. In an earlier stage of this project, an initial design was created [1]. This initial design, however, was mainly based on empirical formulations that do not capture the multidisciplinary complexity of VAPOR. Therefore, this does not provide a full conceptual design. However, using this initial design as a framework, a more detailed analysis of VAPOR's entire mission will be presented. This will be done through the following method.

In Chapter 2, the objectives of VAPOR will be presented along with the market analysis. Here, the objectives of VAPOR shall be made clear, and a clear market gap is identified that VAPOR aims to fill. This is followed by Chapter 3, where the functional diagrams will be presented. They showcase the capabilities and functions of VAPOR with the use of a Functional Flow Diagram (FFD) and a Functional Breakdown Structure (FBS). Then, in Chapter 4, the technical risk shall be assessed. This shall identify the risks of VAPOR's mission along with contingency actions that are taken to mitigate these risks. In Chapter 5, the trade-offs presented in the midterm [1] are summarised. Chapter 6 will discuss the verification and validation procedure that shall be adhered to throughout the design.

Then, the first subsystem, the propulsion system, will be discussed in Chapter 7. This is followed by Chapter 8 where the avionics and electrical system are discussed. Since VAPOR will make use of a secondary propulsion system to maintain altitude during cruise, the design of the avionics and electrical systems follows from the propulsion system such that it complements each other. After this, in Chapter 9, VAPOR's airframe will be discussed. This includes the aerodynamic and structural design, along with the folding mechanism for the wings. After this, these various subsystems will be combined in Chapter 10. This is needed for Chapter 11, which shall discuss the stability & control capabilities of VAPOR. Chapter 12 will assess the flight performance characteristics that define the mission. With this, the secondary propulsion system, the propeller, can be designed in Chapter 13. Chapter 14 will present the various budgets, including a cost breakdown. Then, the operations & logistics of VAPOR are discussed in Chapter 15. This is followed by Chapter 16 that shows the manufacturing & assembly plan that VAPOR shall use, with a focus on sustainability. With this, the development & production plan shall be discussed in Chapter 17. Then, the sustainable strategies will be discussed in Chapter 18. While sustainability is present throughout the entire design, this chapter addresses the strategies and procedures that VAPOR shall adhere to. In Chapter 19, the requirements setup in the Baseline will be checked for compliance [2]. Finally, this report shall draw its conclusions and give its recommendations in Chapter 20.

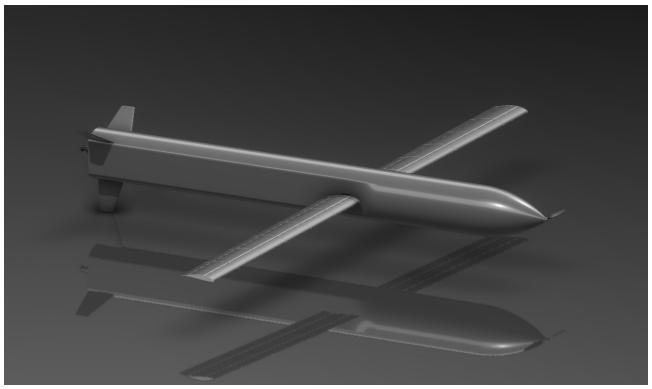

Figure 1.1: Catia Model of VAPOR

2 | Project Description & Market Analysis

This chapter sets the goal of the VAPOR mission and discusses the underlying factors which drive the project. Also, a market analysis will be conducted in order to justify the need for our project.

2.1. Project Objectives *Author(s): Duco*

Mission Statement - VTOL Atmospheric Peroxide-Oxidiser Reconnaissance (VAPOR)

The VAPOR project shall demonstrate rapid-response surveillance capabilities at altitude.

To achieve its mission, VAPOR should meet a number of top-level primary objectives that assess its performance, operational capability, safety, and market viability. They will drive all the design decisions, ensuring that VAPOR not only fulfils a series of technical requirements but also has a meaningful practical purpose.

- The VAPOR project shall demonstrate integration of a liquid bi-propellant engine in an atmospheric UAV.
- The VAPOR project shall demonstrate Vertical Take-Off and Landing (VTOL) capabilities in confined areas with unprepared terrain.
- The VAPOR project shall demonstrate safe use and handling of H_2O_2 in an atmospheric UAV.
- The VAPOR project shall provide faster response capabilities than its electrical-powered competitors.
- The VAPOR project shall be competitive in cost with respect to its electrical-powered competitors.
- Sustainability shall serve as a primary system-level driver for the VAPOR project design.

2.2. Market Analysis *Author(s): Duco, Victor*

The VAPOR project is a unique concept for rapid response surveillance compared to the current UAV industry; however, its theoretical competitiveness is not yet clearly defined. While modern electric VTOL platforms excel in standard payload delivery and endurance missions, they face critical performance bottlenecks in scenarios demanding immediate, high thrust deployment and rapid altitude level. VAPOR's liquid bi-propellant design aims to overcome these specific limitations inherent to purely electric systems. In this chapter, the market outlook with respect to the bi-propellant UAV being designed will be covered. Topics such as the general market context, market segmentation, competitors, future market trends, stakeholder description and requirements will be described.

2.2.1. Market Segmentation

A UAV powered with a liquid bi-propellant engine could have the following use cases in the market: Search and Rescue (SeR), surveillance, and payload delivery. These three main use cases are already addressed by electrical UAVs and helicopters; however, they present limitations, and that could be further improved upon with a liquid bi-propellant design.

The main advantage of the VTOL liquid bi-propellant UAV is its quick response, as it can reach its target location very quickly due to its high thrust-to-weight ratio. This is particularly beneficial to monitor emergency situations such as wildfires, where shaving off seconds in response time could make the difference between a catastrophe and a successful mission. Military applications can also be considered, where a specific target or area has to be rapidly monitored in a predefined amount of time. The same chain of reasoning can be applied to a search and rescue mission where a target might be located in a hard-to-reach area, making rapid response crucial.

This rapidness can also be very useful for emergency payload delivery, for instance, transporting an organ to the helipad of a hospital for a transplant. This would be much cheaper than using a helicopter and potentially much faster. Another case could be transporting food and basic supplies to areas of difficult access in the event of a natural disaster, where other means of transport might not be able to reach. These are the main segments that were identified, and they will be further elaborated upon, alongside examples of (large) commercial players which are already operating in the aforementioned fields.

2.2.2. Competitor Analysis

In this section, a few sample solutions (competitors) will be given for the major use cases. These will then be compared to the bi-propellant UAV concept to find potential gaps or overlap, to hopefully eliminate saturated market segments.

Rapid Payload Delivery To compare the bi-propellant UAV to competitors in the (rapid) payload delivery segment it is important to define the key value drivers. These drivers are payload mass, range, delivery speed, and landing and take-off flexibility. Within this segment, several design concepts can be identified. First, purely multi-rotor designs operate without a lifting wing. Second, hybrid VTOL configurations combine multi-rotor lift capability with the cruise efficiency of a fixed-wing aircraft. Finally, the proposed solution must also be compared with purely winged systems.

Pure multi-rotor The Italian manufacturer FlyingBasket shows the heavy-lift end of this category with their FB3 platform. The FB3 is a 70 kg coaxial octocopter capable of lifting up to 100 kg of cargo, but its fully-electric system imposes an important payload-range trade-off: only 2.5 km when fully loaded, increasing to roughly 25 km with a 5 kg payload, at a cruise speed of approximately 22 m/s[1] [2]. The vehicle is priced at around €77,000 and is targeted primarily at construction, utility, and mountain-logistics operators where cranes or helicopters would otherwise be needed[3]. The strength of this category is landing-site flexibility; the weakness is that battery energy density caps both range and cruise speed well below what fixed-wing solutions achieve.

Hybrid VTOL A larger group of competitors combines vertical take-off with a fixed wing for cruise. The clearest commercial benchmarks here are Zipline's P2 platform, the Wingcopter 198, and Swoop Aero's Kite. Zipline'sp P2 is a tilt-prop hybrid optimised for short, dense, urban routes: it carries up to 3.6 kg over a 16 km service radius at a cruise speed of approximately 110 km/h, with deliveries placed by a tethered "droid" lowered from hover[4] [5]. The Wingcopter 198 (Germany) is a tilt-rotor Electric Vertical Take-Off and Landing (eVTOL) carrying up to 6 kg, with a range of about 75 km at a 5 kg payload and a default cruise speed near 100 km/h (peak 144 km/h)[6] [7]. Swoop Aero's Kite (Australia) sits closest to the performance envelope of the bi-propellant concept being designed: 3 kg over 175 km, or 5 kg over 130 km, at a cruise speed of 122 km/h[8] [9].

Pure fixed-wing At the small end, Zipline's older P1 platform is a catapult-launched fixed-wing glider with a 1.75 kg payload and roughly an 80 km one-way range at 101 km/h, recovered by an arresting-wire tail-hook landing[10]. At the opposite extreme, Bulgaria-based Dronamics has developed the Black Swan, a 350 kg-payload, 2,500 km-range fixed-wing cargo drone with a cruise speed of roughly 200 km/h, capable of operating from short unpaved runways[11] [12]. Both concepts illustrate the inherent strength of the pure-winged approach, which is high cruise speed and long range per unit of stored energy, at the cost of needing prepared launch and recovery sites, which makes them poorly suited to landing-flexible missions such as delivery into a hospital helipad or a disaster zone.

Table 2.1 summarises the relevant performance parameters across all three categories, including the time to complete a representative 25 km one-way delivery at each platform's stated cruise speed.

Table 2.1: Representative payload-delivery UAVs against the key value drivers for the rapid-response segment. Mission time is computed as $t = d / v_{\text{cruise}}$ for a $d = 25$ km one-way delivery, neglecting take-off, climb-out, and descent phases. Values are drawn from manufacturer datasheets and the trade press; full source URLs are listed in the appendix.

Aircraft	Configuration	Payload [kg]	Cruise [km/h]	Range [km]	$t_{25\,\text{km}}$ [min]
FlyingBasket FB3	Multirotor	100 / 5[a]	79	2.5 / 25[a]	19[b]
Zipline P1	Fixed-wing	1.75	101	80	15
Zipline P2	VTOL hybrid	3.6	110	16	out of range
Wingcopter 198	VTOL hybrid	5	100	75	15
Swoop Aero Kite	VTOL hybrid	3 / 5[c]	122	175 / 130[c]	12
Dronamics Black Swan	Fixed-wing	350	200	2,500	8

[a] 2.5 km with 100 kg payload; 25 km with a 5 kg payload.
[b] At the edge of the FB3's 5 kg / 25 km envelope; the aircraft would arrive with negligible reserve.
[c] 175 km at 3 kg payload; 130 km at 5 kg payload.

[1] flyingbasket.com [Date Accessed: June 16] [2] alphageouk.com [Date Accessed: June 16] [3] dronedj.com [Date Accessed: June 16] [4] spectrum.ieee.org [Date Accessed: June 16] [5] dronexl.co [Date Accessed: June 16] [6] wingcopter.com [Date Accessed: June 16] [7] eandt.theiet.org [Date Accessed: June 16] [8] swoop.aero [Date Accessed: June 16] [9] autoevolution.com [Date Accessed: June 16] [10] wikipedia.org/Zipline [Date Accessed: June 16] [11] dronamics.com [Date Accessed: June 16] [12] flyingmag.com [Date Accessed: June 16]

Synthesis The platforms in Table 2.1 already complete a 25 km delivery in roughly 10 to 15 minutes of cruise, an order of magnitude faster than ground transport and similar in speed with a helicopter. A bi-propellant rocket engine could compress this further, but the gain comes at a large cost: the propellant mass needed to sustain high thrust limits range to a small fraction of what the comparable electric hybrids achieve. For rapid-delivery missions (organ transport, time-critical medical missions, disaster-zone resupply), shaving a few minutes off an already short delivery is rarely worth giving up the ability to reach the next town over, and customer choice in this segment is dominated by cost, regulatory acceptance, and reliability rather than just speed. The bi-propellant concept therefore has a weak competitive position in payload delivery.

Search and Rescue

SeR operations in mountainous, coastal or otherwise remote terrain are typically run by helicopter crews and ground teams operated by mountain-rescue services, coast guards, and civil-protection organisations. UAVs have become a standard complementary asset over the last decade, mainly used to scan large areas of difficult terrain for missing persons using thermal and high-resolution optical sensors, with real-time video relayed to the incident commander on the ground[13]. The dominant platforms in this role are multirotors carrying a thermal payload, with the DJI Matrice line (M30T, M350 RTK, and, more recently, the M4T) being the de facto standard. The Austrian Mountain Rescue Service, for example, has deployed the DJI Matrice 4T to locate missing persons in the Alps using thermal imaging and support from Artificial Intelligence (AI)[14], and similar deployments are reported in the Scottish Highlands by the UK Maritime and Coastguard Agency and by SeR teams in the Swiss Alps and the US[15].

Rapid climb to altitude is valuable in alpine SeR, since calls regularly require operating at 2000 m or above, and the survival window for an injured or hypothermic casualty is short. A bi-propellant VTOL UAV could plausibly reach search altitude faster than any electric competitor. However, the dominant value driver in SeR is not time-to-altitude but loiter endurance: a useful search requires the aircraft to remain over the area for tens of minutes to hours while methodically scanning, which is fundamentally incompatible with the short burn time of a bi-propellant engine. The concept could deliver a beacon or first-aid package to a known location quickly, but it cannot perform the search itself, and adding endurance would erode the rapid-response advantage that distinguishes the design. SeR is therefore not considered a primary target segment.

Rapid Surveillance Missions

In contrast to the previous two segments, rapid surveillance is where the bi-propellant VTOL concept likely shows its advantage: high thrust-to-weight ratio and a correspondingly fast climb to altitude. The relevant use cases are situations where the value of surveillance decays with time: the first few minutes of a developing wildfire, an industrial accident, a chemical release, or a military tip-off on a moving target. In all of these, the first overhead view drives the initial response, and the bulk of that value is unlocked only at a higher altitude, where the sensor footprint is large enough to capture the full incident. Compressing the climb phase directly shortens the time to the first useful observation, which is the metric that matters to a wildfire incident commander or a tactical operator.

Key value drivers in this segment are time to altitude, unit cost, payload mass, and endurance. To benchmark the bi-propellant concept, data were aggregated for a set of competing platforms in a comparable take-off-weight class, including civilian electric multirotors widely deployed by emergency services today, military hybrid-fuel and electric VTOL fixed-wings, an unmanned helicopter, a loitering munition, and a rocket-boosted target drone. Time to 3000 m altitude was computed from each vehicle's stated rate of climb, with 3000 m chosen as a representative observation altitude for both wildfire-scale incidents and standoff reconnaissance. For the VAPOR mission, the rate of climb has been computed from a simple preliminary equation and will be further elaborated upon in subsequent chapters. The aggregated dataset is shown in Table 2.2

[13] uavcoach.com [Date Accessed: June 16] [14] offdrones.ca [Date Accessed: June 16] [15] uavcoach.com [Date Accessed: June 16]

Table 2.2: Aggregated specifications for competing surveillance UAVs in a comparable take-off-weight class. Time to 3000 m is computed from the manufacturer-stated rate of climb. Costs are approximate per-unit figures rounded to the nearest $1,000 USD.

Aircraft	Class	Sector	t_{3000} [min]	Cost [k€]	Endur. [min]	Payload [kg]
Bi-propellant VTOL (TU Delft)	Bi-propellant VTOL	Civ.	0.3	30	63	3
DJI Matrice 400 RTK[17]	Electric multirotor	Civ.	7	14	59	6
DJI Matrice 350 RTK[18]	Electric multirotor	Civ.	10	12	55	2.7
Schiebel Camcopter S-100[19]	Unmanned helicopter	Both	8	400	360	50
AeroVironment Switchblade 600[20]	Electric loitering munition	Mil.	8	120	40	15
MotioNew Eule MH675[21]	Gasoline hybrid VTOL	Civ.	12	80	360	30
JOUAV CW-30E[22]	Hybrid VTOL fixed-wing	Civ.	12	80	480	8
YANGDA Sky Whale Max[23]	Gasoline hybrid VTOL	Civ.	12	60	600	15
AeroVironment JUMP 20[24]	Heavy-fuel hybrid VTOL	Mil.	15	1,300	780	13.6
Textron Aerosonde Mk 4.8 HQ[25]	Heavy-fuel hybrid VTOL	Mil.	17	300	840	13.6
Elbit Skylark I-eVTOL[26]	Electric VTOL fixed-wing	Mil.	18	200	150	1.2

Two groups can be identified Civilian electric multirotors (DJI Matrice 350 and 400 RTK) are inexpensive but slow to climb, needing 7–10 minutes to reach 3000 m. Military hybrid VTOL fixed-wings (Skylark I-eVTOL, Aerosonde, JUMP 20) and the Camcopter S-100 helicopter sit at one to two orders of magnitude higher cost in exchange for endurance measured in many hours rather than minutes, but their climb performance is no better, and often worse than that of civilian rotorcraft.

The bi-propellant concept occupies the most favourable region of the design space, combining low unit cost with a short time to altitude. It reaches 3000 m in approximately half a minute while maintaining a unit cost lower than that of any other solution with comparable climb performance. The trade-off is endurance. At a target 63 minutes of total mission time the bi-propellant UAV cannot loiter on station for the kind of patrol or persistent-overwatch missions that the heavy-fuel hybrids are built for. The platform is therefore best understood as a complementary first-responder asset, deployed in a recent incident and where time-to-altitude dominates value, with longer-endurance platforms taking over for sustained monitoring once the situation has stabilised.

2.2.3. SWOT analysis

Based on the previous discussion, it can be concluded that the rapid-response surveillance use case will be the primary application of the bi-propellant UAV. The market research performed for this segment in Table 2.2.2 also covered a general description of the value drivers and functions the UAV would perform. To be competitive in the previously defined segments, it is of the utmost importance to have a high climb rate, low cost, and significant payload capacity. These strengths are listed in the Strengths, Weaknesses, Opportunities, Threats (SWOT) analysis Table 2.3.

[17] drone-parts-center.com [Date Accessed: June 16] [18] enterprise.dji.com [Date Accessed: June 16] [19] wikipedia.org/Schiebel Camcopter S-100 [Date Accessed: June 16] [20] avinc.com [Date Accessed: June 16] [21] motionew.com [Date Accessed: June 16] [22] jouav.com [Date Accessed: June 16] [23] yangdaonline.com [Date Accessed: June 16] [24] avinc.com [Date Accessed: June 16] [25] thedefensepost.com [Date Accessed: June 16] [26] army-technology.com [Date Accessed: June 16]

Table 2.3: SWOT Analysis of the Proposed UAV Design

Strengths	Opportunities	Weaknesses	Threats
Higher Rate of Climb, Higher Payload Capacity (Higher T/W), Lower Emissions (HTP as Oxidiser), Operational Flexibility (VTOL), Autonomous (No ground crew required to operate the UAV)	Rapid Surveillance missions, Remote area operational usage, Rapid Response missions	Cost, Complexity of design, Short endurance, Short Range, Possible reliability issues	Jet-powered UAVs with VTOL, Piston-powered UAVs with hybrid electric for VTOL, TurboProps with VTOL, Smaller Helicopters, Long Range high MTOW more expensive UAVs

2.3. Future Market Trends *Author(s): Victor*

The entire UAV market is growing at an impressive rate. The current market is estimated at 26.12 billion USD in 2025, and it is projected to reach 40.56 billion USD by 2030, growing at a compounded annual growth rate of 9.2%, according to Markets and Markets [16]

In the civilian domain, the strongest tailwind is the growing frequency and severity of climate-related emergencies. Wildfires, floods, and industrial accidents are increasing in both number and scale, placing mounting pressure on emergency response agencies to establish aerial situational awareness faster. Electric multirotor UAVs are already deployed in this role, but their limited climb rate constrains how quickly they can cover remote or mountainous terrain. The bi-propellant VTOL concept directly addresses this gap.

A further enabler is the ongoing evolution of drone regulation. Beyond-visual-line-of-sight approvals are becoming more accessible across European and US markets, and unmanned traffic management infrastructure is maturing. This progressively unlocks the rapid long-range deployment scenarios where the concept is most competitive.

The surveillance drone market is expected to grow strongly over the next decade, increasing from USD 8.3 billion in 2026 to USD 32.9 billion by 2036, corresponding to a compound annual growth rate of 14.8% [17]. This growth is driven by rising demand for aerial monitoring in border surveillance, urban security, industrial perimeter inspection, and public safety operations. Surveillance drones are attractive because they can provide real-time video, cover difficult or dangerous terrain, and reduce the need for manual ground patrols. The report identifies multi-rotor drones as especially useful for urban monitoring, since they can hover, launch from confined spaces, and provide stable imaging near buildings. Beyond-line-of-sight operations and autonomous flight are also expected to become increasingly important, as they allow longer-range and more frequent monitoring missions with reduced operator workload. Overall, the market outlook supports the commercial relevance of VAPOR, particularly if it can offer longer endurance, reliable payload integration, and safe operation in demanding surveillance missions.
Combined, these trends suggest that the addressable market for a high-climb-rate rapid surveillance UAV will continue to grow, and that early market entry, while the competitive landscape is still forming, carries a meaningful first-mover advantage.

[16] marketsandmarkets.com [Date Accessed: June 11] [17] https://www.mouser.be/ProductDetail/Siretta, Last Accessed: June 17th

3 | Functional Diagrams

This chapter contains functional diagrams that are used to identify capabilities and functions that the system should be able to perform. Section 3.1 presents the FFD, while the FBS can be found in Section 3.2.

3.1. Functional Flow Diagram *Author(s): Noah, Duco*

The FFD is a time-sequenced flow of functions that systems have to fulfil; these functions can then be translated into functional requirements. The functions are first arranged in a top-level sequence to show the overall system flow. Each of these high-level functions is then further decomposed into lower-level functions, which are developed and shown beneath them to provide more detail on how each step is carried out.

Furthermore, for each top-level or system-level function, a specific system that has to carry out the function is specified. Logical AND/OR/NOT operators are also used to clarify the sequencing of functions, and to explain the contingencies that are taken into account (NOT is represented by $\bar{G}$ in the diagram). Top-level functions are mission phases, excluding manufacturing and end-of-life disposal, which are only operated once.

3.2. Functional Breakdown Structure *Author(s): Noah, Marco*

The FBS shows the hierarchical importance of each of the functions to be performed by the system from high to low level. It is an AND tree, showing each element as the parent of multiple other subordinate elements that constitute it. Although there are multiple layers of functions tackling subsystems and subsequent mechanisms, design choices as to the exact components and architectures are not yet made.

The functions depicted in the FBS and FFD are consistent and follow the same notation. Additionally, conditional statements are not part of the FBS diagram. The diagram can be found in Figure 3.3.

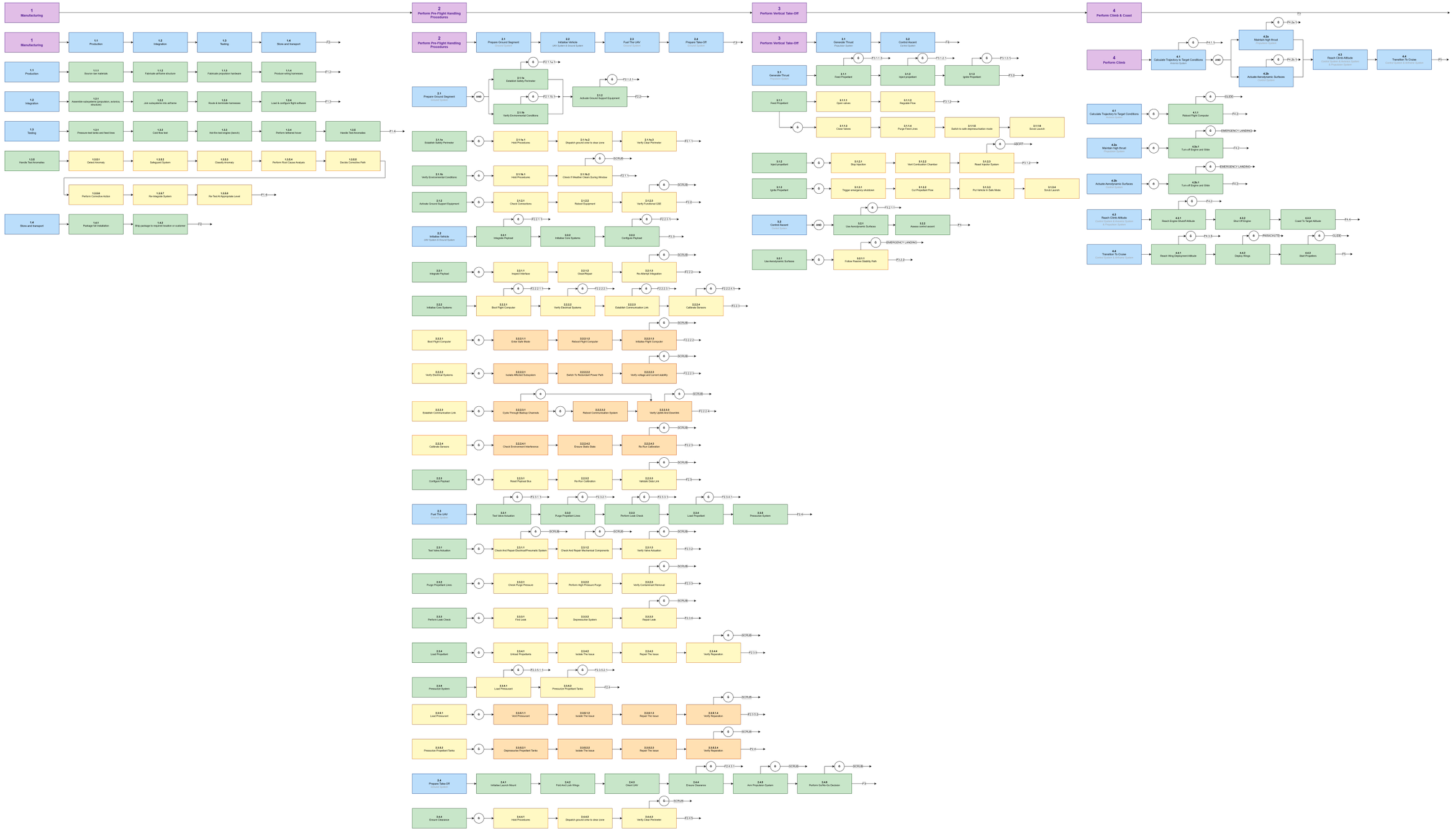

Figure 3.1: Functional Flow Diagram (Steps 1-4)

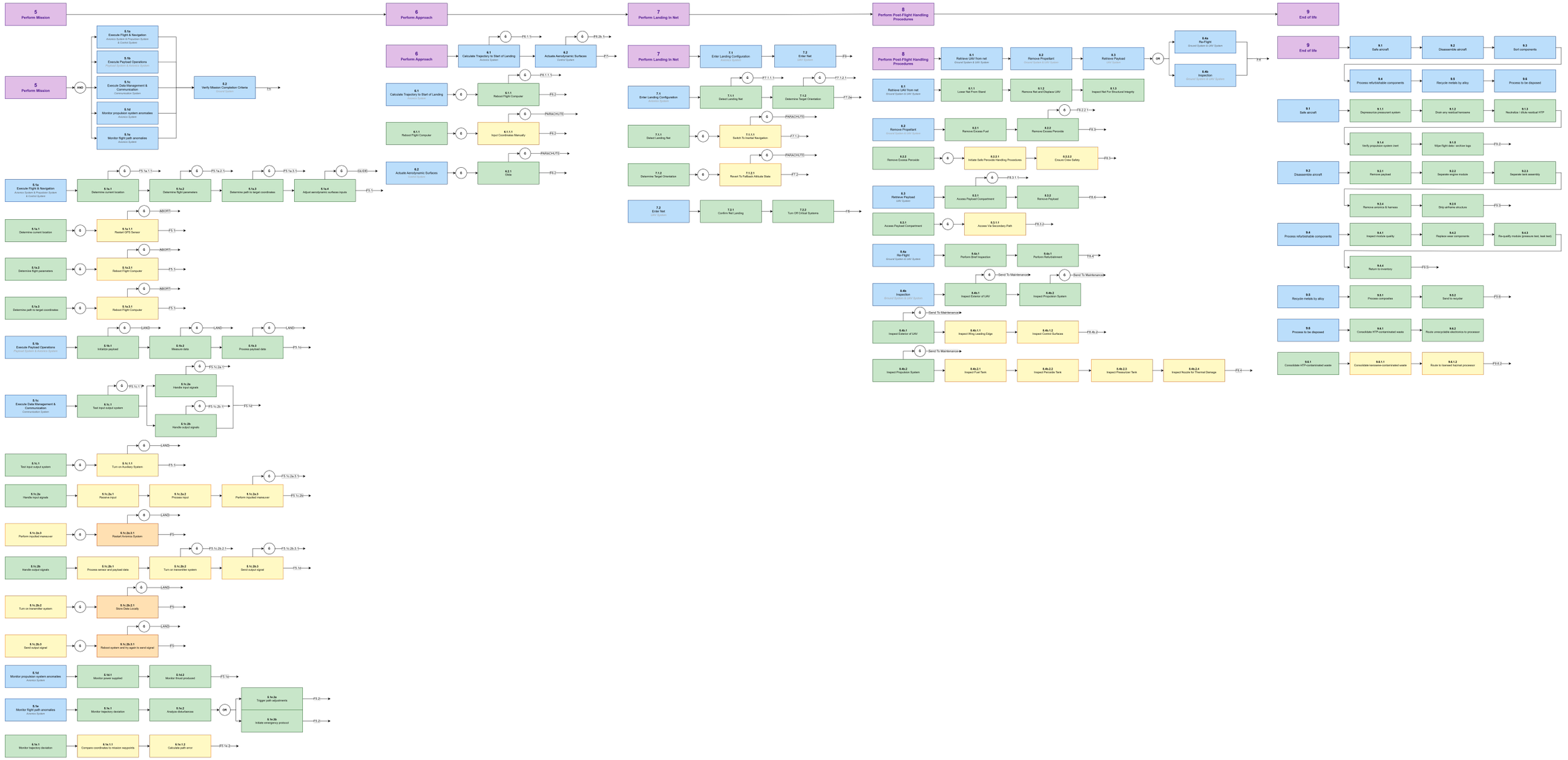

Figure 3.2: Functional Flow Diagram (Steps 5-9)

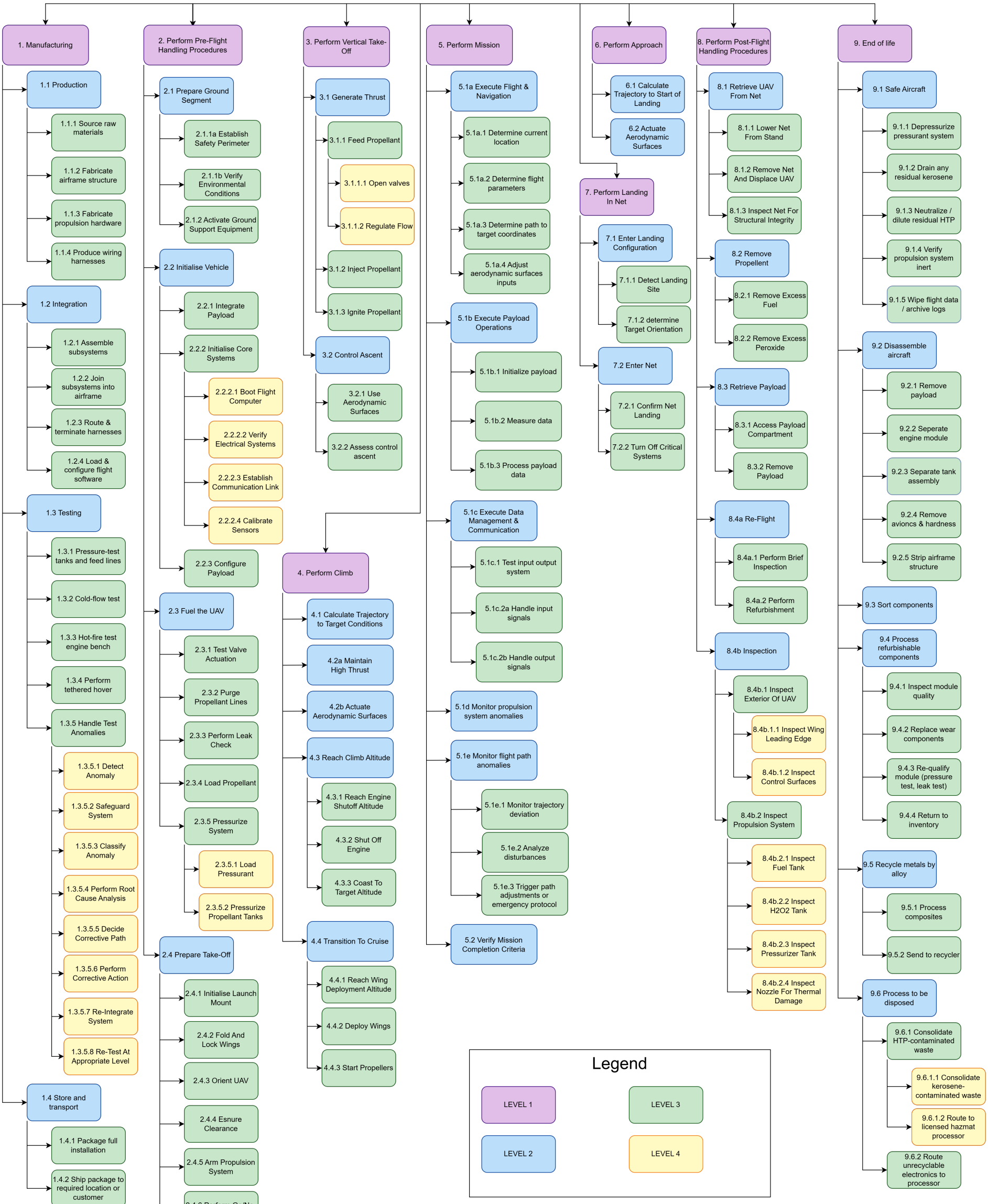

Figure 3.3: Functional Breakdown Structure

4 | Technical Risk Assessment

In this current chapter all risks concerning the success rate of the VAPOR mission are clearly defined and subsequently analysed and accounted for, following the methodology presented in Section 4.1. The full technical risk list has been compiled in excel[1], containing an analysis for all risks associated with the UAV's design. A list of new technical risks identified for the final design is presented in Section 4.2.

4.1. Methodology *Author(s): Vladimir*

For each technical risk likelihood and consequence are defined, alongside their impact on the mission as well as the corresponding abbreviations for unique risk identifiers. Likewise, in a separate table their new risk levels post-mitigation are defined together with a contingency action in the eventual case that these risk do actually occur. Furthermore, a responsible team member is assigned to each, ensuring the applicability of mitigation and contingency actions for traceability and transparency in risk management.

Risk is assessed using likelihood and consequence scores, both normalized to the range [0,1]. Likelihood is classified as Very Low (0.00–0.01), Low (0.01–0.30), Moderate (0.30–0.50), High (0.50–0.70), and Very High (0.70–1.00). Consequence is classified as Negligible (0.00–0.25), Marginal (0.25–0.50), Critical (0.50–0.75), and Catastrophic (0.75–1.00). The overall risk score is then calculated as $R = L \cdot C$, yielding values in the range [0,1] (or 0–100%). Each technical risk is assigned an identifier based on the lifecycle phase or UAV subsystem abbreviations listed in Table 4.1.

Table 4.1: Phases and sub-systems used to associate risks with.

Name	Abbreviation	Name	Abbreviation
Manufacturing	MAN	Propulsion	PRO
Pre-flight	PFH	Airframe	AFR
Post-flight	POF	Control	CTR
End of life	EOL	Avionics	AVN
External	EXT	Design	DES
		Electrical Power System	EPS

4.2. New Technical Risks Considerations *Author(s): Vladimir*

When finalizing the revision of the technical risk assessment for the design new risks have to be considered. These are included in Table 4.2, together with subsequent contingency strategies in Table 4.3. The main design considerations adding to the technical risk list concern manufacturing, preflight handling, end of life, propulsion, airframe, the electrical power system, avionics and the designing process itself. To give but one example, it was not yet determined for the midterm report that the propeller blades would most likely be manufactured, therefore no suitable risk was identified.

Table 4.2: New technical risks derived for final design

ID	Issue	Lik.	Cons.	Risk	Impact	Mitigation
TR-MAN-012	3D printed inconel engine geometry differs from design	0.05	0.50	8.00%	Repeated effort, handover delays	Post-process 3D printed engine through Hot Isostatic Pressing (HIP) and Computer Numerical Control (CNC) milling
TR-MAN-013	Tanks and piping not suitable for operating design pressures	0.10	0.90	9.00%	Repeated effort	CNC machining tanks to exact thicknesses and cylinder dome addition
TR-MAN-014	Propeller manufacturing errors	0.10	0.50	5.00%	Repeated effort, hazard	Supervise proper machine and raw material use
TR-PFH-012	Ground launch rail misalignment	0.10	0.70	7.00%	Performance loss	Include rail alignment procedure in personnel training
TR-EOL-005	Improper disposal of hazardous materials	0.15	0.50	8.00%	Environment degradation	Personnel training, choosing trusted parties to outsource hazardous materials
TR-PRO-016	Feed emergency cut-off fails to activate during test	0.05	0.95	5.00%	Testing schedule affected	Perform verification and validation before fire testing

Continued on next page

[1] Technical Risk Excel link

ID	Issue	Lik.	Cons.	Risk	Impact	Mitigation
TR-AFR-006	Wing and empennage misalignment	0.05	0.80	4.00%	Performance degradation, repeated work	Gentle handling of components and laser alignment measurement
TR-EPS-006	Short-circuit in RACEPOW battery during integration	0.05	0.80	4.00%	Thermal runaway, hazard	Careful handling during assembly and wire connection
TR-EPS-007	Payload voltage drops	0.15	0.50	8.00%	Data loss	Extensive component testing before assembly
TR-AVN-007	Faulty avionics logic	0.20	0.50	10.00%	Degraded controllability	Perform verification and validation of code
TR-AVN-008	Flight sensor failure	0.10	0.70	7.00%	Loss of control, performance loss	Addition of multiple sensors for redundancy
TR-DES-006	Off-the-shelf component selection incompatible	0.10	0.30	3.00%	Performance loss, mission delay	Cross-check subsystem assemblies with connecting parts

Table 4.3: Mitigation strategies and contingencies for new risks

ID	Mitigation	New risk	Contingency Action	Responsible Member
TR-MAN-012	Post-process 3D printed engine through HIP and CNC milling	2.75%	Reevaluate surfaces roughness values and redo post-proce	Mario
TR-MAN-013	CNC machining tanks to exact thicknesses and cylinder dome addition	3.00%	Remanufacture if budget is enough	Paul
TR-MAN-014	Ensuring proper machine and raw material use	1.75%	Remanufacture if budget is enough	Paul
TR-PFH-012	Include rail alignment procedure in personnel training	2.00%	Refurbish systems or prepare for overhaul	Marco, Mario
TR-EOL-005	Personnel training and choosing trusted parties to outsource hazardous materials	3.00%	Find suitable disposal locations	Noah, Victor
TR-PRO-016	Perform verification and validation before fire testing	1.80%	Stop all systems and evacuate personnel	Ivan
TR-AFR-006	Gentle handling of components and laser alignment measurement	1.80%	Reassemble aerodynamic surfaces	Kyle
TR-EPS-006	Careful handling during assembly and wire connection	1.50%	Retest for battery integrity	Kaj
TR-EPS-007	Extensive component testing before assembly	4.00%	Data loss	Kyle
TR-AVN-007	Perform verification and validation of code	3.75%	Emergency landing	Marco
TR-AVN-008	Addition of multiple sensors for redundancy	1.50%	Emergency landing	Mario
TR-DES-006	Cross-check subsystem assemblies with connecting parts	0.75%	Define incompatible parts and assess refitting subsystems	All

To conclude, a final risk map plotting identified risks on likelihood and consequence axes in Figure 4.1a together with a revised risk map post-mitigation showing the effect of risk management in Figure 4.1b.

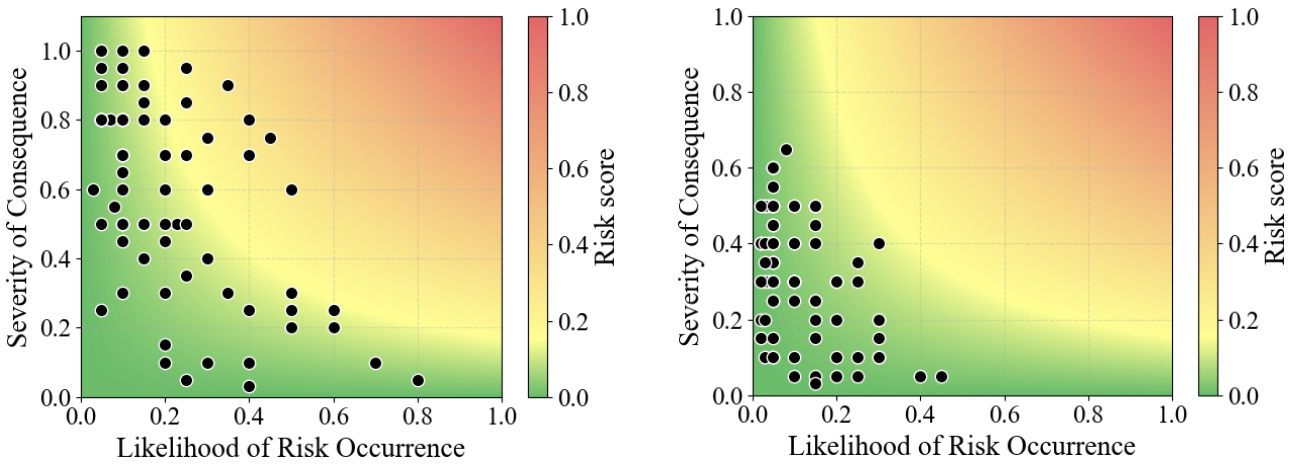

(a) Pre-Mitigation Risk Map

(b) Post-Mitigation Risk Map

Figure 4.1: Comparison of Pre and Post-Mitigation Risk Maps

5 | Trade-Off Summary

The conceptual design of ***VAPOR*** was driven by a series of trade-off studies, each selecting between competing design options at a different level of the system. These studies were carried out throughout the midterm report [1]. This chapter brings their results together so that the choices defining the final concept can be reviewed in a single place. The trade-offs are grouped by the level at which they were made. Section 5.1 covers the three system-level studies that set the overall vehicle concept, while Section 5.2 covers the subsystem-level studies that refine the individual components. In every case a sensitivity analysis was performed, and the selected option remained the winner under reasonable changes to the criteria weights.

5.1. System-Level Trade-Offs *Author(s): Paul*

Three trade-offs were decisive at the system level: the choice of the overall vehicle concept, the airframe configuration, and the Electrical Power System (EPS). Their winners are listed in Table 5.1 and explained below.

Strawman concept

The most important decision was the selection of the overall Strawman concept from six Strawman designs, which combined three secondary propulsion architectures (pure bi-propellant, hybrid-electric, and hybrid micro-turbine) with a fixed or foldable wing variant. The foldable-wing hybrid-electric design won the trade-off as being scored on endurance (40%), sustainability (30%), cost (20%), and reliability (10%). The resulting concept therefore uses a bi-propellant rocket engine for vertical ascent and an electric propeller for cruise, with a high aspect-ratio wing that folds during launch; this pairing gives the best lift-to-drag ratio and thus the longest endurance.

Airframe configuration

Six wing planforms were compared on Lift-to-Drag ratio (L/D) performance, weight, centre-of-gravity range and stability, compatibility with the launch and landing concept, and cost. The conventional configuration won both the fixed-wing and foldable-wing trade-offs, offering the best aerodynamic efficiency and lowest structural mass while remaining the simplest and lowest-risk option to build when considering vertical ascent stability.

Electrical power system

Five battery technologies were evaluated on mass, cost, volume, safety, and sustainability across the non-electric, fixed-electric, and foldable-electric power scenarios. The solid-state battery was the clear winner in all three, thanks to its high energy density and strong safety performance.

Table 5.1: System-Level Trade-Off Winners

Trade-Off	Selected Option	Score
Electrical power system	Solid-state battery	2.80
Airframe configuration	Conventional (fixed and foldable)	2.65 / 2.50
Vehicle concept (Strawman)	Hybrid-electric, foldable wing	3.80

5.2. Subsystem-Level Trade-Offs *Author(s): Paul*

With the concept fixed, a large number of subsystem trade-offs refined the individual components. The selected options are described below and collected in Table 5.2.

Propulsion system

A pressure-fed feed cycle was selected for its simplicity, low mass, and reliability, and Rocket Propellant-1 (RP-1) was chosen over Jet-A for its cleanliness. Regenerative and film cooling was retained as the only option able to sustain the required burn time at acceptable mass and cost, a full catalytic decomposition igniter was preferred for restartability, a pintle injector won on mixing and combustion stability, and helium was selected as the pressurant for its low mass. For the wetted materials, aluminium 6061-T6 was selected for the tanks and rigid feed lines, Teflon for the soft seals, and Inconel 718 for both the chamber/nozzle and the injector.

Airframe and structures
A Y-tail was selected for its stability during both the rocket ascent and cruise, and a single folding propeller was chosen over a contra-rotating arrangement that was incompatible with the folding requirement. Aerospace aluminium 7075-T6 was identified as the leading structural material, with carbon-fibre thermoplastics and thermosets kept as candidates pending detailed load requirements. The avionics were not scored in a matrix; the Pixhawk 6X was selected as a qualitative baseline flight controller.

Operations and safety
Net catching was selected as the landing method, fuelling on site over pre-loaded canisters, and a visual inspection after every flight combined with routine technical inspections over a full technical inspection each flight. A vertical take-off using a reusable supporting structure was selected to avoid the mass penalty of onboard landing gear. A separate recovery-system study favoured a parachute on environmental-safety grounds, to be reconciled with the net-catching landing method during the detailed design phase.

Table 5.2: Subsystem-Level Trade-Off Winners

Trade-Off	Selected Option	Score
Propulsion subsystem		
Feed system	Pressure-fed	2.80
Fuel	RP-1	2.10
Cooling system	Regenerative + film	2.40
Ignition system	Full catalytic decomposition	2.40
Injector type	Pintle	2.70
Pressurising gas	Helium	2.40
Tank material	Aluminium 6061-T6	2.70
Rigid feed material	Aluminium 6061-T6	3.00
Soft feed material	Teflon	2.70
Chamber & nozzle material	Inconel 718 (Ni superalloy)	2.45
Injector material	Inconel 718 (Ni superalloy)	2.40
Airframe & structures subsystem		
Tail type	Y-tail	2.40
Propeller type	Single (folding)	2.55
Structural material	Aerospace aluminium 7075-T6	2.60
Operations & safety		
Landing method	Net catching	2.50
Recovery system	Parachute landing	2.20
Fuelling	Fuel on site	2.40
Inspection	Visual + routine technical	2.60
Take-off manoeuvre	Supporting structure	2.40

6 | Verification & Validation

This chapter presents the verification and validation framework applied to the technical design performed in this report. This is done in alignment with the V-model [3].

Section 6.1 outlines the general Verification and Validation (V&V) procedures followed throughout this report, defining the methods by which requirements are verified or validated. Section 6.2 presents the sensitivity analysis framework, describing the general approach used to assess the robustness of the design with respect to uncertainties in key design parameters.

6.1. Verification & Validation Procedures *Author(s): Noah*

V&V is an essential part of the design process, providing confidence that the system is built correctly and that the right system is being built. In this context, verification ensures that the design complies with its specified requirements, while validation confirms that the final system fulfils the mission objectives and the expectations of the stakeholders. The V&V strategy adopted in this project follows the V-model framework [3], which provides full traceability of requirements throughout the project lifecycle and clearly defines where each V&V activity takes place.

This section is structured as follows. Subsection 6.1.1 describes the V&V procedures applied to the design tools developed and used by the team. Subsection 6.1.2 presents the test campaign, covering subsystem, system-level, and integrated system tests. Finally, Subsection 6.1.6 outlines the mission-level validation strategy.

6.1.1. Design Tool V&V Procedure

To support the design of the VAPOR mission, the team developed and used two categories of tools: in-house simulation tools written in Python and MATLAB, and commercially available software for aerodynamic and structural analysis (e.g. Computational Fluid Dynamics (CFD) and Finite Element Method (FEM) packages).

The in-house tools cover flight performance sizing, propulsion modelling, stability and control analysis, and electrical power system budgeting. Since these tools are developed internally, they carry an inherent risk of programming errors, incorrect physical assumptions, and logic inconsistencies. For commercially available tools such as CFD and FEM packages, since their source code cannot be inspected, alternative verification strategies are applied, including mesh convergence studies, solver convergence checks, and cross-validation against analytical hand calculations.

All in-house code is thus subjected to a structured verification process, as summarised in Table 6.1, where the applied techniques are stated in increasing order of integration level. Additionally, all code is checked by an independent team member before integration testing, to ensure correctness.

Table 6.1: Verification Techniques for In-House Design Tools

Technique	Description	Performer
Unit Test	Verification of individual functions or formulas against hand calculations or known analytical results.	Developer
Module Test	Verification of a self-contained module (e.g. International Standard Atmosphere (ISA) atmosphere model, propellant mass estimator) by comparing outputs to reference values.	Developer
Subsystem Test	Verification of integrated modules forming a functional unit (e.g. the propulsion sizing subsystem) against expected physical behaviour.	System Engineer
System Test	End-to-end verification of the complete sizing or simulation tool (e.g. full mission performance sweep) to confirm correct module interaction and data flow.	Independent Tester
Consistency Check	Verification that physical constraints are preserved throughout a simulation (e.g. total UAV mass decreasing monotonically as propellant is consumed; power budget summing correctly across all modes).	System Engineer

Successful verification does, however, not guarantee that a tool correctly represents real-world physics. Validation therefore complements verification by comparing tool outputs against independent reference data. The following hierarchy of validation sources is used, in order of preference:

1. **Physical test data** obtained from the test campaign described in Subsection 6.1.2, used as the primary validation source for propulsion, aerodynamic, and structural tools.
2. **Published experimental or flight data** from comparable UAV platforms and rocket motors available in the open literature.
3. **Cross-tool validation**, where the output of one tool (e.g. MATLAB flight performance model) is compared against an independent tool solving the same problem (e.g. a Python implementation or a commercial tool).
4. **Monte Carlo analysis**, applied where validation data is sparse, to define the sensitivity of tool outputs to combined parameter uncertainties and to ensure the design remains within acceptable bounds.

Validation criteria and pass/fail thresholds are defined on a per-tool basis, as the acceptable level of discrepancy varies significantly between topics.

6.1.2. Test Campaign

The test campaign is structured in three sequential phases: subsystem tests, system-level tests, and integrated system tests. Each phase builds on the results of the previous one, and failures are expected to be resolved before proceeding to the next phase. A final full-mission demonstration concludes the campaign. Throughout the campaign, the budget allocated for testing activities is constrained to university-accessible or readily available facilities, consistent with academic project constraints.

6.1.3. Subsystem Tests

Subsystem tests isolate individual components to verify that each meets its performance specifications before integration.

Table 6.2: Subsystem Test Objectives And Their Used Facilities

Subsystem	Test Objectives	Facility & Equipment
Chemical Propulsion	• Steady-state thrust and total impulse • Multi-burn re-ignition capability • Burn time and burn-out detection • Structural integrity under firing loads • Noise and vibration characterisation • Propellant delivery and feed system performance	• Static rocket test stand • Load cell • High-frequency pressure transducer • High-speed camera
Electric Propulsion	• Maximum rotor Revolutions Per Minute (RPM) and thrust generation • Motor and propeller efficiency across operating range • Thermal behaviour under sustained load	• Small wind tunnel or thrust stand • Load cell • Power analyser • Thermocouple array
Folding Mechanisms	• Deployment and retraction time (wing and propeller) • Locking mechanism engagement and release reliability • Structural integrity of the mechanism when locked • Repeatability over multiple cycles	• Mechanical test rig • High-speed camera • Cycle counter

Subsystem	Test Objectives	Facility & Equipment
Avionics & Sensors	• Measurement accuracy and noise characteristics of Inertial Measurement Unit (IMU), Global Positioning System (GPS), and barometer • Maximum sensor sample rates • Data logging integrity	• Electronics test bench • Reference measurement equipment
Radio Link	• Signal strength as a function of range • Available data bandwidth and bit rate • Link reliability at maximum operational range	• Open outdoor terrain • Signal analyser • Area ≥ maximum required Radio Frequency (RF) range
Aerodynamic Surfaces	• Lift and drag coefficients of the wing • Control surface effectiveness (lift, drag, pitching moment vs. deflection angle) • Stall onset characteristics	• Low-speed wind tunnel • Scaled aerodynamic model • Three-axis force and moment balance

6.1.4. System Tests

System tests verify that integrated subsystems interact correctly and collectively meet top-level performance requirements.

Table 6.3: System Test Objectives And Their Used Facilities

System	Test Objectives	Facility & Equipment
Propulsion	• Verify electric motor spin-up timing during rocket engine burn • Confirm smooth propulsion handover from rocket to electric motor after burn-out • Confirm thrust levels meet mission requirements across both propulsion modes	• Rocket test stand • Load cell • High-speed camera
Flight Control	• Verify that the flight control law generates correct actuator commands in response to simulated flight states • Validate complete control logic including VTOL, transition, and fixed-wing cruise modes • Verify autonomous safety response to simulated sensor faults	• Hardware-in-the-loop test rig • Flight simulation environment
Airframe Structure	• Verify that the assembled airframe sustains all design load cases without permanent deformation • Confirm structural margins under VTOL and cruise loading conditions	• Structural test rig • Calibrated load application equipment • Strain gauges
Electrical Power System	• Verify total deliverable power and peak load capacity across all mission phases • Confirm correct power distribution and protection behaviour under fault conditions	• Electronics bench • Electronic load emulator • Power analyser

6.1.5. Integrated System Tests

Integrated system tests verify the combined behaviour of multiple subsystems under representative operating conditions, with particular focus on cross-subsystem interactions that cannot be assessed in isolation.

Table 6.4: Integrated System Test Objectives And Their Used Facilities

Systems	Test Objectives	Facility & Equipment
EPS, Avionics & Control	• Confirm that electromagnetic interference from the electric motor and rocket ignition does not corrupt sensor data or actuator commands • Verify correct power sequencing across all flight phases	• Electronics bench • Simulated sensor inputs • Electromagnetic interference analyser
Airframe & Propulsion	• Verify that the airframe withstands vibration and acoustic loads generated during rocket firing • Confirm structural integrity is maintained throughout the full burn duration • Verify that wing deployment occurs correctly following rocket burn-out under realistic vibration conditions	• Rocket test stand • Tri-axial accelerometers • High-speed camera
Full System (Ground)	• Perform a full end-to-end ground functional test of all subsystems operating simultaneously • Verify correct sequencing of all mission phases from pre-launch through net landing • Confirm autonomous safety mode activation under injected fault conditions	• Full UAV assembly • Ground control station • Hardware-in-the-loop flight simulation environment

6.1.6. Mission V&V Procedure

Mission validation has the goal of confirming that the complete VAPOR system effectively fulfils its surveillance and reconnaissance mission objectives under realistic operating conditions. While product verification asks whether the system was built correctly, mission validation asks whether the right system was built.

6.1.7. Simulation-Based Validation

Prior to physical flight testing, the team will conduct full end-to-end mission simulations to verify correct sequencing, timing, and autonomous command execution under nominal conditions. These simulations will test the complete mission profile: vertical take-off, coast, wing deployment, transition to fixed-wing cruise, payload operation over the surveillance area, and net landing. Robustness will be assessed by simulating degraded scenarios, including loss of one sensor, partial communication link failure, and propulsion anomalies, to confirm that autonomous safety responses engage correctly.

Physical mission validation will proceed in an incremental fashion, reducing risk at each step before expanding the scope of the test:

1. **Launch Test** to validate take-off performance.
2. **Transition and cruise tests** to validate the handover from VTOL to fixed-wing flight mode and back, first at reduced rocket impulse levels and subsequently at full mission impulse.
3. **Payload integration tests** to confirm that the surveillance payload operates correctly in flight and that data links function over the required range.
4. **Full-mission demonstration** replicating the complete operational profile, including all flight phases, payload activation, and autonomous return-to-home landing.

At each stage, the outcome is evaluated against pre-defined acceptance criteria before proceeding to the next phase. Any failure to meet acceptance criteria triggers a design review and, where necessary, a design modification prior to re-testing.

Lastly, mission-level requirements related to surveillance area coverage, image quality, endurance, and operational range will be validated using a combination of in-flight data logging and post-flight analysis. Payload performance (e.g. ground resolution, frame rate, data link throughput) will be assessed against the requirements using dedicated test flights over a defined target area. Noise measurements will be taken at defined distances during both VTOL and cruise flight phases to validate regulatory compliance. Where full-

scale testing is constrained by airspace authorisation or safety considerations, representative sub-scale or partial-mission profiles will be used, with scaling factors applied and clearly documented.

6.2. Sensitivity Analysis *Author(s): Noah*

Sensitivity analysis evaluates how uncertainty in input parameters propagates to key performance metrics of a design. Rather than treating the design point as fixed, it examines the response of the system to perturbations in the input variables, allowing the relative importance of design parameters to be quantified. The same methodology is applied throughout all technical chapters to ensure consistent and comparable results.

For each subsystem, a set of design parameters, $\mathbf{x} = x_1, x_2, \ldots, x_n$, is selected for the sensitivity analysis. Parameters are included if they exhibit significant uncertainty at the current design stage or represent design choices that have not yet been finalized. Parameters fixed by requirements, regulations, or other external constraints are generally excluded unless their associated uncertainty is explicitly being evaluated.

A nominal design point, $\mathbf{x}_0$, is defined based on the baseline configuration established in the respective sections. All sensitivity results are evaluated relative to this baseline.

For each perturbation of the input parameters, the key performance functions of the system are re-evaluated using the updated parameter set. The resulting outputs are then compared to the nominal case in order to assess the sensitivity of the system response to individual parameter variations. This allows the influence of each design variable on the overall system performance to be quantified and ranked.

The magnitude of each parameter variation is selected based on available design margins, expected uncertainty ranges, and relevant physical or operational constraints. If strict bounds exist, perturbations are limited to remain within feasible and physically meaningful ranges. This ensures that all sensitivity results remain representative of realistic design variations and do not violate underlying system constraints.

7 | Propulsion System Design

This chapter presents a detailed design of VAPOR's primary propulsion system, this propulsion system is what enables VAPOR to climb to altitude in under 30 seconds, making it a competitive asset in the market. Firstly, a brief description of the system and its subsystem is given in Section 7.1, secondly, the methodology of the design is extensively treated in Section 7.2. Consequently, the results are presented in Section 7.3, afterwards, a sensitivity analysis is performed in Section 7.4. Finally, a discussion on the conclusions and a reflection on the limitations of the design is provided in Section 7.5.

7.1. System Description *Author(s): Marco*

This section outlines the proposed propulsion system and introduces the main components of each subsystem. The sizing methodology and detailed design choices are discussed in Section 7.2.

The propulsion system uses a pressure-fed liquid bipropellant rocket engine with 98% H_2O_2, commonly referred to as HTP, as oxidizer and RP-1 as fuel. Both propellants are stored in separate tanks and pressurized by helium from a dedicated tank.

From the storage tanks, the oxidizer and fuel follow different flow paths before entering the combustion chamber. The RP-1 is routed directly to the injector, while the HTP first passes through regenerative cooling channels, absorbing heat from the chamber walls. It then flows through a catalyst bed, where it fully decomposes, before being injected through a pintle injector to mix with the fuel.

Combustion occurs in an cylindrical chamber, producing high-pressure gases that expand through a convergent-divergent nozzle to generate thrust. As the vehicle operates at low atmospheric altitudes, the nozzle is optimized for sea-level conditions to maximize thrust and take-off performance.

7.2. Methodology *Author(s): Vladimir, Marco, Mario, Noah*

The design process for the propulsion system is a complex task as the various subsystem largely interact with each other, leading to a variety of dependencies within the different parts and an overall complicated optimization problem to solve. This section presents the methodology that has been used for sizing of the following subsystems: storage & feeding, system architecture, thrust chamber, and cooling methods. All of these components interact with each other such that each one should be sized parametrically in order to solve a global optimization problem. This is addressed with the help of a python script developed and dedicated for this specific analysis. The structure and logic of the code and its integral parts to help run the global optimization are further described below in subsequent subsections.

7.2.1. Assumptions

To keep the engine analysis feasible while maintaining sufficient accuracy for the preliminary design phase, several assumptions were made. These can be divided into two categories: assumptions inherent to the Rocket Propulsion Analysis (RPA) software used to determine combustion and flow properties, and assumptions introduced in the Thermal Analysis Model (TAM). The main assumptions considered in each category are listed below.

RPA-1 Combustion is assumed adiabatic and isenthalpic. No heat transfer occurs to or from the combustion chamber, and the total enthalpy remains constant during the combustion process.[4]

RPA-2 Nozzle flow is assumed adiabatic and isentropic. Expansion through the nozzle is considered frictionless, with no dissipative losses and constant entropy throughout the flow. However losses are estimated resulting in nozzle and combustion efficiencies.[4]

RPA-3 Gaseous species are treated as ideal gases. All working fluids obey the ideal gas law.[4]

RPA-4 Infinite-area chamber approximation. When the chamber cross-sectional area is large relative to the throat (area ratio > 4), inlet velocity is considered negligible, such that stagnation and static conditions are taken as equal at the chamber inlet.[4]

TAM-1 The Bartz equation is used for the internal convective film coefficient, which assumes fully developed turbulent boundary layer flow.

TAM-2 Conduction is modelled as purely one-dimensional in the radial direction (no circumferential or axial conduction).

TAM-3 Natural convection on the outer surface is modelled using a Churchill-Chu correlation for a vertical cylinder, assuming sea-level atmospheric air at all locations.

TAM-4 Gas properties in the combustion chamber are linearly interpolated from RPA data between the injector face and the chamber inlet, since only a small variation is present across this region.

TAM-5 The dynamic viscosity in the convergent and divergent nozzle sections is evaluated using a simplified version of Sutherland's law [1], approximately scaling with temperature as $\mu \propto \sqrt{T}$.

7.2.2. Thrust Chamber and Feeding System

The optimization is done by firstly identifying the parameters that can be chosen by design, and secondly by iterating over them in order to pinpoint the global optimum. A number of cost functions have been defined as to provide a mean of quantifying the performance of a certain set of parameters, these will be discussed later. The solution is therefore found by choosing the unique set of parameters that minimizes the weighted sum of the square of the residuals of the cost functions.

Target Parameters

The parameters subject to optimisation are itemised below:

1. **O/F**: This parameter directly governs the efficiency of the engine, the temperatures inside the thrust chamber, and the overall mass & volume performance of the engine. Its value is optimized in the range between 3 and 9, values outside these bounds would worsen the performance to an unfeasible extent.
2. **Chamber pressure** ($\mathbf{p_c}$): This parameter directly influences the pressure ratio and therefore the specific impulse and the thrust chamber's dimensions. Its value is optimized in the range between 1 and 3 MPa. Values lower than 1 Mpa would lead to an extremely low specific impulse, high mass flow, and large throat area, while values above 3 MPa would lead to an increase in risk, a higher required pressure for the pressurants, higher tank masses, and difficulties in manufacturing.
3. **Contraction Ratio (CR)**: This ratio is defined as the ratio between the combustion chamber's area and the throat area (A_{cc}/A_t), it significantly influences the thrust chamber's dimensions and the distribution of gas properties along the nozzle. Its value is optimized in the range between 2 and 10.

These values are also for the most part overlapping with ranges used for optimization studies on peroxide engines provided by A. Okninski et al. [5]. For the rest of this chapter, when referring to a "set of parameters", it is meant a combination of O/F, p_c, and CR.

Geometric considerations

Furthermore, considerations are made with respect to the characteristic length (L*) and the nozzle geometry. The characteristic length is a crucial parameter that determines the combustion chamber geometry, its volume and the residence time of each of the combustion gases, further explanation will be provided later in this section. Performing the optimization while keeping the nozzle's geometry as a variable has proved challenging, as a consequence, a simple geometry is defined at this stage, and optimized in a later stage. The assumed geometry consists of a conical convergent-divergent nozzle with half angles of 30 ° and 15 ° for the convergent and divergent zones respectively. This preliminary geometry is defined for a sample set of parameters (O/F, p_c, CR) = (7.5, 3 MPa, 5) in Figure 7.1.

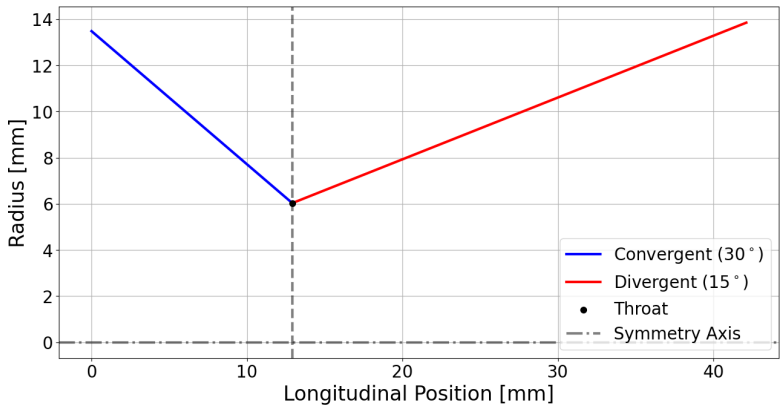

Figure 7.1: Preliminary Nozzle Geometry used for optimization

RPA software data and thermodynamic analysis

Combustion analysis has been performed primarily with the aid of the RPA software [6]. However, the software presents some limitations that are deemed too significant to be neglected, in particular in relation to

[1] Sutherland's Law [Date accessed: June 9]

the distribution of the properties of the gas products along the nozzle. As a consequence, starting from the RPA software, a database of data points has been generated an exported in Python. From that, the gas properties of interest are calculated at any given position along the thrust chamber either analytically or by means of interpolation of the RPA data. The results are always verified against the ones of both the RPA and Chemical Equilibrium with Applications (CEA) software [7].

The database was created as follows: the RPA program was run for a range of combinations of O/F, p_c, and CR inside the bounds specified above, the step in both oxidizer-to-fuel ratio and chamber pressure was of 0.1, while the values of contraction ratio used as data points were: 2, 3.5, 5, 8, and 10 the data points were then linearly interpolated to generate continuous functions.

The conditions at the combustion chamber, including the combustion gases properties, and performance parameters related to these: chamber temperature, specific impulse, characteristic velocity, and thrust coefficient, are assumed to be dependant only on O/F and p_c, in other words the contraction ratio is assumed to only influence the distribution of the gas properties along the nozzle but not the initial (combustion chamber) and final (exhaust) conditions. Moreover, these parameters are directly taken from the RPA software.

In particular, the chamber temperature (T_c) is calculated via thermodynamic equilibrium and mainly depends on the O/F, while p_c has a minimal impact, this is evidently shown in Figure 7.2, where various lines of chamber temperatures in function of chamber pressure are plotted, each for a specific O/F. It can be seen how the chamber temperature is non-linear with respect to the O/F.

The O/F that produces the maximum chamber temperature is the one that ensures stoichiometric conditions, which for this engine is about 7.35. On the other hand, the specific impulse (I_{sp}) varies significantly with both O/F and p_c, as shown in Figure 7.3.

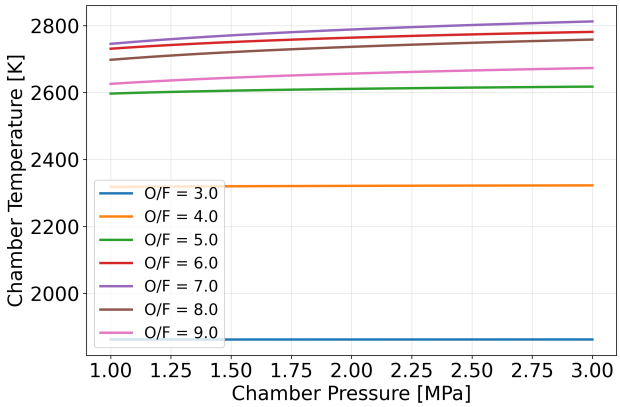

Figure 7.2: Chamber Temperature in function of Chamber Pressure and Oxidizer-to-Fuel ratio

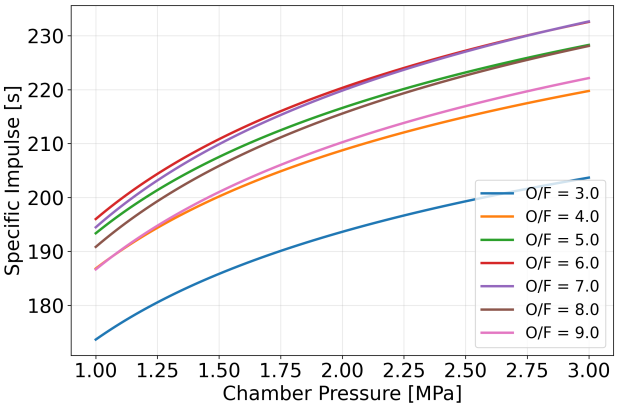

Figure 7.3: Specific Impulse at sea level in function of Chamber Pressure and Oxidizer-to-fuel ratio

Figure 7.3 again shows various graphs of specific impulse against chamber pressure, each for a specific O/F. As shown in the graph, the specific impulse does not reach its maximum for maximum chamber temperature (stoichiometric conditions), this happens because for fuel-rich mixtures both the chamber temperature and average molecular mass of the products decrease, the former is responsible for a decrease in specific impulse while the latter for an increase, as it's shown in Equation 7.1.

$$I_{\text{sp}} = \frac{1}{g_0} \cdot \sqrt{\frac{2\gamma}{\gamma - 1} \frac{R_u T_c}{M_w} \left(1 - \left(\frac{p_e}{p_c}\right)^{\frac{\gamma-1}{\gamma}}\right)} \tag{7.1}$$

Here the square root term represents the nozzle exhaust velocity, v_e, g_0 is Earth's gravitational acceleration at sea level, γ is the specific heat ratio, M_w the average molecular mass, R_u the universal gas constant and p_e/p_c is the expansion ratio, this is where the contribution of the chamber pressure plays a role: while the exhaust pressure is constant, the chamber pressure can be allowed to vary where a higher chamber pressure yields a higher specific impulse. It's important to note that the specific impulse (and other general parameters such as thrust, mass flow and characteristic velocity) are calculated based on gas properties just after

combustion, assuming frozen equilibrium; however, in order to investigate the variation of these parameters along the nozzle, shifting equilibrium is used.

For O/Fs around 6 the decrease in molecular mass is more significant than the decrease in chamber temperature, while lowering the O/F even more yields the opposite effect. From this point of view, increasing the O/F to values above 7.35 yields both a decrease in chamber temperature and an increase in average molecular mass, worsening the performance even further.

Secondly, the volumetric impulse is defined in Equation 7.2, the average density of the propellant in Equation 7.3, the total mass flow in Equation 7.4, and the burn time in Equation 7.5.

$$I_\rho = \bar{\rho} \cdot I_{\text{sp}} \quad (7.2) \qquad \bar{\rho} = \frac{\rho_{\text{ox}} \dot{m}_{\text{ox}} + \rho_{\text{fuel}} \dot{m}_{\text{fuel}}}{\dot{m}_{\text{tot}}} \quad (7.3) \qquad \dot{m} = \frac{F_T}{I_{\text{sp}} \cdot g_0} \quad (7.4) \qquad t_b = M_p / \dot{m} \quad (7.5)$$

where $\bar{\rho}$ is the average density of the propellant, $\dot{m}$ the mass flow, F_T the fixed sea level thrust of 500 N as specified in the requirements, I_{sp} the sea level specific impulse calculated from Equation 7.1, and M_p the total propellant mass. The subscripts ox and fuel refer to the oxidiser and fuel, respectively. The individual mass flows for the oxidiser and fuel are later calculated in Equation 7.24 and Equation 7.25. The thrust is set to be equal to 500 N at sea-level such that at any altitude it will be higher than the required thrust, as it increases with decreasing atmospheric pressure.

Next, the area expansion ratio for a given pressure expansion ratio and gas properties can be computed with Equation 7.6, with the throat area A^* as defined in Equation 7.7 from the characteristic velocity c^*.

$$\frac{A_e}{A^*} = \frac{\Gamma(\gamma)}{\sqrt{\frac{2\gamma}{\gamma-1}\left(\frac{p_e}{p_c}\right)^{\frac{2}{\gamma}}\left[1-\left(\frac{p_e}{p_c}\right)^{\frac{\gamma-1}{\gamma}}\right]}} \quad (7.6) \qquad A^* = \frac{c^* \dot{m}}{p_c} \quad (7.7)$$

where $\Gamma(\gamma)$ is the Vandekerckhove function [8], p_e/p_c the expansion ratio, c* the characteristic velocity, $\dot{m}$ the mass flow, and p_c the chamber pressure. From Equation 7.6 and Equation 7.7 the throat and exit diameters easily follow, the cross-sectional area of the combustion chamber is related to the contraction ratio as shown in Equation 7.8, hence the combustion chamber diameter is directly a function of one of the parameters subjected to optimization. Given these areas, the nozzle can be designed freely; as already explained, and shown in Figure 7.1, for optimizing a conical nozzle is used; the length of the convergent and divergent parts are:

$$A_{cc} = CR \cdot A^* \quad (7.8) \qquad L_{\text{conv}} = \frac{D^* \cdot \left(\sqrt{CR}-1\right)}{2\tan(\lambda_{\text{conv}})} \quad (7.9) \qquad L_{\text{div}} = \frac{D^* \cdot \left(\sqrt{A_e/A^*}-1\right)}{2 \cdot \tan(\lambda_{\text{div}})} \quad (7.10)$$

where D^* is the throat diameter, and λ_{conv} and λ_{div} are the convergent and divergent half-angles respectively. Lastly, the length of the combustion chamber can also be found by combining Equation 7.11 and Equation 7.12 from Sutton [9].

$$V_c = L^* \cdot A^* \quad (7.11) \qquad V_c = A_{\text{cc}} \cdot L_{\text{cc}} + \frac{A_{\text{cc}} \cdot L_{\text{conv}}}{3}\left(1 + 1/CR + \sqrt{1/CR}\right) \quad (7.12)$$

Here V_{cc} is the combustion chamber volume, that takes into account also the convergent part of the nozzle, L^* is the characteristic length, and L_{cc} is the combustion chamber length (what is solved for). Therefore, it has been shown that the engine performance and nozzle geometry can be found for any set of parameters. However, the distribution of gas properties along the nozzle still has to be defined.

The are two main reasons why the gas properties along the nozzle are of interest. Firstly, they are required for a detailed analysis of the engine's regenerative cooling, in particular in relation to the heat exchange between the gases, the nozzle's walls and the coolant. Secondly, it is essential for the detailed design phase, as it allows a complete description of the flow-field, ensuring that all relevant thermodynamic and gas-dynamic properties are properly captured throughout the nozzle. These properties are studied, as explained above, by creating a database and interpolating between data points.

The RPA software provides information only for four data points, namely: injector, inlet, throat, exhaust; where the inlet is defined as the inlet of the converging part of the nozzle. Some of the gas properties do not vary significantly along the nozzle and are simply linearly interpolated between the four stations, these

include: specific heat ratio, γ, specific gas constant, R, molecular mass, M_w, and specific heat at constant pressure, c_p. All the other parameters are interpolated linearly only between the injector and the inlet, where the variation is minimal, while they are calculated analytically or approximated numerically between the other stations, the resulting values are then checked with both the RPA and CEA software.

The first function defined is the area function, this calculates the nozzle's cross-sectional area based on a given imported geometry, at any location x of either the convergent or divergent segment. Consequently, the variation of Mach number can be defined, Equation 7.13 can be used assuming isentropic flow and ideal gas behaviour [2].

$$\frac{A}{A^*} = \frac{1}{M}\left[\frac{2}{\gamma+1}\left(1+\frac{\gamma-1}{2}M^2\right)\right]^{\frac{\gamma+1}{2(\gamma-1)}} \quad (7.13) \qquad \frac{A}{A^*} = \left(\frac{\gamma+1}{2}\right)^{-\frac{\gamma+1}{2(\gamma-1)}}\left(\frac{p}{p_c}\right)^{-\frac{1}{\gamma}}\sqrt{\frac{\gamma-1}{\frac{2\gamma}{\gamma-1}\left[1-\left(\frac{p}{p_c}\right)^{\frac{\gamma-1}{\gamma}}\right]}} \quad (7.14)$$

Here A/A^* is the area at a certain location in the engine divided by the throat area and M is the Mach number at said location x, where $x = 0$ is . The equation has two distinct solutions for the same area ratio and cannot be solved for the Mach number analytically, as a consequence, a numerical solver is employed, this solver approximates the two solutions numerically and assigns the subsonic one to the convergent section and the supersonic one to the divergent section. It has to be noted that if the pressure ratio is not high enough then supersonic flow does not develop inside the nozzle, however for the considered pressure bound this was never found to be the case. Errors with respect to values reported by the mentioned softwares are in the order of 2%.

Furthermore, the pressure distribution along the nozzle is also a function of area ratio, it can be calculated via Equation 7.14 assuming isentropic flow and ideal gas behaviour [9]. Equation 7.14 also has two solutions and cannot be solved analytically, the same solver as previously mentioned is used to solve this equation as well; firstly the critical pressure ratio is calculated, this is the pressure ratio at the throat, where the area ratio is equal to 1, then the two solutions are approximated numerically, if the pressure ratio is higher than the critical pressure ratio, then the solution is valid for the convergent part of the nozzle, if the pressure ratio is lower than the critical one, the solution is valid for the divergent section.

Subsequently, the temperature distribution can be calculated analytically, the derivation is made from simple relations shown in Equation 7.15, Equation 7.16 and Equation 7.17. Combining these relations and solving for temperature yields Equation 7.18.

$$p = \rho RT \quad (7.15) \qquad v = M\sqrt{\gamma RT} \quad (7.16) \qquad \dot{m} = \rho v A \quad (7.17) \qquad T = \frac{\gamma}{R}\cdot\left(\frac{pMA}{\dot{m}}\right)^2 \quad (7.18)$$

Here T represents the temperature at a certain location x along the nozzle; p, M, and A represent the pressure, Mach and area respectively at said location x, while $\dot{m}$ is the constant mass flow calculated in Equation 7.4. This equation was implemented to calculate the temperature distribution, however, results were not satisfactory with errors up to 8-10%. After investigating, it was found that the mass flow that the RPA and CEA softwares calculate along the nozzle is different than the one calculated from performance analysis from Equation 7.4, this created an internal inconsistency inside the software that generated significant errors for the temperature. As a consequence, by comparing the values provided by the softwares to literature, it was decided to ultimately consider correct the values provided along the nozzle. Therefore, a correction factor was generated for the analytical model presented in Equation 7.18, this correction factor is constructed by calculating its value at data points and then applying piecewise linear interpolation between the stations.

Subsequently, all of the variables that depend on temperature can now be computed at any location and for any set of parameters. Starting with the density, it can be computed from the ideal gas law, as shown in Equation 7.19. Secondly, the viscosity is a function of temperature and can thus be computed, this is shown in Equation 7.20, which represents Sutherland's Law [3].

$$\rho = \frac{p}{RT} \quad (7.19) \qquad \mu(T) = \mu_{ref}\left(\frac{T}{T_{\text{ref}}}\right)^{\frac{3}{2}}\frac{T_{ref}+S}{T+S} \quad (7.20)$$

[2] NASA Compressible Flow [Date accessed: June 8] [3] Sutherland's Law [Date accessed: June 9]

Here $\mu(T)$ represents the viscosity at any temperature T, μ_{ref} and T_{ref} represent a reference value of viscosity and the temperature at which that viscosity is calculated respectively, and S is Sutherland's constant, specific for each mixture. Since the Sutherland's constant is not known it's difficult to estimate the viscosity, therefore a simplification was performed. Since the temperatures in the engine will be much higher than the Sutherland's constant, the following approximations are made: $T + S \approx T$ and $\left(\mu_{\text{ref}} \cdot (T_{\text{ref}} + S)\right) / T_{\text{ref}}^{3/2} = K$, such that Equation 7.20 becomes Equation 7.21 where K is a constant calculated with known data points and T is the temperature calculated with Equation 7.18 corrected with the correction factor. Lastly, the conductivity can be calculated with Equation 7.22 which represents the Eucken Thermal Conductivity Model[4].

$$\mu(T) \approx K \cdot \sqrt{T} \quad (7.21)$$

$$\kappa(\mu) = \frac{\mu}{M} \cdot \left(f_{\text{int}} \cdot C_p \left(\frac{15}{4} - \frac{5 \cdot f_{\text{int}}}{2} \right) \right) \quad (7.22)$$

$$\kappa(\mu) = C \cdot \mu \quad (7.23)$$

where κ is the thermal conductivity. μ is the viscosity, M is the molar mass, c_p is the heat capacity at constant pressure and f_{int} is a dimensionless constant. Again, using the full equation to compute the conductivity is difficult, therefore an approximation is made, in particular it is assumed that $1/M \cdot (f_{int} c_p (15/4 - 5 f_{int}/2)) = C$, where C is a constant calculated with known data points. Therefore, Equation 7.22 becomes Equation 7.23 where μ is the viscosity previously calculated in Equation 7.21.

Thermal Management

Thermodynamic analysis softwares (RPA and CEA) show that for almost any combination of O/F and p_c, cooling of the engine will be needed as chamber temperatures are mostly above 2000 K, peaking at 2800 K for stoichiometric conditions and high chamber pressure, this is well shown in Figure 7.2.

Since the engine is manufactured from Inconel 718, which has a melting range of approximately 1260–1336 °C [10] and exhibits a recommended continuous service temperature on the order of 650–700 °C due to time-dependent degradation of its high-temperature mechanical properties [5], active cooling is required to ensure structural integrity. Regenerative cooling was therefore analysed as a thermal management strategy. In this configuration, the oxidiser, 98% H_2O_2, is routed through a network of cooling channels integrated into the combustion chamber and nozzle walls. The decision of whether to utilize the oxidizer or the fuel as coolant comes from an analysis of the respective mass flows, these can be calculated with Equation 7.24 and Equation 7.25.

$$\dot{m}_{ox} = \frac{O/F}{O/F + 1} \cdot \dot{m} \quad (7.24)$$

$$\dot{m}_{\text{fuel}} = \frac{1}{O/F + 1} \cdot \dot{m} \quad (7.25)$$

where $\dot{m}_{ox}$, $\dot{m}_{fuel}$, and $\dot{m}$ are the mass flows of the oxidizer, fuel, and total propellant respectively. As can be seen in Figure 7.2 and Figure 7.3, the O/F will be greater than one, whereby the the oxidizer will have a larger mass flow than the fuel.

To numerically model the heat flow, the one-dimensional heat equation, shown in Equation 7.26, is discretised. Its thermal diffusivity α, defined in Equation 7.27, is determined from material properties.

$$\frac{\partial T}{\partial t} = \alpha \frac{\partial^2 T}{\partial x^2} \quad (7.26)$$

$$\alpha = \frac{\kappa}{\rho c_p} \quad (7.27)$$

here κ is the conductivity, ρ is the density and c_p is the heat capacity at constant pressure.

Although RP-1 and H_2O_2 exhibit similar heat capacities and viscosities [11–13], H_2O_2 has both a higher thermal conductivity and a higher mass flow rate. Because a high mass flow rate is beneficial for regenerative cooling and the increased conductivity promotes heat transfer, the oxidiser is selected as the coolant.

The discretisation approach of the heat equation, however, varies depending on the region of application. Within the wall domain, heat transfer is solely governed by conduction, allowing the second spatial derivative to be approximated using a central difference scheme, as shown in Equation 7.28. This discretisation, as well as the subsequent ones, is applied along a longitudinal one-dimensional mesh of the engine, such that the heat equation is evaluated at discrete axial slices.

In this model, only radial conduction through the wall thickness is considered. Longitudinal and circumferential conduction are neglected, consistent with established practice in simplified regenerative cooling models [14, 15]. A post-processing analysis of the converged wall temperature field confirms that the longi-

[4] Conductivity Model [Date accessed: June 9] [5] Inconel Properties [Date Accessed: June 11]

tudinal conductive flux never exceeds 5% of the radial conductive flux through the wall thickness anywhere along the engine. Furthermore, since the wall temperature peaks at the throat, axial conduction acts to concentrate additional heat away from this location toward the cooler surrounding regions. Neglecting it therefore yields a conservative estimate of the peak wall temperature, as including it would marginally decrease rather than increase the thermal load at the throat.

$$T_j^{t+\Delta t} = T_j^t + \Delta t \cdot \left(\frac{\kappa}{\rho \cdot c_p}\right)_{w,j} \cdot \frac{1}{(\Delta z)^2} \cdot \left(T_{j+1}^t - 2 \cdot T_j^t + T_{j-1}^t\right) \tag{7.28}$$

Where the subscript j represents nodes radially distributed through the wall and the superscript t denotes the time step. Therefore, $T_j^{t+\Delta t}$ represents the temperature at station j at the next time step, while T_j^t denotes the temperature at the current time step. Similarly, T_{j+1}^t, T_j^t, and T_{j-1}^t represent the temperatures at stations $j+1$, j, and $j-1$, respectively, at the current time step. Finally, Δt and Δx denote the temporal and spatial step sizes, respectively, which are taken as $\Delta t = 30\,\mu$s and $\Delta x = 0.909\,$mm.

Since the wall temperature is updated using an explicit Forward Euler scheme, the time step must satisfy the stability criterion for the one-dimensional heat equation. This criterion is expressed in terms of the Fourier number, Fo, defined in Equation 7.29. For numerical stability, the Fourier number must satisfy $Fo \leq 0.5$.

$$Fo = (\alpha_w \cdot \Delta t) \,/\, (\Delta z)^2 \leq 0.5 \tag{7.29}$$

At the hot gas-side boundary, both conduction within the wall and convective heat transfer from the hot gas must be considered. Since this is a boundary node, however, a forward Euler discretisation is employed for the conduction, as shown in Equation 7.30, where $T_{\text{gas, wall}}$ represents the adiabatic wall temperature as defined in Equation 7.31.[16]

$$T_j^{t+\Delta t} = T_j^t + \Delta t \cdot \left(\frac{\kappa}{\rho \cdot c_p}\right)_{w,j} \cdot \frac{2}{\Delta z} \cdot \left[\frac{h_{g,\text{gas}}}{\kappa_{w,j}} \cdot \left(T_{\text{gas, wall}} - T_j^t\right) - \frac{1}{\Delta z} \cdot \left(T_j^t - T_{j+1}^t\right)\right] \tag{7.30}$$

$$T_{\text{gas, wall}} = T_{\text{gas, stat}} \cdot \left(1 + Pr^{1/3} \cdot \left(\frac{\gamma - 1}{2}\right) \cdot M^2\right) \tag{7.31}$$

$$Pr = \frac{\mu \cdot c_p}{k} \tag{7.32}$$

Where Pr is the Prandtl number of the gas, as expanded in Equation 7.32, and $T_{\text{gas, stat}}$ is the static gas temperature derived from Equation 7.18. The convective heat flux is modelled using a gas heat transfer coefficient h_g, calculated through Bartz's correlation [17], which is stated in Equation 7.33.

$$h_{g,\text{gas}} = \frac{0.026}{(D^*)^{0.2}} \left(\frac{\mu^{0.2} \cdot c_p}{Pr^{0.6}}\right)_{gas,ns} \left(\frac{p_c}{c^*}\right)^{0.8} \left(\frac{D^*}{r_c}\right)^{0.1} \left(\frac{A^*}{A}\right)^{0.9} \sigma \tag{7.33}$$

Here D^* is the throat diameter, μ is the viscosity, c_p the heat capacity at constant pressure, c^* is the characteristic velocity, r_c is the radius of curvature at the throat, A^*/A is the local area ratio with respect to the throat area, Pr is the Prandtl number, and σ is the correction factor for properties variations across the boundary layer, defined in Equation 7.34. [17]

$$\sigma = \left(\left[\frac{1}{2}\frac{T_w}{T_c}\left(1 + \frac{\gamma - 1}{2}M^2\right) + \frac{1}{2}\right]^{0.8 - 0.2\omega} \left(1 + \frac{\gamma - 1}{2}M^2\right)^{0.2\omega}\right)^{-1} \tag{7.34}$$

Here T_w/T_c is the ratio of the local wall temperature to the chamber temperature, M is the local Mach number, γ is the local specific heat ratio, and ω is a correction factor accounting for the temperature dependence of the combustion-gas transport properties. A value of $\omega = 0.6$ is adopted following Bartz [17], which provides a conservative estimate for the present combustion products, since larger values of ω generally reduce the predicted gas-side heat transfer coefficient h_g, thereby yielding higher predicted heat fluxes and wall temperatures.

Similarly, at the coolant-side boundary, both conduction within the wall and convective heat transfer to the coolant are taken into account. As shown in Equation 7.35, a forward Euler scheme is again employed at this boundary.

$$T_j^{t+\Delta t} = T_j^t + \Delta t \cdot \left(\frac{\kappa}{\rho \cdot c_p}\right)_{w,j} \cdot \frac{2}{\Delta z} \cdot \left[-\frac{h_l}{\kappa_{w,j}} \cdot \left(T_j^t - T_{\text{cool}}^t\right) + \frac{1}{\Delta z} \cdot \left(T_{j-1}^t - T_j^t\right)\right] \tag{7.35}$$

Where the liquid heat transfer coefficient h_l depends on the local coolant flow conditions. As the coolant channel geometry varies with the local segment radius, the coolant velocity, derived in Equation 7.36, also varies along the channel. As a result, the local Reynolds number, defined in Equation 7.37, changes, leading to laminar, transitional, or turbulent flow regimes. The Reynolds number is defined using the hydraulic diameter as characteristic length, which is given in Equation 7.38 [18, pp. 6].

$$v_{\text{cool}} = \frac{\dot{m}_{ox}/N_{\text{chan}}}{\rho_{\text{liq}} \cdot A_{\text{chan}}} \quad (7.36) \qquad Re = \frac{\rho_{\text{liq}} \cdot v_{\text{cool}} \cdot d_h}{\mu_{\text{liq}}} \quad (7.37) \qquad d_h = \frac{2 \cdot w_{\text{chan}} \cdot h_{\text{chan}}}{w_{\text{chan}} + h_{\text{chan}}} \quad (7.38)$$

In the laminar regime ($Re < 2300$), h_l is evaluated using the Sieder–Tate correlation given in Equation 7.39 [19], while in the turbulent regime ($Re > 3000$), the Gnielinski correlation in Equation 7.40 is applied [20, 21]. The Darcy–Weisbach friction factor required in the turbulent correlation is computed using Petukhov's smooth-tube formulation, as given in Equation 7.41 [21]. In the transitional regime ($2300 \leq Re \leq 3000$), h_l is determined by linear interpolation between the laminar and turbulent values.

$$h_l = \left(\frac{\kappa_{\text{liq}}}{d_h}\right) \cdot 1.86 \cdot \left[Re_{\text{liq}} \cdot Pr_{\text{liq}} \cdot \left(\frac{d_h}{\Delta x}\right)\right]^{1/3} \quad (7.39)$$

$$h_l = \left(\frac{k_{\text{liq}}}{d_h}\right) \cdot \left(\frac{(f/8) \cdot (Re_{\text{liq}} - 1000) \cdot Pr_{\text{liq}}}{1 + 12.7 \cdot \sqrt{f/8} \cdot \left(Pr_{\text{liq}}^{2/3} - 1\right)}\right) \quad (7.40) \qquad f = \left(0.79 \cdot \log\left(Re_{\text{liq}}\right) - 1.64\right)^{-2} \quad (7.41)$$

Next, the oxidiser temperature within the coolant channels must be monitored. Although 98% H_2O_2 has a boiling point of approximately 141 °C (414.15 K) at atmospheric pressure[6], thermally induced decomposition can occur at significantly lower temperatures. Because this reaction is strongly exothermic, elevated coolant temperatures may trigger oxygen formation within the channels. In regeneratively cooled engines, this is undesirable as the gas bubbles would reduce liquid wall contact, lowering the local heat transfer coefficient, thereby lowering cooling performance. The resulting rise in wall temperature would further accelerate peroxide decomposition, creating a positive feedback loop that can lead to thermal runaway and catastrophic engine failure. [22, pp. 4.85–4.86]

To maintain a safety margin and keep the validity of the single-phase heat-transfer assumptions used in this model, the coolant temperature is kept below ≈60 °C (333.15 K) throughout the cooling cycle. [23]
To ensure safe operating conditions, the coolant temperature is modelled using Equation 7.42, allowing verification that it remains below the decomposition threshold throughout the cooling cycle. This equation is not applied at the nozzle exit, where the coolant is replenished with room-temperature peroxide.

$$T_{\text{cool}}^{t+\Delta t} = T_{\text{cool}}^{t} + \Delta t \left[\left(\frac{h_l \cdot P_{\text{heat}}}{\rho_{\text{liq}} \cdot c_{p,\text{liq}} \cdot A_{\text{chan}}}\right)\left(\left(T_{w,\text{int}}^{t} - T_{\text{cool}}^{t}\right) + \left(T_{w,\text{ext}}^{t} - T_{\text{cool}}^{t}\right)\right) + \left(\frac{v_{\text{cool}}}{\Delta x}\right)\left(T_{\text{cool, next}}^{t} - T_{\text{cool}}^{t}\right)\right] \quad (7.42)$$

Where P_{heat} denotes the effective wetted perimeter, defined as the portion of the channel perimeter in thermal contact with the inner wall. It consists of the channel width plus contributions from both ribs, each weighted by an efficiency factor, as given in Equation 7.43. [18, 24]

$$P_{\text{heat}} = w_{\text{chan}} + 2 \cdot h_{\text{chan}} \cdot \frac{\tanh\left(h_{\text{chan}} \cdot m_{\text{chan}}\right)}{h_{\text{chan}} \cdot m_{\text{chan}}} \quad (7.43) \qquad m_{\text{chan}} = \sqrt{\frac{h_l \cdot (2 \cdot (w_{\text{chan}} + h_{\text{chan}}))}{\kappa_w \cdot A_{\text{chan}}}} \quad (7.44)$$

To ensure stability of the advection term in Equation 7.42, the time step must also satisfy the Courant-Friedrichs–Lewy (CFL) condition for an explicit Forward Euler scheme. This requirement is expressed through the Courant number, $C = (v_{\text{cool}} \cdot \Delta t)/\Delta x$, which must satisfy $C \leq 1$. [25, p. 88]

Lastly, the convection between the external wall and the outside air must be modelled. For this, a conservative approximation was made, where the outside air is assumed to be stagnant. This is conservative as the air will be moving during the take-off of the UAV and moving air tends to have a h_g which is an order of magnitude higher, which would cool the surface faster.

The convection with the air can be modelled with Equation 7.30, as defined before, but with the heat transfer coefficient $h_{g,\text{air}}$ defined by the Churchill-Chu relation stated in Equation 7.45. [26]

$$h_{g,\text{air}} = \left(\frac{\kappa_{\text{air}}}{d_e}\right)\left(0.825 + \frac{0.387 \cdot Ra^{1/6}}{\left(1 + (0.492/Pr)^{9/16}\right)^{8/27}}\right)^2 \quad (7.45)$$

[6] H_2O_2 Boiling Temperature

where the Rayleigh number, Ra, is defined as the product of the Prandtl number, Pr, and the Grashof number, Gr. Substituting the definition of the Grashof number yields the expression given in Equation 7.46, where β is the volumetric thermal expansion coefficient, defined in Equation 7.47. Both the Prandtl number and the thermal expansion coefficient are evaluated at the film temperature, $T_f = (T_w + T_{\text{amb}})/2$, where T_w is the wall temperature and T_{amb} is the ambient air temperature [27].

$$Ra = Pr \cdot Gr = Pr \cdot \frac{g \cdot \beta \cdot (T_w - T_\infty) \cdot D_e^3}{\nu^2} \quad (7.46)$$

$$\beta = \frac{-1}{\rho} \cdot \left(\frac{\partial \rho}{\partial T}\right)_p = \frac{1}{T} \quad (7.47)$$

Cost functions of the optimization

As mentioned previously, the global optimization problem is based on a number of cost functions, these are summarized below.

1. **Total dry mass**: This cost function evaluates the total dry mass of the propulsion system, including the fuel, oxidiser, pressurizer, tanks, piping, and thrust chamber; it's an extremely crucial cost function as the overall mass is a driving requirements, both during ascent and during cruise. As a consequence, the weight given to this function is 40%.
2. **Total Volume**: This cost function evaluates the total system volume of the propulsion system, in particular in regard to the volumes of the 3 tanks, since volume is not a driving requirement anymore, as will be explained in Chapter 9, the weight given to this function is only 10%.
3. **Emissions**: This cost function evaluates the fraction of exhausted pollutants with respect to the total mass of propellant used, this is a crucial characteristic of the VAPOR mission from the sustainability point of view in comparison to other electric or air-breathing aircraft, it's important to note that for any set of parameters the VAPOR missions has less emissions than comparable aircraft. The weight given to this function is 30%.
4. **Thermal Management**: This cost function evaluates whether the engine can be feasibly be cooled and operational for any given set of parameters, this function does not have a weight as it immediately discards parameters that cannot satisfy cooling requirements.
5. **Ascent Performance**: This cost function evaluates whether the UAV can feasibly reach target altitude for any given set of parameters, it also takes into account how much propellant has to be used to reach said altitude. The weight given to this function is the remaining 20%.

Firstly, all the masses and volumes for the thrust chamber, propellant, pressurizer, tanks and piping are defined. It is important to differentiate between the absolute masses and mass flows of the oxidizer and of the fuel. The masses of the fuel and oxidizer can be quickly determined in function of the O/F, as defined before in eqs. (7.24) and (7.25). Their respective volumes are then calculated based on the densities, as shown in Equation 7.48 and Equation 7.49.

$$V_{\text{fuel}} = m_{\text{fuel}}/\rho_{\text{fuel}} \quad (7.48) \qquad V_{ox} = m_{ox}/\rho_{ox} \quad (7.49)$$

Helium is used as a pressurizer for the propellant, it is stored in a tank itself, therefore its initial volume will be equal to the helium tank volume, then it will fill the tanks as the propellant is expended. As a consequence, when all propellant is used, the final volume occupied by helium will be equal to the volume of the propellant tanks plus the volume of the helium tank. The process is also assumed to be isothermal, such that the initial and final temperatures of helium are the same. For this reason Equation 7.50 holds.

$$p_{i,\text{He}} \cdot V_{i,\text{He}} = p_{f,\text{He}} \cdot V_{f,\text{He}} \quad (7.50) \qquad V_{\text{tank, He}} = \frac{p_{\text{prop}} \cdot (V_{\text{fuel}} + V_{\text{ox}})}{p_{i,\text{He}} - p_{\text{prop}}} \quad (7.51)$$

$p_{i,He}$ and $p_{f,He}$ are the initial and final helium pressures respectively, and the final volume is dependant on the initial volume and the volume of the propellant, solving this equation for the initial helium volume yields Equation 7.51. p_{prop} is the pressure at which the propellant is stored and is designed to equal to the final pressure of the helium after all propellant is used. This pressure is a function of the chamber pressure, this is shown in Equation 7.52

$$p_{\text{prop}} = \Pi_{\text{proptank-cc}} \cdot p_c \quad (7.52) \qquad p_{\text{He}} = \Pi_{\text{regulator-proptank}} \cdot \Pi_{\text{helium-proptank}} \cdot p_{\text{prop}} \quad (7.53)$$

where p_c is the chamber pressure, the pressure ratio is used to take into account pressure drops across the injector, the catalytic bed and pressure losses in pipes, this is conservatively chosen to be equal to 2, as already done by A. Okninski et al [5]. The initial pressure of helium is again determined using pressure ratio, and can be chosen to ensure safe and efficient feeding procedures. This equation is shown in Equation 7.53,

where $\Pi_{\text{regulator-proptank}}$ is the pressure ratio between the regulator and helium tank is chosen to be equal to 1.05 and $\Pi_{\text{helium-proptank}}$ is the pressure ratio between the propellant tanks and helium tank and chosen to be equal to 6 [28]. This value can be chosen arbitrarily from literature as this determines the required tank volume for the helium, fixing one of the two variables determines the other.

The mass of the helium can then be found from the ideal gas law, when both the volumes and pressures are known, as stated earlier the process is assumed isothermal, this is shown in Equation 7.54 and Equation 7.55.

$$p_{\text{i,He}} \cdot V_{\text{i,He}} = m_{\text{He}} \cdot R_{\text{He}} \cdot T \tag{7.54}$$

$$m_{\text{He}} = \frac{p_{\text{i,He}} \cdot V_{\text{i,He}}}{R_{\text{He}} \cdot T} \tag{7.55}$$

Here R_{He} is the specific gas constant of helium equal to 2077 J/(kg K), and T the constant assumed temperature, equal to 300 K. In reality, the process will be in between isothermal and isentropic, however, given the low burn time on the engine, the process can be reasonably assumed to be isothermal, as stated by Cervone [29].

In order to determine the mass of the tanks, their respective structural volumes are required. From this, the geometry, as constrained by the total fuselage diameter is determined. Having the tanks as spheres is always beneficial in terms of minimizing mass, however, if the diameter of the fuselage is too small, a sphere would not fit and thus a cylinder with domes is chosen instead. The diameter required by a spherical tank, the most surface area efficient shape for minimizing the tank mass, is easily found with Equation 7.56.

In case the diameter of this tank is larger than the diameter of the rocket fuselage, taken with an appropriate margin of $D_{\text{fus-limit}} = 0.9 \cdot D_{\text{true-fus}}$, then the shape of the tank transitions to that of a cylinder with semi-spherical domes and increasing length l in Equation 7.57, with $L = l + D$ being the total length of the tank.

$$D_{\text{sphere}} = 2 \cdot \left(\frac{3 \cdot V_{\text{vol}}}{4\pi} \right)^{1/3} \tag{7.56}$$

$$l = \frac{V_{\text{vol}} - \frac{4}{3}\pi \left(\frac{D}{2}\right)^3}{\pi \left(\frac{D}{2}\right)^2} \tag{7.57}$$

Having determined whether the tank is a cylinder or a sphere, the thickness of the tank can be calculated for either propellant or helium tank. The material of the tanks is set to be aluminium Al 6061-T6 with a density of $\rho = 2700 kg/m^3$ and a yield strength $\sigma_y = 276$ MPa. Equation 7.58 and Equation 7.59 represent the equations to calculate the thickness of the tanks.

$$t = SF \cdot \frac{p_{\text{tank}} \cdot D_{\text{sphere}}}{4 \cdot \sigma_{\text{y}}} \tag{7.58}$$

$$t = SF \cdot \frac{p_{\text{tank}} \cdot D_{\text{cylinder}}}{2 \cdot \sigma_y} \tag{7.59}$$

where p_{tank} is the pressure of the tank, σ_y is yield stress of aluminium Al6061-T6 and D_{sphere} and D_{cylinder} are the diameters of the spherical and cylindrical tank respectively. The final thickness values are multiplied with a safety factor $SF = 1.25$ to ensure sufficient stress resistance. It's important to mention that thicknesses were rounded to 1 mm whenever their value was smaller than this, for manufacturability purposes.

Now that the tank surface area, thickness and material density are all known quantities, the mass of each tank structure can be successfully determined, where Equation 7.63 contains an extra component compared to Equation 7.60.

$$A_{\text{sphere}} = 4\pi \left(\frac{D_{\text{sphere}}}{2} \right)^2 = \pi D_{\text{sphere}}^2 \tag{7.60}$$

$$V_{w,\text{sphere}} = A_{\text{sphere}} \cdot t \tag{7.61}$$

$$m_{\text{sphere}} = V_{w,\text{sphere}} \cdot \rho_{\text{mat}} \tag{7.62}$$

$$A_{\text{cyl}} = 4\pi \left(\frac{D_{\text{cyl}}}{2} \right)^2 + \pi D_{\text{cyl}} \cdot l_{\text{cyl}} \tag{7.63}$$

$$V_{w,\text{cyl}} = A_{\text{cyl}} \cdot t \tag{7.64}$$

$$m_{\text{cyl}} = V_{w,\text{cyl}} \cdot \rho_{\text{mat}} \tag{7.65}$$

Now that all other components are defined, the piping system needs to be designed and its mass estimated, firstly the pipe diameter is estimated from the definition of mass flow, as shown in Equation 7.66

$$D = \sqrt{\frac{4\dot{m}}{\pi \rho v_{\text{max}}}} \tag{7.66}$$

$$V_{\text{pipe}} = \left(\pi \frac{(D + 2t)^2}{4} - \pi \frac{D^2}{4} \right) \cdot L \tag{7.67}$$

$$m_{\text{pipe}} = V_{\text{pipe}} \cdot \rho \tag{7.68}$$

where $\dot{m}$ is the mass flow through the pipe, ρ the density of the material, which again is Aluminium 6061-T6, and v_{max} is the maximum allowable velocity. The required thickness is calculated in the same way as shown in Equation 7.59. The total volume can be calculated with Equation 7.67 where the first term represents the

total area, while L is the total length of the pipe. Lastly, the total mass can be computed with Equation 7.68. Additionally, the piping is based on the following diagram highlighted in Figure 7.4.

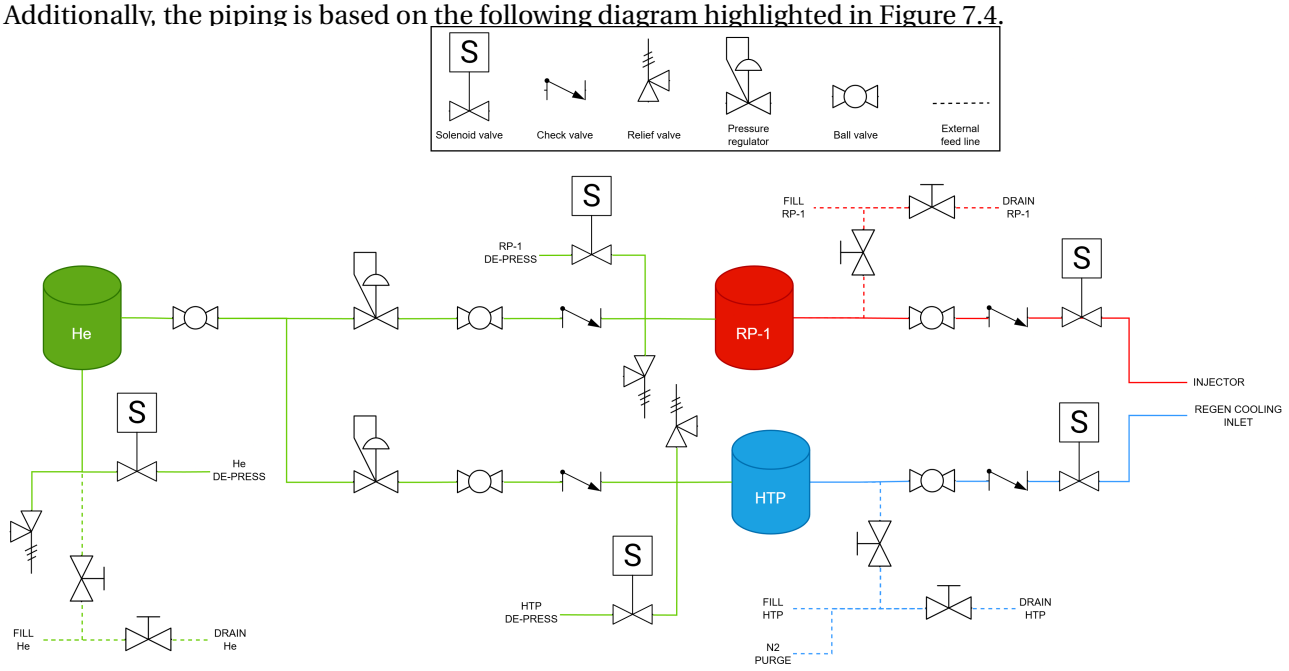

Figure 7.4: Feed line diagram

Finally, the mass and volume of the thrust chamber, consisting of both combustion chamber and nozzle, is calculated based on a model developed in CATIA [30]. The cost functions developed therefore converge towards one all-encompassing function for the total mass and one for the total volume. These are used for the optimization.

To investigate the evolution of these cost functions with respect to O/F and p_c, their relations are plotted. Figure 7.5 shows the relation of the total dry mass of the propulsion system. It shows the total dry mass of the propulsion system (excluding the thrust chamber and catalyst) considering a total propellant mass of 6 kg. It is shown in function of chamber pressure and each line refers to a specific O/F. The considered masses therefore include the tanks and the piping, as previously stated, while the masses of the thrust chamber and catalyst are calculated based on a Computer-Aided Design (CAD) model.

Secondly, the cost function for total volume can be plotted, this takes into account the total volume of the tanks, i.e. the sum of the volumes of oxidizer, fuel, and pressurizer tanks. The plot is shown in Figure 7.6.

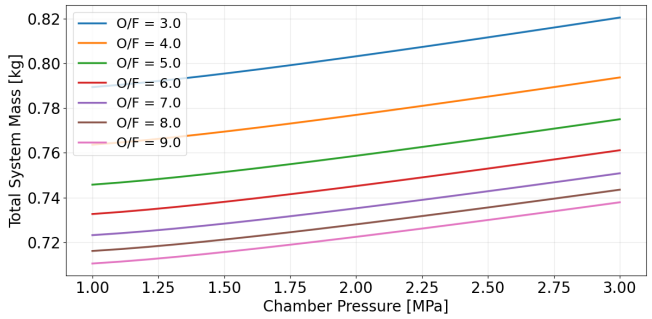

Figure 7.5: Dry mass of the propulsion system excluding thrust chamber and catalyst with 6 kg of propellant

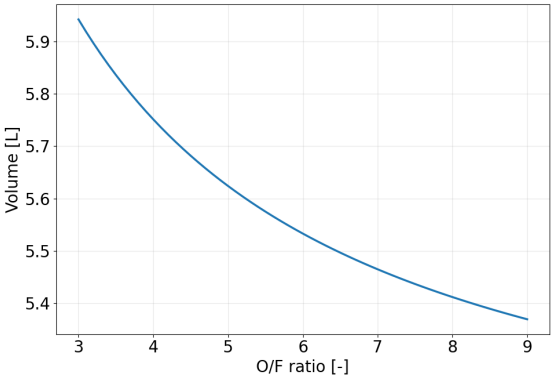

Figure 7.6: Total volume vs oxidiser-to-fuel ratio

Once the pressure ratios between the combustion chamber and the propellant tank, and between the propellant tank and the helium tank are defined, the total volume and the volumes of the individual tanks do not actually depend on the chamber pressure. Figure 7.6 clearly shows that a high O/F yields a lower volume, and thus a higher volumetric impulse, due to a higher density of the HTP.

Figure 7.7 shows the evolution of each of the three tanks with O/F. In the graph the volume of the peroxide is increasing with O/F, while the volumes of fuel and helium are decreasing. As can be noted, the increase in peroxide volume with respect to O/F is less than the decrease in volume of fuel and helium, thus confirming the expected trend of higher volumetric impulse with O/F.

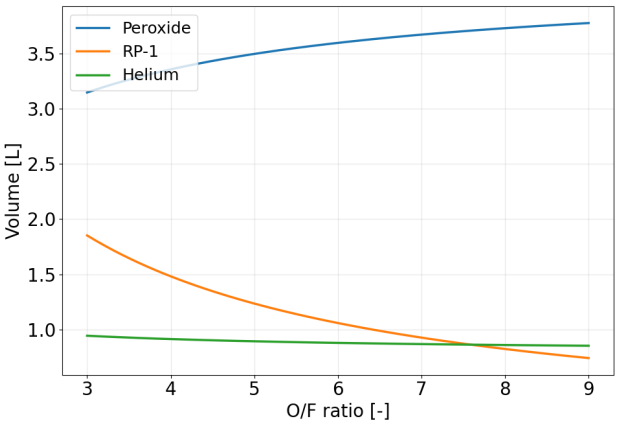

Figure 7.7: Peroxide, Fuel and Helium volumes in function of O/F ratio

Next, the emissions are considered, a cost function is made from the database constructed via the RPA software, the identified pollutants are carbon dioxide and carbon monoxide, the cost function calculates the sum of the fractions of these two pollutants, in particular carbon monoxide is toxic and takes approximately two months to oxidise in standard atmospheric conditions [31]. The emissions mainly depend on the O/F ratio and to a lesser extent on the chamber pressure p_c.

Firstly, the total fraction of pollutants with respect to the overall used propellant is plotted in function of O/F and p_c. This is shown in Figure 7.8, where the total pollutants (CO + CO_2) mass fraction is plotted against chamber pressure, and each line corresponds to a specific O/F. As can be seen, the total pollutants do not increase significantly with chamber pressure, but they strongly vary with O/F. At high O/Fs the mixture becomes oxidiser-rich and the pollutants fraction drops, while for low O/Fs the emissions rise significantly as more fuel is added to the mixture.

Additionally, the three main species, which include the above-mentioned pollutants and water vapour, are plotted with varying O/Fs at a fixed chamber pressure of 2 MPa, This plot is shown in Figure 7.9.

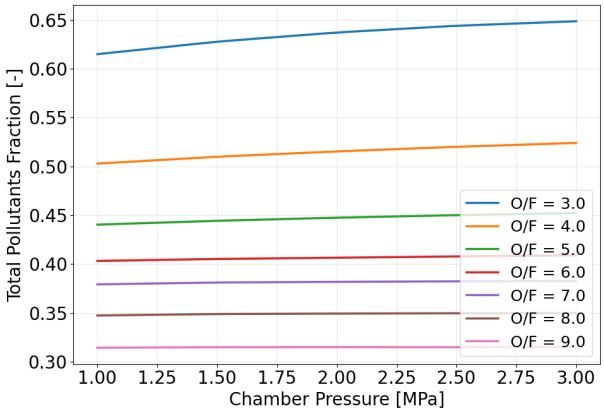

Figure 7.8: Total mass fraction of carbon dioxide and carbon monoxide combined

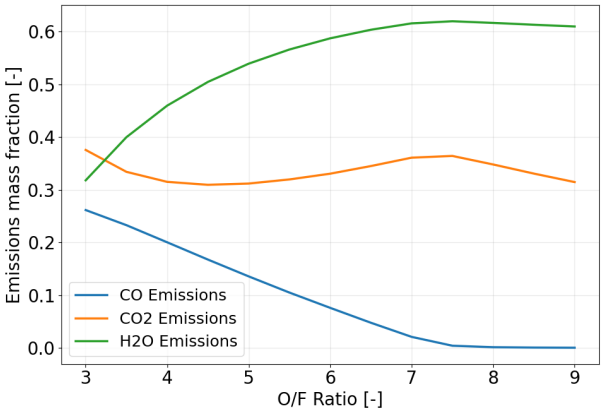

Figure 7.9: Water Vapour, Carbon Dioxide and Carbon Monoxide plotted against oxidiser-to-fuel ratio

Figure 7.9 shows how the CO emissions steadily decrease with O/F, this is because carbon monoxide is a sign of incomplete combustion, therefore it is present only for fuel-rich mixtures, reaching its minimal fraction for stoichiometric conditions and remaining constant afterwards. Logically, water vapour also steadily increases with increasing O/F, as the mixture becomes more and more oxidiser-rich. Lastly, carbon dioxide emissions initially decrease up to an O/F of about 4.5, then they increase until stoichiometric conditions; initially the emissions decrease because of the decrease in fraction of RP-1 used, but then they start increasing as the excess oxygen from the peroxide favours CO_2 formation and complete combustion.

The summation of the emissions of water vapour, carbon monoxide and carbon dioxide fractions oscillates between 95% and 99%, other species do form and are reported in Table 7.1, but their mass fraction is considered negligible.

So, even though the emissions increase for fuel-rich mixtures, they are still much lower than air-breathing propulsion emissions, which are estimated based on typical literature values for aircraft emissions [32], these are reported in Table 7.2. This makes the VAPOR mission highly competitive from the sustainability point of view. This can be proven by looking at Figure 7.9 where the emissions per kg of total propellant are in the order of 0.3-0.6.

Table 7.1: Selected negligible species present in rocket exhaust products

Category	Species
Organic oxygenates	COOH, HCOOH, HCO
Hydrogen species	H_2O_2
Radicals	OH, HO_2
Atoms	H, O
Mono-atomic Molecules	O_2, H_2

Table 7.2: Typical Aircraft Emissions Per Kilogram of Jet-A Fuel Burned

Emission Product	Emission Index
CO_2	3.16 kg/kg_{fuel}
H_2O	1.24 kg/kg_{fuel}
SO_X	0.84 g/kg_{fuel}
NO_X	~ 15 g/kg_{fuel}

As can be observed in Table 7.2, carbon dioxide emissions of air-breathing propulsion are much higher than the ones of the bi-propellant engine. Furthermore, new emissions such as NO_X and SO_X would be introduced, which are both environmentally concerning. Both are responsible for air acidification. NO_X also generates ground-level ozone, while SO_X is responsible for respiratory illnesses.[7].

Moreover, a cost function in relation to thermal management is constructed, this function works differently than the previous ones because, for a given set of parameters, the engine is either melting or not, and the peroxide either exceeds its maximum safe temperature or it does not. Therefore the cost function only evaluates if the given set of parameters fulfils cooling requirements, sets of parameters that do not allow for sufficient cooling are immediately discarded.

Lastly, a function in relation to the take-off performance is constructed, this function works similarly as the one for cooling; for a given efficiency (specific impulse) and a certain maximum propellant mass, the UAV either reaches target altitude (2500 m) or not, therefore any set of parameters that do not reach target altitude are immediately discarded, remaining sets of parameters are ranked with respect to minimising required propellant mass.

7.2.3. Injector Design

The injector is the component of the engine responsible for mixing and distributing the fuel and oxidiser in the thrust chamber to allow an efficient combustion process. In this case, since it was chosen to decompose all the hydrogen peroxide before mixing it with the kerosene, a gas-liquid injector is needed. From the different possibilities, the pintle injector was selected due to its simplicity, mixing capability and combustion stability properties. As shown in Figure 7.10, the pintle injector works by flowing the liquid and gas axially with the liquid on the inside. At the end of the injector the liquid impinges with the tip of the pintle spraying outwards in a cone shape, which then impinges with the annular gas curtain. This generates a cone of mixed gas and liquid propellants.

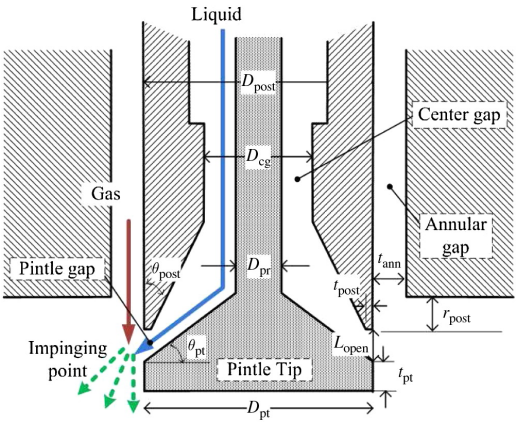

Figure 7.10: Pintle injector geometry. Figure by Son et al. [33].

To analyse and size the injector for VAPOR's main engine, the method presented by Son et al. [33] was used. The goal of this method is to optimise the characterising geometry parameters seen in Figure 7.10 in order to have the smallest possible chamber volume required for adequate mixing. The procedure starts by computing the computing the mass flows of the liquid and gas propellants, as defined in Equation 7.25 and Equation 7.24 respectively.

The inlet area of the liquid and the gas are calculated through eqs. (7.69) and (7.70) based on geometry, which will later be used to compute flow characteristics. Afterward, the minimum area of the liquid opening

[7] SO_X Properties [Date Accessed: June 12]

is calculated with Figure 7.11a.

$$A_{\text{liq}} = \pi \left(\frac{D_{\text{cg}} - D_{\text{pr}}}{2} \right)^2 \quad (7.69) \qquad A_{\text{gas}} = \pi \left[\left(\frac{D_{\text{pt}}}{2} + t_{\text{ann}} \right)^2 - \left(\frac{D_{\text{pt}}}{2} \right)^2 \right] \quad (7.70)$$

$$A_{\text{min}} = \frac{\pi}{\sin\theta_{\text{pt}}} \left[(R_{\text{post}} - t_{\text{post}})^2 - (R_{\text{post}} - t_{\text{post}} - L_{\text{open}} \sin\theta_{\text{pt}} \cos\theta_{\text{pt}})^2 \right] \quad (7.71)$$

If this minimum area is greater than the liquid inlet area shown in Figure 7.11a, the flow characteristics are determined by the central gap rather than the pintle tip, and the discharge coefficient decreases lowering performance. Therefore, it is imposed as a constraint in the optimisation process that the minimum area has to be smaller than the liquid inlet area, otherwise the geometry is rejected.

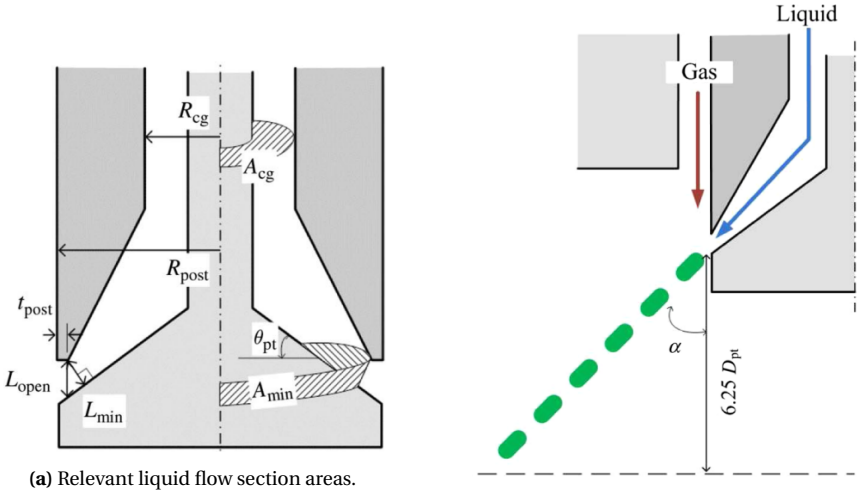

(a) Relevant liquid flow section areas. Figure by Son et al. [33].

(b) Spray angle. Figure by Son et al. [33].

Figure 7.11: Definition of injector analysis parameters.

Now the velocity of the gas and liquid propellants at the moment of impingement is computed:

$$V_{\text{liq}} = \frac{\dot{m}_{\text{liq}}}{A_{\text{min}} \rho_{\text{liq}}}, \quad V_{\text{gas}} = \frac{\dot{m}_{\text{gas}}}{A_{\text{gas}} \rho_{\text{gas}}} \quad (7.72) \qquad M_{\text{gas}} = \frac{V_{\text{gas}}}{\sqrt{\gamma_{\text{gas}} R_{\text{gas}} T_{\text{gas}}}} < 0.6 \quad (7.73) \qquad \Delta P_{\text{liq}} = \frac{1}{2} \rho_{\text{liq}} \left(\frac{V_{\text{liq}}}{C_d} \right)^2 \quad (7.74)$$

The density of RP-1, ρ_{liq}, is taken to be 810 kg/m^3 from general literature, as liquids can effectively be considered incompressible. The density of decomposed peroxide ρ_{gas} is obtained from the outlet conditions of the catalyst, which is analysed in Subsection 7.2.4. Note that the model only considers a pressure drop over the injector for the liquid propellant, so the pressure of the gas at impingement is assumed to be the same as the chamber temperature.

In order to have predictable behaviour, the gas flow should be subsonic. In order to verify this, the sound speed of the decomposed peroxide is calculated using the ratio of specific heats γ_{gas} and the specific gas constant R_{gas} of the gases at the combustion chamber, which is obtained from the RPA software [6].

If the Mach number 0.6 or larger, the geometry configuration is rejected. A further constraint is that the pressure loss of the liquid along the injector should not exceed 5 bar, as this would unnecessarily increase the system pressure upstream by use of Equation 7.74. Here C_d is the discharge coefficient, which measures the efficiency of the injector accounting for friction and contraction losses. Based on experimental data for pintle injectors [34], this value is taken to be 0.7 for the purpose of estimating the pressure drop.

To obtain the spray characteristics of the pintle, multiple nondimensional parameters have to be calculated. Firstly, the Weber number We and and special characteristic parameter K are obtained:

$$W_e = \frac{(\rho_{\text{gas}})(L_{\text{open}}) \left(V_{\text{gas}} - V_{\text{liq}} \right)^2}{\sigma_{\text{liq}}} \quad (7.75) \qquad K = \frac{V_{\text{gas}}}{V_{\text{liq}}} \frac{t_{\text{ann}}}{L_{\text{open}}} = \frac{\dot{m}_{\text{gas}} \rho_{\text{liq}}}{\dot{m}_{\text{liq}} \rho_{\text{gas}}} \left(\frac{D_{\text{pt}}}{D_{\text{pt}} + t_{\text{ann}}} \right) \quad (7.76)$$

Here σ_{liq} is the surface tension of RP-1, taken to be 0.0275 N/m. These parameters define relations between the flow characteristics and spay or atomization properties. Now the spray angle α and Sauter mean diam-

eter D_{32} can be computed using empirical relations:

$$\alpha = 90(\xi)\exp\left[\frac{s-0.2}{1+(K/90)^p} - s\right] \tag{7.77}$$

$$D_{32} = 10^3(L_{\text{open}})(\xi^{-1})\exp[4.0 - q(We^{0.1})] \tag{7.78}$$

where

$$\xi = \frac{90-\theta_{\text{pt}}}{90}, \quad s = 1.15 + 1.35\xi, \quad p = 1.30 + 0.90\xi, \quad q = 3.455 - 0.225\xi$$

The spray angle, depicted in Figure 7.11b, represents the angle of the atomized spray cone with respect to the pintle longitudinal axis. The the Sauter mean diameter relates to the droplet size of the spray.

Finally the vaporization distance x^* can be computed from another empirical relation:

$$x^* = \left(\frac{D_{32}^2}{4}\right)\left[\frac{u_{d0}}{\sqrt{\gamma_c R_c T_c}} + \frac{3}{\Gamma}\left(\frac{A_t}{A_c}\right)\frac{S}{10}\right]\frac{c_{p,c}\rho_{\text{liq}}}{k_c}\frac{\sqrt{\gamma_c R_c T_c}}{\ln(1+B)}\frac{1}{(2+S)} \tag{7.79}$$

where

$$\Gamma = \left(\frac{\gamma+1}{2}\right)^{(\gamma+1)/2(\gamma-1)}, \quad S = \frac{9}{2}\frac{Pr_c}{B}, \quad B = \frac{T_c - T_{\text{cr}}}{T_{\text{cr}} - T_{\text{liq}}}$$

Here all the parameters with subscript c refer to the combustion gas, and are obtained with the RPA software [6]. Furthermore, T_{cr} is the critical temperature of RP-1, taken as 722 K [35], $\frac{A_c}{A_t}$ is the contraction ratio of the engine, k is thermal conductivity and u_{d0} is the initial droplet velocity, assumed to be equal to the liquid velocity. The vaporization distance x^* measures how far the mixture travels before fully mixing into gas for combustion, and together with the spray angle α characterises the spray cone created by the pintle. Together, these two parameters determine the minimum thrust chamber diameter D_c, length L_c and therefore volume v_c required to reach complete mixing to allow for efficient combustion:

$$D_c = 2(x^*)\sin\alpha + D_{\text{pt}}, \quad L_c = (x^*)\cos\alpha + L_{\text{open}} + r_{\text{post}}, \quad v_c = \pi\left(\frac{D_c}{2}\right)^2 L_c \tag{7.80}$$

The minimum chamber volume v_c is the parameter that will be optimised in order to select a final pintle geometry, as a smaller thrust chamber results in a lighter engine, which is a driving factor for the design.

The range of geometries to analyse was defined by taking the baseline design used in the experiments by Son et al. [33] and varying the most influential parameters within reasonable bounds considering the engine size, machining accuracy and *OF* ratio. The aforementioned baseline design as well as the range of variable parameters are presented in Table 7.3.

Table 7.3: Geometrical configurations used for injector optimization.

Parameter	Unit	Baseline value	Min. value	Max. value	Interval
Pintle tip diameter D_{pt}	mm	8.0	-	-	-
Annular gap thickness t_{ann}	mm	-	1.0	5.0	0.1
Center gap diameter D_{cg}	mm	6.0	-	-	-
Pintle rod diameter D_{pr}	mm	3.0	-	-	-
Post recess length r_{post}	mm	3.0	-	-	-
Pintle tip angle θ_{pt}	deg	-	20	40	5
Post angle θ_{post}	deg	30	-	-	-
Pintle tip opening L_{open}	mm	-	0.2	1.0	0.1
Pintle tip thickness t_{pt}	mm	1.0	-	-	-
Post tip thickness t_{post}	mm	0.5	-	-	-

7.2.4. Catalyst Bed Design

It was previously decided that VAPOR's main engine will rely on a catalyst bed in order to provide propellant ignition. The catalyst bed decomposes the hydrogen peroxide as the latter flows through it, producing a hot gas stream of oxygen and water. This gas then mixes with the RP-1 in the injector and the mixture ignites spontaneously due to the high temperatures.

Before sizing the catalyst bed, it is necessary to choose a type, as there are multiple options. This was done by considering the main options and making a trade-off using relevant criteria. The types of catalyst considered are the following:

- **Silver**: This option has extensive history in peroxide monopropellant systems. It has high catalytic activity and a simple screen based construction. Its melting point however is 962 ºC, which makes it only suitable for lower peroxide concentrations, as higher ones can approach this temperature and damage the bed.
- **Manganese dioxide**: This option is very inexpensive and has a high melting point. It can be used in pellet form adapting to any catalyst bed shape. It is not as reactive as other materials, requiring a larger bed size, however its cost and thermal properties make it a strong candidate.
- **Platinum**: This last option has extremely high catalytic activity and thermal resistance, often being considered the benchmark for peroxide decomposition. Its main downside is that platinum is a very expensive and scarce material.

The criteria used for trading-off these options are **cost** (**35%**), **thermal resistance** at high peroxide concentrations (**35%**) and chemical **reactivity** (**30%**). The three options are then assign a score from 1-3 or DIS in each of the criteria, where DIS means that the option is not feasible and is therefore discarded. This trade-off is shown in Table 7.4.

Table 7.4: Catalyst type trade-off

Criteria	Weight [%]	Silver	MnO_2	Platinum
Cost	35	2	3	1
Thermal resistance	35	DIS	3	3
Reactivity	30	3	2	3
Total	**100**	**DIS**	**2.7**	**2.3**

The silver catalyst was discarded since the temperatures of decomposed 98% peroxide of around 1200 K are close the melting point of silver, making it unfeasible. Between manganese dioxide and platinum, manganese was chosen due to its high affordability compared to the elevated cost of platinum. Even though manganese dioxide is less reactive, the cost difference outweighs the increase in catalyst bed size. Manganese oxide is therefore the choice for the catalyst bed type. Specifically, pellet form will be used, as it is available off-the-shelf and can adapt to any bed shape and size without machining unlike monolithic beds.

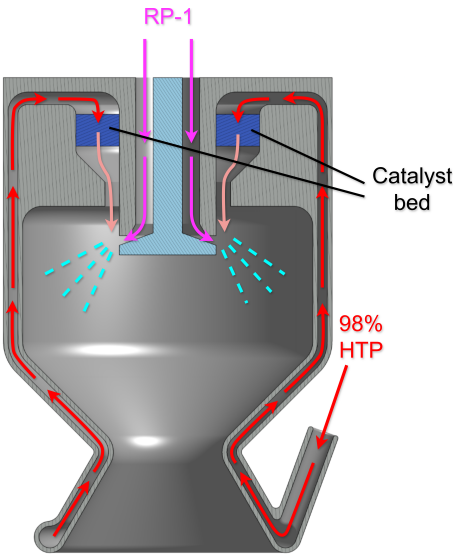

Figure 7.12: Catalyst integration in VAPOR's main engine.

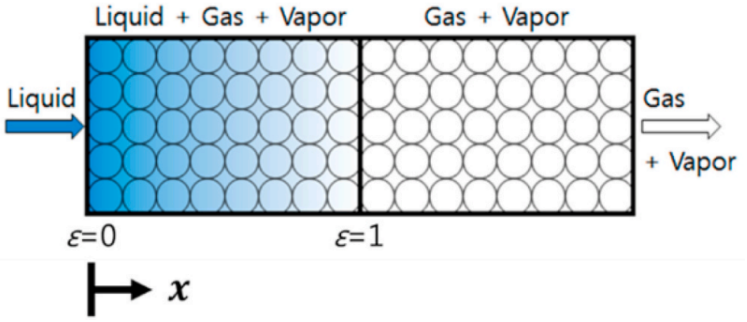

Figure 7.13: Catalyst flow model. Figure by S. Jung et al. [36].

To model and size the catalyst bed used in VAPOR's engine, the method presented by S. Jung et al. [36] was used. In this article, the flow over the catalyst is modelled as 1D, creeping and two-phase, as illustrated in Figure 7.12. The aim of the method is to obtain the temperature, pressure and decomposition fraction profile along the length of the length of the catalyst for a given geometry, inlet conditions, peroxide concen-

tration and catalyst properties such as pellet size. Note that this method considers a cylindrical catalyst bed, while VAPOR uses an annular shape to integrate with the pintle injector, as shown in Figure 7.12. However, since the model represents 1D flow, only the cross sectional area influences the outcome. Therefore the annular catalyst will be modelled as an equivalent cylindrical catalyst with equal cross sectional area.

For a given case, the analysis starts by computing the molar flow rates of H_2O_2, H_2O and O_2 as a function of the molar flow rate of decomposed peroxide λ:

$$\dot{n}_{H_2O_2}(\lambda) = \frac{Y\dot{m}}{M_{H_2O_2}} - \lambda, \quad \dot{n}_{H_2O}(\lambda) = \frac{(1-Y)\dot{m}}{M_{H_2O}} + \lambda, \quad \dot{n}_{O_2}(\lambda) = \frac{1}{2}\lambda \tag{7.81}$$

Here $\dot{m}$ is the total mass flow of peroxide and Y is its mass concentration. Introducing the evaporation parameter ε which represents the phase of the fluid, with $\varepsilon = 0$ being fully liquid and $\varepsilon = 1$ fully gas/vapor, the molar flow of the species can be expressed as:

$$\begin{gathered} \varepsilon = \varepsilon_{H_2O_2} = \varepsilon_{H_2O}, \quad \dot{n}_{H_2O_2(g)} = \varepsilon\dot{n}_{H_2O_2}, \quad \dot{n}_{H_2O(g)} = \varepsilon\dot{n}_{H_2O}, \\ \dot{n}_{H_2O_2(l)} = (1-\varepsilon)\dot{n}_{H_2O_2}, \quad \dot{n}_{H_2O(l)} = (1-\varepsilon)\dot{n}_{H_2O} \end{gathered} \tag{7.82}$$

Here the subscript l refers to liquid and g to gas. Now the partial pressures of the species can be computed and added together leading to an expression depending on temperature T and evaporation parameter ε:

$$\begin{gathered} p = p_{O_2} + p_{H_2O_2(g)} + p_{H_2O(g)} \\ \Rightarrow \left[1 - \frac{\dot{n}_{O_2}}{\dot{n}_{O_2} + \varepsilon(\dot{n}_{H_2O_2} + \dot{n}_{H_2O})}\right] p = \frac{\dot{n}_{H_2O_2} p_{sat,H_2O_2}(T) + \dot{n}_{H_2O} p_{sat,H_2O}(T)}{\dot{n}_{H_2O_2} + \dot{n}_{H_2O}} \end{gathered} \tag{7.83}$$

In the latter equation p_{sat} is the saturation pressure of the different species, which are modelled empirically as functions of temperature provided in the article by S. Jung et al. [36].

Next, conservation of enthalpy inside the catalyst is considered to arrive to another equation depending on temperature T and evaporation ε:

$$\begin{gathered} h_{initial} = h_{gas} + h_{liquid} \\ \Rightarrow \left[\dot{n}^{(i)}_{H_2O_2} h^{(i)}_{H_2O_2(l)} + \dot{n}^{(i)}_{H_2O} h^{(i)}_{H_2O(l)}\right] = \dot{n}_{O_2} h_{O_2}(T) + \varepsilon\left[\dot{n}_{H_2O_2} h_{H_2O_2(g)}(T) + \dot{n}_{H_2O} h_{H_2O(g)}(T)\right] \\ + (1-\varepsilon)\left[\dot{n}_{H_2O_2} h_{H_2O_2(l)}(T) + \dot{n}_{H_2O} h_{H_2O(l)}(T)\right] \end{gathered} \tag{7.84}$$

In the latter equation h is the enthalpy of the species, which is again empirically modelled as a function of temperature [36].

Since both Equation 7.83 and Equation 7.84 are functions of temperature T and evaporation ε, they can be solved implicitly using numerical techniques to obtain the value of both parameters at a given point where the molar flows are known.

Having the temperature T and evaporation ε, the flow characteristics can be computed, starting with the volumetric fluxes of the gas and liquid phases:

$$\begin{aligned} \dot{V}_l &= \sum_j \frac{\dot{m}_{j(l)}}{\rho_{j(l)}} = (1-\varepsilon)\frac{\dot{n}_{H_2O_2} M_{H_2O_2}}{\rho_{H_2O_2(l)}} + (1-\varepsilon)\frac{\dot{n}_{H_2O} M_{H_2O}}{\rho_{H_2O(l)}} \\ \dot{V}_g &= \sum_j \dot{n}_{j(g)} \frac{RT}{p} = \left(\dot{n}_{O_2} + \varepsilon(\dot{n}_{H_2O_2} + \dot{n}_{H_2O})\right)\frac{RT}{p} \end{aligned} \tag{7.85}$$

Here the density ρ of peroxide and water is also an empirical model based on temperature [36]. Also the concentration of the species can now be computed:

$$C_{H_2O_2} = \frac{\dot{n}_{H_2O_2}}{\dot{V}_l + \dot{V}_g}, \quad C_{H_2O} = \frac{\dot{n}_{H_2O}}{\dot{V}_l + \dot{V}_g}, \quad C_{O_2} = \frac{\dot{n}_{O_2}}{\dot{V}_l + \dot{V}_g} \tag{7.86}$$

Lastly the density ρ, dynamic viscosity μ and kinematic viscosity ν of the homogeneous flow:

$$\rho = \frac{\dot{n}_{H_2O_2} M_{H_2O_2} + \dot{n}_{H_2O} M_{H_2O} + \dot{n}_{O_2} M_{O_2}}{\dot{V}_l + \dot{V}_g} \tag{7.87}$$

$$\mu \cong \mu_l(1-\alpha) + \mu_g \alpha \tag{7.88}$$

$$\nu = \mu/\rho \tag{7.89}$$

$$\alpha = \frac{\dot{V}_g}{\dot{V}_l + \dot{V}_g} \tag{7.90}$$

Before finally calculating decomposition and pressure, some parameters related to the catalyst bed need to be evaluated. These are the porosity $\tilde{\varepsilon}$ and the Arrhenius pre-exponential factor A_{f2}:

$$\tilde{\varepsilon} = 0.375 + 0.34\frac{D_p}{D_{\text{bed}}} \tag{7.91}$$

$$A_{f2} = a_s A_{\text{specific}} \tag{7.92}$$

$$a_s = (1-\tilde{\varepsilon})\frac{6}{D_p} \tag{7.93}$$

In these equations D_{bed} is the diameter of the catalyst bed, D_p is the particle diameter of the pellets and A_{specific} is the Arrhenius pre-exponential factor per unit specific area of the catalyst, which has a value of 19.7941 kmol/m$^2\cdot$s for $MnO_2/PbO/Al_2O_3$ catalysts [36]. At last, the derivatives of pressure p and decomposition λ with respect to the position x along the catalyst can be computed:

$$\frac{d\lambda}{dx} = \frac{\dot{V}_l + \dot{V}_g}{u} A_{f2} e^{-\frac{E_{f2}}{RT}} N_s \frac{K_1 C_{H_2O_2}}{1 + K_1 C_{H_2O_2}} \tag{7.94}$$

$$\frac{dp}{dx} = -\left(150\frac{1-\tilde{\varepsilon}}{Re_p} + 1.75\right)\frac{1-\tilde{\varepsilon}}{\tilde{\varepsilon}^3}\frac{\rho u^2}{D_p} \tag{7.95}$$

where $Re_p = \frac{uD_p}{\nu}$. Here E_{f2} is the activation energy of the catalyst, having a value of 15,000 kJ/kmol for $MnO_2/PbO/Al_2O_3$ catalysts [36]. Having computed these derivatives at one x coordinate of the catalyst bed, the next point can be evaluated by using a numerical integration technique with some interval Δx and repeating the process until reaching the complete length of the bed.

The procedure just explained is used to evaluate one particular catalyst geometry. However, some method is still needed to determine the optimal geometry for VAPOR's catalyst bed. In order to do this, first two constrains are established; firstly, the fraction of decomposition λ at the end of the catalyst shall be at least 0.99, and secondly, the pressure drop across the catalyst shall not exceed 5 bar. This is to ensure complete decomposition while keeping the disturbance on the flow within an acceptable limit. Afterwards, the minimum area to achieve full decomposition is computed by simulating geometries of increasing diameter. This is because in a catalyst with too small cross sectional area, the modelled flow loses all the pressure before fully decomposing, making the geometry configuration not possible. This area is determined by setting a long enough catalyst length and gradually increasing the bed diameter until the decomposition fraction λ at the end of the catalyst is at least 0.99.

After this minimum area is found, it is set as the starting point for the optimization process. The process consists of gradually decreasing the length of the catalyst in 1 mm steps until the decomposition factor λ at the end no longer reaches 0.99. When this happens, the last length for which the the 0.99 λ was achieved is considered, and the pressure drop is checked. If the pressure drop does not exceed 5 bar, the geometry is selected as the optimal and the loop stops. If the pressure drop is greater than 5 bar, then the bed diameter is increased by 1 mm and the process is repeated until the optimal geometry is found.

After obtaining the final bed diameter D_{bed} and length L_{bed}, the geometry has to be converted back to annular as explained before. In order to do this, it is assumed that the inner diameter D_{in} of the annulus is equal to the post diameter D_{post} of the pintle injector. This is because post of the injector is a geometric boundary for the catalyst as shown in Figure 7.12, so it cannot have a smaller inner diameter as it would intersect it. With this assumption, the outer diameter D_{out} of the annular shaped catalyst can be obtained:

$$D_{\text{out}} = \sqrt{{D_{\text{bed}}}^2 + {D_{\text{in}}}^2} \tag{7.96}$$

At the end of this process the optimal catalyst geometry for VAPOR's main engine as well as the temperature, pressure and decomposition profiles along its length are obtained, which can then be used as an input for other components in an iterative design process.

7.3. Results *Author(s): Marco, Mario, Noah*

The global optimization problem has been solved as explained in Section 7.2. The optimal set of parameters that followed from the optimization are the following (O/F, p_c, CR) = (4, 2, 10), with a characteristic length

L* of 0.8 m, excluding the catalytic bed. These results were mainly driven by the cooling requirements; results showed that a low oxidiser-to-fuel ratio is required to significantly decrease the chamber temperature and improve cooling performance, even if this solution is not the most optimal one, nor the most environmentally-clean, it was necessary to ensure that the engine can indeed be successful, performance requirements are still met. If film-cooling were to be used instead of regenerative cooling, the amount of fuel required [37, Chap. 4] would worsen both the performance and the emissions even more than what achieved with regenerative cooling, hence proving that this solution is the most performing and environmentally sustainable one.

All performance and geometrical parameters can now be calculated from the optimized set of parameters. The nozzle geometry is presented first in Figure 7.14, followed by plots of the gas properties along the nozzle in figs. 7.15, 7.17 and 7.18. For simplicity, the most important results are also presented in Table 7.6.

The engine geometry in Figure 7.14 was defined through the formulas presented in Subsection 7.2.2, with the resulting values summarized in Table 7.5. The distance from the injector of the combustion chamber ($x = 0$) to the throat is given by $L_{\text{cyl}} + L_{\text{conv}}$, with a chamber diameter D_{cc} maintained over the cylindrical section. The convergent part is defined through a 30°slope, which is rounded off by an arc of radius 50 mm at the chamber wall and blended into the throat by an arc of radius 10 mm on each side, with the throat located at a diameter D^*. The divergent part is a bell nozzle, spanning the length L_{div}, which is 80% of length of a 15° conical nozzle, and expanding to an exit diameter D_e.

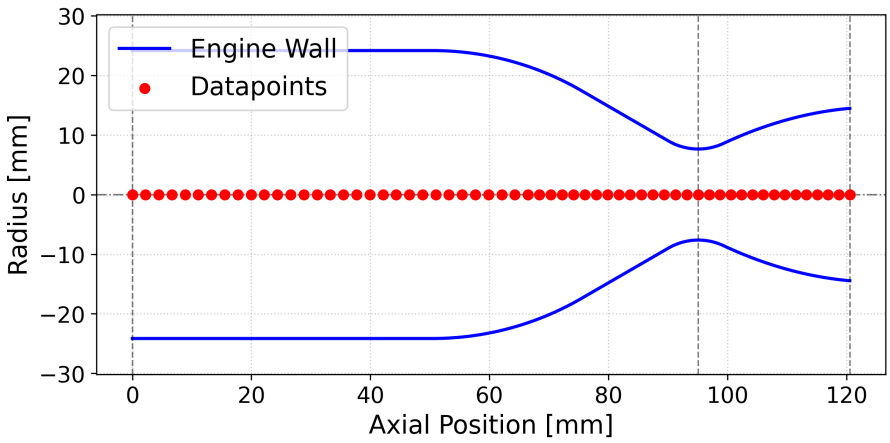

Figure 7.14: Cross-section of the rocket engine geometry, showing the engine wall profile (blue) and the discrete axial stations used in the thermal analysis (red). Dashed vertical lines indicate the injector face, nozzle throat, and nozzle exit, from left to right respectively.

Table 7.5: Geometric dimensions of the thrust chamber, consisting of the combustion chamber, convergent, and divergent section

Parameter	Value [mm]
L_{cyl}	66.50
L_{conv}	28.60
L_{div}	25.46
D_{cc}	48.29
D^*	15.27
D_e	28.91

Figure 7.15 shows the temperature along the engine, quasi-constant in the combustion chamber and rapidly decreasing in the nozzle. Figure 7.16 shows the area-normalised temperature along the engine, reaching a peak at the throat due to the small local diameter and high combustion temperatures, similarly to the results by van den Berg et al. [38]. Alternatively, Figure 7.17 shows the evolution of the Mach number, increasing monotonically with x, lastly Figure 7.18 represents the pressure in MPa that follows a similar trend to the temperature. As can be observed from the graphs, all expected trends and behaviours are well captured by the simulation, it can be noted how the Mach number is equal to 1 in the throat, as expected for any supersonic nozzle, and the exit pressure is equal to the sea-level atmospheric pressure, as expected for a sea-level optimised engine.

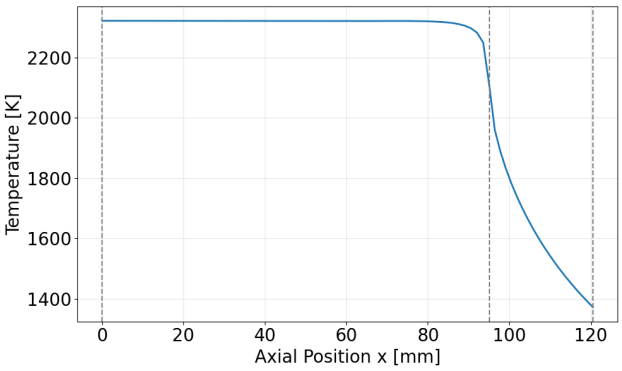

Figure 7.15: Temperature distribution along the engine

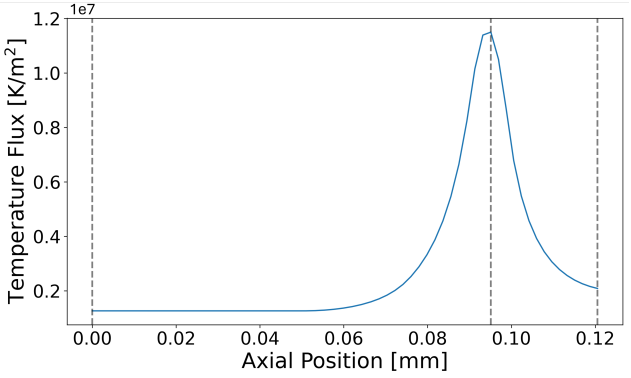

Figure 7.16: Area-normalised temperature along the engine

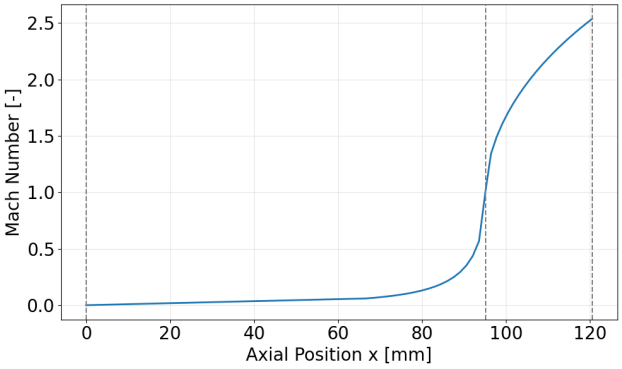

Figure 7.17: Mach distribution along the engine

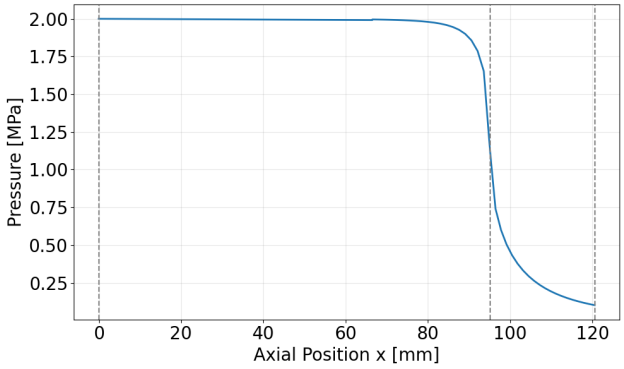

Figure 7.18: Pressure distribution along the engine

Table 7.6: Overview of Engine Performance Parameters

Parameter	Value	Parameter	Value	Parameter	Value	Parameter	Value
p_c	2 MPa	$M_{w,cc}$	19.1 g/mol	t_b	25.49 s	A_e	6.57×10^{-4} m^2
O/F	4	$\dot{m}$	0.244 kg/s	c^*	1500 m/s	A_t	1.83×10^{-4} m^2
CR	10	v_e	2048 m/s	C_F	1.36	A_e/A_t	3.58
T_c	2321 K	I_{sp}	208.8 s	p_c/p_e	19.7	A_{cc}	1.83×10^{-3} m^2
γ_{cc}	1.2015	T_{sl}	500 N	V_c	1.47×10^{-4} m^3	L^*	0.8 m
$t_{w,int}$	1 mm	$t_{w,ext}$	2 mm	h_{chan}	0.5 mm	N_{chan}	24
t_{rib}	1.5 mm						

The temperature distributions of the optimised design are shown in Figure 7.19. The wall temperature reaches its maximum in the throat region, consistent with the peak in convective heat flux that occurs there. Downstream, in the diverging section, the expanding flow causes a progressive drop in gas temperature, which translates into decreasing thermal loads along the nozzle wall. However, the combustion chamber exhibits somewhat lower wall temperatures than the divergent section despite operating at higher stagnation temperatures. This is due to the larger chamber diameter, which reduces the local heat flux.

The coolant temperature rises continuously along its flow path as heat is transferred from the chamber wall, with its maximum reaching 62.73°C (335.88 K). In the throat region, though, the reduced nozzle diameter reduces the cooling channel cross-section. Thereby the coolant velocity increases locally, which in turn shortens the residence time. Thus limits the heat absorbed per unit channel length and causes a local reduction in the slope of the coolant temperature.

The total residence time of the HTP within the cooling channels is approximately 36.9 ms. Given this short exposure time, significant thermal decomposition of the peroxide within the cooling circuit is not expected, despite the elevated temperatures. As a result, only a limited reduction in peroxide concentration is antici-

pated before the propellant reaches the catalyst bed.

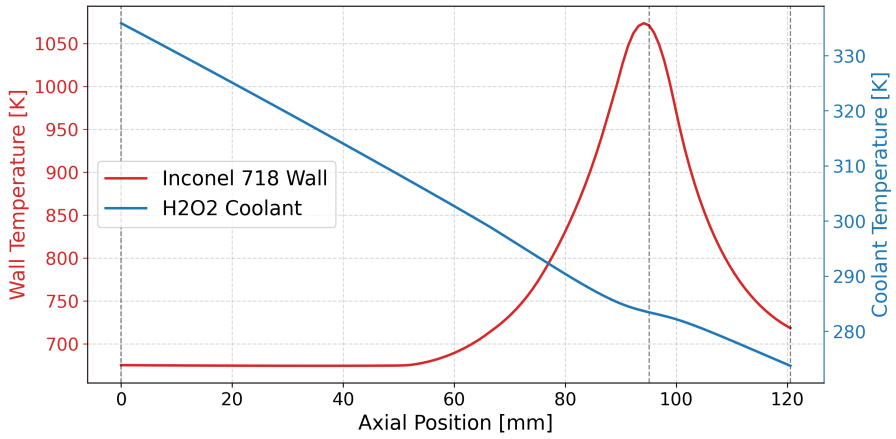

Figure 7.19: Temperature distribution along the engine after the 25 second burn, showing the Inconel 718 inner wall temperature (red, left axis) and H_2O_2 coolant temperature (blue, right axis). The wall temperature peaks at the nozzle throat region (≈95 mm).

The peak wall temperature across the entire engine is 800.52°C (1073.67 K). This value lies comfortably below the melting point of Inconel 718 (1260–1336 °C) [10]. However, for reusable operation the relevant design threshold is not the melting point but the long-term operating temperature limit, which for Inconel 718 is approximately 750°C (1023.15 K)[8].

Beyond the global peak, localised hotspots develop in the throat region at positions midway between adjacent cooling channels, where the distance to the nearest coolant channel is greatest. At these locations the thermal resistance through the wall material is higher, whereby heat removal is less effective and wall temperatures exceed the global peak. The hotspot temperatures are expected reach approximately 837.89°C (1111.04 K) [39].

At temperatures above approximately 750 °C (1023.15 K), Inconel 718 becomes increasingly susceptible to oxidation and thermally induced degradation, most notably low-cycle fatigue [40]. Nevertheless, the severity of this concern is mitigated by the short operating profile: each firing lasts 25 seconds, such that the total cumulative hot-fire time over 10 reuse cycles amounts to approximately 250 seconds. Given this limited thermal exposure, the elevated temperatures at the throat and hotspot locations are considered acceptable for the present design iteration. Nevertheless, this represents a primary driver for future refinements in thermal management.

As it was found that the temperatures approached and sometimes exceeded the service limit, supplementary film cooling was evaluated as a potential mitigation measure. A localised film cooling belt positioned at the aft end of the combustion chamber was considered, intended to generate a protective film layer over the converging section and reduce wall temperatures by approximately 300 K.

A first-order analysis [37, Chap. 4] indicated that the coolant mass flow rate required to achieve this level of heat absorption would be on the order of grams per second. While this is small in terms of environmental impact, the corresponding film layer thickness would be on the order of microns, rendering uniform distribution across the wall impractical. Non-uniformity would introduce dry spots, i.e. localised regions of film breakdown, that could produce wall temperatures in excess of those observed without film cooling [37, Chap. 4]. Furthermore, the orifice dimensions required to deliver such a thin film are below practical manufacturing tolerances. The concept was therefore not pursued further.

Extending the film cooling to the full engine length was also considered. This approach would inherently carry greater environmental implications due to the higher fuel consumption, and, as noted by Cervone [29], falls outside the scope of the present analysis, since accurate modelling of full-engine film cooling requires a combustion CFD analysis to capture film–flow interactions. Should film cooling be revisited in future work, a trade-off study between combined regenerative–film cooling and solely film cooling should

[8] Inconel 718 Maximum Operating Temperature [Date Accessed: June 15]

be performed.

Finally, RP-1 was also considered as an alternative coolant, due to its higher thermal decomposition threshold and safer handling compared to 98% H_2O_2. However, its substantially lower thermal conductivity, combined with storage at ambient temperature, resulted in significantly reduced cooling performance [11, 12].

Now that the cooling results are defined, it is important to evaluate the cost functions presented in Section 7.2, allowing to compute the overall dry mass, volume and emissions of the propulsion system, considerations on performance are instead later presented in Chapter 12. Table 7.7 shows the final occupied volumes of the various components, while Table 7.8 shows the dry masses. Lastly, Table 7.9 shows the exhaust gases emitted in the atmosphere.

Table 7.7: Volume

Component	Volume [L]
Peroxide tank	3.36
Fuel tank	1.48
Helium tank	0.91
Combustion chamber	0.15
Catalyst	0.017
Piping	0.14
Total	**6.06**

Table 7.8: Dry Mass

Component	Mass [kg]
Peroxide tank	0.293
Fuel tank	0.170
Helium tank	0.402
Helium	0.037
Piping	0.155
Thrust chamber	1.170
Catalyst	0.011
Total	**2.238**

Table 7.9: Emissions

Component	Mass Fraction [-]
CO_2	0.32
CO	0.2
H_2O	0.46
Total pollutants	**0.52**

Results shows that about 52% of the emitted gases will be pollutants, on an ascent that burns about 6 kg of propellant, a total of 3.12 kg pollutants will be exhausted in the atmosphere, as mentioned in Subsection 9.5.1, these concentration of pollutants are much lower than for typical aircraft missions. Since VAPOR is not burning any additional fuel during the mission, and given that the total endurance is about 1 hour per mission, direct emissions per flight hour can be quantified to be ≈ 3.12 kg/hr. Of course, indirect emission due to recharging the battery and end-of-life strategies still need to be addressed.

Once the thrust chamber is sized, the injector needs to be designed following the methodology presented in Section 7.2. Running the optimization algorithm for the range of geometries in Table 7.3 and the engine performance parameters previously obtained yields the final design presented in Table 7.10 and Figure 7.20:

Table 7.10: Dimensions of the final injector.

Parameter	Value
Pintle tip diameter D_{pt}	8.0 mm
Annular gap thickness t_{ann}	2.1 mm
Center gap diameter D_{cg}	4.55 mm
Pintle rod diameter D_{pr}	3.0 mm
Post recess length r_{post}	3.0 mm
Pintle tip angle θ_{pt}	20 deg
Post angle θ_{post}	30 deg
Pintle tip opening L_{open}	0.2 mm
Pintle tip thickness t_{pt}	1.0 mm
Post tip thickness t_{post}	0.5 mm

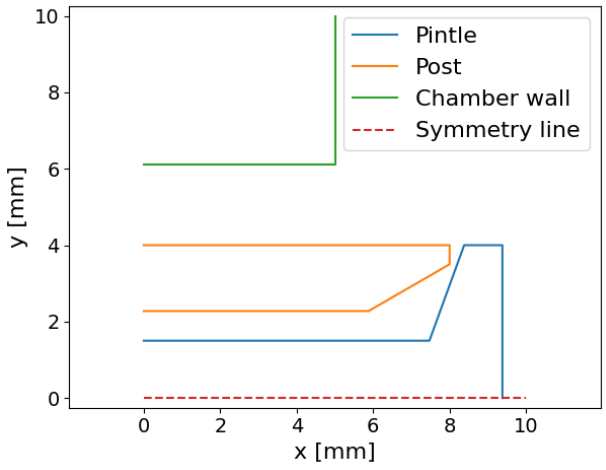

Figure 7.20: Plot of the final injector geometry.

As previously explained, this configuration corresponds to the geometry with smallest required chamber volume for complete vaporization while meeting all the constraints. The flow and spray characteristics associated to this geometry are presented in Table 7.11.

It is important to note several aspects in these results. Firstly, the vaporization distance x^* is extremely small, only 0.14 mm. This makes the chamber volume and dimensions marginally larger than the part of the injector sticking into the chamber. The reason for this is that the droplet diameter D_{32} of 4.08 μm is significantly smaller than the sizes in the order of 100 μm from the case considered by Son et al. [33]. This is because in VAPOR's engine the oxidizer is gaseous rather than the fuel therefore having a gas mass flow $\dot{m}_{gas}$ four times greater. This leads to a much higher gas injection speed V_{gas} for the same annular gap area A_{gas}. This higher speed then carries to Equation 7.75 and Equation 7.76, ultimately leading to the small droplet size and chamber dimensions. Another factor contributing to these discrepancies is that the density ρ_{gas} of methane, the gaseous fuel used in the study [33], is roughly twice that of decomposed 98% at injection conditions.

Table 7.11: Calculated injector flow and spray characteristics.

Parameter	Value
Injection gas velocity	432.64 m/s
Injection liquid velocity	8.44 m/s
Pressure drop ΔP	0.59 bar
Spray angle α	8.19°
Droplet diameter (D32)	4.08 μm
Vaporization distance x^*	0.14 mm
Minimum chamber diameter D_c	8.04 mm
Minimum chamber length L_c	3.34 mm
Minimum chamber volume	0.17 cm^3

Once the pintle injector has been designed, the catalyst must be sized accordingly; to size it, a pellet size of 16-18 US standard sieve opening (1.18-1.00 mm) was used. This was the smallest pellet size used in the experiments by S. Jung et al. [36], which provided the best performance. The inlet conditions of the peroxide were 300 K and 25 bar, obtained from the 20 bar chamber pressure and assuming the maximum pressure drop of 5 bar. Note that the inlet temperature of the peroxide will be higher in reality due to the regenerative cooling, however this will have a positive effect on the performance of the catalyst and therefore using 300 K is conservative and accounts for some contingency. The catalyst dimensions and 1D analysis obtained from the optimisation algorithm is presented in Table 7.12 and Figure 7.21:

Table 7.12: Optimised catalyst parameters

Parameter	Value
Inner diameter D_{in}	8.0 mm
Outer diameter D_{out}	44.0 mm
Length L_{bed}	11.0 mm
Outlet temperature T_{end}	1208 K
Outlet decomposition λ_{end}	0.991
Pressure drop ΔP	4.26 bar

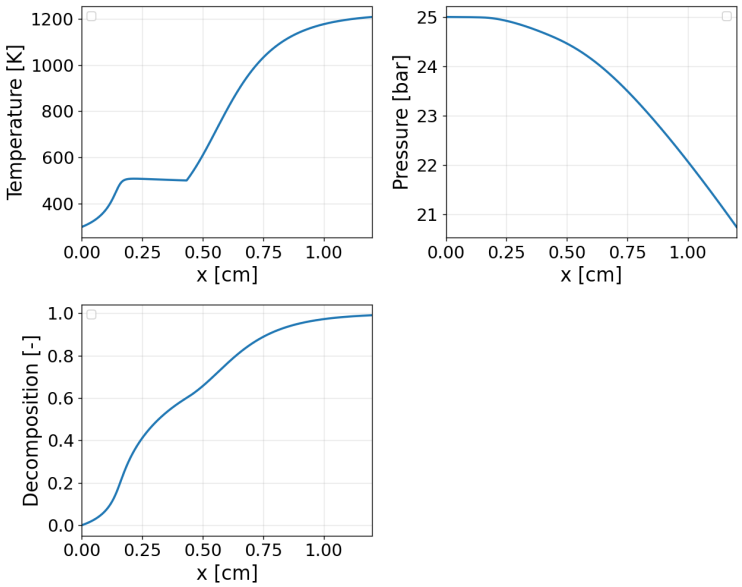

Figure 7.21: Optimised catalyst flow profile

These profiles closely resemble the ones from the study [36], which proved to be accurate when compared to experimental data. This results can therefore be trusted with a high level of confidence, however test data is still needed to fully validate it.

7.4. Sensitivity Analysis *Author(s): Marco*

A sensitivity analysis has been performed by firstly changing the weights of the cost function by ± 5% and secondly by discarding the volume cost function entirely; results showed that the optimised set of parameters did not change, meaning that the presented one is the one that best reconciles the challenging aspects and demands of regenerative cooling to sufficient performance and low emissions.

7.5. Discussion and Limitations *Author(s): Marco, Vladimir*

The results highlighted so far in this report demonstrate the feasibility of the final design. It is worth noting however that there are a number of underlying assumptions and simplifications adding to uncertainty of the final results.

A major limitation is the use of RPA and CEA software for prediction of combustion and nozzle flow properties. RPA is a well known tool and is based on one-dimensional thermodynamic models but cannot accurately predict more complex flow phenomena such as combustion instabilities, flow separation and three-dimensional effects; the estimated inefficiencies cannot be taken as absolute truth as explained in Subsection 7.2.1 Therefore the predicted performance should be regarded as an approximation of the real engine behaviour.

The flow field inside the combustion chamber and nozzle was not analysed by validated CFD. Instead, a database was created that was subject to the above uncertainties and numerical errors. While these methods are suitable for initial design they cannot consider local complex phenomena that may occur in practice.

Thermal analysis introduces another layer of uncertainty. The heat transfer coefficients were estimated using simplified thermal resistance models, including empirical relations used to estimate heat transfer between both the gas and coolant, several other assumptions in thermal modelling were made as outlined in Subsection 7.2.1. Though these methods are often utilized in early design stages, they are unable to fully capture the unpredictable thermal environment within a regeneratively cooled rocket engine, especially at this small scale. Local hot spots, non-uniform combustion, and manufacturing imperfections, may lead to wall and coolant temperatures that differ from those predicted by the model. As a consequence, testing in facilities may reveal different thermal behaviour than what presented in this report.

Moreover, the cooling analysis is made under the assumption that the coolant distribution is ideal, along with the channel geometry. In practice, the tolerance error during manufacturing, as well as the presence of uneven flow, may result in lower cooling performance, especially in the throat area where high heat fluxes occur. However, it seems that the model correctly represents the anticipated behaviour, since, at least, the wall temperature at the throat is the highest one and the temperatures in the other areas have reasonable distribution.

Also, the structural analysis did not consider some factors, such as thermal fatigue and creep, among others. Nevertheless, the engine will be fired only for 25 s during 10 missions, which does not seem to cause significant problems regarding fatigue in the engine.

Finally, the model is based on analysis and numerical techniques, and literature findings, but has not been experimentally verified yet. Hot firing of the engine is necessary to check the performance, thermal behaviour, cooling efficiency and overall validity of the model. Hence, the results obtained can only be considered as estimates that are only appropriate for a conceptual design phase.

Future research efforts should involve extensive CFD computations of the combustion process, experimental verification of thermal and mechanical analyses, hot firing experiments, etc. In addition, future research efforts should address an estimation of thermal stresses and creep, so as to quantify the lifetime of such type of engines.

8 | Avionics and Electrical Systems

This chapter addresses the systems that turn VAPOR from an airframe into an autonomous vehicle: the sensing, computation, command and power-distribution hardware that let the vehicle fly its mission without a pilot on board. The chapter first describes the flight intelligence and its peripherals and establishes their power demand (Section 8.1), then combines this with the propulsion demand into a single power budget that sizes the battery (Section 8.2), and finally documents how the components are wired and how data flows between them and the outside world (Section 8.3 and Section 8.4).

8.1. Flight Intelligence and Peripherals *Author(s): Duco, Victor*

At the centre of the avionics architecture sits the flight controller, a PixHawk 6C, which acts as the single processing unit of the vehicle. It runs the autopilot firmware (more detail on the control systems is given in Chapter 11), combines the sensor data, executes the pre-loaded mission and issues the commands to the control surfaces and the propulsion system during both the rocket-boost and the electric-cruise phases. The IMU, the accelerometers, gyroscopes and barometer needed for attitude and altitude estimation are integrated within the PixHawk itself, which is one of the reasons this controller was selected. Drawing 5 V at up to roughly 0.4 A, the flight controller together with its integrated sensors accounts for about 2 W. [1]

Absolute positioning is provided by a GPS receiver. The receiver is paired with a cellular (SIM) module that offers redundant connectivity beyond line-of-sight of the primary radio link. Together these consume on the order of 2 W [2]. Air data is measured by a pitot-static airspeed sensor, which feeds the cruise-speed control loop and provides stall protection during the low-speed phases of flight; its draw is small, a few tenths of a watt, and is listed only for completeness.

The control surfaces are driven by five Volz DA 22 actuators, one per movable surface across the V-tail and the ailerons. These were selected for their metal gear train and integrated position feedback, which deliver the precise and repeatable deflections that the stability and control analysis depends on. At 12 V each actuator is rated at 0.4 A, giving a peak draw of around 25 W for the five units and dropping below 0.1 A per unit in standby[3]. As the surfaces are only active for a fraction of the flight, a duty cycle of roughly 20% peak and 80% standby is assumed for the energy estimate, although the peak figure is retained in the power table as a conservative bound.

The radio transceiver maintains the bidirectional command-and-telemetry link to the ground station and, in the surveillance configuration, also carries the payload video downlink. As discussed in Section 8.4, this link is asymmetric: the uplink carries only low-rate commands, while the downlink sustains higher-rate video feeds, which is what mostly drives the transmit power to between 2 and 3 W when video is active.

Finally, a set of propulsion sensors monitors the RP-1 and HTP feed pressures, the temperatures, and the state of the bi-propellant engine. These are concentrated toward the end of the vehicle and report over a shared Controller Area Network (CAN) bus (Section 8.3). Because they are only active during the short rocket-boost phase, their contribution is carried as an energy term (conservatively 4 Wh) in the budget of Section 8.2 rather than as a steady cruise load. To the steady loads a power-distribution allowance of about 2 W is added, representing the conversion and routing losses in the power-distribution unit and the splitter board that fans power and data out to the peripherals.

Finally, payload is treated here as part of the avionics, since it draws from the same battery and is commanded and read out through the same flight control and communication chain as the other peripherals. VAPOR is sized to carry a payload of up to 7kg, and the bay is deliberately kept payload-agnostic so that the vehicle can be reconfigured for different surveillance tasks without redesign. The power demand of the payload spans a wide range depending on the sensor fitted. For the primary surveillance role, an Electro-Optical/Infrared (EO/IR) gimbal such as the DJI Zenmuse H30T[4] is representative: it combines a wide-angle camera, a zoom camera, an infrared thermal camera and a laser range finder in a single 920 g unit and draws only about 28 W, which is well suited to detecting and tracking a wildfire or mapping a disaster area day or night. Other configurations, such as a LiDAR scanner or a multispectral camera, fall in a comparable power band. At the high end, however, an active-illumination payload such as a high-power searchlight for night

[1] Holybro.com [Accessed Date: 16 June] [2] Holybro M10 GPS Module [Date Accessed: 16 June]
[3] `https://www.volz-servos.com/fileadmin/user_upload/Downloads/Datasheets/DA-22_Datasheet_Rev_D.pdf`. Accessed at: 16-06-2026 [4] DJI Zenmuse H30 Series [Date Accessed: June 10]

time search-and-rescue can draw up to 100 W, depending on the flashlight strength. To keep the platform compatible with the full envelope of foreseeable payloads, the power budget is sized against this 100 W worst case rather than against the nominal camera load, and this figure is therefore the value summed in Table 8.1.

Summing these steady state loads gives a continuous avionics power requirement of approximately 13–14 W, as listed in Table 8.1. This value forms the avionics contribution to the overall power budget of Section 8.2, where it is combined with the cruise propulsion and the payload power requirement to size the battery.

Table 8.1: Avionics Power Consumption Estimations

Component	Power [W]	Notes
Flight Controller (PixHawk 6C)	2.0	5 V, max 0.4 A; includes integrated IMU & barometer
GPS & Cellular Module	2.0	Positioning and redundant connectivity
Airspeed Sensor	0.3	Pitot-static; cruise control and stall protection
Actuators (Tail & Aileron)	25.0	5× Volz DA 22 (105 g, 0.18 A, 28 V). <0.01 A standby; peak value retained
Radio TX / RX (w/ video)	3.0	High rate downlink dominates
Power Distribution Losses	2.0	Power Distribution Unit (PDU) and splitter board
Payload	≤ 100	Sized to worst case (high power spotlight). EO/IR camera (e.g. DJI Zenmuse H30T) draws ~28 W
Total Estimated Power	**134**	Payload-dominated worst case; ~62 W with a 28 W camera fitted

8.2. Total Power Budget *Author(s): Duco*

The previous section, Section 8.1, calculated the estimated total power draw for the avionics. This is equal to 134 W for a maximum endurance (cruise + glide) of 68 minutes which comes down to an energy requirement of 152 Wh. In Chapter 13, the power draw for the secondary propulsion system will be calculated. The electrical propulsion unit will be active for the full 35 minute endurance time, which results in an energy demand of 7000 mAh. The sum of these two values forms the basis for sizing the battery.

Previously, in the midterm report the type of battery and a suitable manufacturer was already found. This was the solid state battery built by RacePow[5], which offers relatively high energy density of around 350 kg/wh. In Subsection 13.1.3, it was also discussed that a 12S (or 44.4V) power system offers benefits over the previous 6s battery due to energy losses. This is a change from the requirements.

Summing all sensors, peripherals and the secondary propulsion comes down to an energy requirement of a little under 462 Wh, or 10500 mAh. The minimum battery size Racepow offers is 11000 mAh which also meant that this battery was automatically chosen, putting the VAPOR mission at a comfortable position to fulfil the 35 minute cruise and additonal glide phase (in which the avionics and payload is powered but not the electrical propulsion unit) with enough headroom[6], with a mass of 1.6 kg. Below, in Table 8.2, the statistics of this battery are tabulated.

Table 8.2: Key specifications of the Racepow 11000 mAh 12S LiPo battery.

Parameter	Value	Parameter	Value
Capacity	11000 mAh	Discharge rate	5C
Configuration	12S	Specific energy	350 Wh/kg
Nominal voltage	44.4 V	Dimensions (L × W × H)	166 × 60 × 72 mm
Energy	488.4 Wh	Weight	1620 g

[5] RacePow Solid State Battery [Date Accessed: June 9]

[6] RacePow Solid State Battery 11,000 mAh [Date Accessed: June 17]

8.3. Electrical and Data-Handling Block Diagram *Author(s): Duco, Victor*

Figure 8.1 gives a single overview of every electrical and data-handling component carried by VAPOR and of how these components are wired together. Conventionally, the Electrical Block Diagram (EBD) and the Data-Handling Block Diagram (DHBD) are drawn as two separate figures, the former describing power provision, switching and conversion, and the latter describing the routing of data between sensors, processors and links. For VAPOR these two diagrams are combined. The electrical side is simple: a single battery supplies the entire vehicle, so a standalone EBD would consist of little more than the battery and two loads. The data-handling side reduces almost entirely to sensor wiring into one flight controller.

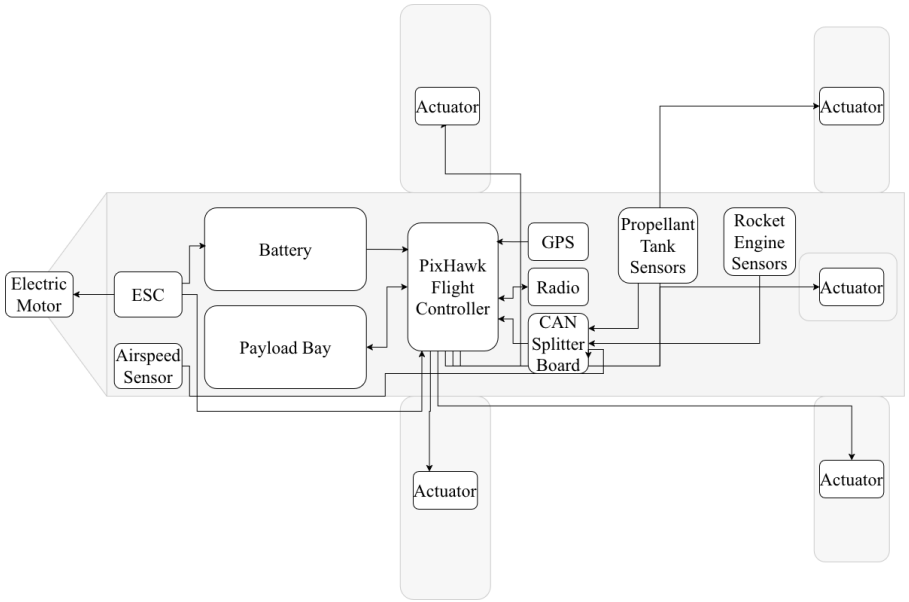

Figure 8.1: Combined electrical and data-handling block diagram of the VAPOR vehicle.

Power provision, the EBD content, is built around the solid-state battery selected in Section 8.2. The battery is the only electrical source on board and feeds two branches. The first branch runs through the Electronic Speed Controller (ESC) to the electric motor of the secondary (cruise) propulsion system; this is the high-current path and is kept as short and direct as possible. The second branch supplies the PixHawk flight controller, which in turn distributes regulated power to the lower-current peripherals such as the GPS receiver, the radio, the airspeed sensor and the control surface actuators.

Data handling, the DHBD content, is organised around the PixHawk flight controller as the central node. Navigation data enters the controller directly from the GPS receiver, the radio carries the bidirectional telemetry and command link to the ground station, and air-data is supplied by the airspeed sensor. The propulsion sensors are handled differently. The propellant tank sensors and the rocket engine sensors that monitor the kerosene and high-test-peroxide feed and the state of the bipropellant engine are located toward the rear of the vehicle, away from the avionics bay. Rather than running a separate cable from each sensor back to the flight controller, these sensors share a single CAN bus through a CAN splitter board, which acts as a hub and connects to the PixHawk over one CAN link. The control surface actuators are commanded by the flight controller: those near the fuselage centreline are driven directly from its servo outputs, while the actuators mounted out on the booms and tail are routed via the splitter board to limit the number of long cable runs back to the avionics bay. Together these connections cover all command and sensing paths needed for both the rocket boost phase and the electric cruise phase of the mission.

8.4. Communication Flow Diagram *Author(s): Duco*

Since VAPOR is operated remotely, without the operator being in physical contact with the vehicle, the communication chain between the ground segment and the air segment is an essential part of the design. Figure 8.2 presents the communication flow diagram, showing all elements that take part in the exchange of data and commands, together with the interactions between the system and its physical environment. Solid

arrows represent data and command flows, while dashed arrows represent physical interactions that do not pass through the communication chain.

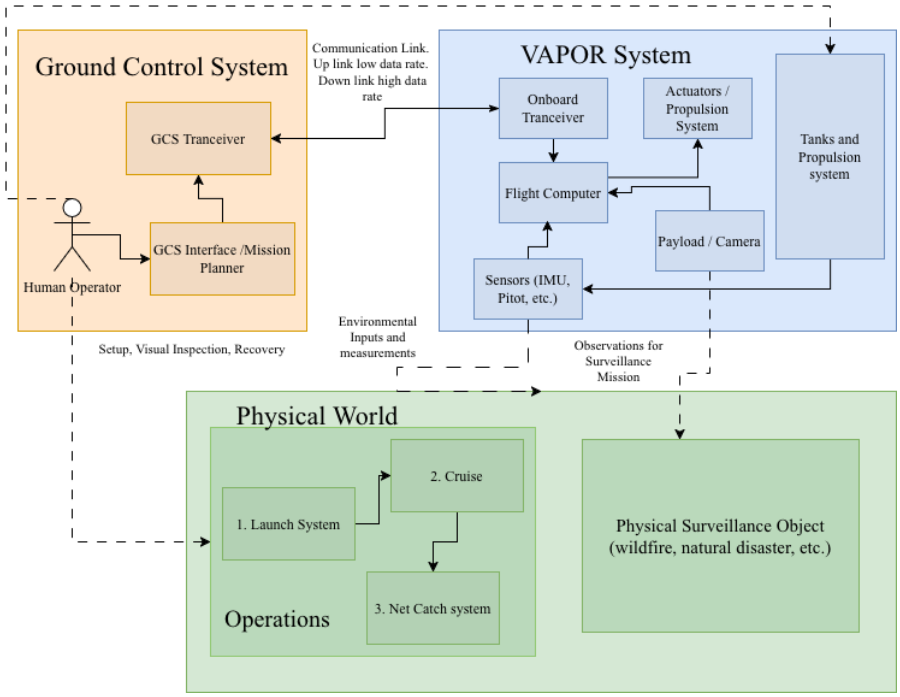

Figure 8.2: Combined electrical and data-handling block diagram of the VAPOR vehicle.

The ground segment consists of the human operator, the Ground Control Station (GCS) interface running the mission planner software, and the GCS transceiver. Before flight, the operator defines the mission in the mission planner, including the waypoints and the surveillance target area. This translates into commands transmitted through the GCS transceiver. During flight the same interface displays the telemetry and payload data received from the vehicle, allowing the operator to monitor the mission and intervene where necessary.

The air segment mirrors this structure. The onboard transceiver forms the vehicle end of the radio link and passes received commands to the flight computer, which acts as the central node of the air segment: it executes the mission, reads the onboard sensors (IMU, pitot tube and the propulsion sensors discussed in Figure 8.1), commands the actuators and propulsion system, and collects the observations made by the payload camera.

The diagram also shows the interactions with the physical world that fall outside the communication chain. The vehicle senses its environment directly through its air-data and inertial sensors and observes the surveillance object such as a wildfire, natural disaster or similar. This happens through its payload. The operator, in turn, interacts physically with the system during the ground phases of the mission: setting up and visually inspecting the vehicle before launch, operating the launch system, and recovering the vehicle from the net-catch system after landing. These interactions complete the operational loop in which the operator plans the mission remotely, VAPOR executes it autonomously, and the operator handles the vehicle only at launch and recovery. The operator also interacts with the VAPOR mission directly by refuelling the propellant tanks and replacing the battery.

8.4.1. Communication Link Sizing

The communication subsystem is sized with a link budget analysis, the standard procedure for determining whether a radio link closes with enough margin [41]. The method expresses the power arriving at the receiver as the transmitted power modified by the antenna gains and by the propagation and implementation losses, and compares this received power against the minimum power the receiver requires to understand the signal. The difference between the two, the *link margin*, must be positive for the link to be considered closed.

Because VAPOR operates within the line of sight of the GCS, free space spreading is the most important loss mechanism. The atmospheric absorption, rain and system noise contributions that govern spacecraft links are negligible at the frequencies and ranges considered here and are absorbed into the link margin [42]. The subsystem is sized for the most demanding geometry. With a maximum horizontal range of $R_h = 40\,\text{km}$ and a cruise altitude of $h = 2.5\,\text{km}$, the range between the ground and air segments is approximately $d = 40.1\text{km}$. Under the standard 4/3 effective earth model, the radio horizon for an antenna at this altitude exceeds 210 km [42]. This means that the link is limited by the available power and not by the curvature of the earth, which also justifies treating the path as free of obstructions.

The free-space path loss is obtained from the Friis transmission equation, which, when expressed in logarithmic form, reads as given in Equation 8.1 [41, 43]. The power available at the receiver follows as Equation 8.2, such that the link margin is as defined in Equation 8.3.

$$L_{\text{fs}} = 32.44 + 20\log_{10}\left(d_{[\text{km}]}\right) + 20\log_{10}\left(f_{[\text{MHz}]}\right), \tag{8.1}$$

$$P_r = P_t + G_t + G_r - L_{\text{fs}} - L_\ell, \tag{8.2}$$

$$M = P_r - S_r, \tag{8.3}$$

where d the slant range, f the carrier frequency, P_t is the transmit power, G_t and G_r are the transmit and receive antenna gains, L_ℓ includes cable and implementation losses, and S_r the receiver sensitivity.

The asymmetry between the two links is found in the hardware selection. The command and telemetry link is realised with an ExpressLRS module in the 868 MHz band transmitting at 1 W (30 dBm), whose long-range packet modes reach a receiver sensitivity of approximately −108 dBm [7]. The payload downlink that carries the surveillance imagery uses a 2.4 GHz digital data link transmitting at 1 W into an omnidirectional onboard antenna, received by a directional tracking antenna at the GCS. A representative module of this class achieves −95 dBm sensitivity at a throughput of several Mbit/s [8]. Evaluating the expressions above for both links yields the budgets summarised in Table 8.3.

Table 8.3: Link budget for the command and payload links at maximum slant range.

Parameter	Symbol	Command	Payload	Unit
Carrier frequency	f	868	2400	MHz
Slant range	d	40.1	40.1	km
Transmit power	P_t	30	30	dBm
Transmit antenna gain	G_t	3	2	dBi
Receive antenna gain	G_r	2	20	dBi
Free-space path loss	L_{fs}	123.3	132.1	dB
Implementation loss	L_ℓ	3	3	dB
Received power	P_r	−91.3	−83.1	dBm
Receiver sensitivity	S_r	−108	−95	dBm
Link margin	M	**16.7**	**11.9**	dB

Both links close with positive margin: 16.7 dB on the command link and 11.9 dB on the payload downlink. These margins comfortably exceed the order of 10 dB allowance typically retained on line of sight UAV links, and both budgets are met with commercially available radio hardware operated at 1 W. The payload downlink yields the smaller margin and therefore drives the design of the communication subsystem, as can be expected from the uplink downlink asymmetry. Operating at 1 W exceeds the unlicensed power limits in The Netherlands of these bands, so the VAPOR mission is assumed to be operated under an appropriate license.

[7] Open-source long-range RC link. Accessed: 16 June 2026 `https://www.expresslrs.org/hardware/hardware-selection/`

[8] Receiver sensitivity −108 dBm at 30 dBm output. Accessed: 16 June 2026 `https://www.microhardcorp.com/pMDDL2450.php`

9 | Airframe Design

In this chapter, the airframe design shall be discussed. This will firstly be done with the aerodynamic wing design in Section 9.1, followed by the tail sizing in Section 9.2. Then, the structural components will be described in Section 9.3. Thirdly, the hinge mechanism needed to fold the wings is designed in Section 9.4. The vibrational loads will be analysed in Section 9.5. The fuselage structural design is discussed in Section 9.6. Lastly, the aerodynamic analysis of the full configuration will be discussed in Section 9.7.

9.1. Aerodynamic Wing Design *Author(s): Kyle*

In order to efficiently design a wing optimised for aerodynamic performance, multiple steps need to be taken. Firstly, in Subsection 9.1.1, the airfoil will be selected, which will then be analysed and optimised in Subsection 9.1.2. The methods used will be verified and tested, while also performing a sensitivity analysis in Subsection 9.1.3. Subsequently, the wing will be optimised in Subsection 9.1.4. These methods will again be verified and tested, and a sensitivity analysis will be performed in Subsection 9.1.5.

9.1.1. Airfoil Selection

The first step in a wing design is choosing the airfoil. The chosen airfoils that were analysed are the following: E387, NACA 0012, NACA 2412, NACA 4412, NACA 63(2)A-015, NACA 747A315, S1223, and WORTMANN FX 63-137. These have been chosen based on the research done by Selig [44], which investigated airfoils for low speed. From here, airfoils have been chosen for optimised range or endurance. Analysis was performed on XFLR5. With the aid of this software, the performance of each airfoil has been plotted in Figure 9.1. Analysis has been done for a Reynolds number of 491900, and a Mach number of 0.08 from the initial design of Armeli et al [1].

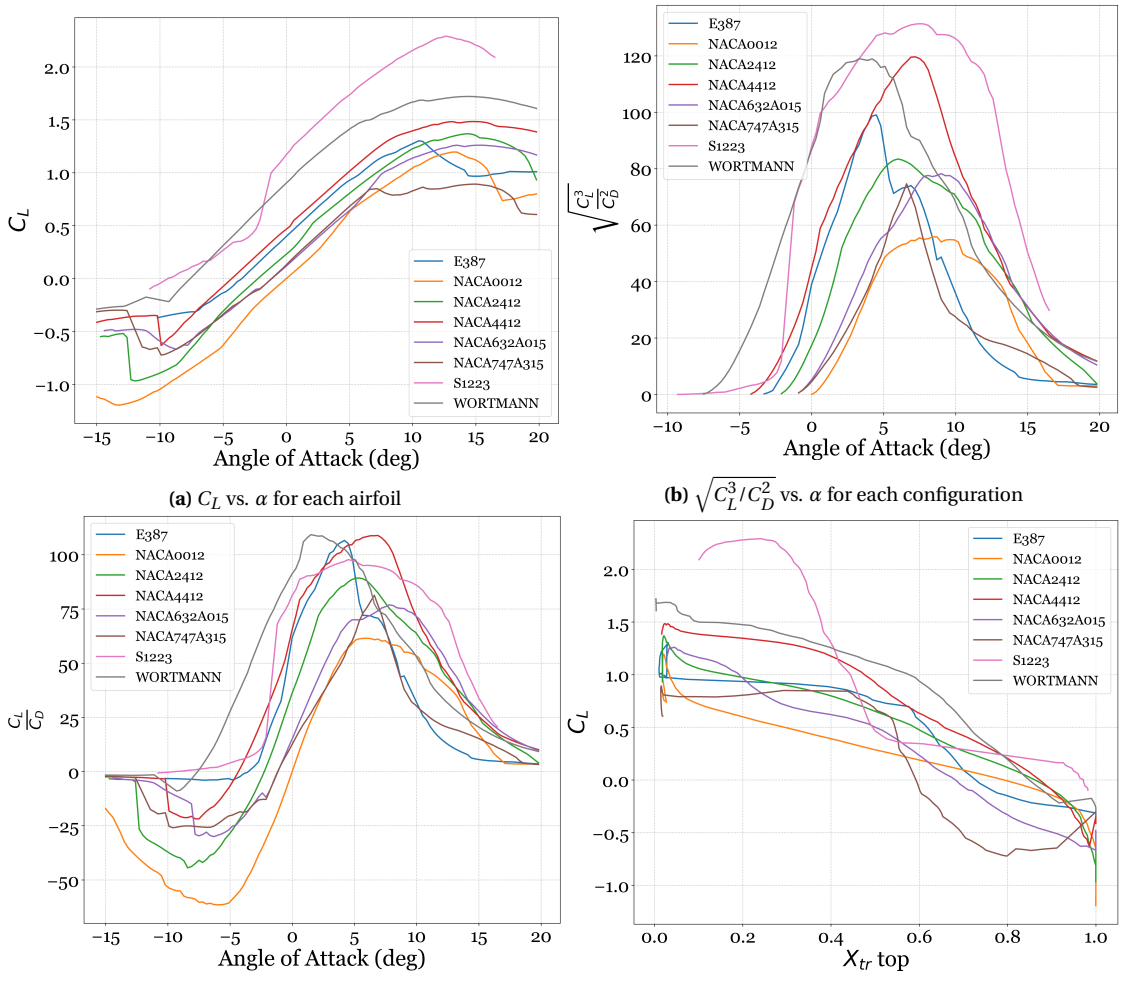

(a) C_L vs. α for each airfoil

(b) $\sqrt{C_L^3/C_D^2}$ vs. α for each configuration

(c) C_L/C_D - α for each configuration

(d) C_L - X_{tr} top for each configuration

Figure 9.1: Analysis graphs from XFLR5 for each airfoil.

From Figure 9.1, multiple observations can be made. Firstly, the analysis for angles of attack lower than -8 °cannot be considered valid, as clearly seen in Figure 9.1a and Figure 9.1c, where there are discontinuities in

the graphs of each airfoil. This phenomenon is an indication of numerical instability. Secondly, the graphs are used to choose the airfoil; from Figure 9.1b, it can be seen that the S1223 and WORTMANN FX 63-137 have the best performance for endurance. However, from Figure 9.1d, it can be seen that the performance of the S1223 decreases significantly when the transition point moves too far aft. Considering that this airfoil needs a high angle of attack for optimal performance (as seen in Figure 9.1b), the WORTMANN FX 63-137 has been chosen for further optimised design.

9.1.2. Airfoil Design & Optimisation Methodology

Before optimising the airfoil, the methodology used will be described. With the aid of this algorithm, both the airfoil and wing have been optimised. For the airfoil, this is done in XFLR5. For the wing, it is done with its successor, FLOW5.

Optimisation Procedure

The optimisation process used in XFLR5 and FLOW5 is the Multi-Objective Particle Swarm Optimisation (MOPSO). This is performed by using an initial design and using small increments to modify the geometry and increase performance. Indeed, this works most efficiently on already good-performing airfoils, and that is why it will be applied only on the chosen airfoil from Subsection 9.1.1.

The algorithm is initialised with a population (swarm) of possible solutions (particles). The particles then update their position and velocity based on the following: particle's inertia, knowledge of the particle's personal best, and knowledge of the global best. The algorithm ends when either one particle achieves all the objectives or the maximum number of iterations is reached [1]. For further details on the optimisation process, please refer to reference [45].

Airfoil Optimisation

With the algorithm described in the previous section, the airfoil has been optimised. Since XFLR5 does not allow for optimising directly for endurance $\left(\sqrt{C_L^3/C_D^2}\right)_{\max}$, it is chosen to optimise for range $(C_L/C_D)_{\max}$. The same conditions as in Subsection 9.1.1 apply. The newly designed airfoil will be called the WORTMANN FX 63-126 based on the 12.6% thickness. In Figure 9.2, the two airfoils are compared to each other. The chosen airfoil is then used to design the wing.

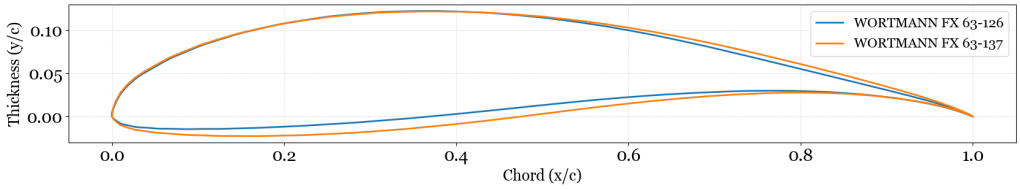

Figure 9.2: Comparison between WORTMANN FX 63-126 and WORTMANN FX 63-137

9.1.3. Airfoil Analysis Verification & Convergence

The last part of the airfoil design is verification of the design tool. While validation needs to be done with wind tunnel testing, the tool itself can be verified. This will be done by briefly discussing the method and its limitations, and testing panel convergence. As the airfoil does not exist commercially, the verification will be done based on the WORTMANN FX 63-137 with the difference in airfoil as seen in Figure 9.2.

Methods & Limitations of XFLR5

The method both XFLR5 and Flow5 use to analyse airfoils is directly connected to XFoil. XFoil is a widely used software for airfoil design. In this software, the vortex panel method is used [2]. The vortex panel method means that it applies a vortex at each panel and calculates the circulation for each of these panels. It then applies Kutta's condition, which says that the total flow is the freestream + vortex and leaves the trailing edge smoothly. Indeed, this method only works for inviscid flow. However, a 2D method for viscosity is also included in Xfoil. This is done with the Boundary Layer Equations and the Interactive Boundary Layer (IBL) loop [3]. More about these boundary layer equations can be found in [46]. The IBL loop is needed for the coupling between the potential (inviscid) flow and the viscous flow, such that the solution satisfies both models. While this loop is active in the 2D solver for airfoils, it is omitted in the 3D solver for wings. This will

[1] flow5 - MOPSO [Date Accessed: June 9] [2] XFLR 5 inviscid method [Date Accessed: June 9] [3] XFLR 5 viscous method [Date Accessed: June 9]

be further explored in Subsection 9.1.5.

While the airfoil analysis in Flow5 and XFLR5 are both widely used in the market, some limitations apply. Firstly, as was explained in Subsection 9.1.1, numerical errors occur at low angles of attack, making the software invalid to use in that regime. Secondly, as explained by Drela, the methods of Xfoil have been designed for low Reynolds numbers (10^4 to 10^6). This regime, however, fits within our design space. Another limitation is that the simulations only work for low speeds (M < 0.3), as it does not account for compressibility effects like shock waves. Lastly, as will be further discussed in Subsection 9.1.5, the wing-body interaction does not provide accurate results and is not recommended to be included in the analysis by the author [4]. For more information regarding the methods and limitations, please refer to reference [46].

Panel Convergence

Since both XFLR5 and Flow5 make use of the panel method, the convergence of the panels should be investigated. By applying the same conditions as described in Subsection 9.1.1, Figure 9.3 is created.

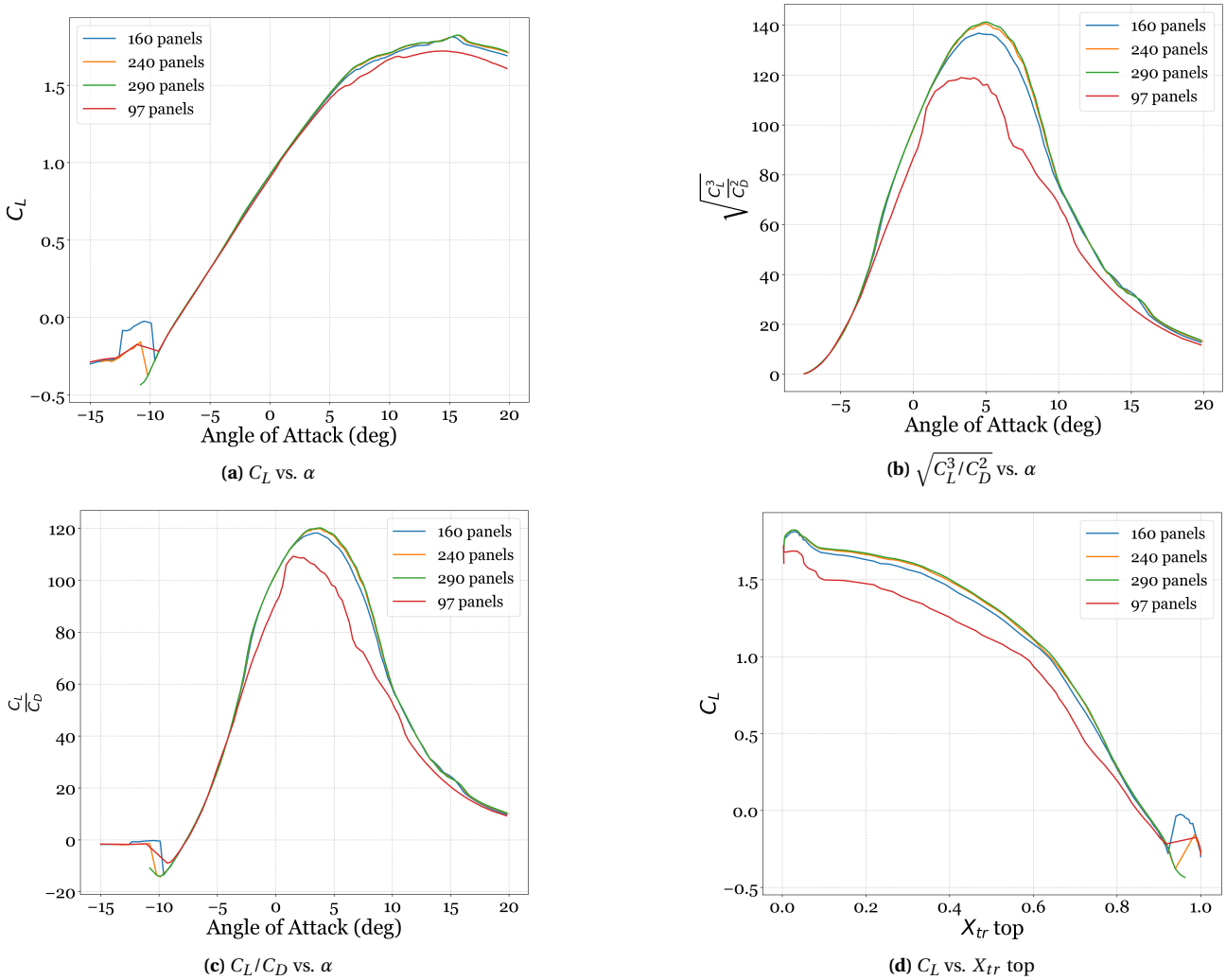

(a) C_L vs. α

(b) $\sqrt{C_L^3/C_D^2}$ vs. α

(c) C_L/C_D vs. α

(d) C_L vs. X_{tr} top

Figure 9.3: Panel graphs from XFLR5.

As can be seen in Figure 9.3, all plots converge as the number of panels increases, with the greatest change from 97 to 160 panels. These 97 panels were the original number of panels in Figure 9.1. From here, it is determined that using between 210 and 290 (max) panels is preferred for better accuracy of the results.

With these results for the airfoil design, the next step is designing the wing for endurance performance.

9.1.4. Wing Design Optimisation

With the airfoil design described in Subsection 9.1.2, the wing shall now be designed and analysed.

Optimisation Method

[4] Flow5 limitations [Date Accessed: June 9]

The optimisation method has the same procedure as described in Subsection 9.1.2 (MOPSO). However, instead of XFLR5, its successor, Flow5, is used. This is done for a more accurate result due to the different method Flow5 uses. Flow5 integrates Gmsh in its panel method. This means it uses a combination of triangles and quads in its mesh instead of quads. This increases results accuracy compared to XFLR5 [5]
Another aspect to consider is which parameters can vary. The wing designed in the preliminary design phase by Armeli et al. [1] only provides a rough estimate. However, an important constraint is placed on the wing based on the matching diagram described by them. This constraint is that the surface area must equal 1.09 m^2. Moreover, the hinge mechanism that will be discussed in Section 9.4 also provides constraints on the wing. These are the conditions under which the taper ratio equals 1, and the sweep angle equals 0. These design decisions are made to ensure that the wing can unfold at altitude and that the UAV remains stable during the vertical launch phase.

Lastly, the structural components place a constraint on the maximum aspect ratio. Since a full iterative loop between the aspect ratio and the structural integrity is not possible due to time complexity, it has been chosen to set this upper limit to an aspect ratio of 15. This means the parameters to be varied are the wing span, chord length, dihedral angle, and tip twist angle. From the optimisation method, the wing shall be optimised for endurance $\left(\sqrt{C_L^3/C_D^2}\right)_{\max}$. The wing parameters are obtained as seen in Table 9.1.

Table 9.1: Wing parameters after optimisation

Wing Component	Value	Wing Component	Value
Wing span	4.0 m	Aspect Ratio	14.679
Wing area	1.09 m^2	Taper Ratio	1.0
Chord length	0.273 m	Root-Tip Sweep	0 °
Tip twist	-2.261 °	Dihedral	3.06 °

From Table 9.1, it can be observed that the wing has a higher aspect ratio compared to the initial design, which had an aspect ratio of 10. Moreover, the inclusion of dihedral and tip twist improves the endurance performance. The performance of this wing design has been plotted in figs. 9.4 and 9.5. This includes the C_L vs. α, endurance, range, and drag polar. Moreover, the results of the glide performance during the glide phase have also been plotted in these plots. Note that for the C_L-α graph, they coincide.

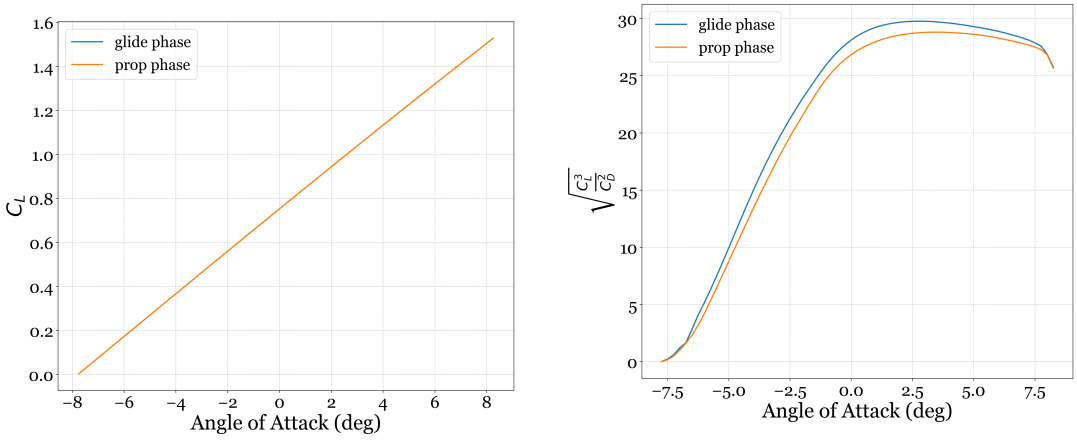

(a) C_L vs. α

(b) $\sqrt{C_L^3/C_D^2}$ vs. α

Figure 9.4: Analysis graphs from Flow5 for the wing.

[5] Flow5 3D analysis [Date Accessed: June 10]

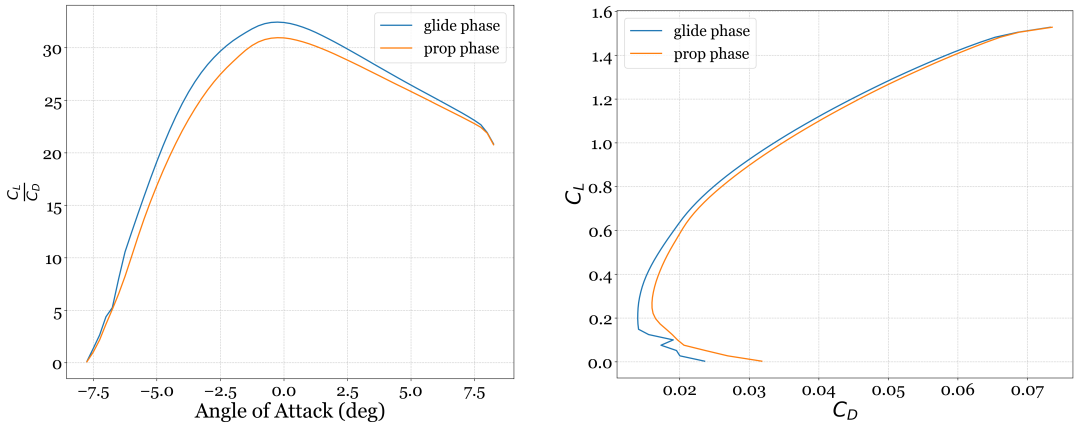

(a) C_L/C_D - α

(b) Drag Polar

Figure 9.5: Analysis graphs from Flow5 for the wing.

The graphs shown in figs. 9.4 and 9.5 show the performance of the wing only. It can be perceived that the optimal angle of attack for the glide phase lies around 3 °. This is optimised for endurance and corresponds to a lift coefficient of around 1.04 as seen in Figure 9.4a. The propeller phase has a different optimal performance since this is based on the minimum power required. This will be further explored in Chapter 12. Another aspect that can be observed in Figure 9.4a compared to Figure 9.1a is that the lift curve is linear and no longer shows the non-linear regime of stall. This is due to the limitation of the viscous flow that will be described in Subsection 9.1.5. It should be noted, however, that the maximum C_L as observed in Figure 9.4a shall be taken as the stall point in the rest of the design. These results are consistent with the expected behaviour of the wing.

9.1.5. Wing Optimisation Methods Verification & Sensitivity

Limitations of Flow5

While Flow5 is a widely used program, it also presents limitations. Firstly, the performance graphs as seen in Figure 9.4 and Figure 9.5 only apply to the wing. This does not include the contribution and effect of the fuselage to the airflow over the wing. While this is theoretically possible in Flow5 to include, it currently provides numerical errors and will not be included in the analysis due to the unreliability of the result.

Secondly, briefly mentioned in Subsection 9.1.3, the inclusion of viscous flow in the solver for wings is limited. It interpolates the 2D viscous flow to 3D instead of solving the boundary layer equations for 3D. While it makes the results more accurate than not including viscosity at all, it is not a perfect representation of the viscous flow. This could also be observed in Figure 9.4a as the solver is not able to produce points beyond stall. A more advanced CFD solver would be needed for that. However, that is not possible at the current stage due to time constraints.

A third aspect is the inclusion of the tail surfaces. While this is not relevant for the wing design, it does affect the results of tail sizing. Due to the vortex method used on the wing, it is crucial that the wake panels do not intersect with the tail itself, or numerical errors occur. It is for this reason that they have to be 'cheated' and placed slightly above or below the wing[6].

Panel Convergence

The last aspect of this section is testing the convergence of the panel method for the wing design. This has been tested for performance during the cruise phase. The results can be seen in Figure 9.6

[6] Flow 5 Modelling [Date Accessed: June 10]

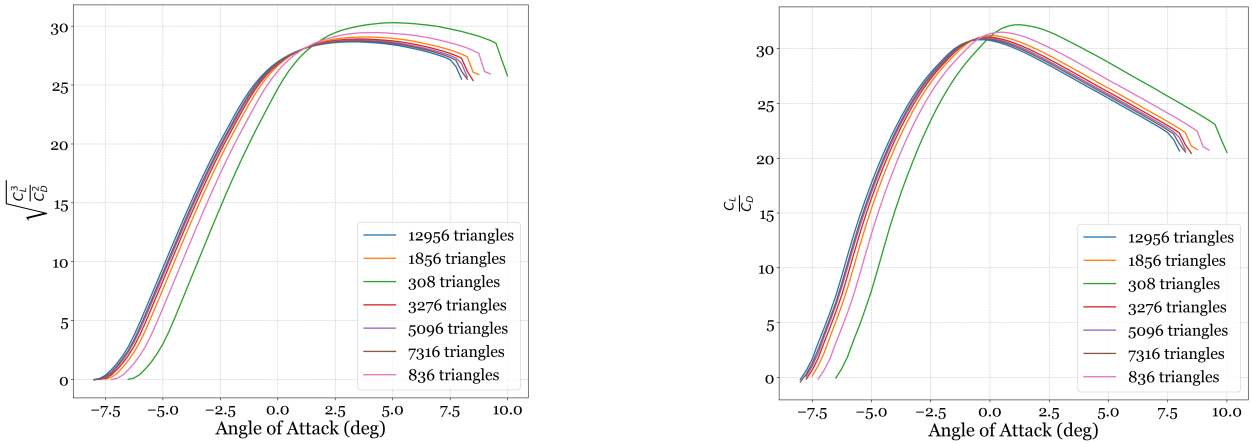

(a) $\sqrt{C_L^3/C_D^2}$ vs. α for various triangles.

(b) $\frac{C_L}{C_D}$ - α for various triangles.

Figure 9.6: Triangle graphs from Flow5.

The results, as seen in Figure 9.6, show the convergence as the number of triangles increases. The analysis done in Subsection 9.1.4 used 5096 triangles, and it can be seen that doubling that number does not add to the accuracy of the result.

9.2. Tail Sizing *Author(s): Duco, Paul*

As was already discussed in the midterm report, stability and control characteristics are crucial during take-off, cruise and approach. In the midterm report, a general tail shape was sized for cruise static stability and controllability but the (rocket) ascent phase was not analysed. In this phase of the design this ascent phase cannot be neglected. All these considerations will be discussed in this section, with a final output of tail shape and size that complies with ascent stability and cruise stability and controllability. First, ascent stability characteristics will be discussed. Then, cruise stability and controllability will be discussed. Afterwards, the fin planform is presented, the limiting mode is selected and the final fin shape is given. Finally, the directional stability of the configuration is analysed.

9.2.1. Rocket stability

During the ascent phase the wings are stowed and VAPOR flies vertically as a finned rocket. For this phase the vehicle must be statically stable, which requires the Centre of Pressure (C.P.) to lie aft of the Centre Of Gravity (cg) [47]. The restoring moment that returns the vehicle to its trimmed attitude is produced almost entirely by the fins, and sizing these surfaces for ascent sets an important bound on the tail area.

Because the wings are folded against the fuselage during ascent, the external geometry exposed to the airflow can be approximated as a nose cone, a cylindrical body, and fixed fins. The vehicle can therefore be treated as a clean, slender, finned body, for which the centre of pressure is estimated using the Barrowman method [47]. The method is based on seven assumptions: small angle of attack (near zero), subsonic flow, steady and smooth flow without rapid changes, a slender body with length much greater than diameter, a nose that tapers smoothly to a point, a rigid and axially symmetric vehicle, and thin flat-plate fins.

VAPOR satisfies these conditions to the fidelity required for preliminary sizing. The fuselage is shaped so that the folded wings are enclosed (the exact shape is treated in Section 9.6), preserving the axisymmetric slender-body geometry that assumptions (4) to (6) require. One simplification must be made explicit: the stowed wings do not fold perfectly flush with the fuselage, so the flow over the body is not strictly steady or attached. Assumption (3) is therefore *not* conservative for VAPOR. It is nonetheless retained, since the resulting error in C.P. location is small relative to the stability margin targeted, and a higher-fidelity unsteady treatment falls outside the scope of the preliminary design. However, for future research, CFD analysis or wind-tunnel tests should be performed to further validate these assumptions.

In the Barrowman method the centre of pressure of the complete vehicle is found by summing the normal force contribution of each component, weighted by its own centre of pressure. A body section of constant diameter has a normal-force-curve slope of zero, so a cylindrical fuselage produces no net normal force and does not shift the C.P. (body lift is neglected, consistent with the small-angle-of-attack assumption). In VA-

POR's simplified model the only contributing components are therefore the nose cone and the fins.

The nose cone contributes a normal-force-curve slope of $(C_{N_\alpha})_n = 2$, acting at $X_n = k_n L_n$, where k_n is a shape factor ($k_n = 0.466$ for an ogive, 0.666 for a cone) and L_n the nose length. A set of N fins contributes

$$(C_{N_\alpha})_f = \left(1 + \frac{R}{s+R}\right) \frac{4N\left(\frac{s}{d}\right)^2}{1+\sqrt{1+\left(\frac{2l_m}{c_r+c_t}\right)^2}} \tag{9.1}$$

where the leading bracket is the fin-body interference factor, R is the body radius at the root, s the fin semi-span, d the reference diameter, l_m the fin mid-chord length, and c_r, c_t the root and tip chords. For VAPOR, $d = R$. The fin centre of pressure is

$$X_f = X_{LE} + \frac{x_r\,(c_r + 2c_t)}{3(c_r+c_t)} + \frac{1}{6}\left(c_r + c_t - \frac{c_r c_t}{c_r+c_t}\right) \tag{9.2}$$

with X_{LE} the axial position of the fin root leading edge and x_r the fin sweep (root to tip leading edge). The global centre of pressure follows by combining the two contributions,

$$X_{CP} = \frac{(C_{N_\alpha})_n X_n + (C_{N_\alpha})_f X_f}{(C_{N_\alpha})_n + (C_{N_\alpha})_f} \tag{9.3}$$

$$\text{SM} = \frac{X_{CP} - X_{cg}}{d} \tag{9.4}$$

and the static stability is expressed as a static margin in calibres, where one calibre equals the body diameter d and all axial positions are measured from the nose tip. Static stability requires SM > 0; a margin of one to two calibres is conventionally targeted [47]. Figure 9.7 shows the resulting model with the cg, C.P. and static margin indicated. Equations Equation 9.1 to Equation 9.4 relate the fin geometry to the static margin, but the dependency can be inverted to size the surface area of the fins for a given static margin. To achieve this, a fin taper ratio, sweep and aspect ratio are defined. A single value of c_r can then directly be related to surface area for comparison with the surface area required in the next section. Below are the equations that relate the various planform parameters to each other.

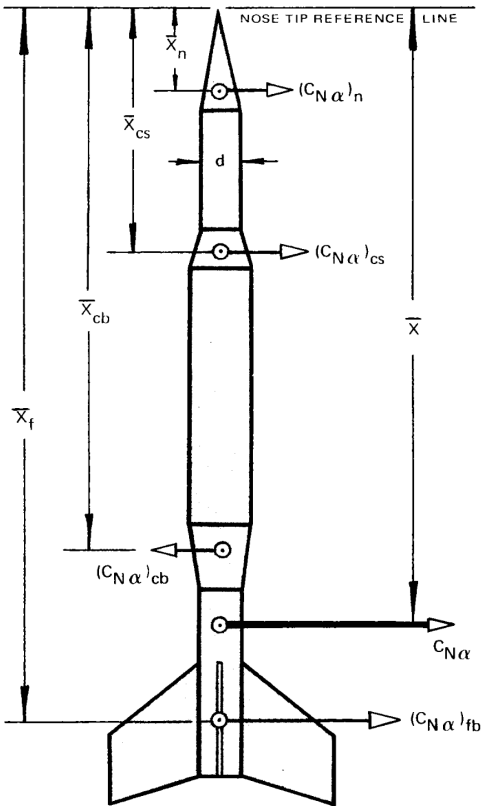

Figure 9.7: Aerodynamic normal forces acting on the different regions of a typical rocket. Figure by Barrowman [47]

Solving Equation 9.2 to Equation 9.9 for tip chord and surface area to calculate the static margin results in Figure 9.8 which displays in red the minimum static margin, defined to be exactly 1 calibre, and in blue the static margin for a given fin root chord and thus fin area. From this plot it can be seen that a fin surface area of at least 0.0843 m^2 is required for stability during ascent.

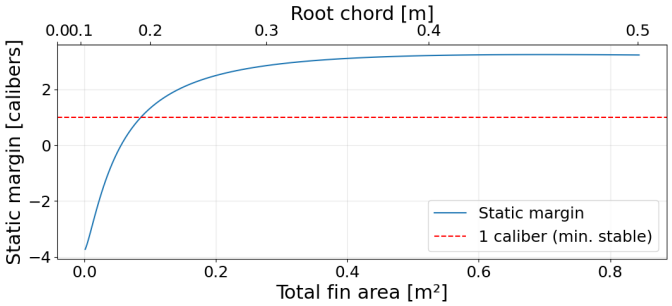

Figure 9.8: Static margin plotted as a function of single fin surface area and root chord of a fin for an aspect ratio of 2, taper ratio of 0.5 and sweep of 0.1 m

$$\lambda = \frac{c_t}{c_r} \tag{9.5}$$

$$\bar{c} = \frac{1}{2}(1+\lambda)\, c_r \tag{9.6}$$

$$b = A\,\bar{c} \tag{9.7}$$

$$S = \bar{c}\, b = \frac{b^2}{A} \tag{9.8}$$

$$A = \frac{b}{\bar{c}} = \frac{b^2}{S} \tag{9.9}$$

9.2.2. Cruise stability and controllability

In the midterm report, control and stability during cruise were evaluated through a scissor plot. This approach provides many advantages due to its simplicity and reliability; however, it must be adjusted for the Y-tail configuration VAPOR will adopt. This is done through the simplified vee-tail theory of Purser and Campbell [48], in which the contribution of *two* symmetric panels is composed into equivalent horizontal and vertical tails via a $\cos^2\Gamma$ projection. Although this theory is applied to the vee-tail, it still applies to lateral static stability and controllability of the Y-tail as the vertical part of the tail plays no role in the horizontal plane.

Once more, the method described below closely follows that of the midterm, with a single adjustment: the two tail panels set at a dihedral angle Γ no longer deliver their full lift to the longitudinal plane. Following Purser and Campbell, their effectiveness in pitch is scaled by $\cos^2\Gamma$, applied here to the tail lift-curve slope $C_{L_{\alpha_h}}$ and the deflected-tail lift coefficient C_{L_h}. One factor of $\cos\Gamma$ accounts for the projection of the panel area onto the horizontal plane, and a second for the projection of the panel lift onto the vertical, pitch-generating direction. The third, purely vertical panel of the Y-tail produces no force in the pitching plane and is therefore neglected in this longitudinal analysis; only the two dihedral panels are sized here. Apart from this projection, the theory is identical to that of the midterm and follows the methodology of [49–51] and [52].

The leading equations in the scissor plot are the controllability and stability lines. These are defined by Equation 9.10 and Equation 9.11.

$$\frac{S_h}{S} = \frac{\bar{x}_{cg} - \bar{x}_{ac_{A-h}} + \mathrm{SM}}{\dfrac{C_{L_{\alpha_h}}}{C_{L_{\alpha_{A-h}}}}\left(1 - \dfrac{\mathrm{d}\varepsilon}{\mathrm{d}\alpha}\right)\dfrac{l_h}{\bar{c}}\left(\dfrac{V_h}{V}\right)^2} \tag{9.10}$$

$$\frac{S_h}{S} = \frac{\bar{x}_{cg} + \dfrac{C_{m_{ac}}}{C_{L_{A-h}}} - \bar{x}_{ac_{A-h}}}{\dfrac{C_{L_h}}{C_{L_{A-h}}}\dfrac{l_h}{\bar{c}}\left(\dfrac{V_h}{V}\right)^2} \tag{9.11}$$

Assumptions have to be made about some of the variables in the above equations, before being able to generate the scissor plot. These assumptions concern the following parameters: downwash gradient, local reduction of dynamic pressure at the tail, lift coefficient of the tail, lift slope of the tail and of the aircraft-less-tail, the moment coefficient about the aerodynamic centre of the aircraft, the aerodynamic centre of the aircraft-less-tail, and the stability margin. It is also assumed that no high-lift devices are present, such that the aerodynamic centre of the aircraft is the same during cruise and approach. The scissor plot is now generated, resulting in Figure 9.9. Because only the two dihedral panels enter the longitudinal analysis, the surface area returned by Equation 9.10 and Equation 9.11 is that of these two panels alone. The total tail area follows by multiplying this result by a factor of 1.5: the rocket stability requirement constrains all three fins to be identical in planform, so completing the Y-tail with the third, identical panel is equivalent to scaling the two-panel area by 3/2.

From this figure, at the VAPOR centre of gravity point, which is precisely defined in Chapter 10, a minimum vee-tail to main wing surface area ratio of 0.176 is found. This relates to a minimum required total surface area (for all three fins combined) of 0.29 m^2, limited by stability with a static margin of 0.05.

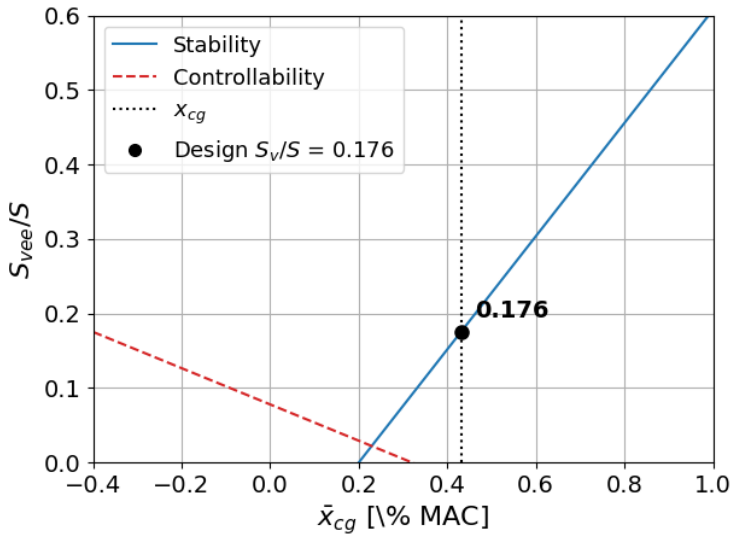

Figure 9.9: Scissor plot with the controllability and stability lines. The limiting mode is stability.

9.2.3. Tail planform iteration and optimisation

Finally, the resulting tail planform can be defined. Ascent stability requires a total tail area of 0.2529 m^2 (three fins of 0.0843 m^2 each), whereas cruise stability requires a total tail area of 0.2878 m^2. These two requirements lie close together, with cruise remaining the limiting mode by only a small margin, such that the tail is sized accordingly. As previously mentioned, the three fins are sized identically and do not differ in surface area. A summary of the exact fin planform is given below, including a schematic.

Parameter	Value
Root chord c_r [m]	0.292
Tip chord c_t [m]	0.146
Taper $\lambda = c_t/c_r$	0.50
Aspect ratio A (per fin)	2.0
LE sweep [m]	0.292
Span/fin b [m]	0.438
Area/fin S_1 [m^2]	0.0959
No. of fins n	3
Total area S_h [m^2]	0.288
S_h/S_w	0.264

Table 9.2: VAPOR fin geometry after the limiting values are found from the scissor plot.

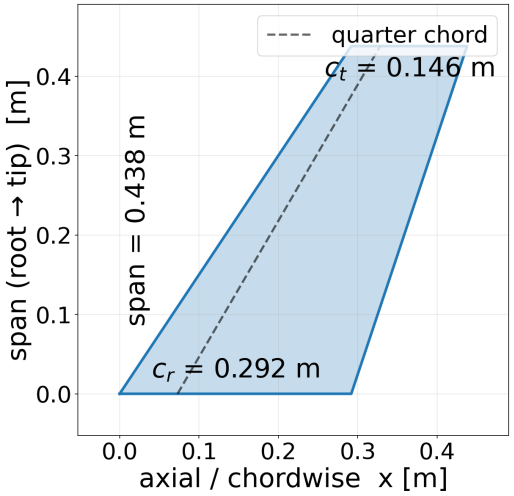

Figure 9.10: Planform of the VAPOR fin (c_r = 0.292 m, c_t = 0.146 m, span 0.438 m, sweep 0.292 m offset, A = 2, λ = 0.5).

The fin dimensions depend strongly on the centre of gravity location, which enters the equations for ascent and cruise stability. Varying this location showed that the required tail area grows rapidly once the centre of gravity lies more than about 15 cm aft of the main wing aerodynamic centre, a consequence of the wing aerodynamic centre sitting relatively far forward compared to, for instance, conventional airliners where it falls roughly mid-fuselage. The fin sizing is therefore a sensitive aspect of the design since the centre of gravity is fixed within a narrow range by the overall configuration, however, this sensitivity is acknowledged here rather than explored through a dedicated study.

9.2.4. Directional Stability Analysis

All fins of the Y-tail are sized equally to have a symmetric cross-section for rocket-powered ascent, however, an analysis must be done to determine whether this configuration has enough directional stability.

Empirical formulas described by TU Delft's ADSEE course[53]. were taken to estimate the directional stability contributions of the wing, fuselage and propeller. The empirical formulas can be seen in the following:

$$C_{n_{\beta_f}} = -k_\beta \frac{S_{fs} l_f}{Sb} \left(\frac{h_{f_1}}{h_{f_2}}\right)^{\frac{1}{2}} \left(\frac{b_{f_2}}{b_{f_1}}\right)^{\frac{1}{3}} \tag{9.12}$$

$$k_\beta = 0.3\frac{l_{cg}}{l_f} + 0.75\frac{h_{f_{max}}}{l_f} - 0.105 \tag{9.13}$$

$$C_{n_{\beta_p}} = -0.053 B_p \sum \frac{l_p D_p^2}{Sb} \tag{9.14}$$

$$C_{n_{\beta_i}} = \begin{cases} -0.017, & \text{high wing} \\ +0.012, & \text{mid wing} \\ +0.024, & \text{low wing} \end{cases} \tag{9.15}$$

By applying these empirical formulas and imposing a minimum acceptable C_{n_β} at (+) 0.001 per radian, the minimum necessary vertical tail area can be calculated as presented in Table 9.3 and Table 9.4. The figure clearly shows that for directional stability, the vertical fin is not needed during horizontal cruise. The vertical fin also has an effect on roll and spiral stability; however, the main wing has the largest contribution to this stability parameter, meaning the vertical fin sizing is deemed sufficient.

Table 9.3: $C_{n\beta}$ destabilizing contributions.

Contribution	C_{n_β} [rad^{-1}]
Fuselage	−0.0712
Propeller	−0.0020
Wing interference	+0.0110
Total destabilising	−0.0622

Table 9.4: Vertical tail sizing results.

Quantity	Area [cm^2]
Required vertical tail area, S_v	562.9
Area from panels only	480.0
Minimum top fin area required	82.9
Final fin area used	960.0

9.3. Wing Structural Analysis *Author(s): Ivan*

Having determined the geometry and airfoil of the wing planform, as shown in Subsection 9.1.4, its internal structural layout must be sized. The wing structure is responsible for carrying and distributing the loads generated during the cruise, manoeuvring, landing, and launch phases. Therefore, the structure must provide sufficient strength to withstand the critical loading conditions considered throughout the mission. For this reason, the structural design is critical to the success of the project and mission.

The wing box is the primary structural component of a wing and is formed by the integration of spars, ribs, and skin. The spars are placed along the span. These act as beams and are the primary backbone of the structure, carrying the shear and bending loads. The ribs ensure the aerodynamic profile of the wing is maintained along the span. Finally, the skin completes the wing surface, primarily carrying torsional loads.

The design of the wing structure involves the definition, sizing, and material selection of its primary structural members. Given the complexity of this process, due to the strong interaction between the components, a well-structured methodology has been set and followed during the design. First, the number of spars is determined, derived from the needed bending bearing capacity that the wing must withstand. Then, its position along the chord is determined along with the geometrical shape of the spar cross section. The number of ribs placed along the span is then derived from the column buckling limitation of the spars. Finally, the skin thickness is derived from torsional and manufacturing limitations.

9.3.1. Internal and Reaction Forces

The internal normal, shear and bending forces during the critical phases of the mission have to be acquired for sizing of the structure. From these forces, web-boom analysis and panel methods can be used to find the internal stresses and shear flows, a comparative evaluation of the methods will be carried out in the following sections.

Regarding the loading of the wing, the aircraft will be subject to two different critical loading conditions, flight and launch. During flight, the aircraft must withstand the load factors associated with manoeuvring and gusting. Positive load factors are associated with pull-up maneuvers, and negative factors are associated with diving maneuvers. From the requirements, the aircraft shall be sized for a positive maximum load factor of n = 1.75, given it is the most critical flight case. On the other hand, during launch, the wing will be in its folded configuration and will therefore experience only axial loads.

During flight, the lifting force is distributed along the span, acting in the upward direction, while the wing's distributed weight acts downward and the drag forces acting longitudinally. From Flow5, the aerodynamic forces of the wing were acquired. These forces are taken at the maximum lifting capacity of the wing, and by consequence at the maximum positive loading factor. The program outputs the force components along the three principal axes, the vertical force acting in the positive z axis F_z, the lateral force F_y, and the longitudinal force F_x, together with the pitching moment T_y. These quantities are presented as a function of the span in Figure 9.11.

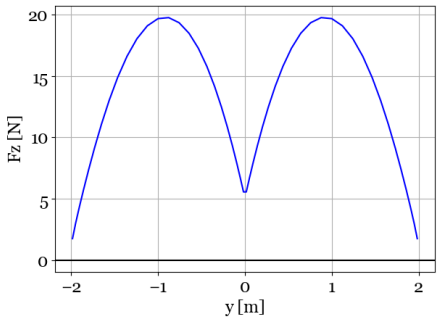

(a) Distributed Force in the z axis as a function of the wing span

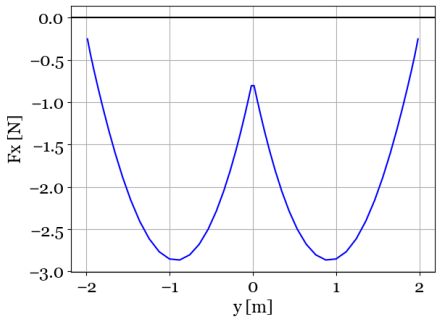

(b) Distributed Force in the x axis as a function of the wing span

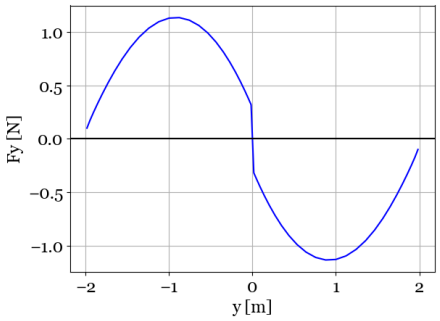

(c) Distributed Force in the y axis as a function of the wing span

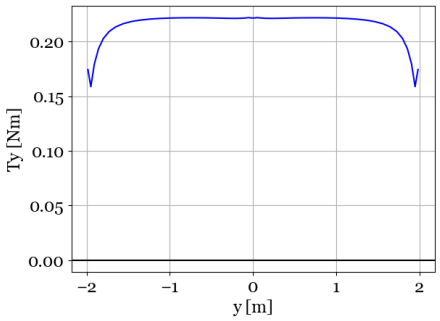

(d) Distributed twisting moment in the y direction as a function of the wing span

Figure 9.11: Aerodynamic forces acting on the wing plotted as a function of the span

Having determined the forces that act on the beam at a given flight condition, the reaction forces and moments at the root of the wing can be acquired. These reaction forces represent the loads that are transferred onto the fuselage from the wing. These forces and moments in the body-fixed cartesian coordinates x, y, and z direction can be acquired by stating the equilibrium of forces and setting their acceleration equal to zero such that the reaction forces V_{r_z}, V_{r_x} , N_{r_y} and reaction moments M_{r_x}, M_{r_z} and T_{r_y} can be found.

Table 9.5: Reaction Forces and Moments for Load factor of n = 1.75

Moments [Nm]		Forces [N]	
M_{r_x}	-233.6	V_{r_z}	258.1
M_{r_z}	40.1	V_{r_x}	-43.6
T_{r_y}	-5.3	N_{r_y}	0

The internal forces and moments along the span of the wing can be found following a similar analysis as for the reaction forces. However, this is done by placing an imaginary cut at a given spanwise location, isolating one side, and enforcing force and moment equilibrium such that the internal shear, normal, and moment forces are determined. These distributions along the span are displayed in Subsection 9.3.1

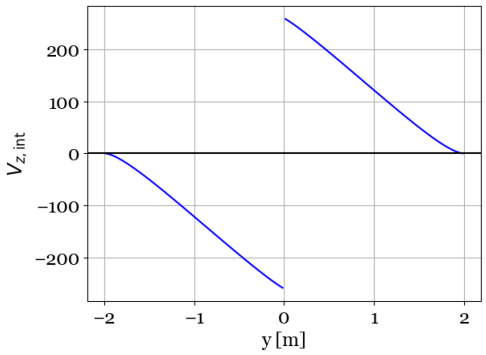

(a) Internal shear force in the z-direction as a function of the span

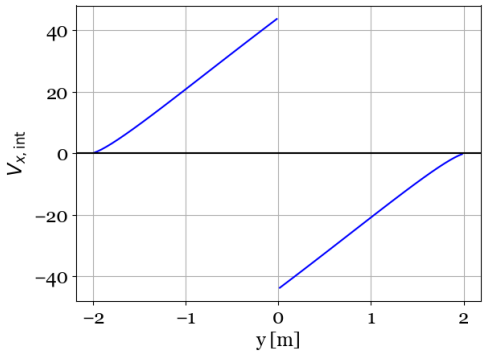

(b) Internal shear force in the x-direction as a function of the span

Figure 9.12: Internal shear-force diagrams

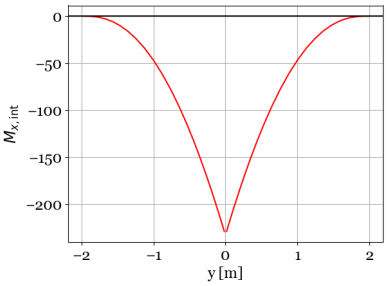

(a) Internal moment about the x-axis as a function of the span

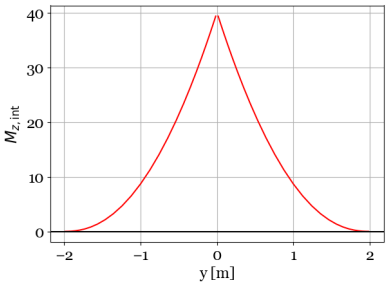

(b) Internal moment about the z-axis as a function of the span

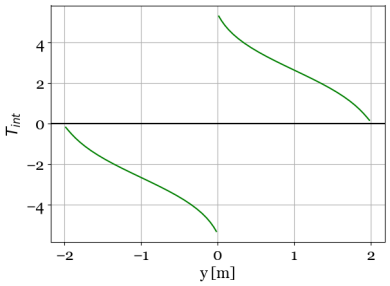

(c) Internal twisting torque about the y-axis as a function of the span

Figure 9.13: Internal bending-moment and twisting-torque diagrams

Regarding the forces during the ascent of the rocket, a maximum longitudinal acceleration of a = 0.8g was derived. As mentioned previously, during this phase of the mission the wings are folded towards the fuselage and hence only experience normal force in the axis of the span due to the launch acceleration. The same analysis as for the horizontal flight case can be performed to acquire the normal internal load. The distribution of internal normal forces is displayed in Figure 9.14 for half the span.

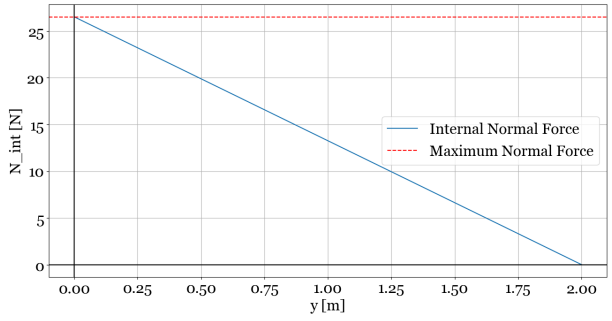

Figure 9.14: Internal normal force during launch as a function of span.

Table 9.6: Load results for flying, launch, and landing conditions.

Load	Flying ($n = 1.75$)	Launch	Landing
V_z [N]	258.1	–	–
V_x [N]	-43.6	–	146.0
M_x [Nm]	-229.5	–	–
M_z [Nm]	39.4	–	-144.8
T [Nm]	5.3	–	–
N [N]	0	26.5	–

A similar analysis was performed for the landing case, in which the UAV decelerates and inertial loads act on the wing. A summary of the maximum internal forces and moments for the launch, landing, and flying cases is presented in Figure 9.6.

9.3.2. Stress & Shear Flow Analysis Methods

Two methods are available for the analysis of the cross-sectional load, the skin panel and the web-boom methods. Both methods rely on idealizing the cross-section into booms that carry bending and normal

stresses and webs that carry shear stresses. The skin panel methods retain the actual skin panels and their structural behavior, providing a more accurate representation of the stress distribution and buckling behavior. This method has higher accuracy and incorporates panel buckling into its analysis; however, it is more complex to implement and requires greater computational effort. On the other hand, web-boom analysis provides a simpler and faster method at the cost of lower accuracy than the skin panel method. However, given the preliminary stage of the wing structure design process, web-boom is found as a more suitable method as it allows to adequately understand the global load paths, it is computationally inexpensive and allows for rapid sizing and iteration while still providing accurate results.

Web-boom analysis relies on the idealization of the cross-sectional shape into booms and webs. Boom areas carry the normal and bending stresses, while the webs carry the shear and torsional loads. The spar flange geometries are idealized as circular boom areas, they are placed at the same position as the spar and have the same area. Figure 9.15 displays the idealization of the cross section.

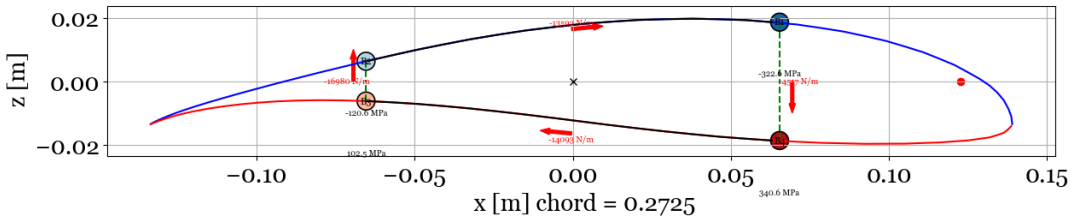

Figure 9.15: Wing Cross Section Idealization

Once the boom position and areas have been determined, the section centroid and second moment of inertia can be calculated. The section's centroid can be calculated using:

$$\bar{x} = \frac{\sum A_i x_i}{\sum A_i} \quad (1) \qquad \bar{z} = \frac{\sum A_i z_i}{\sum A_i} \quad (2) \qquad (9.16)$$

Where the x-coordinate of the centroid $\bar{x}$ with respect to the airfoil leading edge is calculated by summing the product of all individual boom areas A_i with their x-coordinate x_i by the sum of all boom areas. The same follows for the z-coordinates of the centroid $\bar{z}$. Having found the centroid, the coordinates of the airfoil profile and booms can be transformed such that they are relative to the cross sectional centroid using Equation 9.17 and Equation 9.18.

$$x' = x - \bar{x} \qquad (9.17) \qquad z' = z - \bar{z} \qquad (9.18)$$

The second moment of inertia terms in the x-direction, z-direction, and xy-direction I_{xx}, I_{zz} and I_{xz} can be calculated using Equation 9.19, Equation 9.20 and Equation 9.21.

$$I_{zz} = \sum A_i \cdot (x_i')^2 \qquad (9.19) \qquad I_{xx} = \sum A_i \cdot (z_i')^2 \qquad (9.20) \qquad I_{xz} = \sum A_i \cdot (z_i')(x_i') \qquad (9.21)$$

Where as mentioned previously, A_i refers to the ith boom area, x_i' and z_i' refer to the x and z coordinates of the ith boom area with respect to the centroid.

Once the section properties for the idealized section have been calculated and the internal shear, normal and bending forces and moments are known, the stresses acting on the boom and shear flows in the skin can be acquired. Regarding the stresses acting on the boom due to bending, these can be calculated using Equation 9.22.

$$\sigma_y = \frac{(M_x I_{zz} - M_z I_{xz}) \cdot z}{I_{zz} I_{xx} - I_{xz}^2} + \frac{(M_z I_{xx} - M_x I_{xz}) \cdot x}{I_{zz} I_{xx} - I_{xz}^2} \qquad (9.22)$$

The quantity σ_y denotes the bending stress in the boom section. By sign convention, positive values correspond to tensile stress induced by bending, whereas negative values correspond to compressive stress.
The analysis in order to determine shear flows along the wing box is more complex. For this analysis, it is also important to determine the number of cells in the wing box. This number is determined by the number of spars placed with the wing. For a wing box composed of two spars, as shown in Figure 9.15, the wing box

is composed of 1 cell. For simplicity of the analysis, the outer cells are ignored.

Given that the internal shear forces in the z and x direction V_z and V_x do not act in the cross-section shear center, they will induce pure shear forces plus additional torsional forces. The shear flow along the cell will be composed of a base shear flow q_{s0} plus a variable shear flow q_b. In order to acquire these, an imaginary cut is made at a given section of the cell, setting the variable shear flow at that component equal to zero. Then the variable shear flows around the cell are calculated using Equation 9.24. The variation of shear flows is only dependent of boom area and position, hence shear flow will be constant along a shear web.

$$\Delta q_i = -\left(\frac{V_z I_{zz} - V_x I_{xz}}{I_{xx} I_{zz} - I_{xz}^2}\right) A_i z_i' - \left(\frac{V_x I_{xx} - V_z I_{xz}}{I_{xx} I_{zz} - I_{xz}^2}\right) A_i x_i' \tag{9.23}$$

Where Δq_i represents the change in variable shear flow due to the ith boom. Hence, the variable shear flow for each web can be acquired by cumulatively summing the change in shear flow as described in Equation 9.24

$$q_{b_i} = \sum_{n=0}^{i} \Delta q_n \tag{9.24}$$

Where q_{b_i} is the variable shear flow for the ith web. The base shear flow, which is constant along the entire cell, can be calculated by performing moment equivalence. For a chosen point with coordinates (η, ϵ), the moment generated by the constant and variable shear flows should be equal to the moment generated by the internal shear forces, as stated by Equation 9.25.

$$V_x \epsilon - V_z \eta = \sum M_i + q_{s_0} 2A \tag{9.25}$$

$$M_i = q_{b_i} l_{z_i} (x_i' - \eta) - q_{b_i} l_{x_i} (z_i' - \epsilon) \tag{9.26}$$

Where M_i is the moment contribution due to the variable shear through web i, l_{z_i} and l_{x_i} are the vertical and horizontal length of the ith web. Finally, the shear flow distribution around the cell can be found by adding the base shear flow with the variable shear flow for each web, as stated by Equation 9.27.

$$q_i = q_{s_0} + q_{b_i} \tag{9.27}$$

$$t_{i_{\min}} = \frac{q_i}{\tau} \tag{9.28}$$

From the calculated shear flows, the minimum required thickness for the web can be derived using Equation 9.28, where τ is the material shear yield strength.

9.3.3. Buckling Analysis Methods

While the strength analysis performed in the abovementioned section is a fundamental step in verifying the structural integrity of the design, compliance with the strength requirements does not alone guarantee a non-failing structure. Buckling of elements subject to compressive loads must be carefully analyzed as these can fail at loads well below the strength limit. For the structural analysis of the wing, Euler column buckling of the spars was evaluated, with the critical buckling load governed by Equation 9.29.

$$P_{cr} = \frac{\pi^2 EI}{(KL_{eff})^2} \tag{9.29}$$

Where the P_{cr} is the critical compressive load, E is the material's Young's modulus, I is the area moment of inertia, L_{eff} is the effective length, and K is a coefficient that depends on the end supports. For the wing analysis, K is set equal to 1. In this case, the effective length L_{eff} refers to the length between ribs. From Equation 9.29, the critical buckling load can be increased by decreasing the rib spacing, increasing the area moment of inertia of the spar, and choosing a material with a higher Young's modulus.

9.3.4. Wing Structural Element Sizing

Having established the internal loads acting on the wing and the analytical methods used to determine the stresses, shear flows, and buckling behaviour of the structure, the sizing of the individual structural elements can now be performed. For sizing purposes, the calculated internal loads are multiplied by the prescribed factor of safety of 1.5 to obtain the corresponding design loads.As briefly introduced in the previous sections, the wing structure design follows a sequential methodology in which the primary load-carrying members are defined and sized according to the critical strength and stability requirements. Due to the strong interaction between the different structural components, the sizing process must be carried out in a systematic manner such that the design of each element provides the necessary input for the subsequent

steps. Therefore, the sizing procedure begins with the determination of the required number and placement of spars, as these define the wing box configuration and govern the primary load paths within the structure. Once the wing box layout has been established, the spar geometry is sized based on the bending loads acting on the wing. Subsequently, the rib spacing is determined from the column buckling limitations of the spars, after which the skin thickness is sized.

The wing structure is designed using aluminium rather than a thermoplastic carbon-fibre composite. Although aluminium has a higher density and may therefore result in a greater structural mass, it offers important advantages from a sustainability and end-of-life perspective. As a metallic material, aluminium can be efficiently recovered, remelted, and recycled through well-established industrial processes, while retaining much of its material value and mechanical performance. In comparison, the recycling of carbon-fibre composites remains more complex and typically involves greater limitations in material recovery and reuse. The mechanical properties of both Aerospace Aluminium (7075-T6) and thermoplastic composite Carbon-Fibre-Reinforced PEEK (CF/PEEK) are summarized in Table 9.7 and Table 9.8

Table 9.7: Key Mechanical Properties of Aerospace Aluminum (7075-T6)

Property	Value	Unit
Density	2.8	g/cm^3
Elastic Modulus	70	GPa
Shear Modulus	26	GPa
Tensile Strength	400	MPa
Shear Strength	330	MPa
Fatigue Strength	160	MPa

Table 9.8: Key Mechanical Properties of CF/PEEK

Property	Value	Unit
Density	1.4	g/cm^3
Elastic Modulus (Young's)	28	GPa
Tensile Strength (Proof)	265	MPa

Spar Configuration Analysis

The first step in the wing structural sizing process is the determination of the number of spars and their position along the chord. The number of spars directly determines the number of cells within the wing box and therefore influences the structural behaviour of the wing. Given the relatively low mass of the aircraft, with a maximum take-off mass of 35 kg, together with the limited design load factor requirements presented previously, a wing box composed of two spars is found to provide sufficient strength and stiffness to withstand the expected loading conditions. Therefore, a two-spar configuration is selected, resulting in a single-cell wing box.

Having determined the number of spars, their position along the chord must be established. In general, it is beneficial to maximize the distance between the front and rear spars, as this increases their separation and enclosed area of the wing box, improving its bending in the z-direction and torsional load-carrying capability. However, practical and geometrical constraints limit the possible location of the rear spar. Firstly, sufficient space must be left between the rear spar and the trailing edge to accommodate the ailerons and their associated mechanisms. Secondly, as the airfoil profile converges towards the trailing edge, the available spar height decreases significantly. Since the bending stiffness in the x-direction and area moment of inertia of the spar are strongly dependent on its height, placing the spar excessively close to the trailing edge would reduce its structural efficiency. For these reasons, the rear spar is fixed at 0.75 of the local chord.

Once the position of the rear spar has been established, the location of the front spar can be determined. Similar to the rear spar, it is desirable to maximize the separation between both spars, as this reduces the bending stresses generated by moments in the z-direction M_z and increases torsional stiffness. However, moving the front spar towards the leading edge also results in a reduction of the available spar height due to the airfoil geometry. Therefore, a trade-off exists between increasing the spar separation and maintaining a sufficiently large spar height to efficiently carry the bending loads.

To determine the most suitable location, a parametric study was performed in which the position of the front spar was varied between 0.10 and 0.35 of the chord. For each configuration, the cross-sectional stresses induced by the critical bending loads were calculated using the methodology described in the previous section. The maximum stress within the cross-section was then evaluated as a function of the front spar position and is presented in Figure 9.16. From these, it can be concluded that for a given boom area, the

optimal position of the front spar is 0.27 of the chord. Moreover, the variation of the area does not directly impact the spar placement, but does decrease the magnitude of tensile and compressive stresses as the area is increased. This hints that it is beneficial to increase the area of the booms; however, this comes at the price of higher boom weight.

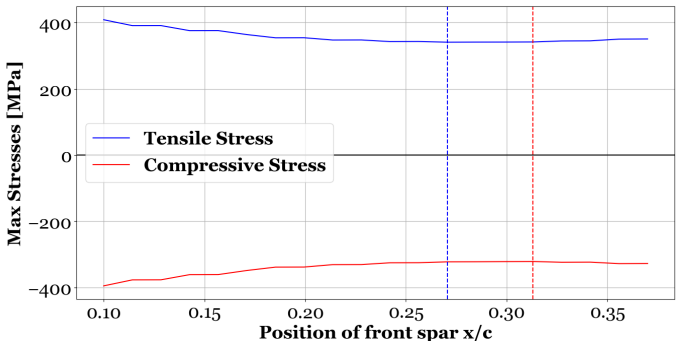

Figure 9.16: Variation of maximum tensile and compressive stress in the cross section plotted as a function of the front spar position

Boom Area and Rib Spacing Determination

In order to determine the boom areas, column buckling analysis of spars is performed. As stated previously in Subsection 9.3.3, column buckling depends on the section area moment of inertia I and rib spacing L_{eff}. Both of these parameters being interdependent.

The first step in the sizing for withstanding buckling is determining the maximum compressive force the spar beam is subject to. The maximum compressive force is calculated from the point in the wing subject to maximum compressive stress and boom area, as stated in Equation 9.31.

$$P = \sigma_{max} \cdot A \tag{9.31}$$

$$A = \frac{P(K \cdot L_{eff})^2}{2\pi^2 E z^2} \tag{9.32}$$ (9.32)

Where σ_{max} is the maximum stress experienced along the entire wing, and A is the boom area. To determine weather the rib spacing should be decreased or the boom area should be increased in order to satisfy the buckling constraint the following method was followed. Firstly, an assumed rib spacing L_{eff} was taken, from this the minimum amount of boom area was calculated by rearranging Equation 9.29 into Subsection 9.3.2 and setting P_{cr} as our maximum compressive force P. However, as the number of ribs is increased, the minimum area needed in order to satisfy buckling decreases up to the point where the stresses experienced in that boom surpass the material yield strength. For this reason, there is a limit on how much the boom areas can be decreased. Then for the given configuration of the wing analysed, for that given rib spacing, the mass off the spar and rib elements was calculated. This analysis was performed for rib spacing L_{eff} in between 0.222 m up to 2 meters, corresponding to a number of rib elements from 10 down to 1. The results of this analysis is displayed by Figure 9.17.

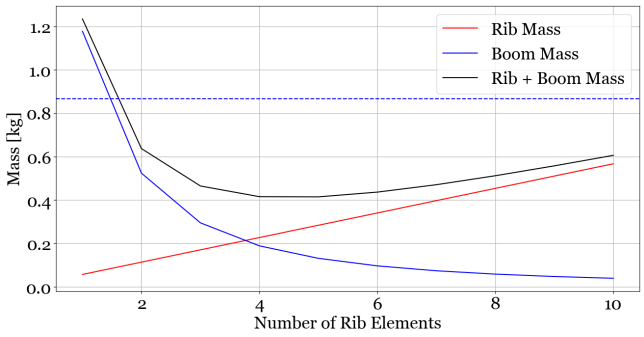

Figure 9.17: Variation of Rib and Boom mass as a function of number of ribs

As it can be seen by Figure 9.17, the mass of the booms decreases exponentially as the number of ribs is increased, while the rib mass increases linearly. These results hint that it is beneficial to satisfy the buckling constraint by increasing the number of ribs rather than by increasing the area. The blue horizontal dashed line represents the minimum weight of the boom, derived from the minimum area in order to satisfy yielding conditions. For this reason, the boom area was set to its minimum value of $2.02 \cdot 10^{-5}$ m^2 with a minimum amount of ribs equal to 1.

Although a single rib was found to be sufficient to satisfy the buckling constraint, as mentioned at the beginning of this section, ribs also serve important structural and aerodynamic functions within the wing. For this reason, a configuration with only one rib would not provide sufficient support for the skin or ensure the preservation of the desired aerodynamic shape. Therefore, a total of 7 ribs were selected for the final structure, as they provide adequate support along the wing while maintaining a relatively low structural mass.

Spar Cross Sectional Geometry Determination

Having determined the cross-sectional area of each boom, the spar geometry has to be set. The spar type was set as an I-beam, for which the boom areas are set as the flange area. This way, it is ensured that the calculated area moment of inertia of the actual spar geometry exceeds that of the idealization, hence, providing better structural efficiency. However, this comes at the cost of additional mass, as extra material area has to be set for the web connecting the flanges.

In order to calculate the lengths of the flanges, a python code was written which took the boom area, spar height and flange thickness and outputs the entire geometry of the spars. The web and flange thickness was set to 1.2mm for which the program output the geometries displayed in Figure 9.18a and Figure 9.18b.

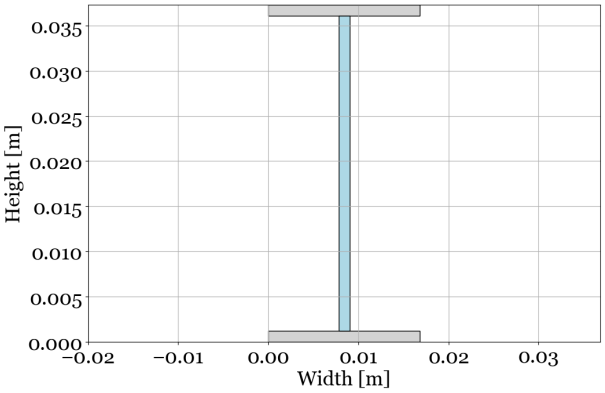

(a) Front Spar Cross Sectional Geometry

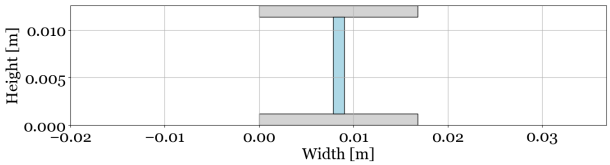

(b) Aft Spar Cross Sectional Geometry

Skin Thickness Determination

Having determined the spar cross-sectional geometry, the minimum skin thickness required to withstand the shear flows caused by the combined action of shear force and torque was calculated along the wing span. The resulting thickness distribution is presented in Figure 9.19. As expected, the maximum required thickness occurs near the wing root, where the internal loads are highest, and progressively decreases towards the wing tip.

The calculated values represent only the theoretical minimum thicknesses required to withstand the applied shear flows. As shown in Figure 9.19, these values remain significantly below the minimum thickness that can be reliably manufactured and assembled. Therefore, due to manufacturing constraints, the skin thickness was increased and set to a constant value of 0.5 mm along the entire wing span.

A further increase in skin thickness was considered unnecessary, as the wing box already contains seven ribs distributed along the span. These ribs provide sufficient structural support to the skins, limiting their unsupported length and improving the overall stability of the wing box. Consequently, a skin thickness of 0.5 mm was selected as a compromise between manufacturability, structural integrity and additional mass.

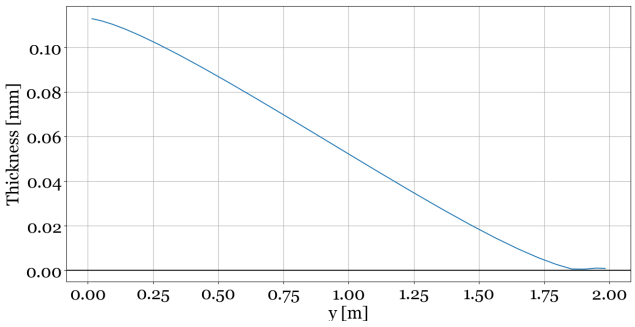

Figure 9.19: Minimum required skin thickness plotted as a function of the wing span

Final Wing Structural Mass Budget

Having completed the sizing procedures for the skins, ribs and spars, the final structural configuration of the wing can be summarized as presented in Table 9.9. All structural components were manufactured from aluminium alloy 7075-T6, with a density of 2810 kg/m 3 . The mass of each component was initially calculated for one half-wing and subsequently doubled to obtain the mass of the complete wing structure.

For each half-wing, the skin accounts for 1.58 kg, while the seven ribs account for 0.35 kg. The front and aft spars have masses of 0.46 kg and 0.30 kg, respectively. This results in a total structural mass of 2.691 kg per half-wing. Therefore, considering both sides of the aircraft, the complete wing structure has a total mass of 5.382 kg.

Table 9.9: Final wing structural mass summary.

Component	Length / Quantity	Material	Density [kg/m^3]	Mass per Half-Wing [kg]	Total Mass [kg]
Skin	2.00 m	Al 7075-T6	2800	1.58	3.16
Ribs	7	Al 7075-T6	2800	0.35	0.70
Front Spar	2.00 m	Al 7075-T6	2800	0.46	0.92
Aft Spar	2.00 m	Al 7075-T6	2800	0.30	0.60
Total	–	–	–	**2.691**	**5.382**

9.3.5. Wing Structure Sensitivity Analysis

In order to evaluate the sensitivity of the wing structural design, the main geometrical parameters were varied and their effect on the structural results was analyzed. For this analysis, the front spar position, boom area, rib spacing, and skin and web thicknesses were considered. Each parameter was varied independently within a selected range, while the remaining parameters were kept constant. For each configuration, the stress, shear flow, and buckling analyses described in the previous sections were repeated.

The resulting maximum tensile and compressive stresses, shear stresses, buckling loads, and structural mass were then compared. Regarding the spar configuration, the front spar position was varied for different boom areas in order to determine whether the selected position was dependent on the boom size. Similarly, the boom area and rib spacing were varied in order to evaluate their effect on the column buckling capacity of the spars. Finally, the skin and web thicknesses were modified to determine their influence on the shear stress and structural mass.

From this analysis, it was found that the structural design is not highly sensitive to small variations in the parameters considered. Changes in the front spar position, boom area, rib spacing, and skin and web thicknesses produced limited variations in the overall structural response and did not significantly affect the selected configuration. Therefore, the final design can be considered sufficiently robust against small geometrical and sizing variations, while still satisfying the strength and buckling requirements.

9.3.6. Wing Structure Design Evaluation & Recommendations

Having completed the sizing of the wing structure, the obtained design can be evaluated with respect to the assumptions and limitations of the analysis. From the results, the structure satisfies the considered strength and buckling requirements for the flight, launch, and landing load cases. However, several effects were not included and should be considered in future analysis.

Regarding the web-boom idealization, this method provides a suitable preliminary representation of the global load paths within the wing. However, it does not fully capture the local stress distribution or the load transfer between the skin, spars, and ribs. Therefore, local stress concentrations may not be accurately represented. A finite element analysis is recommended in order to verify the stress distribution within the complete structure.

The current analysis also does not consider the elastic deformation of the wing. Excessive bending or twisting may modify the aerodynamic shape and influence the load distribution acting along the span. For this reason, a deflection analysis should be performed in future work in order to determine the bending displacement and twist of the wing under the critical loading conditions.

Additionally, aeroelastic effects were not evaluated. The interaction between the aerodynamic loads and the structural deformation may result in instabilities such as divergence, control reversal, or flutter. Therefore, a modal and flutter analysis should be performed once the final mass and stiffness distributions of the wing have been determined.

Finally, the analysis does not consider the effect of repeated loading during the operational life of the aircraft. Fatigue should therefore be evaluated using the expected mission load spectrum, particularly at joints and other regions where stress concentrations may occur.

9.3.7. Wing Structure Verification & Validation

Verification and validation of the wing structural analysis code were performed in order to assess the correctness of the implemented calculations and the reliability of the obtained results. Verification was performed progressively, starting with the individual equations and functions and continuing with the complete structural analysis.

Unit tests were performed using the pytest framework. These tests were used to verify that the individual functions within the code produced the expected results for predefined input cases. Regarding the reaction and internal force calculations, these were compared with independent hand calculations obtained from force and moment equilibrium at selected spanwise locations. Similarly, the centroid, second moment of area, bending stress, and shear flow calculations were compared with analytical calculations performed for simplified cross-sections.

In addition, consistency checks were performed in order to verify that the code followed the expected physical behaviour. These included checking that the internal loads decreased towards the wing tip, that increasing the boom area decreased the bending stress, and that decreasing the rib spacing increased the critical Euler buckling load.

Regarding validation, the next step is to perform a finite element analysis of the selected wing structure. The stress distribution and structural behaviour obtained from the FEM model will be compared with the results from the analytical tool. From this comparison, the assumptions made in the web-boom analysis can be evaluated and the obtained sizing results can be further validated.

9.3.8. Tail Structural Design

For the tail structure design, the same methodology as for the wing was used. However, the material chosen for the skin is a thermoplastic composite CF/PEEK in order to minimize the mass of the stabilizer structure and consequently help shift the cg forward.

Given the lower magnitudes of forces the stabilizers have to withstand, its structure will only be composed of 1 spar, 2 ribs and a skin thickness of 0.8mm. Regarding the ribs, these are sized with a thickness of 3mm, a lower thickness would not provide sufficient rib stiffness. Regarding the spar section, this was determined to have a total flange area equal to $2 \cdot 10^{-5}\ m^2$. A summary of the stabilizer structure components is displayed in Table 9.10

Table 9.10: Stabilizer mass summary

Stabilizer Structure	Area (m^2)	Thickness (mm)	Density (kg/m^3)	Mass (kg)
Rib 1	0.00300	3.0	2800	0.0252
Rib 2	0.00080	3.0	2800	0.0069
Skin	0.14400	0.8	1400	0.1612
Spar	0.00004	–	2800	0.0224
Stabilizer mass ($\times 1$)				**0.2157**
Total stabilizer mass				**0.6473**

9.4. Folding Mechanism *Author(s): Kaj*

This section provides an overview of the folding mechanism that will be implemented in the VAPOR mission. First, an overview of the system is provided, including its functions and the considerations to be taken into account. Following that, a trade-off will be conducted, and subsequently, a sensitivity analysis of that trade-off will be performed. Secondly, the mechanism will be sized, including the analysis methodology, results, and component selection. Lastly, a sensitivity analysis will be conducted on the sizing method.

9.4.1. Sub-system Description

This section provides a general overview of the subsystem components needed and the considerations taken into account when developing this architecture. Three distinct states can be identified in which the wings can be:

- Stowed position: this is the position in which the wings are folded back in preparation for the launch phase. The wings are locked in that position by a locking mechanism.
- Free Position: this is the position in which the actuating mechanism is rotating the wing to its final position. The wings are here, free to move.
- Unfolded position: this is the position in which the wings are in their glide configuration. The wings are again locked in this position.

The folding mechanism will be responsible for transitioning between these states and, therefore, depends on the stowed position. This position will be traded off in Subsection 9.4.1. The mechanism itself consists of two distinct parts. The first part is the load-bearing structure, and the second part is the actuating mechanism. These two parts are highly coupled as the load-bearing part needs to be able to rotate or move along as the wing folds, which is dependent on the way the mechanism is actuated.

Trade-offs

To fully define the subsystem, some trade-offs must be made first. First, a trade-off has to be made about how the stowed configuration will look and where they will be stored. The second part is how the wings are brought from that position into their unfolded level position.

For the stowed position, multiple options were considered and are illustrated in Figure 9.20:

- On-Configuration: The wings are rotated about a vertical axle and are stored on top of each other on a flattened side of the fuselage.
- In-Configuration: The wings are rotated about a vertical axis and are stored next to each other, protruding out of the fuselage.
- Side-Configuration: The wings are rotated about a two-axis hinge and are stored next to the fuselage.

The configurations are traded off based on the following criteria:

- Stability: this measures how much force and what kind of force the wings produce in the stowed configuration, as this will have a big influence on the stability during the rocket phase. It also takes into account the effects of the fairing that is added to minimise the impact of the forces during the rocket phase. This is the most important criterion, as this determines if the UAV will be able to take off; it has therefore been given a weight of 50%.
- Interference: this measures how much the wings will interfere with the internal and external structure of the fuselage. This has been given a weight of 30% because it can affect the overall system weight.
- Folding mechanism: this depends on how complex the mechanism needs to be to accommodate the transition from stowed to folded. This has been given a weight of 20%, as it determines the hinge's complexity and, therefore, its reliability.

For stability, the side configuration scores best, as head-on winds are countered by symmetry around that axis. The on configuration is unstable, as a larger fairing is required to accommodate the stacked airfoils. Also, the side winds will create an up force. The in configuration will also have stability problems, mainly due to the wing extruding out of the fuselage, which will act as a very long but short wing and therefore produce lift. For side winds, a force and moment will also be created. The side configuration of the forces created by a wind from the top can be minimised by placing the airfoil as close to the fuselage as possible. This is more difficult to achieve for the stacked airfoils.

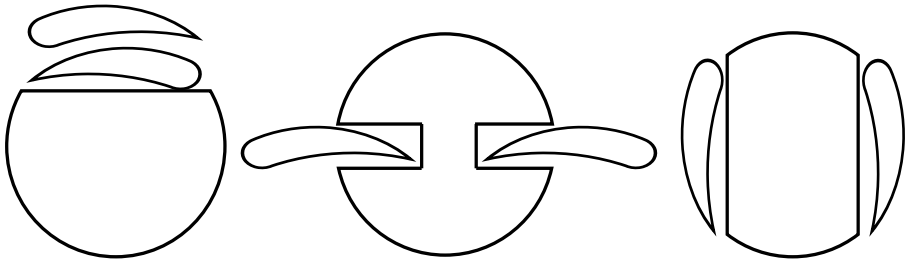

Figure 9.20: The three configurations considered, On-, In- and Side-Configurations, respectively listed from the left

For interference, all get a deduction, as in all configurations, the fuselage has to be extended to cover the wing tips, placing them out of the engine plume, which reduces vibration and melting risk. It is also necessary for stability, as uncovered wingtips will generate aerodynamic forces, induced by side winds. The in configuration performs worse than the other two, as it requires a slit in the middle of the fuselage, which reduces strength and impairs tank space. For the other two, only the top or the sides have to be flattened.

The folding mechanism criteria is the best for the in configuration, as this has a one-axis rotation with non-stacked wings. Because the wings are stacked in the on configuration, this performs worse. The side configuration is the worst due to the two-dimensional rotation that is required.

Table 9.11: Stowing configuration trade-off

Criteria	Weight [%]	On-Configuration	In-configuration	Side-Configuration
Stability	50	1	1	3
Interference	30	2	1	2
Folding Mechanism	30	2	3	1
Total	**100**	**1.50**	**1.40**	**2.30**

As shown in Table 9.11, the side configuration is preferred; the next step is to determine a folding mechanism for it. Two options were considered: a slanted hinge, with a 45-degree bend into the x-z plane and a 45-degree bend into the x-y plane. The second option considered was a three-linkage design, illustrated in Figure 9.21. The two options will be traded off based on the following criteria:

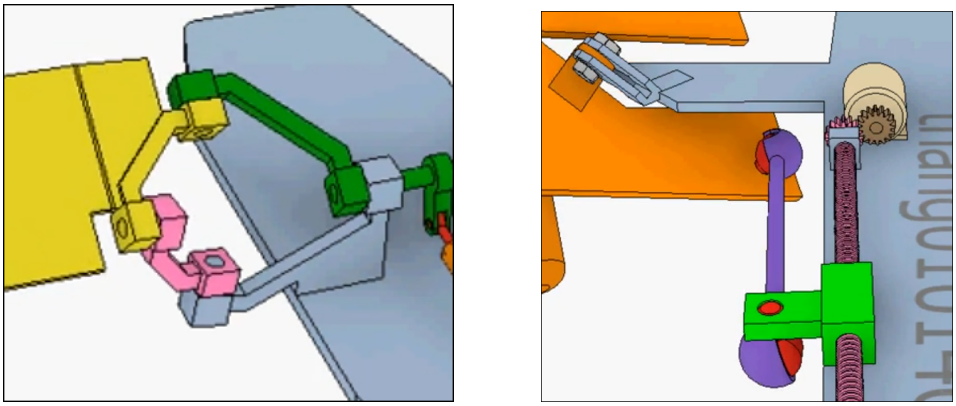

(a) Three Linkage Mechanism **(b)** Skewed Hinge

Figure 9.21: Folding Mechanisms

- Strength: This measures how well it can withstand the load during unfolding and is given a weight of 40%, as this will have a major influence on the folding mechanism's weight and feasibility.
- Reliability: This ranks the complexity of the hinge mechanism and the number of failure points in the design. This is given a weight of 20% as this is important due to the high consequence of a failure during the unfolding
- Actuating: this evaluates how easy it is to engage the system with a mechanical actuator, which is given a weight of 10%, because it does not have a major impact on the design's functionality.
- Aerodynamics: this ranks how close to the fuselage the wing can be, and if there are any elements of the fuselage visible to the flow. This has been given a weight of 30% as this can have an influence on the stability or on the shape of the fuselage

For strength, the 3 linkage option scores low due to the difficulty of transferring the main aerodynamic load through three rotating joints, which are also used for the actuating mechanism. The skewed hinge option performs better because it separates the actuating mechanism from the load-bearing path. The reliability ranking follows the same logic, as the three rotating points introduce multiple points of failure. The actuating, on the other hand, is better in the three-linkage design due to only needing one actuator, and therefore being synchronised. The folding is also better with the three-linkage design, as it does not require a separate actuator rod, which would require another attachment point and increase the spacing between the fuselage and the wing. It also does not have the hinge and actuating rod protruding from the fuselage, which will be visible to the flow, increasing the size of the fairing needed.

Table 9.12: Folding mechanism trade-off

Criteria	Weight [%]	3 Linkage	Skewed Hinge
Strength	40	1	3
Reliability	20	1	3
Actuating	10	3	2
Aerodynamics	30	3	2
Total	**100**	**1.80**	**2.40**

Table 9.12 shows that the skewed hinge won the trade-off mainly due to being more suited to carry the aerodynamic loads during the unfolding of the wing.

Considerations

To further improve the integration of the folding mechanism into the fuselage, such that a more beneficial aerodynamic shape is produced when the wings are stowed, as this is important for the stability during the launch phase. To achieve this, the folding mechanism imposed constraints on the overall wing shape.

First of all, the wing root chord should be minimised, as this reduces the required fuselage diameter; however, it increases the required fuselage length. This, however, makes the UAV more slender during the rocket phase, which is beneficial. The second constraint is the sweep angle, as including sweeps makes it more difficult to fold the wings parallel to the fuselage. Lastly, some form of fairing must be included in the fuselage design, as the wing's folding will create protrusions that must be covered during launch.

Sensitivity Analysis

The same methodology used in the midterm report [1] was used for the sensitivity analysis of the stowing configuration and folding mechanism trade-off.

For the stowing configuration trade-off, the weights assigned to the stability and interference criteria were modified by ±10%, and the same was done for the stability and folding mechanism criteria. In addition, the interference criterion was removed, while the weights of the endurance and sustainability criteria were increased accordingly; the same was also done for the folding mechanism criterion

For the folding mechanism trade-off, the weights assigned to the strength and aerodynamics criteria were modified by ±10%. In addition, the actuating criterion was removed, while the weights of the strength and aerodynamics criteria were increased accordingly.

Overall, both chosen options still achieved the highest score in the trade-off, confirming that the selected option is the most suitable and robust to uncertainties in the weighting factors.

9.4.2. Methodology

This section will give the analysis method used to size the hinge and actuating mechanism. It is divided into distinct parts; first, the general formulas and the coordinate system will be discussed. Second, the aerodynamic and inertial loads generated by the wing are given. Subsequently, the needed torques produced by the push rod are calculated. Finally, the actuator and hinge are sized. For actuator sizing, two distinct approaches are described, depending on the choice of actuator: a spring or an electric-mechanical linear actuator.

General Considerations

First, a right-handed coordinate system is set up based on the wing's unfolded position, with the x-axis pointing along the leading edge (no sweep) of the right wing. The y-direction points from the nose of the UAV, parallel to the fuselage. Equation 9.33 gives then subsequently the direction vectors of the leading edge $\hat{\mathbf{l}}_{\text{LE}}$ and chord $\hat{\mathbf{c}}$ direction of the left wing and normal. The left wing will be analysed, but the process will be the same for the right wing.

$$\hat{\mathbf{l}}_{\text{LE}} = \begin{pmatrix} -1 \\ 0 \\ 0 \end{pmatrix}, \qquad \hat{\mathbf{c}} = \begin{pmatrix} 0 \\ -1 \\ 0 \end{pmatrix} \qquad \hat{\mathbf{n}} = \hat{\mathbf{l}}_{\text{LE}} \times \hat{\mathbf{c}} \tag{9.33}$$

To analyse the wing, the following points and directions should be defined at each rotation angle (θ) of the wing. Where $\theta = 0°$ it is unfolded (θ_{deploy}), and when $\theta = -120°$ it is completely stowed (θ_{fold}). The points of interest are:

- $\mathbf{P}_{\text{hinge}}$: The centre point of the rotating axes; the hinge point.
- $\mathbf{P}_{\text{BW}}$: The point at which the pushrod connects to the wing.
- $\mathbf{P}_{\text{BA}}$: The point at which the pushrod connects to the actuator.
- $\mathbf{P}_{\text{cg}}$: The centre of gravity of half the wing.
- $\mathbf{P}_{\text{AC}}$: The Aerodynamic Centre (AC) of half the wing.

Apart from the leading edge, chord and normal direction of the wing, the following directions also have to be defined:

- $\hat{\mathbf{k}}$: The axis around which the wing rotates.
- $\hat{\mathbf{g}}$: The direction of gravity.
- $\hat{\mathbf{a}}$: The direction in which the actuator is free to move.

The hinge axis is inclined at 45° to both the y- and z-axes. The gravity direction is dependent on the pitch angle (ϕ) at unfolding. The actuator moves parallel to the fuselage and therefore in the y-axis. The directions are given in Equation 9.34

$$\hat{\mathbf{k}} = \frac{1}{\|\mathbf{k}\|}\begin{pmatrix} -1 \\ \tan 45° \\ \tan 45° \end{pmatrix}, \qquad \hat{\mathbf{g}} = \frac{1}{\|\mathbf{g}\|}\begin{pmatrix} 0 \\ -\sin\phi \\ -\cos\phi \end{pmatrix}, \qquad \hat{\mathbf{a}} = \begin{pmatrix} 0 \\ 1 \\ 0 \end{pmatrix} \tag{9.34}$$

These directions and points should be known at each rotation angle of the wing. For that, the Rodrigues' rotation formula is given below first, for a direction vector, and secondly, modified for the rotation of any point ($\mathbf{P}$) rigidly attached to the wing around the hinge axis.

$$\hat{\mathbf{d}}'(\theta) = \hat{\mathbf{d}}\cos\theta + (\hat{\mathbf{k}} \times \hat{\mathbf{d}})\sin\theta + \hat{\mathbf{k}}(\hat{\mathbf{k}} \cdot \hat{\mathbf{d}})(1 - \cos\theta) \tag{9.35}$$

$$\mathbf{P}'(\theta) = \mathbf{P}_{\text{hinge}} + \left(\mathbf{v}\cos\theta + (\hat{\mathbf{k}} \times \mathbf{v})\sin\theta + \hat{\mathbf{k}}(\hat{\mathbf{k}} \cdot \mathbf{v})(1 - \cos\theta)\right) \tag{9.36}$$

Where in Equation 9.35 $\hat{\mathbf{d}}'(\theta)$ is the direction rotated by θ degrees, $\hat{\mathbf{d}}$ is the original direction vector in the unfolded position. $\hat{\mathbf{k}}$ is the axis around which the direction vector is rotated; in this case, this will be the hinge axis. In Equation 9.36 $\mathbf{P}_{\text{hinge}}$ is the hinge origin, $\mathbf{v} = \mathbf{P} - \mathbf{P}_{\text{hinge}}$ is the position vector from the hinge

origin to the point in the deployed configuration. The last thing needed is the torque contribution of a force along the hinge axis. This torque of any force $\mathbf{F}$ applied at a rotated point $\mathbf{P}'$ about the hinge axis is obtained by projecting the moment onto $\hat{\mathbf{k}}$.

$$\tau = (\mathbf{r} \times \mathbf{F}) \cdot \hat{\mathbf{k}} \tag{9.37}$$

where $\mathbf{r} = \mathbf{P}'(\theta) - \mathbf{P}_{\text{hinge}}$ is the moment arm from the hinge origin to the point of force application.

Wing Torques

Gravitational torque: The gravitational force acts on the wing centre of gravity $\mathbf{P}_{\text{cg}}(\theta)$:

$$\mathbf{F}_{\text{grav}} = \frac{m_{\text{wing}}}{2} G \hat{\mathbf{g}} \tag{9.38}$$

where m_{wing} is the wing mass and $G = 9.81\,\text{m/s}^2$ is the gravitational acceleration. The resulting torque about the hinge axis follows from Equation Equation 9.37 with $\mathbf{r} = \mathbf{P}_{\text{cg}}(\theta) - \mathbf{P}_{\text{hinge}}$.

Aerodynamic torque: The effective velocity at the aerodynamic centre is made up of both the free-stream velocity and the rotational velocity induced by the deploying wing:

$$\mathbf{v}_{\text{eff}} = V_\infty \hat{\mathbf{y}} - \dot{\theta}\,\hat{\mathbf{k}} \times \mathbf{r}_\perp \tag{9.39}$$

where V_∞ is the free-stream airspeed, $\hat{\mathbf{y}}$ is the flight direction, $\dot{\theta}$ is the instantaneous angular rate of the wing, and $\mathbf{r}_\perp = \mathbf{r}_{\text{AC}} - (\mathbf{r}_{\text{AC}} \cdot \hat{\mathbf{k}})\hat{\mathbf{k}}$ is the component of the aerodynamic-centre moment arm $\mathbf{r}_{\text{AC}} = \mathbf{P}_{\text{AC}}(\theta) - \mathbf{P}_{\text{hinge}}$ perpendicular to the hinge axis.

The effective velocity is projected onto the local wing frame to obtain the effective angle of attack. At each fold angle θ, the leading-edge direction $\hat{\mathbf{l}}_{\text{LE}}(\theta)$, chord direction $\hat{\mathbf{c}}(\theta)$, and surface normal $\hat{\mathbf{n}}(\theta)$ are first obtained by rotating their reference body-frame directions using Equation 9.35. The in-plane velocity vector $\mathbf{v}_{\text{2D}}$ is then obtained by removing the leading-edge component from the effective velocity, leading to the effective angle of attack:

$$\mathbf{v}_{\text{2D}}(\theta) = \mathbf{v}_{\text{eff}} - \big(\mathbf{v}_{\text{eff}} \cdot \hat{\mathbf{l}}_{\text{LE}}(\theta)\big)\hat{\mathbf{l}}_{\text{LE}}(\theta) \tag{9.40}$$

$$\alpha_{\text{eff}} = \arctan\left(\frac{v_n}{-v_c}\right) + \alpha_0 \tag{9.41}$$

where $v_c = \mathbf{v}_{\text{2D}} \cdot \hat{\mathbf{c}}(\theta)$ is the chord-wise velocity component, $v_n = \mathbf{v}_{\text{2D}} \cdot \hat{\mathbf{n}}(\theta)$ is the normal velocity component, and α_0 is the angle of attack at which the UAV is currently flying. The lift and drag coefficients are calculated according to the model described in Equation 9.42. This accounts for two distinct phases: pre- and post-stall. Pre-stall, the lift and drag coefficients of the wing are used, which are calculated in Subsection 9.3.2. As the wing rotates, it starts out at a zero angle of attack and rotates towards negative angles of attack until it reaches the stall angle (α_{stall}). From that point, it is assumed to be a flat plate, for which the C_L and C_D are known [].

$$C_L = \begin{cases} C_{L,0} + C_{L,\alpha}\,\alpha_{\text{eff}} & \alpha_{\text{eff}} \geq \alpha_{\text{stall}} \\ \sin(2\alpha_{\text{eff}}) & \alpha_{\text{eff}} < \alpha_{\text{stall}} \end{cases}, \qquad C_D = \begin{cases} C_D(\alpha_{\text{eff}}) & \alpha_{\text{eff}} \geq \alpha_{\text{stall}} \\ 2\sin^2(\alpha_{\text{eff}}) & \alpha_{\text{eff}} < \alpha_{\text{stall}} \end{cases} \tag{9.42}$$

where $C_{L,\alpha}$ is the lift-curve slope, $C_{L,0}$ is the zero-angle lift coefficient, α_{stall} is the negative stall angle, and $C_D(\alpha_{\text{eff}})$ is interpolated from the drag polar of the wing. The aerodynamic forces and pitching moment acting on a single wing panel are:

$$\mathbf{L} = C_L \tfrac{1}{2}\rho V_{\text{eff}}^2 \tfrac{S}{2}\hat{\mathbf{l}}(\theta), \qquad \mathbf{D} = C_D \tfrac{1}{2}\rho V_{\text{eff}}^2 \tfrac{S}{2}\hat{\mathbf{v}}_{\text{2D}}(\theta), \qquad \mathbf{M}_{\text{AC}} = C_{m,\text{AC}} \tfrac{1}{2}\rho V_{\text{eff}}^2 \tfrac{S}{2}\bar{c}\,\hat{\mathbf{l}}_{\text{LE}}(\theta) \tag{9.43}$$

where ρ is the air density at the flight altitude, S is the total wing reference area, and $V_{\text{eff}} = \|\mathbf{v}_{\text{2D}}\|$ is the effective airspeed in the wing plane. The lift unit direction $\hat{\mathbf{l}}(\theta)$ is perpendicular to $\mathbf{v}_{\text{2D}}$ in the wing plane and is obtained by projecting the rotated surface normal $\hat{\mathbf{n}}(\theta)$ onto the plane perpendicular to the flow.
$C_{m,\text{AC}}$ is the pitching moment coefficient about the aerodynamic centre, and $\bar{c} = S/b$ is the mean aerodynamic chord with b the wing span. The torques due to lift, drag, and pitching moment about the hinge axis each follow from Equation 9.37, with moment arms taken to $\mathbf{P}_{\text{AC}}(\theta)$ for $\mathbf{L}$ and $\mathbf{D}$, and the pitching moment projected directly onto $\hat{\mathbf{k}}$.

Actuator Torques

The wing is driven by a push-rod of fixed length L_{rod} connecting a actuator-fixed ball-end $\mathbf{P}_{\text{BA}}(\theta)$ to a wing-mounted ball-end $\mathbf{P}_{\text{BW}}(\theta)$. As the wing rotates, the actuator must translate along its axis to maintain the rod length. The required actuator stroke is:

$$s(\theta) = \Delta y_{\text{req}}(\theta) - \Delta y_{\text{ref}}, \qquad \Delta y_{\text{req}}(\theta) = \sqrt{L_{\text{rod}}^2 - \Delta x(\theta)^2 - \Delta z(\theta)^2} \tag{9.44}$$

where Δx, Δy, Δz are the components of the vector from $\mathbf{P}_{\text{BW}}(\theta)$ to $\mathbf{P}_{\text{BA}}$, and $\Delta y_{\text{ref}} = \Delta y_{\text{req}}(\theta_{\text{fold}})$ is the stroke at the fully folded reference position. From the stroke length at each angle $\mathbf{P}_{\text{BA}}$ at each angle is $\mathbf{P}_{\text{BA}}(\theta) = \mathbf{P}_{\text{BA},0} + s(\theta)\,\hat{\mathbf{a}}$.
The spring force is a function of the current stroke:

$$F_{\text{spring}}(s) = \max(F_1 - k\,s(\theta),\, 0)\,, \qquad k = \frac{F_1 - F_2}{s_{\max}} \tag{9.45}$$

where F_1 is the spring pre-load force at the folded position, F_2 is the spring force at full extension, $s_{\max}$ is the maximum stroke, and k is the spring stiffness. The spring torque follows from Equation 9.37 with $\mathbf{F} = F_{\text{spring}}\,\hat{\mathbf{r}}_{\text{rod}}$. The net torque on the wing then drives a forward-Euler time integration of the rotational equation of motion:

$$\frac{m_{\text{wing}}}{2}\|\mathbf{r}_\perp\|^2\,\ddot{\theta} = \tau_{\text{spring}} + \tau_{\text{grav}} + \tau_L + \tau_D + \tau_M \tag{9.46}$$

τ_{spring} is the spring torque, and τ_{grav}, τ_L, τ_D, τ_M are the gravitational, lift, drag, and pitching-moment torques, respectively. Where $\mathbf{r}_\perp = \mathbf{r}_{\text{cg}} - (\mathbf{r}_{\text{cg}} \cdot \hat{\mathbf{k}})\hat{\mathbf{k}}$ is the component of the centre-of-gravity moment arm perpendicular to the hinge axis.

The unfolding is simulated using a forward Euler scheme. The simulation is initialised with $\theta_0 = \theta_{\text{fold}}$ and $\dot{\theta}_0 = 0$. The integration proceeds until one of two stop conditions is met: either the wing reaches the deployed angle $\theta \geq \theta_{\text{deploy}}$, in which case deployment is considered successful, or the angular rate becomes negative ($\dot{\theta} < 0$), indicating that the net torque has reversed the wing motion before reaching the deployed position, and deployment has failed.

Actuator Sizing

The push-rod is sized against Euler column buckling with pinned ends. For a thin-walled hollow rod, the minimum second moment of area required to resist the maximum compressive load with a safety factor n_s is:

$$I_{\text{req}} = \frac{F_{\max}\, n_s\, L_{\text{rod}}^2}{\pi^2\, E} \tag{9.47}$$

$$r = \left(\frac{I_{\text{req}}}{\pi\, t}\right)^{1/3} \tag{9.48}$$

where $F_{\max}$ is the maximum compressive actuator force, L_{rod} is the push-rod length, and E is Young's modulus of the rod material. From the thin-walled approximation $I \approx \pi r^3 t$, the required outer radius is calculated via Equation 9.48, where t is the wall thickness. The push-rod mass is then $m_{\text{rod}} = \rho\, A\, L_{\text{rod}}$, where $A = 2\pi r\, t$ is the cross-sectional area and ρ is the material density.

Hinge Sizing

The inertial forces are calculated with Equation 9.49 and are assumed to act at the centre of gravity.

$$\mathbf{F}_{\text{I}} = \frac{m_{\text{wing}}}{2}\left[\boldsymbol{\alpha} \times \mathbf{r}_{\text{cg}} + \boldsymbol{\omega} \times \left(\boldsymbol{\omega} \times \mathbf{r}_{\text{cg}}\right)\right] \tag{9.49}$$

Here $\boldsymbol{\alpha}$ is the angular acceleration around the hinge axis, $\boldsymbol{\omega}$ is the angular speed around the hinge axis, and $\mathbf{r}_{\text{cg}}$ is the moment arm to the centre of gravity. Summing all the forces and moments around the hinge axis and decomposing them along $\hat{\mathbf{k}}$

$$\mathbf{F}_{\text{tot}} = \mathbf{F}_{\text{grav}} + \mathbf{L} + \mathbf{D} + \mathbf{F}_{\text{act}} + \mathbf{F}_{\text{I}} \tag{9.50}$$

$$\mathbf{M}_{\text{tot}} = \mathbf{r}_{\text{cg}} \times (\mathbf{F}_{\text{grav}} + \mathbf{F}_{\text{I}}) + \mathbf{r}_{\text{AC}} \times (\mathbf{L} + \mathbf{D}) + \mathbf{r}_{\text{BW}} \times \mathbf{F}_{\text{act}} + \mathbf{M}_{\text{AC}} \tag{9.51}$$

The minimum axle diameter is determined from the peak bending moment $M_{\text{bend,max}}$ using the solid circular shaft formula:

$$d = \left(\frac{32\, M_{\text{bend,max}}\, n_s}{\pi\, \sigma_y} \right)^{1/3} \qquad m_{\text{axle}} = \rho\, \frac{\pi d^2}{4}\, L_{\text{hinge}} \tag{9.52}$$

where $M_{\text{bend,max}}$ is the maximum bending moment over all deployment angles, n_s is the safety factor, and σ_y is the material yield strength. ρ is the material density. The mass of the bearings and actuator is given when an off-the-shelf component is selected. The bearing radial load is estimated by adding the reaction force from the bending moment to the direct radial force; this is based on a simple beam loaded at the two ends, as is illustrated in Figure 9.22.

$$F_r = F_{\text{radial,max}} + \frac{M_{\text{bend,max}}}{L_{\text{hinge}}} \tag{9.53}$$

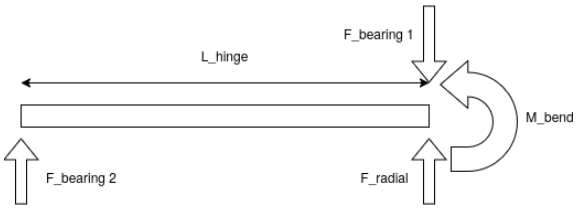

Figure 9.22: Free Body Diagram (FBD) of hinge loading

where $F_{\text{radial,max}}$ is the peak radial force on the axle and L_{hinge} is the distance between the two bearings. Two bearings are needed in order to properly carry the bending. To select a bearing, a static rating (C_0) is required. Since the axial load is much smaller than the radial load, the static rating is simply $2F_r$. The hinge axle mass is simply calculated as a solid cylinder; the max radial load is felt by the first bearing.

9.4.3. Results

This section discusses the results of the folding mechanism sizing. The performance results will be calculated, and finally, the peripherals will be selected. The environmental parameters under which the simulation is performed are given in Table 9.13.

The locations of the centre of gravity, aerodynamic centre, hinge point, wing-ball point and actuator ball point were determined by CAD modelling. This is done to arrive at a physically reasonable design that does not interfere with itself. After this, the method described in Subsection 9.4.2 was applied to analyse mechanical feasibility; any changes were subsequently updated in the CAD to ensure feasibility.

Table 9.13: Simulation input parameters

Parameter	Value	Unit
Flight conditions		
V_∞	26.75	m/s
h	2500	m
ρ	0.957	kg/m^3
ϕ	0	°
Aerodynamic & wing properties		
$C_{L,\alpha}$	0.0978	deg^{-1}
$C_{L,0}$	0.8	-
α_{stall}	−7.5	°
S	1.09	m^2
b	4	m
$C_{m,\text{AC}}$	−0.221	-
α_0	0	°
m_{wing}	5.0	kg
Structural properties		
E	69	GPa
ρ_{mat}	2700	kg/m^3
n_s	1.5	-
L_{hinge}	0.05	m
t	1	mm

A normal compression spring cannot be used because it does not provide enough force; a gas spring is used instead. The characteristics of a gas spring are as follows:

- F_1: this is the force that it provides when fully compressed.
- F_2: this is the force that it provides when fully extended.
- S_{max}: this is the stroke size of the spring and needs to correspond to the stroke at θ_{fold} calculated with Equation 9.44

To size the mechanism, commonly provided force combinations were tested, starting with the lowest force and increasing the stroke length until the next force combination was tested. This was done until an optimal force-stroke combination was found. Figure 9.23 shows the torque at the hinge during the unfolding. Here, it can be seen that the total torque does not go to zero, so it keeps accelerating until a certain point, where it

decelerates. The hinge, therefore, produces considerable inertial forces due to the high accelerations. This inertial force is decomposed into the commonly used directions. Here, you can see that they have the same magnitude as the other aerodynamic forces and therefore are not negligible, as is the case with a linear actuator.

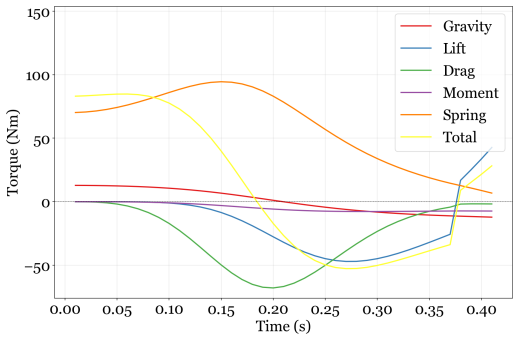

Figure 9.23: The torques acting along the hinge axis at each time step.

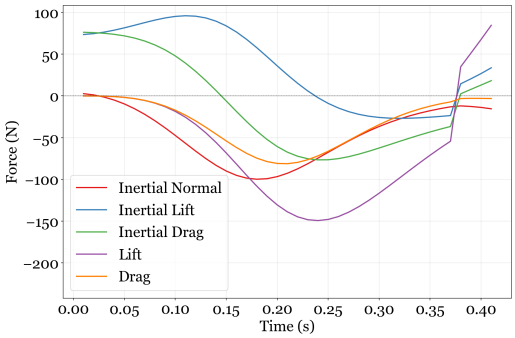

Figure 9.24: The forces acting at the hinge point at each time step

In Figure 9.25, it can be seen that there is a much higher radial force at the bearing. From Figure 9.26, it can also be seen that the bending in level flight is not the most critical design scenario anymore.

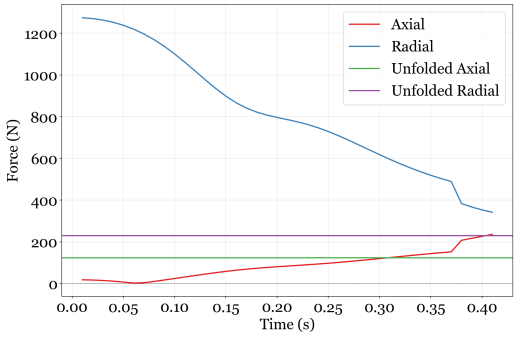

Figure 9.25: The force at the hinge point decomposed into axial and radial components at each time step

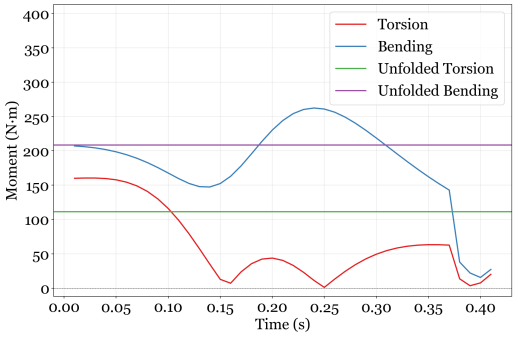

Figure 9.26: The moment at the hinge point decomposed into torque and bending moment at each time step

Conclusion and Sensitivity

Table 9.14 presents the performance metrics for the folding system. This is based on a preliminary selection of a gas spring[7], and bearings[8] Here, deployment speed and weight are the distinguishing factors, as the spring-powered mechanism has a much lower deployment time. This is beneficial for the system as it ensures a better transition to the glide phase. Also, the mass is about half as much. The bearings and forces are, however, larger, requiring higher-rated bearings. Other factors should also be considered, such as the system's reliability. Here, the linear actuator has the upper hand, as it does not depend on a single burst of power, making it a far more reliable system. It, however, increases EPS complexity. Ultimately, the very high deployment speed of the linear actuator makes it the least suitable for the system, and the spring mechanism will be used.

Table 9.14: Performance of deployment mechanism

Parameter	Unit	Spring
Max torsion	N·m	160.4
Max bending	N·m	262.4
Bearing C_0 rating	N	13044
Axle diameter	mm	19.97
Pushrod diameter	mm	11.40
Deployment speed	s	0.41
Mechanism mass	kg	0.709
Total system mass	kg	2.909

The last components to be addressed are the mechanisms for releasing and locking the wing in the horizontal position. To release the wing, a normally closed solenoid pin will be used for risk mitigation. Because it is normally closed, a power outage will not release the highly energetic springs. For the locking mechanism,

[7] www.sgs-engineering.com [Date Accessed: June 14] [8] rs-online.com [Date Accessed: June 14]

long-nose spring plungers will be used; they will be compressed by the rotation of the wing and slide into a hole in the wing root, locking the wings passively.

Further, it is important to clarify the model's assumptions; the biggest inaccuracy is the point-mass assumption, which drastically simplifies the underlying physics. Lastly, it is assumed that there are no wind disturbances. This is quite accurate, as the actuation is so quick that it is a valid assumption. It is also of utmost importance that the mechanism is properly tested and validated during testing, as it is among the most critical subsystems in the UAV.

The sensitivity analysis shows that the whole system is incredibly sensitive to changing conditions. The most sensitive parameter is the speed at which the wing is unfolded (V_∞), as the dominant forces scale quadratically with it. The same is true for other environmental properties, such as the density at which it flies. Lastly, the wing span is another critical parameter, as this has a huge impact on all the moments generated. To verify the numerical simulation and model, multiple standard unit tests were implemented, as described in Section 6.1. Also, during debugging, additional tests were performed and subsequently implemented to resolve modelling errors that produced unrealistic answers.

9.5. Vibrations *Author(s): Kaj*

This section will analyse the UAV's vibrational modes during take-off. This will be done by first analysing the engine noise, as this is one of the main causes of vibration. A simplified model of the UAV is then created to analyse its response to vibrations. Finally, the acoustic loads are applied to the UAV's structural model to combine and assess the impact of noise on the UAV's vibrational modes.

9.5.1. Noise

The aim of this section is to provide a noise profile of the engine during take-off. This is not only important for vibrations but also for logistical and safety reasons. From this noise profile, the loading at an arbitrary point along the rocket can be calculated. First, the methodology will be presented, followed by the results, which have an influence on the operational side of noise.

Methodology[-8pt]

The modelling approach follows the second discrete-source method presented in the NASA SP-8072 guidelines [54] and is implemented in Python.

First, a coordinate system is set up with the x-axis pointing horizontally away from the nozzle exit, the y-axis pointing upward, and the origin at the nozzle exit plane. Two speeds of sound are required throughout the model these are the ambient speed of sound a and the nozzle exit speed of sound a_{exit}.

The nozzle exit diameter D_e and the potential core length L_c are the two geometric parameters that determine the shape of the source distribution. The exit diameter is derived from momentum conservation at the nozzle exit plane of a perfectly expanded nozzle, given in Equation 9.54 where V_{exit} is the mean exit velocity, $\dot{m}$ is the mass flow rate through the nozzle throat, and p_∞ is the ambient static pressure. The unconstrained potential core length L_c^* is then calculated using the empirical formula of [55], which has the first coefficient halved relative to the original SP-8072 expression to better match experimental data, as given in Equation 9.55.

If the jet core would touch the ground before reaching its end, the potential core is cut off at the ground [56], as shown in Equation 9.56, where h_n is the height of the nozzle above the ground.

$$D_e = \frac{2\,a_{\text{exit}}}{V_{\text{exit}}}\left(\frac{\dot{m}\,V_{\text{exit}}}{\pi\,p_\infty\,\gamma_{\text{exit}}}\right)^{1/2} \quad (9.54) \qquad L_c^* = 1.75\,D_e\left(1+0.38\,\frac{V_{\text{exit}}}{a_{\text{exit}}}\right)^2 \quad (9.55) \qquad L_c = \min\left(L_c^*,\,h_n\right) \quad (9.56)$$

The total acoustic power W_{OA} emitted by the jet is obtained by scaling the mechanical kinetic power of the engine by an acoustic efficiency η, as in Equation 9.57. The acoustic efficiency η is computed using the empirical relation [55], replacing the constant 0.1% approximation used in the original SP-8072 method.

$$W_{\text{OA}} = \tfrac{1}{2}\,\dot{m}\,V_{\text{exit}}^2\,\eta \qquad \eta = K\,\frac{\gamma_{\text{exit}}}{\gamma}\left(\frac{a_{\text{exit}}}{a}\right)^3\left(\frac{a_{\text{exit}}}{V_{\text{exit}}}\right)^2 \quad (9.57)$$

Where $K = 1.2\times10^{-3}$ is an empirical constant. The overall acoustic power level in decibels, referenced to 10^{-12} W, then follows from Equation 9.58.

The jet plume is then discretised into N point sources of equal spacing Δx. The centre position of the k-th source along the jet axis is given in Equation 9.59, with the normalised axial coordinate $\xi_k = x_k / L_c$, where f_{ext} is a length fraction that controls how many core lengths, downstream of the potential core, the source distribution is extended.

$$L_W = 10\log_{10}(W_{\text{OA}}) + 120 \tag{9.58}$$

$$x_k = \left(k - \tfrac{1}{2}\right)\frac{f_{\text{ext}}\, L_c}{N}, \qquad k = 1, \ldots, N \tag{9.59}$$

For sources whose axial position exceeds the nozzle height h_n, the source location is mirrored across the y-axis. The power of each source and its mirror is reduced by 3 dB to conserve total radiated energy.

The Normalised Relative Sound Power per unit core Length (NRSPL) assigns a relative sound power to each source slice as a function of the normalised axial coordinate ξ, using a Nagamatsu curve [57] in place of the SP-8072 distribution, as given in the following equation:

$$\text{NRSPL}(\xi) = \begin{cases} 10.8\log_{10}(\xi_k) - 3.2, & \xi_k \le 1.6 \\ -1.0 - 153.22\left(\log_{10}(\xi_k) - \log_{10}(1.6)\right)^2, & \xi_k > 1.6 \end{cases} \tag{9.60}$$

As Equation 9.60 is acquired by fitting it to the Nagamatsu curve, a normalisation offset of $10\log_{10}(1.1629)$ is subtracted to ensure the integrated distribution sums to the correct total power. The sound power level of slice k then follows from Equation 9.61.

$$L_{W,k} = \text{NRSPL}(\xi_k) + L_W + 10\log_{10}\left(\frac{\Delta x}{L_c}\right) \tag{9.61}$$

Combining the slice power level, and the one-third-octave bandwidth $\Delta f_j = f_j\left(2^{1/6} - 2^{-1/6}\right)$, gives the band sound power level for slice k at frequency f_j, as given in Equation 9.62, where f_j is the j-th International Organisation for Standardisation (ISO) 266 one-third-octave centre frequency and is a function of a modified Strouhal number $St_{k,j}$.

$$L_{W,k,j}^{\text{band}} = L_{W,k} + 10\log_{10}\left(\frac{1.93\, St_{k,j}}{9.63 + St_{k,j}^{\,3.32}}\right) - 10\log_{10}\left(\frac{V_{\text{exit}}\, a}{x_k\, a_{\text{exit}}}\right) + \log_{10}(\Delta f_j) \qquad St_{k,j} = \frac{x_k\, f_j\, a_{\text{exit}}}{V_{\text{exit}}\, a} \tag{9.62}$$

Sources with $x_k \le h_n$ lie on the y-axis of the jet and are placed at $(0, -x_k)$; sources with $x_k > h_n$ lie in the horizontal segment and are placed at $(x_k - h_n, -h_n)$. At each 2D point the displacement vector is: $\mathbf{p} = \mathbf{d}_k = \mathbf{p} - \mathbf{s}_k$. The propagation distance is $r_k = \|\mathbf{d}_k\|$. The directivity correction follows the closed-form expression [58]. To account for the difference in emission effectivity for each frequency, an effective emission angle $\theta_{E,k,j}$ is first defined by Equation 9.63, where $St_{k,j}^{(D)} = f_j D_e / V_{\text{exit}}$ is the Strouhal number based on exit diameter. $\hat{\mathbf{e}}_k$ is the unit vector along the local jet axis at source k, pointing downward for sources in the vertical segment and in the positive x-direction for sources in the horizontal segment. The spectral directivity correction D is then calculated using Equation 9.64.

$$\theta_{E,k,j} = \arccos\left(\frac{\mathbf{d}_k \cdot \hat{\mathbf{e}}_k}{r_k}\right) - \frac{\pi}{180}\left(9.61\log_{10}\left(\frac{St_{k,j}^{(D)}}{0.0515}\right)\right) \tag{9.63}$$

$$D\left(\theta_E, St^{(D)}\right) = 10\log_{10}\left(\frac{c_1\left(1 + \cos^4\theta_E\right)}{\left[(1 - M_{ec}\cos\theta_E)^2 + 0.3\, M_{ec}^2\right]^{2.5}\left(1 + c_2\, e^{-c_3\theta_E}\right)}\right) - c_4\log_{10}\left(St^{(D)}\right) - c_5 \tag{9.64}$$

where $M_{ec} = 0.75$ is the effective convection Mach number, and the empirical constants take the values $c_1 = 0.37$, $c_2 = 310$, $c_3 = 9$, $c_4 = 0.698$, and $c_5 = 1.67$.

The one-third-octave band sound pressure level at point $\mathbf{p}$ and frequency f_j is obtained by summing the contributions of all N_{total} sources wit the addition of the mirrored sources, as given in Equation 9.65.

$$L_{p,j}(\mathbf{p}) = 10\log_{10}\left(\sum_{k=1}^{N_{\text{total}}} 10^{\dfrac{L_{W,k,j}^{\text{band}} - 10\log_{10}(r_k^2) + D\left(\theta_{E,k,j},\, St_{k,j}^{(D)}\right) - 11}{10}}\right) \tag{9.65}$$

where the $-10\log_{10} r_k^2$ term accounts for spherical spreading, the constant -11 dB converts acoustic power level to pressure level in a free field, and the propagation distance is set to a minimum of $\Delta x/2$ to avoid the infinite values at $r_k = 0$.

Spatial Distribution To calculate the spatial spreading of the sound pressure level, the most interesting is the Overall Sound Pressure Level (OASPL). This is obtained by logarithmically summing across all frequency bands. This is done for a grid of points over the area of interest for noise propagation. For this area, a grid is constructed with a uniform point spacing δ. For each point, then the OASPL is calculated.

Acoustic Loading The sound pressure level calculated with Equation 9.65 is converted into a broadband force excitation applied at each point. For each point $\mathbf{p}$, the one-third-octave band sound pressure level $L_{p,j}$ is first calculated, then the displacement Power Spectral Density (PSD) is calculated from Equation 9.66. Here $p_{\text{ref}} = 20\,\mu$Pa is the standard acoustic reference pressure. Δf_j is the bandwidth of the corresponding ISO 266 one-third-octave band. $A(\mathbf{p})$ is the associated area at that point

$$S_{FF}(f,\mathbf{p}) = A(\mathbf{p})^2 \frac{p_{\text{ref}}^2\, 10^{L_{p,j}(\mathbf{p})/10}}{\Delta f_j} \tag{9.66}$$

The Root Mean Square (RMS) force at each node is obtained by integrating the force PSD.

$$F_{\text{rms}}(\mathbf{p}) = \sqrt{\int_{f_{\min}}^{f_{\max}} S_{FF}(f,\mathbf{p})\,\mathrm{d}f} \approx \sqrt{\sum_{j=1}^{N_f} S_{FF}(f_j,\mathbf{p})\,\Delta f_j} \tag{9.67}$$

Results

This section presents the results of the noise analysis for operational and safety purposes. For this, the OASPL will be evaluated on a grid at launch conditions, as shown in Figure 9.27. Here, the potential core and the maximum sound pressure level in the exhaust are indicated. It can also be seen that there is an increase in sound pressure level at ground level; this is due to the exhaust impinging on the ground. A final contour is also drawn at 135 dB. This corresponds to the lower limit of the maximum peak sound pressure a worker is allowed to experience according to the 2003/10/EC directive of the European Commission [59]. It can be seen that this zone is about 5 to 10 centimetres. From this, it can be concluded that there are no operational limits during launch.

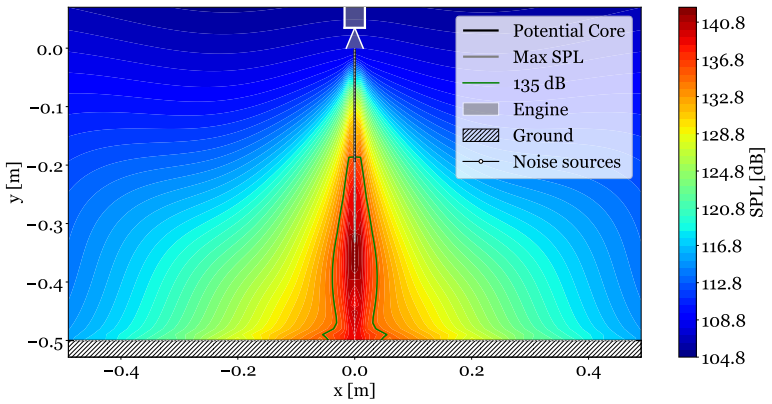

Figure 9.27: Spatial spreading of the exhaust noise during take-off, with 400 sources and a nozzle height of 0.05 metres

9.5.2. Structural Model Methodology

The rocket structure is modelled as a lumped 5-point system that is connected by springs. Each point has a weight and an area. Also, each point-to-point connection has a stiffness (k) depending on the connecting structure.

The mass matrix $\mathbf{M}$ is diagonal, with the point masses m_i on its diagonal. The stiffness matrix $\mathbf{K}$ is assembled from three spring constants: k_1 connecting the nozzle node to the centre node, k_2 connecting the

centre node to the top node, and k_3 connecting the centre node to each of the two side nodes, as given in Equation 9.68.

$$\mathbf{K} = \begin{bmatrix} k_1 & -k_1 & 0 & 0 & 0 \\ -k_1 & k_1+k_2+2k_3 & -k_2 & -k_3 & -k_3 \\ 0 & -k_2 & k_2 & 0 & 0 \\ 0 & -k_3 & 0 & k_3 & 0 \\ 0 & -k_3 & 0 & 0 & k_3 \end{bmatrix} \tag{9.68}$$

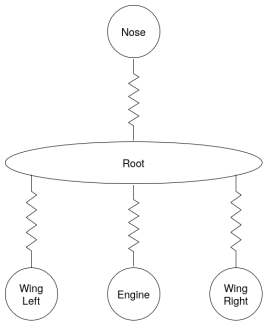

Figure 9.28: Spring-Mass model of the UAV

The undamped natural frequencies $\omega_{n,r}$ and mode shapes $\boldsymbol{\phi}_r$ are obtained from the eigenvalue problem. The mode shape matrix $\boldsymbol{\Phi}$, whose columns are the eigenvectors $\boldsymbol{\phi}_r$, which decouple the system into n independent single-degree-of-freedom systems.

Modal damping is then applied by assigning a constant damping ratio ζ to each mode independently. A value of $\zeta = 0.01$ is used, which is the lower bound recommended by NASA SP-8050 [60] for welded and machined aluminium. The Frequency Response Function (FRF) of the r-th mode is given by Equation 9.69.

$$H_{rr}(\omega) = \frac{1}{\omega_{n,r}^2 - \omega^2 + 2i\zeta\omega_{n,r}\omega} \tag{9.69}$$

Where $\omega_{n,r}$ is the natural frequency of the r-th mode and $\omega = 2\pi f$. The response PSD is then obtained by first transforming back from modal to physical coordinates to get $\mathbf{H}(\omega)$. The response matrix $\mathbf{S}_{XX}$ is then obtained from Equation 9.70.

$$\mathbf{S}_{XX}(\omega) = \mathbf{H}(\omega)\,\mathbf{S}_{FF}(\omega)\,\mathbf{H}^*(\omega) \qquad \mathbf{H}(\omega) = \boldsymbol{\Phi}\,\mathrm{diag}(H_{rr}(\omega))\,\boldsymbol{\Phi}^T \tag{9.70}$$

where $(\cdot)^*$ is the conjugate transpose. The diagonal entries of $\mathbf{S}_{XX}$ give the displacement PSD at each node. The RMS displacement at $\mathbf{p}$ is then obtained by integrating over the full frequency range and taking the square.

9.5.3. Results

This section will give the results of the above-mentioned methodology. First, the spring model will be set up and presented. The frequency response will then be discussed. Lastly, a sensitivity discussion will be performed.

Spring Model

The UAV is discretised into points based on its two main structural elements. These are the stowed wings and the fuselage structure. For each wing, a separate point at the tip is assumed, each responsible for accounting for a quarter of the wing; it is also assumed that the wings are rigidly joined to the fuselage at the midpoint. The fuselage is divided into three points. The bottom point is responsible for half of the fuselage, the midpoint is responsible for half of the fuselage, half of the wings and half of the nose cone, the top point is responsible for the upper half of the nose cone. A schematic of the model is given in Figure 9.28

The mass allocation is based on the placement of each component of the UAV, as discussed in Section 10.3. Each component is assigned to its closest node. The weight of each wing is evenly divided between the wing end node and the node at the root chord.

The area allocation is based on the assumption that the UAV is a pure cylinder. From the root chord to the tail and from the root chord to the tip, a different radius is assumed. Then the area is simply: $A = 2\pi rl$. Where l is the length of the section each point is responsible for. If a percentage of the length covered by a folded wing, then half the total area for that fraction is subtracted and split over the two closest wing points.

For each connection between the points, it is assumed that everything goes through the structure. The spring constants for the wing structure $\frac{EA}{l}$ and the fuselage $\frac{2\pi rtE}{l}$. The values are given in Table 9.15.

Table 9.15: Mass allocation and spring constants

Component	x [m]	y [m]	Mass [kg]	Area [m^2]
Engine	0.00	0.0	9.478	0.4084
Root	0.00	2.0	16.807	1.2331
Nose	0.00	3.5	0.692	0.8247
Wing Right	0.13	0.0	1.345	0.2042
Wing Left	-0.13	0.0	1.345	0.2042
Total	–	–	**29.667**	**2.8745**

Spring	k [N/m]
k_1	1.225×10^8
k_2	2.566×10^8
k_3	4.720×10^7

Results

The RMS force is given in Table 9.16; this is the average force each point feels due to the noise. It also shows the RMS displacements; neither is very large. This is mainly due to the engine's relatively low mechanical power. If it is assumed that these displacements happen perfectly out of sync, then the maximum stress can be calculated from: $\sigma = \frac{E\delta x}{l}$. This gives a maximum stress of 0.02 Mpa.

To check for resonance, the PSD of the displacements is plotted in Figure 9.29. Here are the response functions of each node plotted. The nodes of both wings are taken together as they have the same FRF and Force PSD. Here, it can be seen that there is no significant excitation at the natural frequencies, indicated by a vertical line. The frequencies are placed at 215 Hz, 298 Hz, 327 Hz, and 990 Hz. The fifth mode is absent here, as the system is free-free and thus at 0 Hz. From the figure, it can be seen that the natural frequencies are adequately damped by the structure. Therefore, there is no risk of structural failure due to acoustic loading.

Table 9.16: RMS forces and displacements per node

Node	RMS Force [N]	RMS Displacement [mm]
1	1.8927	2.17×10^{-4}
2	0.8667	1.83×10^{-4}
3	0.4229	1.95×10^{-4}
4	1.0110	4.02×10^{-4}
5	1.0110	4.02×10^{-4}

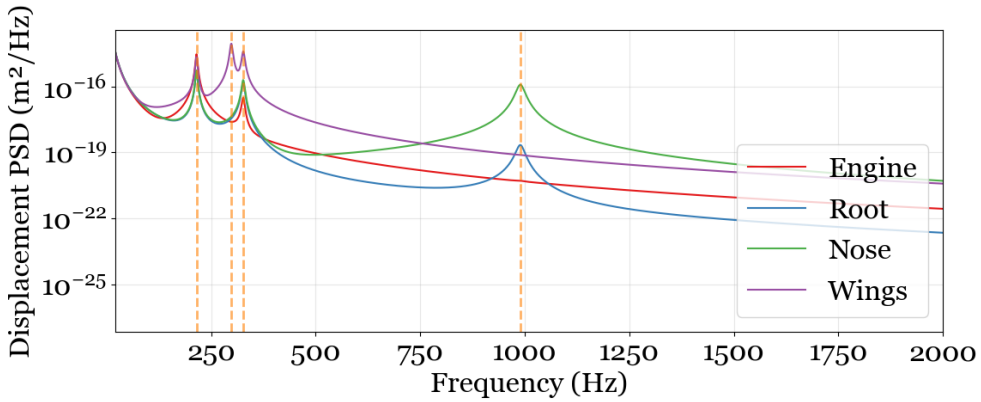

Figure 9.29: Displacement PSD for each node, plotted over half the broadband spectrum

9.5.4. Sensitivity and Discussion

To conduct this sensitivity analysis, multiple parameters were changed, and the impact was observed. From this, the variable to which the method is most sensitive is the thrust of the engine. This increases the mechanical power and thus the overall sound loading of the system. Another parameter to which the system responds significantly is the distance at which the nodes are placed from the centre line of the engine. This is due to the directivity factor, which makes it easier for the sound to propagate downstream instead of back directly towards the nozzle. This increases the loading on points which are not directly upstream of the jet.

Besides that, a higher stiffness also increases the stresses generated by the system.

Further recommendations are to model the UAV with a higher amount of nodes, in order to include more vibrational modes. As in the sensitivity analysis, it was observed that especially off-axis nodes suffer more from these acoustic loadings. Also, for the sound model, the actual reflectivity of the jet axis has to be further investigated, as this does have a large impact on the outputs of the model. This was also investigated during the sensitivity analysis. This especially has a large impact on the operations during the VAPOR mission.
The written code has been verified by implementing at least one of each standard unit test, which has been described in Section 6.1. Additional unit tests have been performed when necessary in order to help pinpoint bugs during the coding process and troubleshoot unexpected results.

9.6. Fuselage Structural Design *Author(s): Paul*

This section contains the structural sizing of the UAV fuselage (a 2m oval cylinder) and the nose cone (a 1.5m circular cone with a 175 mm base radius). Sizing is evaluated against yield, Euler column buckling, local skin-panel buckling, frame hoop yield, and frame web crippling under the main mission loads: axial compression during rocket-powered vertical takeoff, net recovery deceleration, and aerodynamic bending. Performance and mass margins are traded between aerospace aluminium (7075-T6) and carbon-fibre-reinforced PEEK (CF/PEEK).

9.6.1. Fuselage Cross-section and Nose Cone Properties

Although the fuselage cross-section seen later in Section 10.1 is not a perfect circle, it can be closely approximated for structural sizing as an ellipse, with a semi-major axis of $a = 175$ mm and a semi-minor axis of $b = 125$ mm. This oval shape matches the actual geometry far better than a circle, while still allowing the same structural sizing approach developed for circular fuselages. This method which will be used is the "boom" method idealisation with skin, longitudinal stringers, ring frames at intervals, where the circular section properties are simply reused with their elliptical equivalents.

Oval Fuselage

The nose cone, on the other hand, remains a circular cone, with its base radius set equal to the fuselage's semi-major axis ($R_{\text{base}} = a = 175$ mm). This means the top and bottom of the nose cone line up with the oval fuselage at the joint, while only its left and right sides taper inward slightly compared to the fuselage cross-section, as seen in Section 10.1. This is a convenient simplification, as the wings fold flat against the sides of the fuselage to minimise their effects in the folded configuration during take off. The main issue this solves is the high instability an exposed folding wing would create with marginal sideslip. Furthermore, the fuselage is at a length of 2 meters so that the wings do not extend behind the rear of the UAV, which would otherwise impose unnecessary thermal and aerodynamic loads to the wing tips.

Cross-Section Properties

Since the cross-section is now elliptical rather than circular, the simple closed-form expressions used for a circular fuselage no longer apply. Furthermore, the perimeter of an ellipse cannot be written as an exact formula. The same applies to the second moment of area of the skin around the ellipse. For this reason, these quantities are instead calculated through numerical integration. A point on the ellipse can be written as $(b\cos\theta,\ a\sin\theta)$. The length of one small segment of the ellipse is then given by Equation 9.71 and adding up all the steps around the full ellipse gives the perimeter in Equation 9.72.

The cross-sectional area is then the skin area and stringer "boom" areas, which is the same method done for circular fuselages:

$$ds(\theta) = \sqrt{(b\sin\theta)^2 + (a\cos\theta)^2}\, d\theta \quad (9.71) \qquad P_{\text{ell}} = \oint ds(\theta) \quad (9.72) \qquad A = P_{\text{ell}}\, t + N_s A_s \quad (9.73)$$

where t is the skin thickness, N_s the number of stringers, and A_s the area of one stringer.

For bending, the relevant section properties are the second moments of area I_{xx} and I_{yy}. Each is obtained by summing y^2 or x^2 over the same small steps used for the perimeter, plus the parallel-axis contribution of each stringer at its position (x_i, y_i):

$$I_{xx} = t \oint y(\theta)^2\, ds(\theta) + A_s \sum_{i=1}^{N_s} y_i^2, \quad (9.74) \qquad I_{yy} = t \oint x(\theta)^2\, ds(\theta) + A_s \sum_{i=1}^{N_s} x_i^2. \quad (9.75)$$

Stringer Placement

As a baseline for the structural design, the stringers will be spaced evenly along the perimeter, rather than evenly in angle, so that the skin panel width between adjacent stringer is the same all the way around to minimize flat-panel skin-buckling.

9.6.2. Loads

Takeoff Load

During vertical ascent the critical cross-section is loaded not by net thrust minus weight, but by the inertial load of the mass carried above that section. Applying d'Alembert's principle, the vehicle's net upward acceleration is calculated via Equation 9.76 so that the axial inertia load at a section carrying mass m_{above} above it is $m_{\text{above}} \cdot T/m_{\text{total}}$. The aerodynamic drag acting on the portion of the airframe above the section is also added, $D = \frac{1}{2}\rho V^2 S_{\text{ref}} C_{D0}$, giving the total takeoff axial load:

$$a = \frac{T}{m_{\text{total}}} - g \tag{9.76}$$

$$P_{\text{to}} = m_{\text{above}} \frac{T}{m_{\text{total}}} + D \tag{9.77}$$

For the cylinder base at the rear of the UAV, m_{above} is essentially the total vehicle mass minus the cylinder itself, so this load case is evaluated with $m_{\text{above}} \approx m_{\text{total}}$.

Landing load

Recovery is via a net, which decelerates the vehicle from its vertical approach speed v_{approach} to rest over the net's stretch distance s_{net}. The net itself is outlined later in Chapter 15. Treating this as a constant deceleration gives Equation 9.78 and the resulting axial inertial load:

$$a_{\text{landing}} = \frac{v_{\text{approach}}^2}{2 \cdot s_{\text{net}}} \tag{9.78}$$

$$P_{\text{land}} = m_{\text{above}} \cdot a_{\text{landing}} \tag{9.79}$$

The design axial load at each section is taken at the maximum load case of take off and landing, where in this case the landing phase is the limiting factor due to n_{landing} being around $4.9g$ and a safety factor of 2 is applied for determining deceleration results in an average value below the true peak deceleration.

Bending

Two independent bending moments are considered, acting in the pitch plane. Ascent aerodynamic bending arises because horizontal gusts during vertical ascent impose an effective angle of attack on the body. Both the dynamic pressure and the gust-induced angle of attack vary continuously throughout the ascent as the UAV accelerates from rest, hence a worst-case bending moment scenario is defined conservatively by combining the maximum expected gust angle α_{design} with the ascent dynamic pressure evaluated at the maximum ascent velocity V_{ascent}. The aerodynamic normal force is then obtained using the slender-body approximation formulated in Barrowman's research at NASA [47], in which the normal-force coefficient is $C_N \approx 2\alpha$, giving:

$$q = \tfrac{1}{2}\rho_{\text{air}} V_{\text{ascent}}^2. \tag{9.80}$$

$$N_{\text{aero}} = C_N \cdot q \cdot A_{\text{ref}} = 2q \cdot \alpha_{\text{design}} \cdot A_{\text{ref}} \tag{9.81}$$

where $A_{\text{ref}} = \pi ab$ is the elliptical frontal area. This is the standard form of $N = C_N qS$ with $C_N = 2\alpha_{\text{design}}$. Hence, The bending moment at the cylinder base, is presented in the following equation, where the moment arm is the full body length:

$$M_{\text{aero}} = N_{\text{aero}} \cdot L_{\text{total}}, \qquad L_{\text{total}} = L_{\text{cyl}} + L_{\text{nose}}. \tag{9.82}$$

Cruise wing-root bending arises once the vehicle transitions to fixed-wing flight, where the wing is mounted at the cylinder/nose cone junction, and the nose cone and forward fuselage act as a cantilevered mass under the cruise manoeuvre load factor n_{maneuver}. This contribution is the sum of the nose cone's own overhang moment and that of the cylindrical section ahead of the wing station using reiterated mass assumptions,

$$M_{\text{hang}} = m_{\text{nose}} \cdot n_{\text{maneuver}} \cdot g \cdot \frac{L_{\text{nose}}}{2} + m_{\text{cyl}} \cdot n_{\text{maneuver}} \cdot g \cdot \frac{L_{\text{cyl}}}{2} \tag{9.83}$$

Combined Load cases

The three previously mentioned load cases mostly do not occur simultaneously, as they correspond to different parts of the UAV mission phase. Hence, the three phases are evaluated separately for the maximum load case producing the highest internal stress, where the the total stress is calculated with the standard compression stress formula and bending flexure formula.

$$\sigma_{max} = \frac{P}{A} + \frac{Ma}{I_{xx}}, \tag{9.84}$$

In this case, a is used as it is maximum cross-sectional distance from the center axis ($y = \pm a$) and I_{xx} is the second moment of area about the horizontal axis which is the axis in direction of the maximum bending moment. The compression forces and bending moments are summarized in Table 9.17.

Table 9.17: Combined (P, M) load cases for the fuselage cylinder base.

Case	Phase	P [N]	M [N m]
Ascent	Powered vertical ascent	617.4	$M_{\text{aero}} = 504.2$
Landing	Net recovery	2911.7	N/A
Cruise hang	Fixed-wing cruise	N/A	$M_{\text{hang}} = 138.4$

For the current design, the ascent phase dictates the highest stress despite its lower axial load, as M_{aero} is more than three times larger than M_{hang}.

9.6.3. Failure Modes

For a given combination of skin thickness, stringer layout, frame spacing, and frame size, the design must survive every load case presented in Subsection 9.6.2 without failing. Each failure mode below gives a load capacity that must be multiplied by at least the safety factor SF.

Axial and combined bending yield

The simplest check is that the material itself does not yield under the applied stress. A is the cross-sectional area from Subsection 9.6.1. When bending is also present, the stress from Subsection 9.6.2, must also stay below yield:

$$\sigma = \frac{P}{A}, \tag{9.85}$$

$$SF \cdot \sigma_{\max} \le \sigma_y, \tag{9.86}$$

where $\sigma_{\max}$ from Equation 9.84 is evaluated for each of the three load cases in Table 9.17, and the critical value is used.

Euler column buckling.

The fuselage can also fail by buckling as a whole, like a column, before the material itself yields. The critical buckling load is

where $L_e = k_e L$ is the effective column length, as k_e accounts for the end-support conditions. $I_{\min}$ is the smallest second moment of area of either the horizontal or vertical axis, as the fuselage buckles about whichever axis it is least stiff in. The structure is safe from global buckling provided

$$P_{cr} = \frac{\pi^2 E I_{\min}}{L_e^2} \tag{9.87}$$

$$P_{cr} \ge SF \cdot P \tag{9.88}$$

Local skin-panel buckling

Between two adjacent stringers and two adjacent frames, the skin forms a flat rectangular panel of width b_s (the stringer pitch) and length a_f (the frame spacing). Under the axial compressive stress, this panel can buckle locally even if the overall fuselage does not. Treating it as a simply-supported flat plate, the critical buckling stress is shown in Equation 9.89. k is the plate buckling coefficient, which depends only on the panel's aspect ratio b_s/a_f and is minimised over the number of buckling half-waves m:

$$\sigma_{cr} = \frac{k\pi^2 E}{12(1-\nu^2)} \left(\frac{t}{b_s}\right)^2 \tag{9.89}$$

$$k = \min_m \left(m \frac{b_s}{a_f} + \frac{a_f}{m\, b_s} \right)^2. \tag{9.90}$$

For a long panel where frame spacing is a lot larger than panel width, a k value of 4 is the standard result for an infinitely long simply-supported plate. The panel is safe provided $\sigma_{cr} \ge SF \cdot \sigma_{\max}$, using the largest stress due to compression or bending.

Frame hoop yield

Because the skin is curved, an axial compressive stress σ produces an inward radial pressure on the ring frames. Over a bay of length a_f, this results in a hoop force in the frame of $N_{\text{hoop}} = \sigma\, t\, a_f$, which is independent of the local radius of curvature. The corresponding frame stress is $\sigma_f = N_{\text{hoop}}/A_f = \sigma\, t\, a_f/(h_f w_f)$, which must satisfy $SF \cdot \sigma_f \le \sigma_y$.

Frame web crippling

The frame's web (the radial-depth part of its blade cross-section) can itself buckle locally under this hoop stress, in the same way the skin panels can. Treating the web as a plate with one free edge ($k = 0.43$), the critical stress is

$$\sigma_{cr,fw} = \frac{0.43\pi^2 E}{12(1-\nu^2)}\left(\frac{w_f}{h_f}\right)^2. \tag{9.91}$$

Together, these five checks (yield, global Euler buckling, local skin buckling, frame hoop yield, and frame web crippling) define the feasible design space. The structure can then be designed to optimize skin thickness, stringer count and size, and frame count and size, selecting the lightest combination that satisfies all failure modes simultaneously.

9.6.4. Thrust Frame Sizing

The thrust frame transfers the engine thrust load from the combustion chamber flange into the fuselage stringers. Using the strut-based load-path methodology detailed by Kulkarni [61], the thrust frame will consist of a central engine ring bolted to the combustion chamber flange, from which N inclined struts radiate outward at an angle θ from the body axis to attachment points on the fuselage stringers.

Strut sizing

The design axial load P is shared equally among the N struts. Equations related to the strut sizing are placed below.

$$F_{\text{leg}} = \frac{P}{N\cos\theta}, \tag{9.92}$$

$$\frac{F_{\text{leg}}}{A_{\text{leg}}} \le \frac{\sigma_y}{SF}. \tag{9.93}$$

$$P_{cr} = \frac{\pi^2 EI}{(KL_{\text{leg}})^2}, \tag{9.94}$$

Each strut is a thin-walled circular tube of outer diameter d and wall thickness t_w. Two checks size the tube. First, the axial compressive stress must stay below yield.

Second, the strut must not buckle as a column. With a fixed-pinned end condition ($K = 0.7$) and strut length $L_{\text{leg}} = H_{\text{frame}}/\cos\theta$, the Euler critical load uses the same formulas as in Equation 9.87.

Engine ring sizing

The radial components of the strut forces load the engine ring in hoop. For N equally-spaced radial point loads on a ring of radius R_{eng}, the resulting hoop force is

$$N_{\text{hoop}} = \frac{F_{\text{leg,radial}}}{2} R_{\text{eng}} \cot\left(\frac{\pi}{N}\right). \tag{9.95}$$

The ring's radial width is then sized so that the hoop stress $\sigma_{\text{ring}} = N_{\text{hoop}}/A_{\text{ring}}$ stays within the material allowable.

Thermal considerations

The engine combustion chamber wall reaches temperatures well above the threshold of common aluminium alloys (around 150 °C). Since the selected frame material is aluminium, a ceramic fibre thermal break or ablative coating between the engine face and the strut attachment points is required to prevent local strength degradation.

9.6.5. Material Properties

Two materials are used for the fuselage structure, selected based on both structural performance and centre-of-gravity requirements. The 2 m cylindrical fuselage section is manufactured from carbon-fibre-reinforced PEEK, while the 1.5 m nose cone uses aerospace aluminium alloy 7075-T6. The motivation for this split is discussed in detail in the stability chapter. In summary, the UAV requires its centre of gravity to sit sufficiently far forward for longitudinal stability, and using the lighter CF/PEEK for the long aft cylinder reduces the structural mass where it would otherwise pull the cg rearward. However, since it is possible to create a stable design with an aluminium nosecone, aluminium is hence chosen for this part as the Aluminium alloy wins the trade-off presented in the midterm report [1] due to it being significantly more cost-effective and sustainable.

9.6.6. Final Structural Design

To determine an optimized structural design, all combinations of skin thickness, stringer count, and frame count are taken into account, selecting the lightest design that satisfies all five failure modes from Subsection 9.6.3 simultaneously, under the load cases of Subsection 9.6.2. The optimal design parameters for the CF/PEEK cylinder are summarised in Table 9.18, and the resulting margins of safety in Table 9.19. The nose cone reuses the same skin thickness, stringer layout, and frame cross-section as the cylinder, since the stringers and frames are assumed to run continuously through the joint.

Table 9.18: Optimal structural design parameters for the fuselage cylinder (CF/PEEK).

Parameter	Value	Unit
Skin thickness t	0.80	mm
Stringers N_s	12	–
Stringer section ($h \times w$)	10×2.0	mm
Stringer pitch b_s	79.1	mm
Ring frames (total)	2	–
Frame spacing a_f	1000	mm
Frame section ($h \times w$)	10×1.5	mm

Table 9.19: Failure-mode margins of safety for the optimal cylinder design (MS = load capacity/($SF \cdot$load) − 1, $SF = 1.5$).

Failure mode	Margin of Safety
Global Euler column buckling	132.667
Local skin-panel buckling	0.015
Frame hoop yield	0.137
Frame web crippling	0.065
yield stress	24.595

The nose cone is manufactured from aerospace aluminium (Al 7075-T6) and shares the same skin thickness, stringer cross-section, stringer count, and frame pitch as the cylinder, as the stringers and frames run continuously through the joint, meaning no geometric discontinuity is introduced. however, The material changes at the joint, as the cylinder uses CF/PEEK while the nose cone uses Al 7075-T6. Structural checks are evaluated at the nose cone base, the critical section with the largest cross-section and highest inertial load. The tapering geometry ensures that if the base is structurally sufficient, the rest of the cone is inherently safe, as both the applied loads and the cross-sectional dimensions reduce toward the tip. Global Euler column buckling is not checked, as it is not a meaningful failure mode for a short tapered cone.

The critical failure modes are local skin-panel buckling (MS = 0.015) and frame web crippling (MS = 0.065), both of which are satisfied with a positive but small margin, indicating a near-optimal design. The large Euler buckling margin (MS = 132.667) confirms that global column instability is not a concern for this cross-section, and the large yield stress margin (MS = 24.595) shows that the material is far from yielding, meaning the design is entirely stiffness-driven rather than strength-driven. Hence, the structural mass breakdown is as follows:

Table 9.20: Structural mass breakdown.

Component	Mass [kg]
Fuselage cylinder (CF/PEEK, 2.0 m)	3.162
Nose cone (Al 7075-T6, 1.5 m)	2.890
Total structural mass	**6.052**

9.7. Aerodynamic Analysis of the Full Configuration *Author(s): Duco*

Now that the full external layout of the aircraft has been defined, a more detailed study can be performed into the two integrated aerodynamic properties that drive the cruise performance: the zero-lift drag coefficient C_{D_0} and the Oswald span efficiency factor e. Where the airfoil and wing optimisation of Section 9.1 produced the sectional and planform performance in isolation, this section closes the loop by assembling the sized wing, fuselage and Y-tail into a single aircraft and extracting the configuration level drag polar that the performance and sizing routines consume in the form

$$C_D = C_{D_0} + \frac{C_L^2}{\pi A_w e}, \tag{9.96}$$

with A_w the wing aspect ratio. The analysis is carried out in AeroSandbox [62, 63], using its AeroBuildup method for the aerodynamics.

9.7.1. Method

Aerobuildup is a component drag build-up: it evaluates each lifting surface and the fuselage separately and sums their contributions. Every wing, tail and fin section is assigned its viscous profile drag by NeuralFoil[9], which is a similar analysis tool to that which underlies the airfoil work of Subsection 9.1.3. The fuselage is treated with a slender body model: turbulent flat plate skin friction scaled by a form factor for its fineness ratio, plus a blunt-base drag term for the aft end of the aircraft. The airfoil used is the one optimised for in Subsection 9.1.2 and is used for the wing. A symmetric NACA0012 airfoil is used for the fins.

Since AeroBuildup returns the total drag $C_D(\alpha)$, in which the parasite drag and the drag due to lift are already mixed, the two must be separated by fitting the drag polar. The angle of attack is swept over $\alpha \in [-12°, 12°]$ at the cruise condition, and the resulting polar is fitted using the least squares method to the quadratic of Equation 9.96, written as $C_D = C_{D_0} + k\,C_L^2$. The fit is restricted to the attached flow part $C_L \in [0.2, 1.1]$: outside this range, the polar is not a clean parabola any more, which would give invalid results.

The zero-lift drag C_{D_0} is then the intercept of this fit, and the induced factor k yields the Oswald efficiency directly from its definition as seen in Equation 9.97.

$$k = \frac{1}{\pi A_w e} \tag{9.97}$$

Equation 9.97 is referenced to the wing aspect ratio. Since k is extracted from the full viscous polar rather than a purely inviscid one, the e obtained is an effective span efficiency: it lumps the inviscid trailing vortex induced drag together with the viscous rise of section drag with lift into the single factor that Equation 9.96 expects, and is consequently below unity.

One thing that has to be noted, however, is the fact that the wing airfoil is cambered: its minimum drag does not occur at $C_L = 0$ but at a positive $C_{L,\min D}$, and the intercept of Equation 9.96 is therefore a slightly off-design extrapolation that the aircraft never actually flies at. The intercept is nonetheless the quantity that every $C_D = C_{D_0} + kC_L^2$ performance relation assumes, so it is the value passed downstream. For transparency, the true drag bucket is also fitted in the shifted form $C_{D,\min} + k_2(C_L - C_{L,\min D})^2$, giving a camber-free measure of the lift penalty about the design point.

9.7.2. Results

Applying the AeroBuildup methodology at the design cruise conditions (velocity of 20.3 m/s at an altitude of 2500 m, corresponding to a cruise C_L of 1.11) yields the baseline aerodynamic properties for the clean airframe. Extracting the intercept and the induced factor from the quadratic fit described above gives the following performance coefficients:

- **Zero-lift parasite drag coefficient (C_{D_0}):** 0.0359
- **Effective Oswald span efficiency (e):** 0.801

These extracted values encapsulate both the parasite and induced drag characteristics of the integrated configuration. Because they represent the baseline aerodynamic performance of the full aircraft, these two parameters are passed directly to the downstream sizing and performance routines.

9.7.3. Recommendations and Sensitivity

The cruise performance of the aircraft is driven mostly by the two integrated coefficients extracted above, so it is worth noting how sensitive the design is. Because C_{D_0} sets the floor of the drag polar, an absolute error in the parasite drag propagates almost linearly into the cruise drag and therefore directly into the achievable range and endurance through the L/D at the cruise lift coefficient. The Oswald efficiency e has a weaker effect near the low-C_L design point but grows quadratically with lift, so it's role is most important in the sensitivity during the high load manoeuvring and pull-up phases of the mission rather than steady cruise. Within the build-up itself, the largest contributors to uncertainty are the fuselage form factor, the blunt base drag term and the absence of any wing, fuselage and tail interference, all of which are first-order modelling choices rather than converged results. The sizing loop is consequently most linked to the fuselage and base drag assumptions, and a conservative margin on C_{D_0} is justified until they are verified.

[9] NeuralFoil [Date Accessed: June 17]

10 | Configuration & Internal Layout

This chapter presents the configuration and internal layout of the UAV, translating the subsystem designs into a single integrated arrangement. Section 10.1 first establishes the overall configuration and three-view drawing of the vehicle. Section 10.2 then estimates the longitudinal centre of gravity and weight distribution across the rocket-ascent and electric-cruise phases, which drives the placement of the major components. Finally, Section 10.3 details the internal layout, showing how the components are stacked along the tail-sitter's longitudinal axis to balance the cg and keep hazardous systems separated.

10.1. Overall Configuration and Three-View Drawing *Author(s): Ivan*

The overall external configuration of the VAPOR UAV is presented in the technical drawing Figure A.1 included in Appendix A. The drawing contains the top, rear and right-side orthographic views, together with isometric representations of the aircraft in both the unfolded-wing and folded-wing configurations.

10.2. Centre of Gravity and Weight Distribution *Author(s): Paul*

The longitudinal cg was estimated by summing the moment of every major component about the rear of the vehicle and dividing by the total mass,

$$x_{\mathrm{cg}} = \frac{\sum_i m_i \, x_i}{\sum_i m_i}, \tag{10.1}$$

where m_i is the mass of each component and x_i its distance from the rear. Two configurations were assessed, because both the wing position and the propellant mass change in flight. In the rocket-ascent phase the wings are folded and the tanks are full, while in the electric-cruise phase the wings are deployed and the tanks are empty. The masses and stations used are listed in Table 10.1.

The estimation gives a cg at 1.68 m from the rear during the rocket-ascent phase, at a total mass of 30.67 kg, moving forward to 1.94 m during electric cruise, at 24.63 kg. The propellant burn and wing deployment therefore shift the cg forward by roughly 0.27 m over the mission, which is later accounted for in the stability and control analysis in Chapter 11.

Furthermore, it is critical to note the fact that the total takeoff mass has been overestimated by previous analyses which placed the figure at 34kg. Due to time constraints executing a complete iterative overhaul of performance models is currently unfeasible, with a full iteration being required for recalculating the maximum flight altitude reached by the now lighter configuration to give but one starting step in the iteration process. Consequently, in order to comply with scheduling constraints while ensuring a conservative margin of safety, in subsequent analyses, the maximum take off mass is assumed to be 34 kg in Chapter 12.

10.3. Internal Layout and Component Placement *Author(s): Paul*

As a tail-sitter, the UAV stacks its components along the longitudinal axis, ordered to balance the cg, keep hazardous components separated. Hence, the internal layout is shown in Figure 10.1, where the internal component locations in the figure stem from the estimated individual cg locations presented in Table 10.1.

The rocket engine, thrust frame, and Y-tail sit at the rear. Ahead of them are the propellant and pressurant tanks, grouped close to the cg to maintain static stability as they empty. They cannot be moved further forward without overlapping the wing folding mechanism, which sets the forward limit of the tank group.

The wing, folding mechanism, Parachute, and wing actuators are placed near mid-body at the cg, so deploying the wings causes only a small cg shift. The battery, avionics, and payload occupy the forward section, and the electric motor and folding propeller are mounted at the nose.

Table 10.1: Component masses and longitudinal stations used for the cg estimation.

Component	Distance from rear [m]	Mass [kg] Cruise	Mass [kg] Ascent
Rocket engine (injector + valves)	0.05	1.614	1.614
Tail	0.10	0.616	0.616
Tail actuators	0.10	0.315	0.315
Thrust frame	0.12	0.036	0.036
Engine pipes	0.69	0.050	0.050
Fuselage	1.00	3.162	3.162
Helium tank	1.20	0.400	0.437
Fuel tank	1.33	0.170	1.370
Oxidiser tank	1.55	0.290	5.090
Parachute System	1.80	0.950	0.950
Wings*	2.00	5.380	5.380
Wing actuators	2.00	0.210	0.210
Folding mechanism	2.15	2.938	2.938
Battery	2.50	1.620	1.620
Payload	2.80	3.000	3.000
Nose cone	2.83	2.890	2.890
Flight controller	3.10	0.100	0.100
ESC	3.38	0.050	0.050
Motor	3.40	0.590	0.590
Avionics	3.50	0.200	0.200
Yoke	3.50	0.020	0.020
Propellers	3.50	0.032	0.032
Total		**24.63**	**30.67**

*The wings are at 2.00 m when deployed (cruise) and fold back to 1.00 m in the ascent configuration.

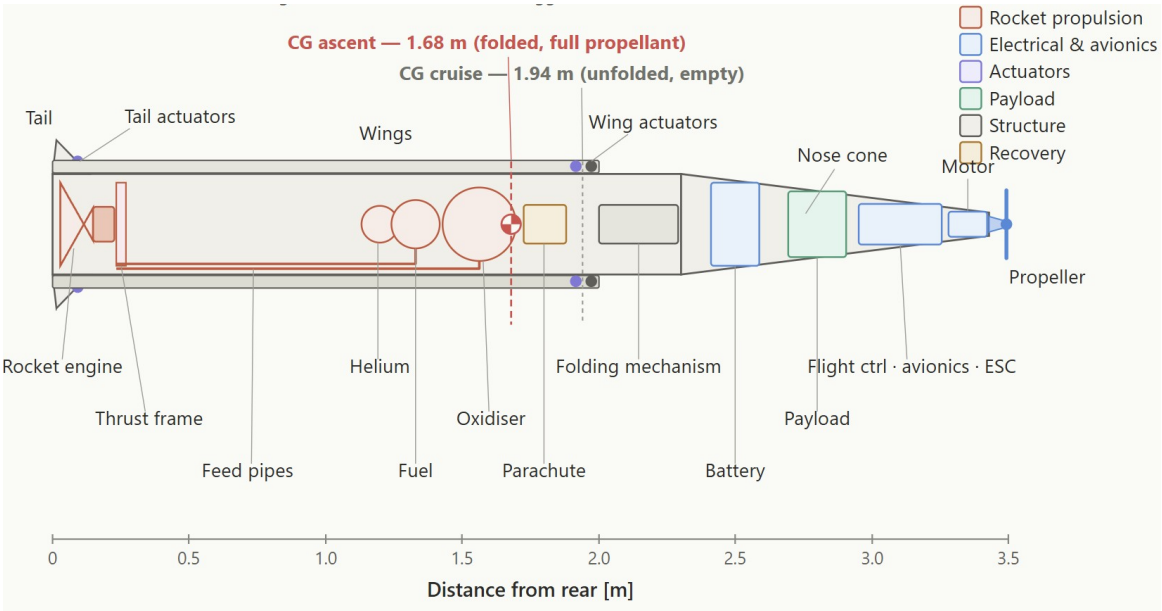

Figure 10.1: Internal Configuration Visualization generated by Claude

11 | Stability & Control

This chapter provides a detailed overview of the stability and control analysis for all mission phases. Section 11.1 follows the stability theory and methodology used for ascent and cruise, while in Section 11.2 the critical mission phase is defined. Furthermore, the control analysis is performed in Section 11.3. Lastly, results are presented in Section 11.4 and discussed with an analysis of the limitations in Section 11.5.

11.1. Stability Analysis Methodology *Author(s): Victor*

This section presents background information on the stability and control aspects of the UAV design. Ensuring both controllability and stability across all operational phases is critical for the VAPOR mission, given the inherent challenges associated with transitioning from a traditional rocket to a fixed-wing UAV.

11.1.1. Rocket Phase Stability Theory

Static stability refers to the ability of the rocket to maintain its attitude during ascent when perturbed by a small increase in angle of attack, $\alpha + d\alpha$. One may again refer to Figure 12.1. The condition that the rocket must fulfil is straightforward: the centre of pressure of the rocket, defined as the point through which the resultant aerodynamic force acts, must be located behind the centre of gravity. The reasoning is as follows. Suppose that α increases by a small amount, $d\alpha$, due to a disturbance. This causes the normal component of the resultant aerodynamic force to increase by a small amount, dF_n, which in turn generates a small clockwise, or pitch-down, restoring moment. This restoring moment counteracts the increase in the angle of attack α and drives the rocket back towards equilibrium. If, instead, the centre of pressure were located in front of the centre of gravity, the moment generated by dF_n would be counter-clockwise, or pitch-up, thereby further increasing the disturbance and rendering the rocket statically unstable.

11.1.2. Cruise Stability Theory

Static stability for any aircraft is fundamentally governed by the balance of forces and moments, such that, following a disturbance in the angle of attack, $d\alpha$, the aircraft or UAV naturally generates a pitch-down response to counteract the disturbance. The condition that the aircraft must satisfy is that the neutral point must lie behind the centre of gravity of the aircraft. A more rigorous derivation is provided by Mulder et al. [64], and the reader is encouraged to consult it for further details.

11.2. Stability Intermezzo *Author(s): Victor*

The previous two subsections have presented the main requirements that an arbitrary rocket or aircraft must meet in order to be longitudinally statically stable. Thus, it is hard to come up with a design that performs well in both flight regimes. For instance, a normal rocket would need relatively small fins to move the centre of pressure backwards, whereas a typical UAV would require a larger tail area to produce a balancing moment.

It is important to mention that the most critical phase of the entire flight profile is the transition between the rocket ascent and cruise phase. This transition consists of highly non-linear changes in pitch angle, pitch rate, centre of pressure, lift and drag distributions and thrust. A separate discussion with assumptions will be treated Subsection 11.5.1, but it is a good moment to acknowledge these problems.

11.3. Control and Transition Manoeuvre *Author(s): Victor, Marco*

This section will treat the control mechanism of the transition manoeuvre between the rocket ascent phase and the cruise phase, as part of the flight profile of the VAPOR mission.

11.3.1. Assumptions

As mentioned in the previous section, the control manoeuvre for the VAPOR mission consists of non-linear changes in the centre of pressure, lift, drag, and inertia. To model these changes and design a controller capable of tracking the reference pitch angle associated with the trajectory selected by the ground station, a simulation was developed in Simulink, using MATLAB for the implementation of the underlying modelling and control logic. The choice for this comes down to a simple requirement: it simplifies tuning and creating a cascaded controller architecture in a visual way.

For the rest of this chapter, all assumptions outlined in Chapter 12 remain valid. Additionally, the following assumptions for control (AC) are added:

- **AC-01: Steady level flight after transition.** After the transition phase, the UAV is assumed to continue in steady, level flight. As such, translational and rotational accelerations are neglected in the cruise condition.
- **AC-02: Negligible inertia variation due to wing deployment.** The change in inertia caused by the folding-wing deployment mechanism is neglected.
- **AC-03: Resultant control moment model.** The moment generated by the control surfaces is modelled as a resultant pitching moment acting about the centre of gravity, given by

$$M_{\text{control}} = C_{m_\delta} \delta \frac{1}{2} \rho V_\infty^2 S_h l_h. \tag{11.1}$$

  where C_{m_δ} represents the derivative of the moment coefficient with respect to deflection angle of the control surface δ [64], l_h is the distance between the aerodynamic centre of the tail and the centre of gravity and S_h is the surface area of the horizontal stabiliser. This analysis assumes that the tail always has a zero angle of attack with respect to incoming flow.
- **AC-04: Linear propellant mass depletion.** The change in mass due to propellant burn is assumed to vary linearly with time according to

$$m(t) = m_{\text{initial}} - \dot{m} t. \tag{11.2}$$

- **AC-05: Negligible inertia change due to propellant burn.** The change in inertia during the propellant burn is approximately $0.2\,\text{kg}\,\text{m}^2$ and is therefore neglected in the control model.
- **AC-06: Availability of pitch feedback.** The IMU is assumed to provide reliable pitch angle and pitch rate feedback to the controller.
- **AC-07: Neglected aerodynamic force variation with angle of attack.** Variations of the aerodynamic forces with respect to the angle of attack are neglected in the cruise control model.
- **AC-08: Pitching moment contributions.** The only moments acting on the UAV are assumed to be the control moment, the moment generated by the resultant aerodynamic force, and the pitch damping moment M_q.
- **AC-09: Control surface deflection limit.** The maximum deflection angle provided by the control surfaces is limited to $\pm 12°$.
- **AC-10: Simplified drag model.** Drag is represented using a constant tangential-force coefficient, and detailed contributions such as base drag, skin-friction drag, pressure drag, and induced drag are not modelled separately.
- **AC-11: Ideal actuator response.** The control surface deflection commanded by the controller is assumed to be achieved instantaneously, apart from the imposed saturation limit. Actuator dynamics, rate limits, backlash, and time delays are neglected.
- **AC-12: Ideal state feedback.** The pitch angle and pitch rate signals used by the controller are assumed to be noise-free and delay-free. Sensor noise, filtering delay, bias, and measurement uncertainty are neglected.
- **AC-13: Simplified transition condition.** The transition from ascent to controlled cruise is triggered by altitude only. The effects of deployment time, aerodynamic transients, structural flexibility, and unsteady flow during transition are neglected.

11.3.2. Methodology Behind the Control Mechanism

To be able to design the controller, the entire flight profile needs to be modelled. A simplified software flow diagram is presented in figure Figure 11.1. The simulation begins with calculating the mass and atmospheric properties at each time step, feeding the information in the *calculate forces and moments* block, which is then fed into the 3 Degrees of Freedom (DoF) block. This block outputs velocity along the horizontal and vertical body axis, pitch rate, pitch angle, altitude and horizontal position.

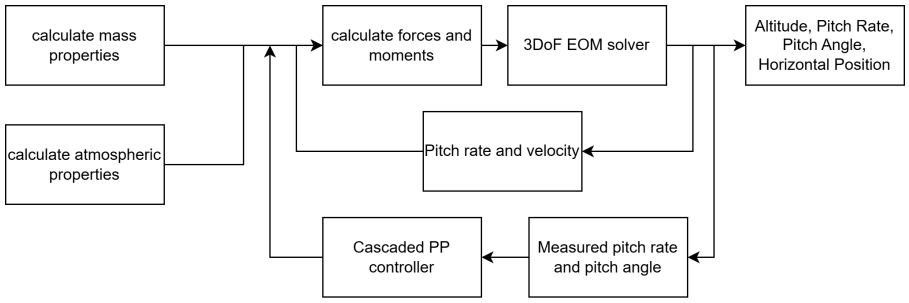

Figure 11.1: Simplified software block diagram

There exists a double feedback loop. The velocity and pitch rate are used to recalculate the new forces and moments at the next time step. Additionally, the pitch rate is also used together with the pitch angle in the cascaded proportional-proportional (P-P) controller feedback loop, to calculate the required control moment needed to hold a desired pitch angle θ_{ref}.

To comply with the altitude requirements, the controller engages at target altitude $h_{target} = 2500$ m. This also represents the moment the wings are deployed, and thrust starts to be generated by the propeller. This change in the dynamics of the plant is assumed to be instantaneous, which would introduce a discontinuity in the state variables. This problem is deemed acceptable for the initial controller design, and the issue shall be addressed at later stages. Figure 11.2 shows the controller block diagram. The ground station selects a desired pitch angle which the UAV should reach at the end of the transition. A good initial θ_{ref} would be the cruise angle of attack, as it would point the UAV in the correct attitude to produce enough lift to maintain steady-level flight, thus, $\theta_{ref} = 5.7°$.

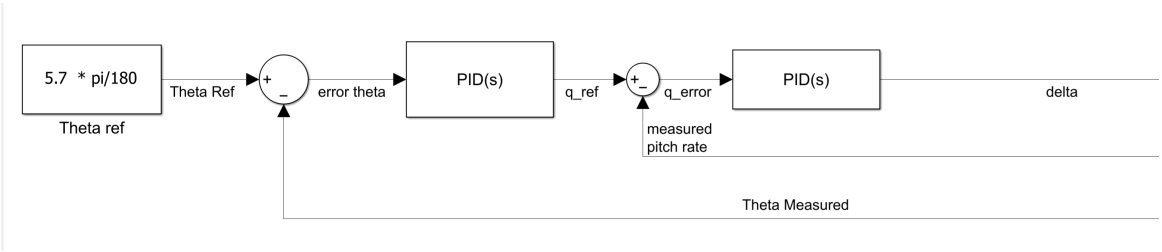

Figure 11.2: Proportional-Proportional Controller

A cascaded P-P controller was chosen due to the combined ease of tuning for the gains $K_{outer} = K_1$ and $K_{inner} = K_2$, combined with good results in tracking θ_{ref}. The output of the outer loop controller represents the desired pitch rate q_{ref} needed to mitigate the error in pitch angle. This is then combined with the measured pitch rate q_{mes} to produce the desired deflection of the control surfaces needed to create a moment around the centre of gravity to hold θ_{ref}. Due to the non-linear relationships between the plant and the controller, the gains have been tuned manually in the time domain, by first tuning the inner loop gain and then the outer loop gain. The following equation shows the feed-forward loop output, bounded by the maximum deflections of the control surfaces :

$$\delta = [(\theta_{ref} - \theta_{mes})K_1 - q_{mes}]K_2 \ \forall \delta \in [-0.21, 0.21] \text{ rad} \tag{11.3}$$

From this equation, it's possible to calculate the deflection and, therefore, the hinge moment where the control surfaces are attached. From Chapter 8, for the control surfaces, a servo that can sustain a torque of 3 Nm for each fin is selected, meaning that the total hinge moment that can be applied, considering 2 fins for controllability, is 6 Nm.

$$H_e = SF \cdot H_{\text{e,max}} = C_{h_e} \frac{1}{2} \rho V_\infty^2 S_e c_e \cos\Gamma \tag{11.4}$$

where C_{h_e} is the hinge moment coefficient, S_e is the control surface area, c_e is the control surface mean

chord and Γ is the dihedral angle. An equation can be found for the product of surface area and chord of the control surfaces.

$$S_e c_e = S_h \frac{S_e}{S_h} c_h \frac{c_e}{c_h} = \frac{2SFH_{\text{e,max}}}{C_{h_\delta} \delta \rho V_\infty^2 \cos\Gamma} \tag{11.5}$$

This equation can be used to size the control surfaces; they should be small enough such that at maximum speed, the hinge does not fail because of extreme torques.

11.4. Results *Author(s): Victor, Marco*

In this section, the results of the control architecture will be presented, alongside a discussion and further recommendations. The most important plot that needs to be shown is the trajectory along a flat earth, which can be seen in fig. 11.3c. This plot conveys the core idea of the VAPOR mission: fast climb to target altitude and then a cruise phase. Some details need to be explained. The following simulation continues with a pitch angle of 5.7°, which in reality would change to the trim condition of the UAV, which has not been modelled for this conceptual design.

Figure 11.3a and Figure 11.3b show the behaviour of the error for the pitch angle and pitch rate, respectively. This shows that gain tuning has been done correctly. The transients converge to 0, while the pitch angle shows a critically damped behaviour and the pitch rate a damped one, with a slight overshoot, as expected.

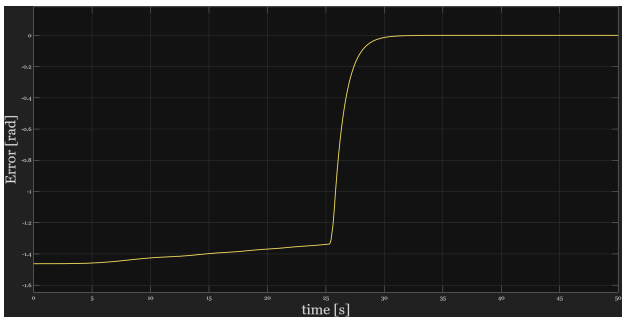

(a) Pitch angle error

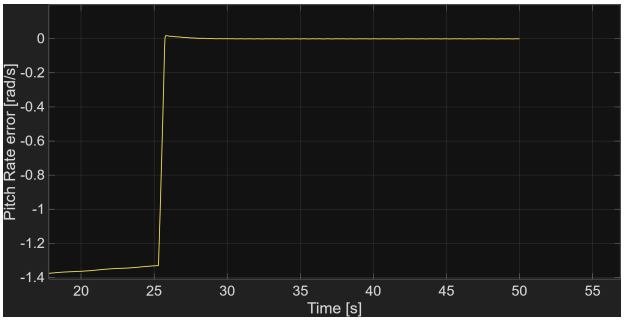

(b) Pitch rate error

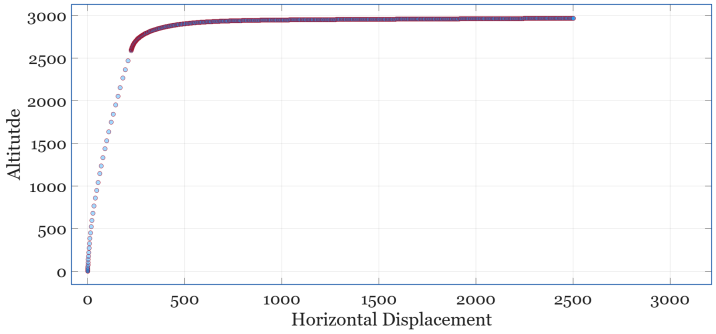

(c) Trajectory of the UAV

Figure 11.3: Pitch angle, Pitch rate and trajectory plots

To size the control surfaces, Equation 11.5 can be used. To do this, various values need to be assumed, these are reported in Table 11.1.

Table 11.1: Calculated and assumed values

Parameter	$H_{e,\text{max}}$	C_{h_δ}	V_{max}	ρ	δ_{max}	Γ	c_e
Value	6	-0.5	140	0.95	12	30	0.0657
Unit	Nm	1/rad	m/s	kg/m^3	deg	deg	m

The control surfaces are assumed to have a chord length equal to 30% of the tail's chord length, and a safety margin of 0.6 is chosen. Consequently, Equation 11.5 can be used to size the control surfaces area. This

yields Equation 11.6

$$S_{\text{e,max}} = 0.296 \cdot S_h = 0.065\ m^2 \tag{11.6}$$

This value is perfectly reasonable as it means that roughly 30% of the total tail's surface area will be occupied by control surfaces, while also taking into account a conservative safety factor and fulfilling control requirements.

11.5. Discussion and Limitations *Author(s): Victor, Marco*

The simulation indicates that the UAV remains statically stable throughout the mission and that the transition manoeuvre is feasible. The controller achieves satisfactory trajectory tracking, while controllability is provided by the fins and attached control surfaces. Their sizing is realistic when compared with conventional aircraft [65].

However, the analysis is limited by several assumptions. The aerodynamic coefficients are assumed constant, neglecting variations with Mach and Reynolds numbers. The angle of attack during ascent is assumed to remain small, and wing deployment is modelled as instantaneous, meaning that transient aerodynamic effects and altitude or velocity losses are not included. In addition, the model is limited to a 3-DoF rigid-body analysis, which restricts the assessment of lateral-directional motion and potential instabilities, as discussed in Section 7.5.

Future work should focus on integrating a 6-DoF model, improving the controller fidelity, and validating the aerodynamic coefficients through flight and wind-tunnel testing. For full-scale production, the model should also include wind-gust effects, roll control, 6-DoF equations of motion, and a more advanced predictive controller.

11.5.1. Sensitivity Analysis

A sensitivity analysis was conducted in order to better understand the behaviour of the UAV during the ascent and transition phase. Due to project limitations, not all results will be presented, but the methodology will be outlined.

The initial pitch angle of the UAV during ascent is perhaps the most important variable that shall be stress tested. For values lower than 89 deg, it has been found that the UAV cannot reach target altitude. The second most important parameters are the two gains used to tune the controller. It has been found that gains above $K_1 = K_2 \geq 1$ require the maximum deflection angle throughout the entire manoeuvre, which shows poor modelling of the controller.

12 | Flight Performance Analysis

This chapter provides a detailed analysis of the UAV's performance throughout all flight phases, these are: vertical take-off and ascent, cruise, and glide. Firstly, the methodology for the analysis is described in Section 12.1, subsequently the results are presented in Section 12.2. Lastly, in Section 12.3, the results, with the appropriate limitations, are discussed.

12.1. Methodology *Author(s): Vladimir, Marco, Victor*

This section provides a detailed explanation of the methodology employed in the analysis of the UAV's flight performance. Firstly, vertical take-off and ascent will be treated, subsequently cruise performance will be assessed, and lastly, gliding flight will be analysed.

12.1.1. Vertical Take-Off and Ascent

Vertical take-off and ascent is a crucial mission phase that extends from engine ignition at take-off up until the attainment of horizontal flight, with the wings fully deployed and the propeller engaged. This mission phase is characterised by 2 main sub-phases: the powered phase is sustained by the liquid bi-propellant engine analysed in Chapter 7, while the coasting phase is unpowered and characterised by trading vertical velocity with altitude, and attaining the horizontal attitude necessary for cruise.

The purpose of the analysis is mainly to determine the maximum altitude that the UAV can reach given a certain amount of propellant. For this, a Python code was developed which numerically integrates the equations of motion via a fourth order Runge-Kutta scheme. Results were also validated with a simulation developed in Simulink. The following assumptions were made in order to perform these calculations.

- **A1** **Initial Conditions:** The UAV is launched from rest with zero initial velocity and an initial pitch angle (θ).
- **A2** **Thrust Alignment:** Thrust is assumed to be aligned with the centre of gravity, in the body reference frame.
- **A2** **Aerodynamic Forces:** The resultant aerodynamic force is decoupled in components along the body-axis.
- **A4** **Engine Model:** Engine performance parameters are obtained from Chapter 7.
- **A5** **Rigid body:** The UAV is modelled as a 3 DoF rigid body, where rotational motion is considered only around the pitch axis, y_b, as introduced in Figure 12.1.
- **A6** **Constant Aerodynamic Coefficients:** Mach and Reynolds number effects on aerodynamic forces are neglected.
- **A7** **Lift Induced Drag:** The tangential component of the aerodynamic force is modelled with a constant tangential force coefficient.
- **A8** **Thrust Dependence:** Thrust is assumed to depend only on altitude; chamber pressure fluctuations and engine ramp-up time are neglected.
- **A9** **Atmospheric Model:** Atmospheric properties are modelled through the ISA [1].
- **A10** **Flat Earth:** Earth radius is neglected in the equations of motion.
- **A11** **Non-Rotating Earth:** Earth rotational rate is neglected in the equations of motions, therefore assuming the Earth reference frame (E-frame) to be inertial. This frame is composed of the following axis: z-axis pointing towards the center of the Earth, x-axis is pointing north and y-axis pointing east.
- **A12** **Constant Gravity:** Gravitational acceleration is assumed constant throughout the trajectory.
- **A13** **No gusts:** Wind gusts are neglected.
- **A14** **Constant Centre of Pressure:** The location of the centre of pressure is assumed constant when the control surfaces are not deflected.
- **A15** **Total take-off mass:** The mass of the UAV at take off is assumed to be 34kg as per the assumptions of Section 10.2.

To visualise the vehicle's dynamics during the rocket ascent phase, a free body diagram is provided in Figure 12.1. This diagram illustrates the rigid-body forces and moments acting within the body-fixed reference frame, F_b. Because F_b is non-inertial, solving the equations of motion requires transforming the vectors into the vehicle-carried, Earth-fixed reference frame, F_E [64].

[1] ISA Model [Date Accessed: June 14]

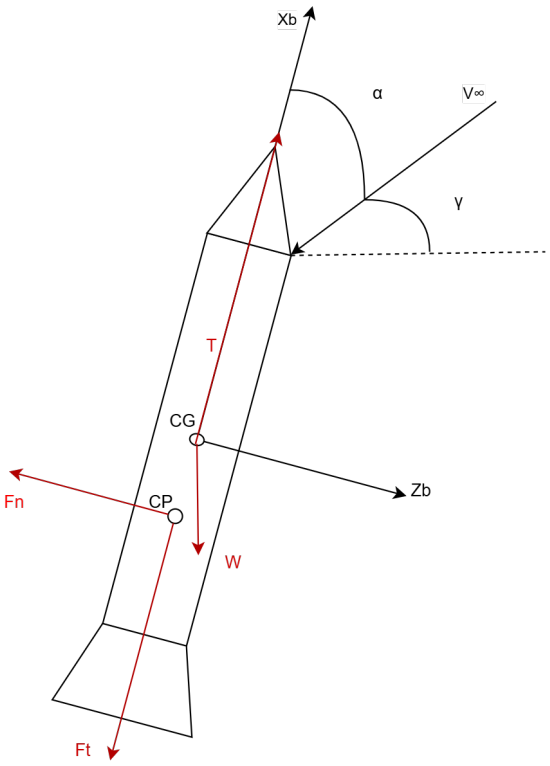

Figure 12.1: Rocket Ascent Phase FBD

One can now express the equations of motion in the body frame and then solve for them in the inertial reference frame F_E, with a small change compared to typical aerospace convention. In this coordinate system, Z_e points upwards, instead of downwards. The following equations of motion are solved.

$$m(t)\dot{V}_{X_e} = (T(h) - F_t(h,V_\infty)\cos\theta - F_n(h,V_\infty)\sin\theta \tag{12.1}$$

$$\dot{x}_e = V_{X_e} \tag{12.2}$$

$$m(t)\dot{V}_{Z_e} = (T - F_t(h,V_\infty))\sin\theta + F_n(h,V_\infty)\cos\theta - W \tag{12.3}$$

$$\dot{z}_e = V_{Z_e} \tag{12.4}$$

$$I_{yy}(t)\dot{q} = (x_{\text{cg}} - x_{\text{cp}})F_n(h,V_\infty) + C_{\text{mq}}\frac{1}{2}\rho(h)V_\infty^2 A_{\text{ref}} c_{\text{ref}} \cdot \frac{\dot{q}c_{\text{ref}}}{2V_\infty} \tag{12.5}$$

$$\dot{\theta} = q \tag{12.6}$$

$$V_\infty = \sqrt{V_{X_e}^2 + V_{Z_e}^2} \tag{12.7}$$

$$\alpha = \theta - \gamma \tag{12.8}$$

$$T(h) = \dot{m}v_{\text{exit}} + (p_e - p_{\text{ambient}}(h))A_e \tag{12.9}$$

$$F_t = C_t\frac{1}{2}\rho(h)V_\infty^2 A_{\text{ref}} \tag{12.10}$$

$$F_n = C_n\frac{1}{2}\rho(h)V_\infty^2 A_{\text{ref}} \tag{12.11}$$

$$A_{\text{ref}} = \frac{\pi c_{\text{ref}}^2}{4} \tag{12.12}$$

In the above equations $m(t)$ represents the UAV's mass as a function of time, $T(h)$ is the thrust as a function of altitude, and $F_t(h,V_\infty)$ and $F_n(h,V_\infty)$ are the tangential and normal components of the resultant aerodynamic force, respectively. These aerodynamic forces depend on the altitude h, through the atmospheric density $\rho(h)$, and on the freestream velocity V_∞. The variables V_{X_e} and V_{Z_e} denote the velocity components of the vehicle in the inertial Earth-fixed frame, while x_e and z_e are the corresponding position coordinates. The pitch angle of the vehicle is denoted by θ, and q represents the pitch rate, such that $\dot{\theta} = q$. The term $I_{yy}(t)$ is the time-varying moment of inertia about the body-fixed Y-axis, while x_{cp} and x_{cg} denote the locations of the centre of pressure and centre of gravity, respectively, C_{cm} is negative and is the moment coefficient of aerodynamic damping. Their difference defines the moment arm through which the normal aerodynamic force F_n generates a pitching moment. The variable W represents the weight of the vehicle. The freestream velocity V_∞ is computed from the inertial velocity components, while γ is the flight-path angle and α is the angle of attack. In the thrust equation, $\dot{m}$ denotes the propellant mass flow rate, v_{exit} is the exhaust velocity, p_e is the nozzle exit pressure, $p_{ambient}(h)$ is the ambient pressure as a function of altitude, and A_e is the nozzle exit area. Finally, C_t and C_n are the tangential and normal aerodynamic force coefficients, A_{ref} is the aerodynamic reference area, and c_{ref} is the reference diameter used to define this

area.

12.1.2. Cruise Performance

Cruise is a powered flight phase where the secondary propulsion system is employed, this consists of an electric powered propeller, which will be sized in Chapter 13. For the following analysis, a 2-term drag polar is always assumed. The power required during cruise is defined in Equation 12.13

$$P_{\text{cruise}} = P_r = D \cdot V_{\text{cruise}} = \frac{W}{L/D} \cdot V_{\text{cruise}} \tag{12.13}$$

where P_r is the power required, W is the weight, L the lift, D the drag and V_{cruise} is the cruise speed. The UAV has to be optimized for endurance during cruise, for a propeller aircraft this translates into minimizing power required, Equation 12.13 can be rewritten in function of the lift and drag coefficients, removing the dependency with velocity, this yields Equation 12.14

$$P_r = \sqrt{\frac{2W^3}{\rho S}} \frac{C_D}{C_L^{3/2}} \tag{12.14}$$

where ρ is the air density, S the wing surface area, C_D the drag coefficient and C_L the lift coefficient. As can be seen, minimizing power required means maximising the ratio $C_L^{3/2}/C_D$, as mentioned already in Section 9.1, the value of the power required cannot be influenced neither by the weight, which is fixed, nor the surface area, also constrained by the matching diagram, therefore only $C_L^{3/2}/C_D$ can be optimized; it can be rewritten as shown in Equation 12.15

$$\frac{C_D}{C_L^{3/2}} = \frac{\pi AReC_L^{1.5}}{\pi AReC_{D,0} + C_L^2} \tag{12.15}$$

where AR is the aspect ratio, designed in Section 9.1, e the Oswald efficiency factor and $C_{D,0}$ is the zero-lift drag coefficient, both estimated in Chapter 9. Thus for a given efficiency, lift coefficient and zero-lift drag coefficient, a higher aspect ratio always yields better endurance performance, however the aspect ratio cannot be infinitely large because of structural constrains, the optimal lift coefficient for endurance for a given aspect ratio can be derived, this is shown in Equation 12.16 [66].

$$C_{L_{\text{opt}}} = \sqrt{3\pi AReC_{D,0}} \tag{12.16}$$

It is not always possible to fly at this lift coefficient because for high aspect ratios it can be in the stall regime, however this solution still generates a lower power required than flying at the optimal lift coefficient for lower aspect ratios. Subsequently, the optimal velocity can be calculated, considering vertical equilibrium, this yields Equation 12.17.

$$V_{\text{opt}} = \sqrt{\frac{2W}{S\rho C_{L_{\text{opt}}}}} \tag{12.17}$$

An equation for the lift-over-drag ratio can also be defined, it has to be noted that this lift over drag ratio is not the maximum one as here the optimization is done via minimum power required rather than minimum drag. This equation is shown in Equation 12.18[66].

$$\frac{L}{D} = \frac{\sqrt{3}}{4} \sqrt{\pi \frac{AR \cdot e}{C_{D,0}}} \tag{12.18}$$

The thrust that the propeller needs to produce in cruise can be derived from equilibrium, this is shown in Equation 12.19.

$$T = D = \frac{W}{L/D} = 4W \sqrt{\frac{C_{D,0}}{3\pi ARe}} \tag{12.19}$$

A proper battery is sized such that, from the power required, sufficient energy can be stored to fulfil the endurance requirement; of course, a better optimized UAV yields to a smaller and lighter required battery.

This has been performed in Chapter 8. The range obtained by the UAV during the cruise phase can also be easily computed with Equation 12.20

$$R = V_{\text{opt}} \cdot E \tag{12.20}$$

where E is the required 35 minutes of powered endurance and V_{opt} is the optimal velocity calculated in Equation 12.17.

12.1.3. Glide Performance

Gliding is the last phase of the mission profile of the UAV, it's the only unpowered phase and its optimisation is different than the cruise one. Again a 2-term drag polar is assumed. The performance parameter which is decided to be optimised is range such that the key parameter to minimise is drag instead of power required [66]. Range for gliding flight can be easily calculated via Equation 12.21

$$R = \frac{hL}{D} \tag{12.21}$$

where R is the range and h the starting altitude, it is clear that to maximise range, maximum L/D (equivalent to minimum drag) has to be achieved, the optimal lift coefficient is straight forward to compute with Equation 12.22[66].

$$C_{L_{\text{opt}}} = \sqrt{\pi ARe C_{D,0}} \tag{12.22}$$

The optimal velocity uses the same relation as Equation 12.17, the lift-over-drag ratio is the maximum one and is computed via Equation 12.23

$$\left(\frac{L}{D}\right)_{\text{max}} = \frac{1}{2}\sqrt{\pi \frac{AR \cdot e}{C_{D,0}}} \tag{12.23}$$

The optimal lift coefficient is much lower than the one for cruise and thus can likely be achieved during gliding, yielding the maximum lift-over-drag and range performance. Lastly, the endurance during glide is calculated as shown in Equation 12.24.

$$E = \frac{R}{V_{\text{opt}}} \tag{12.24}$$

12.2. Results *Author(s): Vladimir, Marco*

This section outlines the results for all VAPOR mission phases. Firstly, the ascent phase is analysed and the UAV's trajectory is plotted; secondly, both cruising and gliding phases are analysed, leading to the calculation of performance parameters and the plotting of the flight profile and payload range diagram.

12.2.1. Pure Ascent

This section covers the pure take-off and ascent of the UAV without the implementation of a controller, this was explored in depth in Chapter 11. The goal of this section is to give an overview of the flight profile during ascent, in particular in relation to the trajectory of the UAV and its transition between vertical and horizontal flight. Figure 12.2a and Figure 12.2b show the UAV's trajectory and attitude over time respectively.

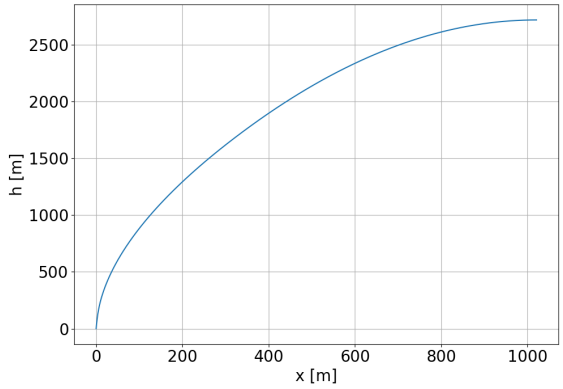

(a) UAV's Trajectory

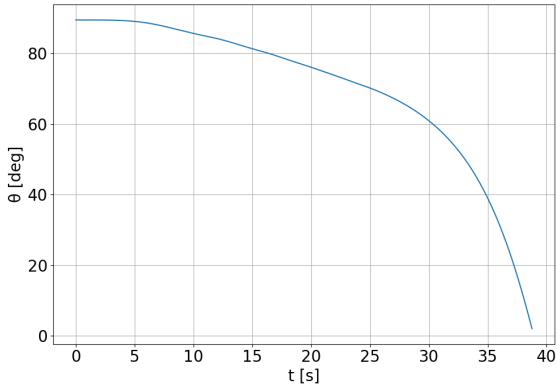

(b) UAV's Pitch Angle over time

Figure 12.2: UAV trajectory and pitch angle over the simulated mission.

These graphs are generated for some initial conditions, reported in Table 12.1

Table 12.1: Initial values for vertical ascent

Parameter	Value	Unit
h_{start}	0	m
m_{tot}	34	kg
m_{fuel}	6	kg
θ_i	89.5	deg

As can be seen, an initial angle very close to 90 degrees already produces satisfactory results in terms of trajectory and horizontal transition. However, the implementation of the controller is still of great importance to dampen the pitch rate at the end of coasting. Subsequently, the wings can be deployed and the propeller engaged, such that the cruise phase can commence.

12.2.2. Performance Parameters for Cruise and Glide

In order to correctly assess the results, its critical to calculate values for the aspect ratio, Oswald efficiency factor, and zero-lift drag coefficient, these parameters were investigated and computed in Chapter 9 and used here for performance analysis. Based on the methodology presented in Section 12.1, results for the cruise and gliding phases are tabulated in Table 12.2 and Table 12.3 respectively.

Table 12.2: Cruise Performance

Parameter	Value	Unit
C_L	1.3	[-]
V	20.13	m/s
L/D	16.63	[-]
T	16.52	N
P_r	332.49	W
R	42.27	km
E	35	min

Table 12.3: Glide Performance

Parameter	Value	Unit
$C_{L_{\text{opt}}}$	1.14	[-]
V_{opt}	21.49	m/s
L/D	16.78	[-]
R	41.95	km
E	32.53	min

These values are computed based on aerodynamic coefficients calculated in Chapter 9; moreover the mass of the UAV is assumed to be 28 kg after ascent, the surface area is equal to 1.09 m^2 based on the matching diagram, and the cruising altitude is assumed to be exactly 2500 m.

As expected, it was not possible to fly at the optimal lift coefficient during cruise, as $C_{L_{\text{opt}}} \approx 1.9$, far beyond stall; therefore, a lift coefficient was assumed for cruise to be as high as possible while also allowing sufficient margin with respect to stall. However, for the gliding phase, the optimal lift coefficient could be achieved, and thus the UAV is gliding optimally.

12.2.3. Performance Diagrams

In order to better assess the final performance figures of the design at this stage it is necessary to look into the flight profile and payload-range diagrams of the VAPOR UAV. These have been presented in the previous midterm report for all 3 strawman concepts differentiated by the secondary propulsion system choice [1]: microjet turbine, electric propeller or the option of no secondary propulsion unit with the main engine relight. The same performance diagrams have been reiterated with the final design parameters concerning aerodynamic performance in Table 12.2 and Table 12.3 depicting the updated flight profile and payload range diagrams in Figure 12.3 and Figure 12.4 respectively.

Starting with Figure 12.3 the variation of altitude is presented with respect to both time elapsed since launch as well as total distance covered. Both plots attain similar shapes as nominal flight is composed of 3 flight phases: rocket launch to target altitude, cruise at constant altitude and gliding flight.

The rocket launch takes up a miniscule fraction of the whole flight, with the UAV reaching target altitude in less than 1 minute. For this reason, the altitude evolution is simplified to a straight, near vertical line from a starting altitude of 0 m at 0 seconds after take-off. Cruising at the constant target altitude is then performed for a duration of 35 minutes, as set by the mission requirements. This corresponds to the flat part of the graph at the top of the plots. The gliding phase is assumed to be steady, straight, and quasi-static, neglecting transient manoeuvres and atmospheric disturbances over both duration and distance. This flight phase operates under the assumption of no propulsive power by either main bi-propellant engine or electric propeller and ends at an altitude of 0 m. The total endurance and range figures are E_{total} = 68.16 min and R_{total} = 85.2 km respectively.

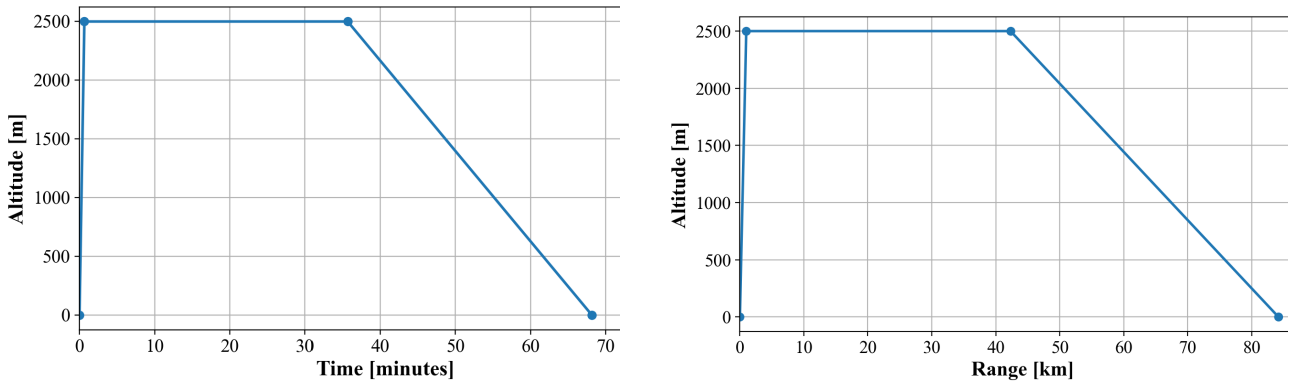

(a) Flight Profile in terms of time elapsed

(b) Flight Profile in terms of distance covered

Figure 12.3: Comparison of Flight Profiles

The payload range diagram, shown in Figure 12.4 is usually constructed by exchanging the payload mass for fuel mass. Given that the final design features the hybrid electric propeller secondary propulsive unit and that this is powered by on-board batteries there is no extra fuel to be exchanged for extra payload. Therefore, the maximum payload mass analysed is the design payload mass, thus justifying why the plot has only a flat part corresponding to the design point and a sloped part with decreasing payload.

The design payload mass is set to be 3kg, however, as denoted in Table 10.1 this leads to a maximum takeoff mass of less than 31kg, whereas the whole performance analysis relies on a mass of 34kg with a payload mass of 3kg being included. For future design iterations, the payload mass remains a point of significant flexibility and a higher margin.

The final point corresponding to zero payload is denoted by "ferry point". This condition attains maximum range because the payload-less UAV would achieve a larger initial altitude than 2500 m, leading to an overall longer gliding phase, ultimately responsible for an increase in both endurance and range.

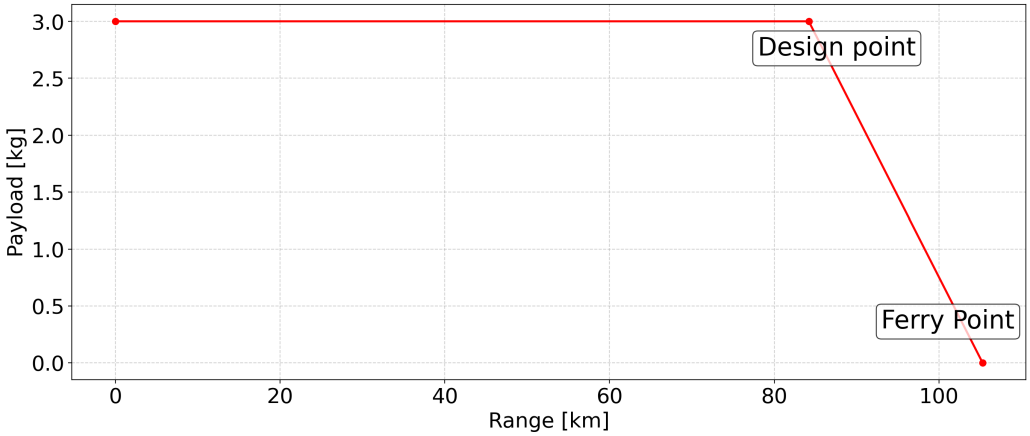

Figure 12.4: Payload Range diagram for the final design

12.3. Discussion and Limitations *Author(s): Vladimir, Marco*

The results provided in this chapter are representative of the feasibility of the design. These underline that performance requirements are met and that the design is competitive between rivals. The UAV meets the minimum endurance and range requirements while also being able to carry the required payload. Furthermore, the hybrid propulsion concept is a complementary solution as it allows the vehicle to benefit from the high energy density of the rocket engine during ascent and the efficiency of electric propulsion during cruise. However, several assumptions were made throughout the performance analysis, and these introduce uncertainty into the final results.

The major limitation concerns the ascent and pitch manoeuvre. The analysis does not take into account wind gusts, atmospheric disturbances, or lateral-directional dynamics, as the vehicle is modelled as a 3-DoF rigid body. As a result, the simulated trajectory represents an ideal flight condition. Additionally, constant aerodynamic coefficients are assumed during ascent; variation of these with Reynolds number and Mach number are neglected. Furthermore, all assumptions made in regarding to engine fluctuations and instabilities that were introduced in Section 7.5 still hold for this analysis. Lastly, the implementation of the controller is not included here, but this was explored in Chapter 11.

From the pure flight performance point of view, the cruise and glide phases assume steady and coordinated flight, neglecting sideslip and potential lateral-directional instabilities. Finally, flight performance figures are highly dependent on coefficients like the Oswald efficiency factor e and the zero-lift drag coefficient $C_{D,0}$, these values were estimated but no real-life tests were performed and therefore the models were not validated.

Future studies should focus on a full-scale 6 DoF modelling for the ascent phase, in order to best compute the UAV's trajectory and react to all kind of disturbances. Secondly, analysis should be also carried out more in-depth with respect to lateral-directional stability and the related eigenmotions. Lastly, the UAV should be tested and flight data should be collected in order to both estimate more accurately aerodynamic coefficient and validate the employed models.

13 | Electric Propulsion Design

Now that performance metrics have been calculated in Chapter 12, the secondary propulsion unit can be sized. It consists of 4 main components: the propeller, the electric motor, the ESC, and the battery. The interaction between these four components is what drives efficiency and ultimately the design. For example, a small propeller with small propeller pitch is matched against a fast spinning motor, but the consequence is more electric losses as fast spinning motors are less efficient. In this chapter, this intricate interaction will be analysed in full and a global optimum (with regards to weight) will be found.

13.1. Theoretical Background *Author(s): Duco, Paul*

To start, the governing theoretical equations and assumptions will be discussed. The models used are often simplified versions of the more precise ones, but this lower fidelity is perfect for the analysis performed here and gives sufficient accuracy.

13.1.1. First Order Electric Motor Model

The analysis used here is taken from the First-Order DC Electric Motor Model by Mark Drela [67]. This model utilises four variables to define a motor: K_V, K_Q, i_0 and R, where the latter two relate to motor electric losses and where the first variable, K_V, often also called just kv, is what primarily drives the motor size in this chapter, and it is defined as the motor rpm per volt applied. These constants are normally stated by motor manufacturers. Additionally we define some motor states. All variables are tabulated in Table 13.1. The reader is referred to the original theory by Mark Drela for the full derivation of the first-order model as only the key results will be shown here.

Table 13.1: First-order motor model as defined by Mark Drela.

Symbol	Description
Ω	Rotation rate
Q_m	Torque
P_{shaft}	Shaft power
η_m	Efficiency
K_V	Speed constant
K_Q	Torque constant
v	Terminal voltage
R	Resistance
i	Current
i_0	Zero-torque current

Firstly, the torque and voltage is defined

$$Q_m = (i - i_0)/K_Q \tag{13.1}$$

$$v_m(\Omega) = \Omega/K_v \tag{13.2}$$

$$v(i,\Omega) = \Omega/K_V + iR \tag{13.3}$$

where Equation 13.1 defines shaft torque Q_m which is assumed proportional to the current i via the torque constant K_Q, minus a friction-related current i_0 [67]. The internal back-EMF v_m in Equation 13.2 is assumed proportional to the rotation rate Ω via the motor speed constant K_V. Then, in Equation 13.3, the voltage across the motor is defined. It should be noted here early on that a combination of motor kv and rpm is limited by the battery voltage, as a combination of high required rpm and low motor kv might exceed the available voltage. Higher motor voltage than the battery can provide implies $V_{\text{batt}} > v(i,\Omega,K_V)$ where we also write motor voltage as a function of kv as it is a design parameter.

Secondly, the motor shaft power can be derived as

$$P_{\text{shaft}}(\Omega, v) = Q_m\Omega = \left[\left(v - \frac{\Omega}{K_V}\right)\frac{1}{R} - i_0\right]\frac{1}{K_Q} \tag{13.4}$$

where the shaft power is the physical power transferred to the propeller. How this relates to actual useful thrust generated will now be discussed.

13.1.2. Actuator Disk Theory

The first-order motor model relates the motor's electrical state to the shaft power it delivers, but says nothing about how much shaft power a given thrust demands. To bridge this and obtain an initial estimate of the propeller operating point, actuator disk theory is used, following [68]. The propeller is idealised as an infinitely thin disk that imparts a uniform pressure jump to the flow passing through it, accelerating the slipstream and thereby producing thrust. As with the motor model, only the result relevant to sizing is reproduced here; the reader is referred to the original notes for the full derivation by Spakovszky [68].

Combining the momentum and energy balance across the disk yields the ideal shaft power required to generate a thrust T at freestream velocity V_∞, given in Equation 13.5.

$$P_{\text{shaft}} = \frac{1}{2} T V_\infty \left(\sqrt{\frac{T}{\frac{1}{2}\rho A V_\infty^2} + 1} + 1 \right) \frac{1}{\eta_p} \tag{13.5}$$

where A is the total propulsive disk area across all propellers, ρ the air density, and η_p a propeller coefficient of performance lumping in the non-ideal losses (swirl, profile drag, non-uniform disk loading) the idealised disk does not capture. A value of $\eta_p = 0.90$ was assumed. The propulsive efficiency, relating useful power output to shaft power input, then follows directly as $\eta = T V_\infty / P_{\text{shaft}}$. Thus Equation 13.5 simultaneously fixes both the power demand and the efficiency of the propeller for a given thrust and flight condition.
This theory already shows that, in general, a larger propulsive disk area increases propeller efficiency.
Equation 13.5 is evaluated to obtain the shaft power from the required thrust, which is then divided by the propeller folding-mechanism efficiency (η_{fold}) and passed into the first-order motor model to recover the motor torque and electrical operating point. The folding mechanism efficiency is assumed at a conservative 95%, as a study from NASA details that the geometry of a foldable propeller creates a loss of between 2 and 5 percent thrust compared to a fixed propeller with the same dimensions[69]. While this disk-theory estimate was ultimately not retained for the final propeller design, it proved a useful first approximation to locate the region in which the efficient operating point of the propulsion system lies, guiding the initial motor and propeller sizing, which is discussed in a later section.

13.1.3. Electric Losses

The third way performance must be evaluated is by looking at electric losses. Power is lost by inefficient components and dissipated by heat. This is an unavoidable consequence of working with electronics, but the effect can be reduced by working with high quality electronics. Within the secondary propulsion system, the key areas where power is lost are in the ESC, the battery through discharge inefficiencies and through cable resistance.

An important concept to understand is that power loss scales by current squared and wire resistance, $P = i^2 R$. This approach is powerful for computing wire resistance but is difficult to apply to individual components such as the battery and ESC. Therefore, a standalone battery discharge efficiency (η_{bat}) and ESC efficiency (η_{ESC}) is defined. It is often cited that battery and ESC efficiency is neglected as its influence is very small [70, 71]. In this analysis both are assumed to be equal to 0.95 which is a conservative estimate. It should be noted that the efficiency for lower, hobby-grade components is often even lower. However, the VAPOR mission will utilise high-end components with minimal losses

Power losses from the high-current lines between the battery and the ESC, and between the ESC and the motor, must also be accounted for. These are losses driven by the wire resistance, scaling with the square of the current. With the current given by $i = P_{\text{ESC}} / V_{\text{batt}}$, the loss follows the standard resistive relation:

$$P_{\text{wire}} = \left(\frac{P_{\text{ESC}}}{V_{\text{batt}}} \right)^2 R_{\text{wire}} \tag{13.6}$$

13.1.4. Consolidation of Theory

All previously discussed theory can now be combined into one full design sweep, showing efficiency of a specific design point (combination of propeller diameter and motor kv). This is shown in Figure 13.1. This figure confirms the theoretical understanding: larger, slow-spinning propellers are more efficient. However, the figure also shows a second dimension that an aerodynamic argument would neglect: the electrical losses in the motor. Because the design holds the propeller tip Mach number fixed, the rotation rate scales as $\Omega \propto 1/D$: a larger propeller must turn slower. To deliver the required shaft power at that lower speed, the motor must supply a proportionally higher torque ($Q_m = P_{\text{shaft}}/\Omega$, with $\Omega \propto 1/D$, so $Q_m \propto D$). For a brushless motor the torque constant is set by the voltage constant ($K_Q = 1/K_V$ in consistent units), so the current is essentially proportional to torque, $i \approx Q_m K_Q + i_0$. The resistive (copper) losses, $i^2 R$, therefore grow steeply as the propeller is enlarged.

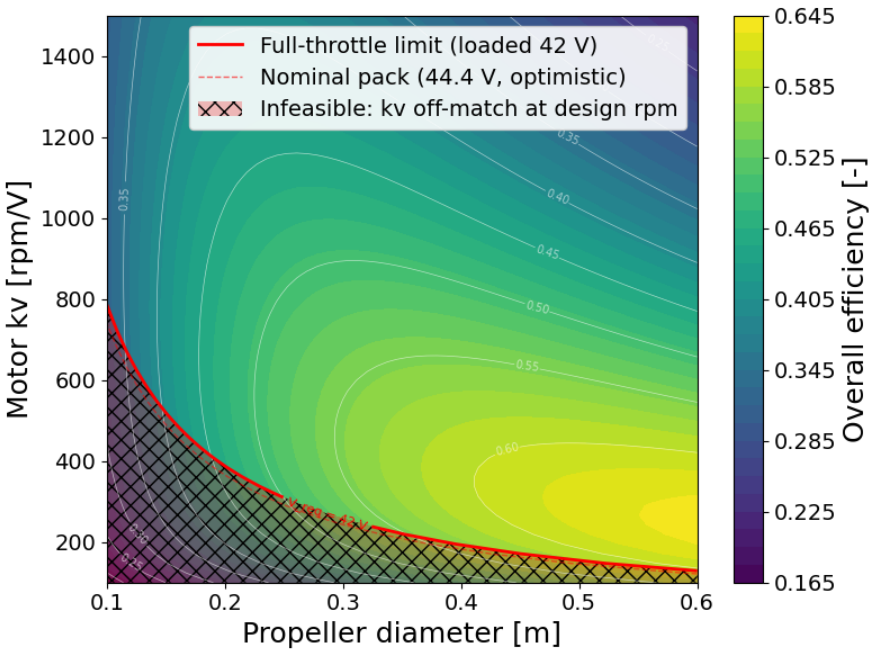

Figure 13.1: Propeller motor design space matching diagram. Overall efficiency (from battery to useful power output) shown by the colour with contour lines of constant efficiency. The design space is limited by the battery voltage. This figure does not take into account physical constraints with regards to motor kv and propeller diameter.

13.1.5. Propeller Data

A key limitation of the actuator disk theory is that it is unable to accurately simulate real life propeller performance as it does not include propeller pitch. For this reason, a data-driven approach was taken to go into one more level of depth. Instead of relying on actuator disk theory, real-life propeller data from APC (advanced precision composites) propellers was taken. This company provides in-depth measurement data for all propellers they sell, which includes data such as thrust (coefficient), efficiency at a given rpm, advance ratio (J) [1]. Advance ratio is a propeller's forward motion over its rotational speed and is crucial for efficiency[2].

In the further analysis, the goal is to match a propeller with VAPOR's operating conditions and mission requirements to ultimately optimise for the lowest energy consumption. To find the most optimal propeller for a given operating condition (thrust, velocity and altitude) the data from APC is interpolated to gain thrust coefficient as a function of velocity and rpm. This coefficient is made dimension-full with rpm, propeller diameter and air density and subsequently solved for required thrust. This function is intercepted with the required thrust and solved for. This is displayed for 4 propellers in Figure 13.2. At the required operating point for the given propeller, a value for advance ratio can be computed which in turn relates to its efficiency. This is shown in the plot on the right Figure 13.3. This figure shows typical curves for propeller efficiency as a function of advance ratio. Propeller efficiency typically rises steadily for an increasing advance ratio (J) up to its peak efficiency, after which the efficiency rapidly drops. Generally, the area on the right of the peak should be avoided as this can result in a sharp decline in performance with a slight increase in advance ratio, which could be induced by a longitudinal wind gust.

[1] www.apcprop.com [Date Accessed: June 15] [2] Wikipedia - Advance Ratio [Date Accessed: June 15]

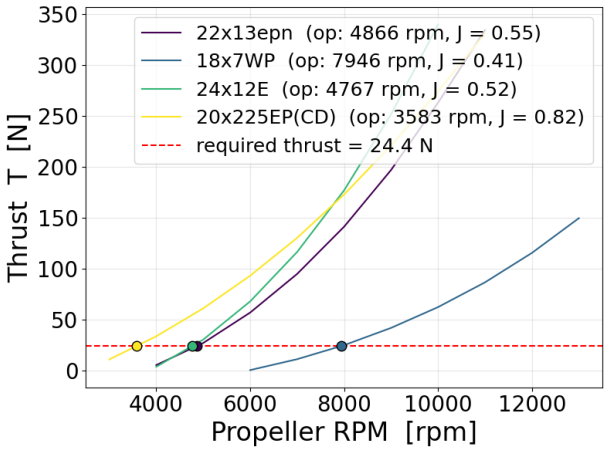

Figure 13.2: The interpolated function of propeller thrust versus rpm, at the operating cruise speed.

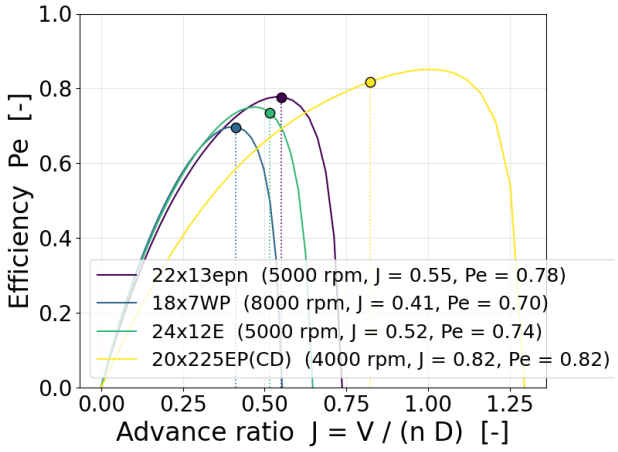

Figure 13.3: Advance ratio versus propeller efficiency. The operating advance ratio is indicated.

13.2. Detailed Electric Propulsion Design Procedure *Author(s): Duco*

Finally, all previously discussed theory can be combined in an optimisation problem which is minimised for energy consumption. This is a trade-off between maximising propeller diameter and minimising motor kv, as was discussed in Subsection 13.1.1 and Subsection 13.1.5, and minimising electric losses, as discussed in Subsection 13.1.3.

In a Python script, a single function `apc_propeller_propulsion_analysis` is defined that computes the performance of a propeller from battery to air power output, for a given propeller. The script starts by computing the propeller operating point given a flight condition (ρ, T, V_{cruise}, a) which computes the required propeller shaft power from the power coefficient and rpm. Subsequently, the motor performance is evaluated using the first-order motor model, described in Subsection 13.1.1. This computes required motor electrical power from a motor rpm, torque (shaft power), kv, and from two motor constants (i_0 and R). Then, ESC losses, wire losses and battery losses are added, as described in Subsection 13.1.3. The final figure is continuous power draw required from the battery. By setting the cruise time at 35 minutes, a battery size can be calculated. The results for a handful out of the 80 propellers with varying performance is displayed below in Table 13.2. These 7 results show the difference in performance and for varying propellers, and show the expected result that larger propeller perform more optimally. This table also shows propeller rpm, propulsive efficiency (η_p), motor efficiency (η_m) and total efficiency (η_{all}).

Table 13.2: Propeller trade-off comparison. Energy E is the mission energy; battery power scales linearly with it ($P_{\text{batt}} \approx E/0.58\,\text{h}$) and is omitted.

Rank	Prop	D [m]	K_V	J	M_{tip}	rpm	η_p	η_m	η_{all}	E [Wh]	v [V]
1	20x15E	0.508	220	0.572	0.34	4156	0.78	0.86	0.64	308	19.5
2	20x15C	0.508	220	0.571	0.34	4166	0.78	0.86	0.64	309	19.6
3	21x135EPN	0.533	220	0.535	0.36	4230	0.77	0.86	0.64	311	19.8
12	19x12E	0.483	430	0.505	0.38	4955	0.76	0.85	0.63	316	12.5
28	22x12WE	0.559	220	0.506	0.38	4268	0.74	0.86	0.61	322	20.0
55	16x8	0.406	430	0.419	0.46	7089	0.71	0.87	0.59	336	17.3
75	17x6E	0.432	430	0.336	0.57	8327	0.65	0.87	0.54	366	20.1

Here, tip Mach (M_{tip}) is also given as it is important to check this value stays well under 0.7 Mach. Tip Mach is calculated through the relation described in Equation 13.7 [68].

$$M_{\text{tip}} = M_\infty \sqrt{1 + \left(\frac{\pi}{J}\right)^2} \tag{13.7}$$

In Equation 13.7, M_∞ is the free stream Mach number. For almost all props, tip Mach was around 0.50, apart

from one propeller, which was excluded from the analysis.

As can be seen from Table 13.2, the optimiser generally prefers the slower spinning 220 kv motor. However, for some smaller propellers, a faster spinning motor is more efficient. This shows the intricate relation between the design variables in the secondary propulsion system. To conclude, the APC 20x15E propeller proves optimal performance at the VAPOR design point and will therefore be used in the mission. It should be noted however, that performance between the first few options is extremely similar and power requirement differs very little. The energy required is 308 Wh which is equal to about 7000 mAh.

Finally, the electrical motor and ESC candidates may be selected. The electric motor which was selected is the T-Motor AT 5330 Fixed Wing[3]. This motor provides sufficient thrust at the VAPOR operating point which was validated through its datasheet. The ESC that was chosen was the T-Motor AT 115A ESC [4] and was matched specifically against the motor per recommendation of the manufacturer. This ESC is rated at 115A which means sufficient margin at the cruise thrust setting.

13.3. Design Sustainability and Sensitivity *Author(s): Duco*

To conclude the secondary-propulsion design, two higher-level aspects are briefly addressed: the sustainability of the chosen system and its sensitivity to the top-level design parameters. Both follow directly from the energy-driven optimisation of the preceding section.

13.3.1. Sustainability

For this design, efficiency and sustainability are effectively the same objective. Because the battery is sized directly from the mission energy, any inefficiency in the chain propagates into a larger battery, which is the heaviest and most resource-intensive component through its use of rare-earth metals and other materials. This effect also cascades, as a heavier battery raises the required cruise thrust, which raises the energy demand and battery size once more. Minimising energy consumption therefore minimises material usage, and no separate sustainability objective was needed during sizing. It is still worth asking whether one component dominates the losses: from Table 13.2 the propeller ($\eta_p \approx 0.78$) and motor ($\eta_m \approx 0.86$) account for nearly all of it, while the ESC, battery and wiring losses are each only a few percent. Future sustainability gains are thus best sought in propeller and motor efficiency, as the electrical components already sit close to their practical limits. Component longevity reinforces this: the high-end motor and ESC have few wearing parts and long lifespans, leaving the battery as the only meaningfully life-limited element, and the smaller battery resulting from the efficient design also degrades more slowly.

13.3.2. Sensitivity Analysis

The sensitivity of the design to its top-level inputs is considered qualitatively, distinguishing between the selected hardware (propeller diameter and motor kv) and the resulting energy requirement. As Table 13.2 shows, the optimum is remarkably flat, with the best propellers separated by only a few watt-hours. The hardware choice is therefore robust: a moderate change in lift-to-drag ratio, weight or cruise speed shifts the required thrust but does not strongly influence the propeller which is optimal, as neighbouring options simply trade places. The energy requirement itself is far more sensitive. Both weight and lift-to-drag ratio set the cruise thrust almost directly, and the feedback described above increases their effect through the battery-sizing loop, making these the two parameters the design is most sensitive to. Cruise velocity instead acts through the advance ratio: because the propeller is deliberately operated to the left of its efficiency peak (Figure 13.3), the design retains a margin against speed increases, though a large enough increase would push the operating point past the peak and cause a sharp efficiency drop and therefore change the optimal propellers completely. In short, the chosen components are somewhat sensitive to the top level parameters, whereas the energy budget, and hence battery mass, is mainly sensitive to weight and lift-to-drag ratio and flight velocity. Therefore, the design is said to be insensitive.

[3] https://store.tmotor.com/product/at5330-a-fixed-wing-motor.html [Date accessed: June 17] [4] store.tmotor.com [Date Accessed: June 3]

14 | Technical Budget Breakdown

This chapter discusses the technical budgets defined in the project planning phase [2]; the cost and time budgets are covered in Section 17.2 and Section 17.4. Only the electrical and mass budgets are treated here. The volume budget is dropped (the redesign removes the volume constraint), the reliability budget awaits subsystem testing, and the propellant budget is no longer relevant since the electric motor and net catch limit propellant use to the ascent stage.

14.1. Electrical Power Budget *Author(s): Paul*

This section reviews the power budget from the baseline [2] and the current budget state, noting the design decisions that drove it.

Table 14.1: Electrical Power Budget: Baseline vs. Final

	Baseline		Final		Difference	
Subsystem	**Power (W)**	**Energy (Wh)**	**Power (W)**	**Energy (Wh)**	**Δ Power (W)**	**Δ Energy (Wh)**
Avionics	252.28	210.23	7.00	7.93	−245.28	−202.30
Control	204.96	0.00	27.00	29.60	−177.96	+29.60
Airframe	117.04	97.53	0.00	0.00	−117.04	−97.53
Payload	180.00	150.00	100.00	112.33	−80.00	−37.66
Propulsion	108.00	0.00	0.00	0.00	−108.00	0.00
Electrical Propulsion	—	—	532.80	308.80	+532.80	+310.80
Subtotal	**862.28**	**457.77**	**666.80**	**462.66**	−195.48	+4.89
Contingency (20%)	172.46	91.55	—	—	—	—
Total	**1034.74**	**549.32**	**666.80**	**462.66**	−367.94	−86.66

Table 14.1 summarises the power budget. Propulsion power is unchanged, as the rocket engine's requirements were not revisited. The UAV's baseline budget was significantly oversized and its assumptions invalid; however, an electrical propulsion system, absent from the baseline, has been added. Overall, peak power rose slightly while the energy requirement retains contingency. Against the actual battery (5C, 488.4 Wh), this leaves a margin 26.4 Wh capacity for further development.

14.2. Mass Budget *Author(s): Paul*

This section gives an updated overview of the UAV's mass against the baseline estimates [2].

Table 14.2: Mass Budget: Baseline vs. Final

	Baseline	Final	Margin
Subsystem	**Mass (kg)**	**Mass (kg)**	**Δ (kg)**
Propulsion (incl. electrical)	5.900	3.232	−2.668
Airframe	8.000	15.006	+7.006
Avionics	1.100	0.300	−0.800
EPS	2.290	1.620	−0.670
Controls	1.710	1.475	−0.235
Dry Mass	**19.000**	**21.633**	+2.633
Propellant	8.000	6.000	−2.000
Payload	3.000	3.000	0.000
Subtotal	**30.000**	**30.633**	+0.633
Contingency	4.000	—	—
Total	**34.000**	**30.633**	−3.367

Table 14.2 compares the two budgets. The propulsion masses were overestimated, in both structure and propellant. Airframe mass rose by nearly 90%, mainly from a larger fuselage. In total the mass shows only a slight surplus of 0.633 kg over the baseline (excluding contingency), and the final 30.633 kg remains 3.367 kg below the 34 kg budget—leaving ample contingency for further development and mission flexibility.

15 | Operations & Logistics

This chapter concerns how the operation and ground handling of the UAV and adequate ground segment are defined. The operational concept is defined in Section 15.1 where the mission planning, execution and recovery after landing. Meanwhile, Section 15.2 describes in detail how the ground segment procedures are to be treated. The list of operational steps is a revised and updated version from the "Operations & Logistic Concept" of the midterm report [1].

15.1. Operational Concept *Author(s): Vladimir*

This section outlines the main activities beyond design and manufacturing that ensure VAPOR can successfully fulfil its mission, with particular emphasis on subsystem integration and communication with the ground segment. The VAPOR Concept of Operations (ConOps) diagram is shown in Figure 15.1. Building on the midterm report [1] and the communication flow diagram in Figure 8.2, it provides an operational view of the interactions between the UAV and ground subsystems, whereas the communication flow diagram describes the hardware interactions in greater detail.

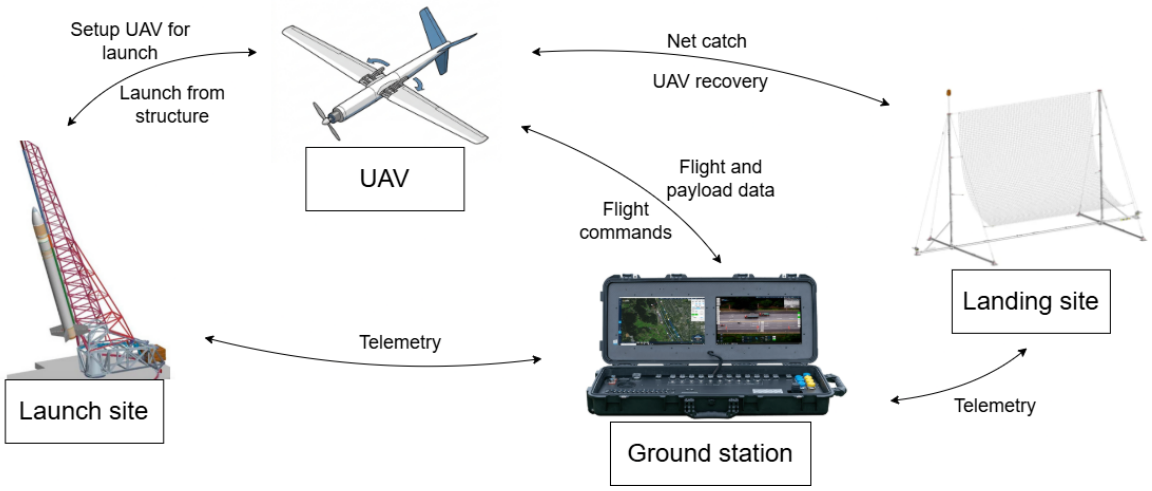

Figure 15.1: VAPOR's ConOps diagram

Mission planning:

- **Define a mission**: Based on some customer need, a mission is defined for VAPOR. For instance, conducting surveillance operations over a given area at a certain altitude.
- **Assess weather and clearance**: Check the weather conditions as well as airspace clearance and ground clearance in the launch and recovery sites to ensure safe operations. If weather and clearance requirements are not met the flight route is modified if possible to comply with them while still achieving the mission goals.
- **Define a fly zone**: Based on the mission and subsequent flight level clearances, a fly zone is defined for the UAV in order to achieve it. This also includes launch and recovery locations if needed.
- **Load flight zone in UAV**: The final flight zone is then loaded into the UAV onboard computer defining clear in-flight bounds.
- **Payload preparation**: The payload is installed into the UAV if not done already and properly calibrated if possible.

Mission execution:

- **Launch and start climbing**: The main bi-propellant engine fires and the vehicle starts its controlled ascent.
- **Shut-off engine**: Once enough speed has been gained, the main engine shuts-off and the vehicle coasts to its target altitude in a controlled trajectory.
- **Unfold wing**: Once a suitable target speed is reached the wing will unfold
- **Transition to horizontal flight**: The vehicle performs a transition manoeuvre from vertical to horizontal flight using its control surfaces, entering cruise conditions.
- **Start propeller**: The electric propeller is switched on such that the cruising phase can begin.
- **Perform surveillance operation**: The UAV performs its surveillance mission according to its flight route, in communication with the ground station.

- **Monitor and control operations**: The ground station monitors the operations and provides any gives any controls or assistance if needed. The ground segment has the ability to manually override the autonomous inputs of the UAV at any time.

Recovery:

- **Prepare net**: The catching net is installed at the recovery site with the designated orientation.
- **Approach**: The UAV starts its gliding (unpowered) approach to the landing site.
- **Identify net**: At a designated distance from the landing site, the UAV should have identified the position of the net with its navigation system, otherwise the catch is aborted.
- **Catch**: The UAV proceeds to fly through the net while gliding, getting trapped by the assembly and ending the flight.

15.2. Ground Handling Procedures *Author(s): Vladimir*

The ground handling procedures outline the operations and logistics behind the actual UAV launch, from launch site readiness to final pre-flight checklist and vehicle checks to storage, transport or turnaround in the post-flight phase. For both pre- and post-flight deployment, human safety takes a central role in defining the checklists, considering the hazardous nature of HTP when in contact with any organic matter and textile fabric. As a consequence, special care was taken when assessing the sequence and logic of the checklists.

15.2.1. Pre-flight deployment

- **Assess launch site safety:** Check that fuel, oxidizer and pressurant gas transport or storage units are functioning in proper working order and are ready for loading and pre-flight procedures and that the launch site is safe to enter.
- **Transport to launch site**: The UAV as well as any other necessary equipment such as the launch structure, propellants and batteries are transported to the launch site.
- **Equip Personal Protective Equipment (PPE):** Suitable equipment for ground crew is used to ensure safety of human operators in case of HTP spills or work-related accidents. This includes splash-proof safety goggles, a face shield, chemical-resistant gloves, and suit.
- **Ensure functionality of water sources :** Check that water is readily available for safety showers as contingency to HTP neutralization in case of a spill
- **Visual inspection of UAV** : Before starting the launch setup, a brief visual inspection of the UAV is performed to ensure no damage or abnormalities that could endanger the mission or the safety of the personnel are present.
- **Visual inspection of launch structure:** Ensure that the vertical launch mount is ready for nominal operational use.
- **Place UAV in launch structure**: The operators install the launch structure at the launch site and place the UAV on it in the launch configuration.
- **Place batteries**: All batteries are installed and connected to the UAV at this point.
- **Start onboard computer**: The UAV's onboard computer is started before loading the propellants to avoid handling of the vehicle when loaded.
- **Check emergency parachute actuation**: Ensure the parachute actuator deploys electronically when aborting and starting emergency procedures.
- **Load zone in UAV**: The final flight zone is loaded into the UAV onboard computer.
- **Load fuel**: The RP-1 tank is filled using the required equipment.
- **Load oxidiser**: Before loading the hydrogen peroxide tank, a nitrogen purge is performed in order to ensure the tank is clean of any residue that could react with the HTP. After purging, the peroxide is loaded in the tank using the necessary equipment.
- **Load helium**: Helium is loaded into the helium tank using a pump, with the valves connecting the helium tank to the propellant tanks open. Once the operating pressure of the propellant tanks is reached, the valves are closed and the helium tank is loaded to its maximum operating pressure.
- **Perform checks**: Safety checks are performed on the vehicle before launch to ensure nominal functioning of the various components. This includes checking the tank pressures, conducting a test sequence on the control surfaces and testing the communications with the ground station and other navigation systems.

- **Clear launch area**: If the checks are successful, all personnel and equipment are cleared from the launch area to a safe distance.
- **Launch command**: Once the safety checks are successfully conducted and the launch area is clear, if the weather is favourable and the airspace is clear, the ground station gives the launch command.

15.2.2. Post-Flight Handling

- **Vehicle safety checks**: After recovery, safety checks are performed to verify that personnel can safely approach and handle the UAV. These include remote monitoring of pressure and temperature.
- **De-pressurise tanks**: The propellant and helium tanks are vented to ambient pressure.
- **Shut-off computer**: The onboard computer is shut-off to avoid any unexpected actuation.
- **Retrieve vehicle**: The operators lower the net to the ground and recover the vehicle, wearing adequate equipment to avoid intoxication and protect them against unexpected minor fires.
- **Unload propellants**: Any remaining propellants are removed from the vehicle using the proper equipment.
- **Remove batteries**: The batteries are removed from the vehicle, cutting all electrical power.
- **Remove payload**: If needed the payload is retrieved from the vehicle.
- **Visual inspection**: A post-flight visual inspection is performed to spot any damage or abnormalities in the vehicle, in which case it is sent for maintenance.
- **Transport back**: Transport to storing location or maintenance location in case of damage or scheduled service.

15.3. Regulatory Compliance *Author(s): Vladimir*

In order to get flight clearance and perform its mission the VAPOR UAV must comply with the legal and regulatory framework for Unmanned Aircraft Systems (UASs) of the European Union, or more specifically European Union Aviation Safety Agency (EASA). There are three categories of UAS as defined by EASA [1]:

- **Open**: UAS with a maximum take-off mass of 25 kg flying at predefined distances from residential, commercial, or recreational areas in urban environments.
- **Specific:** any UAS beyond a MTOM of 25 kg and especially flying Beyond Visual Line of Sight (BVLOS). These require a more extensive certification.
- **Certified:** Reserved for operations with the highest risk covering missions of human transport, international cargo delivery and flight over populated areas.

Since VAPOR has an MTOM of 34,kg, it falls within the "specific" category and therefore requires a Specific Operations Risk Assessment (SORA) assessment.[2] This methodology evaluates both ground risk, determined by the type of areas overflown such as crops, residential, commercial, recreational or more isolated areas, and air risk, determined by the airspace in which the UAV operates. Based on these risks and the implemented mitigation measures, the operation is assigned a Specific Assurance Integrity Level (SAIL) level ranging from low (SAIL I–II) to high (SAIL V–VI)[3]. Factors increasing the regulatory compliance difficulty of the VAPOR project are the introduction of chemical hazards through the bi-propellant kerosene and H_2O_2 rocket motor by handling the latter at possibly volatile pressure states as well as the presence of a wing unfolding mechanism for the primary aerodynamic surfaces. These increase the technical risk and will result in a medium or high risk SAIL classification. As a result, either an Operational Authorisation will be needed for submission to the National Aviation Authority (NAA) together with a potential Design Verification Report (DVR) for EASA for a medium risk classification or an airworthiness certification for high risk[4].

The focus for the DVR should be on structural integrity, software assurance, rocket engine pressure safety, and fail-safes. Conversely, for operations, submissions to the NAA should focus on airspace, ground risk, crew training (on how HTP is to be handled), emergency checklists, and local site safety instead. The goal is to attain both a DVR and an Operational Authorisation.

For autonomous and BVLOS operations, compliance with Step 9 of SORA requires enhanced containment, meaning it must be demonstrated that the UAV cannot leave its designated flight volume[5]. To further reduce the risks associated with a potential fly-away event, VAPOR incorporates an emergency recovery system based on a deployable parachute[5]. In addition, an off-the-shelf landing net is included in the ground

[1] EASA Drones (UAS) categories [Date Accessed: June 15, 2026] [2] What is SORA (Specific Operations Risk Assessment) [Date Accessed: June 15] [3] EU Drone Port - Specific category and SAIL [Date Accessed: June 15] [4] EASA - Design verification report guidelines[Date Accessed: June 15]

segment to safely absorb all kinetic energy on impact within a designated safety perimeter, subject to the landing loads described in Subsection 9.6.2.

15.4. RAMS Analysis *Author(s): Mario*

Some key considerations for VAPOR are its reliability, availability, maintainability and safety characteristics. These aspects are discussed in this section providing an overview of each if these operation factors.

15.4.1. Reliability

Reliability is the probability a system successfully performs its intended mission. For VAPOR, reliability is critical due to its role in rapid-response surveillance missions such as wildfire monitoring, where failure could have severe consequences. The main failure modes and mitigation measures are discussed in Chapter 4.

Key reliability concerns include the propulsion system, which operates under extreme pressure and temperature conditions, where anomalies could lead to melting, explosion, self-decomposition of the hydrogen peroxide, or oxidation of structural materials. The wing and propeller folding mechanisms are also critical, as failure to deploy or snapping under excessive loads could result in mission loss or catastrophic failure. Flight software represents a further risk, as errors have historically caused numerous mission failures.

Mitigation measures for all major risks are described in Chapter 4. General principles include early consideration of failure modes, redundancy where feasible, and extensive testing under representative conditions.

15.4.2. Availability

Availability refers to the access to the vehicle whenever needed. If VAPOR is not readily available to quickly react to an unforeseen scenario that requires urgent monitoring, it does not fulfil its mission goal. In order to grant availability, multiple aspects have to be taken into account:

- **Maintenance:** VAPOR is designed to complete at least 10 missions before requiring scheduled maintenance. To minimise operational disruption, maintenance activities within a fleet should be staggered so that downtime of individual UAVs overlaps as little as possible.
- **Number of UAVs:** The higher the number of VAPOR UAVs an operator has, the more likely it is that one of them will be available at a given moment in time. Therefore, an appropriate fleet size has to be determined for each particular application.
- **Location of the UAVs:** In order to quickly launch VAPOR in case of urgency, there has to be a UAV ready for deployment close enough to the target surveillance location such that the response time is within the acceptable limits for that particular scenario.

15.4.3. Maintainability

Maintainability considers the ease of repair and access the different components of the system. For VAPOR, this was accounted by selecting off-the-shelf components such as actuators, sensors, onboard computer or batteries that are readily available and integrate modularly in the system. Also multiple accessibility openings are present in the frame of the UAV to easily reach these components and perform checks or replace them. The liquid bi-propellant engine, which is the component that requires the most frequent maintenance due to its harsh operating conditions, is held to the frame by eight standard 5 mm screws and two threaded inlets for the propellant pipes. This makes removing and installing the engine a simple and quick process.

15.4.4. Safety

Safety aims to minimise the risk of harm to people, equipment, and the environment. As with reliability, it is closely linked to the risks identified in Chapter 4, focusing on preventing or mitigating their consequences. For VAPOR, the two primary safety hazards are hydrogen peroxide and loss of vehicle control:

- **Hydrogen peroxide:** High-concentration peroxide is corrosive and can damage personnel or equipment if leaked or spilled. It is also sensitive to contamination and elevated temperatures, which may trigger decomposition. To reduce these risks, dedicated handling procedures are defined in Chapter 15, limiting personnel exposure.
- **Loss of vehicle control:** A loss of control could result in a crash over populated areas or critical infrastructure. To mitigate this risk, VAPOR employs robust avionics and control systems with redundancy where possible. In emergencies, a parachute recovery system can be deployed to achieve a controlled descent and reduce impact damage.

[5] What is SORA (Specific Operations Risk Assessment) [Date Accessed: June 15]

16 | Manufacturing & Assembly Plan

This chapter concerns the manufacturing and assembly of the UAV. Section 16.1 describes the selected manufacturing process, material, and post-processing steps for each component. Section 16.2 then outlines the assembly sequence, from parallel component production through sub-assembly integration to final assembly. Finally, the sustainability implications of the manufacturing and assembly choices are discussed in Section 16.3.

16.1. Component Manufacturing *Author(s): Ivan, Paul*

This section describes how each component of the UAV is manufactured. A consistent method is used to select the manufacturing process for every part. Among the processes that are feasible for every part manufacturing process, the final choice is made on cost and sustainability. This keeps the selection aligned with the project's emphasis on affordability and recyclability, and avoids weighing criteria that do not meaningfully separate the feasible options.

16.1.1. Engine

Manufacturing process

Three routes were considered for the thrust chamber, nozzle and injector: conventional subtractive machining from billet, investment casting, and metal laser powder-bed fusion (SLS). Machining cannot economically produce the internal injector and cooling features without splitting the engine into many joined parts, and casting offers poor geometric precision and long tooling lead times for a single prototype. SLS is selected because it produces the complex, consolidated engine geometry in a single build, eliminating joints that would act as leak and failure paths.

Material selection

For the hot, pressure-bearing parts the candidates were stainless steel 316L, titanium alloys, and the nickel superalloy Inconel 718. Inconel 718 is selected for its high-temperature strength and oxidation resistance at the combustion wall temperatures, combined with its compatibility with hydrogen peroxide, which are the two main constraints for this engine.

Post-processing

As printed parts are not yet usable, the engine follows the standard SLS finishing chain. The Inconel 718 receives heat treatment to relieve printing stresses and develop its full strength. Then a HIP is done to close internal voids and ensure it withstands repeated firings. After removal from the build plate and supports, the critical surfaces (sealing faces, flange, threaded ports and injector holes) are CNC-machined to tolerance, as printing alone is not precise enough. Finally, the machined surfaces are cleaned and passivated to prevent surface contaminants from triggering hydrogen peroxide decomposition.

16.1.2. Tanks, Piping, and Valves

Tanks

The tanks are made from aluminium 6061-T6, as selected in the material trade-off in Section [1]. A spherical shape is used because it gives the lowest wall stress for a given pressure and volume, which keeps the tanks light. A few manufacturing routes were considered. Machining each tank from solid billet was rejected as it wastes most of the material and is slow. The chosen route is to form two aluminium hemispheres, by metal spinning or pressing from sheet, and weld them together at the equator to make the full sphere. The fill, drain, outlet and pressurant ports are machined as small bosses and welded into the shells.

The hemispheres are joined by Tungsten Inert Gas (TIG) welding, which is accurate and well suited to the small number of tanks needed for the prototype. After welding, the tanks are cleaned and passivated. This step is essential for the oxidiser tank, as untreated aluminium surfaces can trigger the hydrogen peroxide to decompose.

Piping

The rigid feed lines are also made from aluminium 6061-T6, following the feed system material trade-off defined in the midterm report [1]. The tube is cut to length and bent to route between the tanks, valves and engine, using standard fittings rather than custom parts. The peroxide-side lines are passivated in the same way as the tanks.

Valves

All valves are commercial off-the-shelf, selected for the required pressure rating and for compatibility with

kerosene and high-test hydrogen peroxide.

16.1.3. Wing System

As outlined in Section 9.3, the wing structure is composed of spars, ribs, and skins made entirely out of aluminium. To manufacture this sub-assembly, the manufacturing process for each part has to be outlined.

Rib Manufacturing

Regarding the production of ribs, three processes were selected as suitable: CNC Machining from a flat plate, Laser cutting, and additive manufacturing. For each of these processes, considerations regarding their relative cost, material utilization, and production volume capacity were taken in order to choose the most suitable method. For additive manufacturing techniques, the material utilization is excellent and highly optimized; however, production volumes are low, and costs are very high. CNC Machining techniques have a high relative cost, a moderate production volume output, and poor material utilization, giving it is a subtractive manufacturing process. on the other hand, Laser cutting techniques have a low to medium production volume output but have a high material utilization and have a low cost. For this reason, laser cutting was chosen as the production process for the rib manufacturing.

The production process for manufacturing the rib using laser cutting begins with sourcing a 3 mm thick aluminium sheet. The sheet is then prepared and positioned for laser cutting. Following cutting, the component undergoes deburring and edge-finishing operations to remove sharp edges and improve surface quality. Finally, the rib is inspected to verify dimensional accuracy and compliance with design specifications.

Spar Manufacturing

For the manufacturing process of the spars, given the constant geometry along the span, metal profile extrusion process was chosen. This process was chosen given that its material utilization is highly optimized as the material scrap is low, is compatible with aluminium, part cost are low and production volume output is moderate.

Metal extrusion processes begin with the sourcing of billet material. This billet is heated and forced through a steel die with the required cross-sectional geometry. The extruded material is then quenched to preserve mechanical properties and cut to length. Finally, post-processing operations are performed and followed by part inspection.

Skin Manufacturing

Finally, the wing skin must be manufactured and formed to follow the aerodynamic shape of the airfoil. For this, stretch forming procedures were selected. This method allows to produce a smooth airfoil curvature by stretching a thin sheet of aluminium over an airfoil-shaped die which is then pressed. The wing skin would have to be separated into a lower and upper skin, which then would be assembled onto the wing structure.

16.1.4. Folding Mechanism

The folding mechanism is composed of the frame, which connects the wing structure to the fuselage, the pushrod, pushrod attachment frame, and spring. The material chosen for these parts is also aluminium, and given the complexity of these parts, the available manufacturing methods are CNC Machining and Additive Manufacturing. Even though CNC machining has a moderate material utilization compared to additive manufacturing processes such as metal 3D printing, its cost of production and availability is higher. Hence, CNC machining was chosen for the production of the folding mechanism parts.

The process for machining the parts would first consist of the creation of a 3D CAD model of the part. This model would include considerations regarding tool access, edge fillets, and tolerances. Once the CAD model is completed, the part is transferred into the Computer-Aided Manufacturing (CAM) software where toolpaths are generated by defining how the machine should cut the part, including roughing, finishing, drilling, and profiling operations. Then, appropriate tools are selected, and the G-code file is produced. After all the software work has been prepared, the material billet is firmly clamped into the CNC and the program is run. Finally, once the CNC is complete, the part is deburred, cleaned, and inspected.

16.1.5. Fuselage & Tail

The 2 m fuselage skin and its internal structure are made from CFRTP-PEEK, as well as the tail structure. Two other parts are made from aluminium, which are the internal thrust frame at the rear, which carries the engine loads into the airframe, and the 1.5 m nose cone. Because the airframe combines composite

and metallic parts, the manufacturing plan covers both, and in particular how they are made, joined and protected where they meet.

Manufacturing process
The CFRTP-PEEK parts are produced by compression moulding, which allows both fuselage shells and flat tail surfaces to be manufactured using a single process. Pressing the laminate between heated mould halves also ensures uniform consolidation and a void-free, high-strength structure. The fuselage is moulded as shells, tail surfaces are formed directly, and internal ribs and frames are stamp-formed from flat laminate. As PEEK is a thermoplastic, the parts are joined using fusion welding, where interfaces are locally melted and pressed together to form bonds comparable to the parent material, reducing the need for fasteners and adhesives and lowering structural mass.

The aluminium nose cone and thrust frame are manufactured using established aluminium processes. The nose cone is stretch formed from sheet metal over a die, while the thrust frame is CNC-machined from a billet to withstand engine loads without joints. Both components are mechanically fastened to the composite fuselage to allow disassembly for engine access and assembly.

Thin-skin manufacturing constraints
The fuselage and tail skins are only 0.8 mm thick (a few laminate plies), which strongly influences manufacturing. Their low thickness makes them prone to distortion and difficult to consolidate uniformly, so they are produced in rigid matched-die tooling with tightly controlled temperature and pressure. Wherever possible, skins are co-moulded with stiffeners to provide support during manufacture. Joining is performed using resistance or induction welding with controlled local heat input to avoid overheating or damaging the thin laminate.

Fastening is the main structural constraint. Although most of the airframe is fusion welded, bolts are required at removable interfaces such as the aluminium nose cone, thrust frame, engine mount, and avionics, payload, and tank access panels. A 0.8 mm laminate cannot carry bolt loads directly, as clamping forces would cause crushing or tear-through. Fasteners are therefore only used in reinforced regions, created by local ply build-ups, bonded doublers, or embedded metal inserts. Where possible, loads are transferred into internal frames, ribs, and the thrust frame, which are better suited to point loads, and load-spreading washers and backing plates are used to distribute forces.

Coatings
Wherever the aluminium parts touch the carbon-fibre composite, meaning the nose cone and the thrust frame against the CFRTP-PEEK fuselage, there is a risk of galvanic corrosion. This happens because carbon fibre and aluminium form a galvanic couple that corrodes the aluminium. To prevent this, the aluminium surfaces are anodised and primed, and an insulating barrier such as a glass-fibre layer or sealant is placed at the interface, with isolating sleeves and washers at the fasteners. This breaks the electrical contact between the two materials.

Separately, the parts near the engine are exposed to high temperatures during firing. The aluminium thrust frame and the surrounding structure are therefore given a thermal barrier coating to protect them from the engine's radiated heat, since aluminium loses strength as it heats up and the PEEK matrix has an upper service temperature. This coating keeps these parts within their allowable temperature limits during operation.

16.1.6. Electric Propulsion unit & Avionics
This subsystem requires no manufacturing, as the electric propulsion components, the battery, and the avionics are all Commercial Off-The-Shelf (COTS). Work therefore reduces to selection, procurement and integration. Components are chosen so they meet the power, mass and performance budgets and work well together. This means matching the motor, ESC and propeller, using a common supply voltage, and making sure the avionics can interface with the chosen flight controller. Where possible the team uses well-established suppliers, as this keeps the parts easy to source and reliable for the prototype. The only parts that need to be made in-house are the mounting brackets that attach this hardware to the airframe, which are produced together with the rest of the structural parts. Final assembly and wiring are then covered in the integration chapter.

16.2. Assembly Process & Workflow *Author(s): Ivan, Paul*

The overall production and assembly of the UAV follows a phased, dependency-driven workflow, where independent components are manufactured in parallel and progressively converge into fully integrated subsystems. Final assembly is carried out in a strictly ordered sequence to ensure compatibility and accessibility of all interfaces.

16.2.1. Parallel Component Production

At the start of the manufacturing process, all components from each sub-assembly are manufactured simultaneously in independent production streams. These cover engine additive manufacturing, the propulsion feed system (including tank forming and welding, piping, and procurement of off-the-shelf valves), wing components (including rib, spar, and skin manufacturing), CNC machining of the folding mechanism parts, fuselage and tail moulding and stamp forming, and procurement of the off-the-shelf electric propulsion unit and avionics. Because these streams are independent, they run concurrently and set the pace of the schedule together rather than one after another.

16.2.2. Sub-Assembly Integration

Once the individual parts are ready, they are built up into four sub-assemblies before final assembly. The propulsion module is assembled first, with the engine bolted to the aluminium thrust frame and the tanks, piping and valves connected into the feed system. Assembling the propulsion system as one module reflects the reusability requirement, since it can be removed and refitted as a unit. The fuselage and tail form the airframe sub-assembly, where the moulded fuselage shells are fusion welded together with their internal frames and ribs, the tail is welded on, and the load-spreading inserts for the bolted joints are fitted. The wing sub-assembly is built by joining the spars and ribs into the wing structure, attaching the upper and lower skins, and fitting the folding mechanism. Finally the avionics and electric propulsion unit are mounted onto their brackets and the wiring harness is laid out, so this sub-assembly arrives at final assembly largely pre-wired.

16.2.3. Final Assembly & Integration

Final assembly joins the sub-assemblies in an order set by access, so each part can still be reached when it is installed. The feed system and propulsion module are fitted into the open fuselage and mounted to the thrust frame first, as they sit deepest inside. The avionics, battery and electric propulsion unit are then installed and the wiring is connected, followed by the propellant feed lines between the tanks and the engine. With the internal systems in place, the wings are attached to the fuselage through the folding mechanism. The access panels and the nose cone are fitted last, since they close off the structure and must remain removable for later access.

16.3. Sustainability In Manufacturing, Assembly, & Integration *Author(s): Ivan, Paul*

Sustainability influences three main aspects of the manufacturing plan: material selection, process waste, and end-of-life disassembly.

Aluminium is used wherever possible due to its high recyclability, including in the nose cone, thrust frame, propellant tanks, and wing and folding mechanism components. CFRTP-PEEK is reserved for the fuselage and tail where low weight is required, as outlined in Chapter 10. Unlike thermoset composites, which cannot be remelted once cured, CFRTP-PEEK is thermoplastic and can be reheated and reprocessed, allowing offcuts and end-of-life parts to be reground and reused rather than sent to landfill. Aluminium and the Inconel 718 engine are also fully recyclable via established metal recovery streams, ensuring the large majority of the structure can be recycled.

Manufacturing processes are selected to minimise waste. The engine is produced via laser powder-bed fusion, a near-net-shape method that uses only the powder needed for the part and recovers the rest for the next build, wasting far less material than machining from solid billet. Compression moulding generates minimal scrap, and remaining thermoplastic offcuts and aluminium machining chips are recyclable. Fusion welding of composite parts further avoids the adhesives and solvents that bonded joints would require.

Assembly strategy supports reuse and recycling. The propulsion module is removable and designed to survive at least ten firings, reducing replacement frequency. The use of welds and mechanical fasteners, rather than permanent bonding, enables disassembly for repair and end-of-life separation into clean material streams for recycling.

17 | Development & Production Plan

This chapter discusses the development % production plan after this conceptual design phase. It will also include the cost breakdown.

17.1. Cost Breakdown *Author(s): Victor*

In this section, a detailed overview of the VAPOR academic scale prototype cost will be given. A more in-depth analysis on the entire VAPOR programme and mission cost will be offered in Section 17.2, including not just cost, but more advanced econometrics. Project VAPOR is unique when it comes to its cost, as it is the first-ever UAV powered by a liquid bi-propellant engine, and thus it contains different expenses.

17.1.1. Methodology

The stakeholders of the VAPOR project have allocated a total budget of €30,000 for developing an academic scale prototype/ proof of concept. This budget shall include all aspects related to proving the viability of the VAPOR mission, which also includes ground-station infrastructure, propellant expenses and manufacturing cost. Compared to the last cost breakdown presented in the Baseline report, this time, no empirical and statistical relationships will be used. All information regarding the cost of the VAPOR mission will be presented and motivated. Let us now start with a simple breakdown of the total cost, C_{total}:

$$C_{total} = C_{design} + C_{testing} + C_{UAV} \tag{17.1}$$

Here, C_{design}, represents the total design cost, $C_{testing}$ consists of the total testing cost, such as testing facilities, propellants and other consumables used for system testing. c_{UAV} is the total UAV cost, including materials, off-the-shelf components, manufacturing costs, etc.
The first term in Equation 17.1, C_{design}, is 0. The human resource design cost is free due to the student-run nature of the academic scale prototype. This statement will no longer be true in a full-scale production phase of the VAPOR programme, and design human-resource costs will have to be accounted for.

$C_{testing}$ represents the total cost of testing the VAPOR system. Testing costs will be broken down into testing campaigns. In the following equation, each term represents the cost of a single testing campaign:

$$C_{\text{testing}} = C_{\text{PS}} + C_{\text{WT}} + C_{\text{EPS}} + C_{\text{Struct}} + C_{\text{GS}} + C_{\text{LP}} + C_{\text{LN}} \tag{17.2}$$

where C_{PS} is the propulsion system testing cost, C_{WT} is the wind tunnel testing cost, C_{EPS} is the electrical power system testing cost, C_{Struct} is the structures testing cost, C_{GS} is the ground station testing cost, C_{LP} is the launch pad testing cost, and C_{LN} is the landing net testing cost. A budget of only €5000 may not seem enough for all of the testing procedures presented in Equation 17.2. To account for this, the VAPOR team will heavily rely on the academic nature of the prototype. All testing campaigns will be done in collaboration with the university and other stakeholders of the project, such that facilities, infrastructure, and consumable expenses shall be either fully supported by sponsoring parties or shared between collaborators.

17.1.2. Testing Costs

The most expensive testing campaign will be the rocket propulsion system test, meaning hot fires of the main liquid bi-propellant engine. To reduce costs and ensure budget compliance, hot fire tests will be done in parallel with the Delft-based student team *DARE* at testing facilities provided by the Dutch Aerospace Research Institution *Nederlands Lucht-en Ruimtevaartcentrum* (NLR). This means that the only costs that shall be accounted for are propellant costs, all other facilities and necessities being provided by the sponsoring party.

The costs for the propellant are highly influenced by the cost of the peroxide, which is priced at 429 €/kg. With an O/F of 4, this means that for two hot-fire tests, the HTP cost will be 4129 €, according to HTP providers [1]. Using up-to-date data on kerosene prices and the aforementioned O/F ratio, 2.4 kg of Kerosene

[1] https://labdirect-llc.square.site/product/high-test-peroxide-htp-hydrogen-peroxide-85-h2o2-7722-84-1/136, Last Accessed: June 15

would cost only 8.7€[2]. The rocket will be using RP-1, but for testing purposes, kerosene is deemed sufficient as it is easier to procure. This price is quoted as bulk price, and therefore a margin of 100% shall be added to the cost of kerosene, meaning a total of 17.4€ is reserved. Lastly, the smallest volume of Helium that can be bought, already pressurised at 300 bar, is $1.81 m^3$, which is priced at 340€ [3]. Adding the HTP, kerosene, and helium costs gives a total propellant cost allocation of 4486.4€ for the two hot-fire tests.

Up next, the electrical power system shall be tested in collaboration with *AeroDelft*, as they are already testing an electric propulsion system powered by Hydrogen. All of the testing facilities and necessities will be provided by the sponsoring parties, meaning EPS testing costs will be accounted for as 0. Continuing in the same manner, structural tests will be done in collaboration with the Aerospace Structures and Materials Laboratory at TU Delft, thereby having 0 costs for the academic scale prototype. Launch pad tests, ground station tests and landing net test costs will not be accounted for, as they would also be tested in collaboration with NLR. Therefore, the only costs for testing of the academic scale prototype are consumables for the hot-fire tests, which are summarised in Table 17.1.

Table 17.1: Estimated propellant-related costs for two hot-fire tests.

Propellant	Mass [kg]	Density	Volume	Price per kg
HTP 85%	9.62	1.36 kg/L	7.08 L	429€/kg
Kerosene	2.40	0.80 kg/L	3.00 L	7.25€/kg
Helium	0.323	0.1785 kg/m^3	1.81 m^3	1053€/kg
Total cost	–	–	–	**4486.4€**

The rest of the budget, meaning 513.6€, will be spent on manufacturing a 1:10 scale model of the UAV for wind-tunnel testing purposes.

17.1.3. UAV cost

The total cost of the academic scale prototype represents the total sum of the costs needed to end up with the final product. Total remaining budget is 25,000€, which needs to cover manufacturing, components, material and labour. Therefore, the following equation breaks down the total UAV cost:

$$C_{\text{UAV,total}} = C_{\text{manufacturing}} + C_{\text{components}} + C_{\text{materials}} + C_{\text{labour}} \tag{17.3}$$

Again, labour costs are assumed to be 0. All students who are stakeholders in the VAPOR project will personally manufacture the model. All other costs are cannot be assumed to be 0.
Using the manufacturing methodology presented in Chapter 16, and the estimated price per kilogram of aluminium and CFRTP-PEEK, Table 17.2 presents the estimated material and manufacturing costs for the main airframe materials. The aluminium components include the nose cone, wing, folding mechanism, and thrust frame, while the CFRTP-PEEK is used for the fuselage and tail.
A bottom-up cost estimation approach is used, in which the total cost is obtained by summing the relevant cost elements. This follows standard cost-estimating practice, where a cost estimate is built up from individual cost elements using available technical and pricing data [72, 73]. Since detailed supplier quotations for manufacturing are not yet available, the manufacturing cost is approximated by applying a manufacturing factor to the raw material cost, as shown in Equation 17.4.

$$C_{\text{manufacturing},i} = k_{\text{manufacturing}} C_{\text{material},i} = k_{\text{manufacturing}} m_i p_i \tag{17.4}$$

where m_i is the mass of material i, p_i is the price per kilogram of material i, and $k_{\text{manufacturing}}$ is the manufacturing cost factor. For this preliminary estimate, a value of $k_{\text{manufacturing}} = 1.0$ is assumed. This means that the manufacturing cost is taken to be equal to the raw material cost.
The total material and manufacturing cost is therefore calculated as:

[3] https://www.bocgases.co.uk/shop/helium-n5-0-cp-grade-cylinder-110744-v, Last Accessed: June 15

$$C_{\text{total}} = \sum_i \left(C_{\text{material},i} + C_{\text{manufacturing},i} \right) = \sum_i \left(m_i p_i + k_{\text{manufacturing}} m_i p_i \right) \tag{17.5}$$

Table 17.2: Estimated material and manufacturing costs for the aluminium and CFRTP-PEEK airframe components.

Material	**Main components**	**Mass [kg]**	**Price [€/kg]**	**Material cost [€]**	**Manufacturing cost [€]**	**Total [€]**
Aluminium 6061-T651	Wing, Nose Cone, Folding Mechanism	11.224	15.86	177.98	177.98	355.95
CFRTP-PEEK	Fuselage and tail	3.800	203.98	775.12	775.12	1550.24
Total	–	15.024	–	**953.10**	**953.10**	**1906.19**

The total estimated cost for the aluminium and CFRTP-PEEK airframe material and manufacturing is therefore 1906.19 €. This value is included in the total academic-scale prototype cost estimate.

17.1.4. Commerical Off-The-Shelf Components Cost

The rest of the budget shall be allocated towards buying the necessary COTS components. Table 17.3 shows the price of the main components that will be present in the UAV. The total cost is therefore ≈10,150 €. Some comments need to be made about the total cost of the academic scale prototype. There is a budget of ≈12,000 € left over. This budget is going to be preserved as a margin for unexpected costs and costs that have not been accounted for, such as low-voltage wiring, switches, landing net, take-off pad, etc.

Table 17.3: Priced BOM components

Component	Price [EUR]	Link/Comment
Main battery	140.00	link
Electronic Speed Controller (ESC)	110.00	link
Electric cruise motor	150.00	link
Cruise propeller	20.00	link
Flight controller	230.00	link
GPS receiver	52.20	link
Cellular / SIM module	120.00	link
2 x Pitot-static airspeed sensor	275.00	link
Control-surface actuators	750.00	link
Power distribution unit / splitter board	53.2	link
CAN splitter / CAN bus hardware	50.00	link
Propulsion pressure and temperature sensors	1000.00	Private Quotation
Thrust chamber + nozzle	5000.00	Assumption
Catalyst bed / catalyst	50.00	Assumption
Feed-line check valves	1000.00	Assumption
Relief valves	200.00	Assumption
Pressure regulators	300.00	Assumption
Emergency parachute/recovery system	1500.00	link
Total	**10,150.40**	

17.2. Return On Investment *Author(s): Victor*

In this section, the cost of the VAPOR programme will be estimated, and a first-order calculation for the Net Present Value (NPV) and Opportunity Cost of Capital (OCC) will be given, to motivate potential investors.

Section 17.1 presented the estimated cost for the academic scale prototype and showed compliance with the budget provided by the stakeholders for the proof-of-concept model. The assumptions that labour and design costs are 0 are still appropriate for the prototype, but for a full-scale programme, this is no longer the case.

Programme cost estimation techniques from NASA and the United States government [72, 73] distinguish between recurring and non-recurring costs and use learning curves to model the reduction in recurring costs as production volume increases. A realistic but hypothetical business example will now be presented.

For the purpose of this first-order business case, a constant annual production rate of 300 VAPOR units is assumed. This corresponds to a low-volume aerospace production programme rather than a mass-manufacturing consumer drone product. The academic scale prototype cost of €30,000 is therefore treated only as a lower-bound reference. In commercial production, additional costs arise from paid labour, supplier margins, quality assurance, qualification testing, warranty provisions, production tooling, documentation, compliance activities, and general overhead.

The first production year is assumed to have a recurring manufacturing cost of €48,000 per unit. As production stabilises, it should reduce this cost to €43,500 per unit by Year 5. This gives an average recurring manufacturing cost of approximately €45,600 per unit over the five-year evaluation period. This estimate excludes the cost of the payload, which may be obtained separately depending on the customer application.

Table 17.4: Hypothetical recurring manufacturing cost development for 300 units/year.

Year	Production [units/year]	Unit manufacturing cost [€]	Annual manufacturing cost [€M]
1	300	48,000	14.40
2	300	46,500	13.95
3	300	45,500	13.65
4	300	44,500	13.35
5	300	43,500	13.05

In addition to the direct recurring manufacturing cost, the commercial programme requires fixed yearly expenditures for engineering support, quality assurance, administrative overhead, sales, maintenance support, and warranty management. These are estimated at €4.5 million in Year 1, increasing by 2% annually, due to inflation or other unaccounted expenses. Therefore, the all-in recurring cost including fixed programme overhead is approximately €63,000 per unit in Year 1 and decreases to approximately €59,700 per unit in Year 5.

The non-recurring initial investment is estimated at €18 million. This includes full-scale design finalisation, industrialisation, production tooling, manufacturing jigs, propulsion qualification, safety validation, documentation, initial spares, and working capital. The assumed breakdown is shown in Table 17.5. This value should be interpreted as a preliminary top-down estimate rather than a supplier-quoted development cost.

Table 17.5: Estimated non-recurring initial investment for commercial production.

Cost element	Estimated cost [€M]
Design finalisation and industrialisation	5.0
Qualification, compliance, and safety validation	4.0
Tooling, jigs, and manufacturing equipment	4.0
Initial inventory and working capital	3.0
Quality system, spares, and support equipment	2.0
Total initial investment	18.0

The selling price is determined using value-based pricing rather than simple cost-plus pricing. VAPOR is positioned as a rapid-response surveillance asset, not as a conventional low-cost multirotor. A base selling price of €95,000 per unit is therefore assumed. This places VAPOR above conventional electric public-safety drones, but below larger military or high-end hybrid UAV systems. At a production cost of €48,000–€43,500 per unit, this corresponds to a gross margin of approximately 49–54%, before fixed overhead, taxes, and financing costs.

The annual Free Cash Flow is estimated using

$$FCF_t = (P - C_t)Q - F_t \tag{17.6}$$

where P is the selling price, C_t is the unit manufacturing cost in year t, Q is the annual production quantity, F_t is the fixed yearly programme cost, and T_c is the corporate tax rate. A Dutch corporate tax rate of 25.8% is assumed for profits above the first tax bracket. Depreciation, terminal value, and detailed working-capital recovery are neglected to keep the calculation first-order.

Table 17.6: Base-case five-year free cash-flow estimate.

Year	Units	Revenue [€M]	Manufacturing cost [€M]	Fixed cost [€M]	FCF [€M]
0	–	–	–	–	-18.00
1	300	28.50	14.40	4.50	7.12
2	300	28.50	13.95	4.59	7.39
3	300	28.50	13.65	4.68	7.54
4	300	28.50	13.35	4.78	7.70
5	300	28.50	13.05	4.87	7.85

The opportunity cost of capital represents the minimum return required by investors to justify investing in the VAPOR programme rather than in an alternative investment with similar risk. In corporate finance, this is commonly estimated using the weighted average cost of capital (WACC), which combines the required return from equity investors and lenders. This approach follows the standard valuation framework presented in *Fundamentals of Corporate Finance* by Brealey, Myers and Marcus, where investment projects are evaluated by discounting future cash flows at a rate that reflects their risk [74]. In this context, the WACC is used as the discount rate for the NPV calculation and as the benchmark return that the project must exceed.

Since VAPOR is an early-stage aerospace hardware programme, the financing structure is assumed to consist of 80% equity and 20% debt. Equity represents capital provided by investors who take ownership risk, while debt represents borrowed capital that must be repaid. The cost of equity, r_e, is estimated using a modified capital-asset-pricing model (CAPM). The standard CAPM estimates the return required by equity investors based on the risk-free rate, the market risk premium, and the systematic risk of the project. A technology risk premium is added to account for the additional uncertainty associated with early-stage aerospace hardware development:

$$\mathbb{E}[R] = r_f + \beta(\mathbb{E}[R_m] - r_f) + r_{\text{tech}} \tag{17.7}$$

Here, r_f is the risk-free rate, representing the return on a low-risk investment, such as government bonds. The term $\mathbb{E}[R_m] - r_f$ is the market risk premium, which represents the additional return investors expect from investing in the market rather than in a risk-free asset. The parameter β is the project beta, which measures how sensitive the project return is to market movements. A beta larger than one indicates that the project is riskier than the overall market. Finally, r_{tech} is an additional technology risk premium used to account for the technical, regulatory, and adoption risks specific to VAPOR.

A risk-free rate of $r_f = 3.4\%$, a market risk premium of $\mathbb{E}[R_m] - r_f = 5.5\%$, a project beta of $\beta = 1.4$, and a technology risk premium of $r_{\text{tech}} = 3.0\%$ are assumed. This gives a cost of equity of:

$$r_e = 3.4\% + 1.4 \cdot 5.5\% + 3.0\% = 14.1\% \tag{17.8}$$

The cost of debt, r_d, is the interest rate required by lenders. Since interest payments reduce taxable income, the after-tax cost of debt is calculated as $r_d(1 - T_c)$, where T_c is the corporate tax rate. Assuming a pre-tax cost of debt of $r_d = 8.0\%$ and a corporate tax rate of $T_c = 25.8\%$, the opportunity cost of capital is calculated as:

$$\text{OCC} = \text{WACC} = 0.8r_e + 0.2r_d(1 - T_c) \tag{17.9}$$

$$\text{OCC} = 0.8(14.1\%) + 0.2(8.0\%)(1 - 25.8\%) = 12.5\% \approx 13.0\% \tag{17.10}$$

The assumed project beta of 1.4 is higher than that of a mature aerospace and defence company because VAPOR includes additional technology, regulatory, and market-adoption risk associated with the liquid bi-propellant propulsion system. Therefore, investors would require a higher expected return to compensate for this additional uncertainty.

Using the cash flows in Table 17.6, the five-year net present value is calculated as:

$$\text{NPV} = -I_0 + \sum_{t=1}^{5} \frac{\text{FCF}_t}{(1+\text{OCC})^t} \tag{17.11}$$

In this equation, I_0 is the initial investment, FCF_t is the free cash flow generated in year t, and OCC is the opportunity cost of capital used to discount future cash flows. Discounting is necessary because money received in the future is worth less than money received today, especially when the project is risky. The resulting five-year NPV is:

$$\text{NPV} = €\,8.3 \text{ million}$$

The Internal Rate of Return (IRR) is the discount rate at which the NPV becomes zero. It can therefore be interpreted as the expected annual return generated by the project. For VAPOR, the corresponding IRR is approximately 30.3%. The project alpha is defined here as the difference between the IRR and the opportunity cost of capital:

$$\alpha = \text{IRR} - \text{OCC} \tag{17.12}$$

$$\alpha = 30.3\% - 13.0\% = 17.3\% \tag{17.13}$$

This positive alpha indicates that, under the base-case assumptions, the commercial VAPOR programme generates a return significantly above the required opportunity cost of capital. The result is therefore financially attractive. However, this conclusion is highly sensitive to the assumed annual production volume of 300 units and the selling price of approximately € 95,000 per unit. If production volume is lower, if regulatory or development costs increase, or if the achievable selling price approaches that of conventional electric UAVs, the NPV would decrease substantially.

17.3. Post-DSE Development Logic *Author(s): Vladimir*

This section highlights the project design and development logic visible in Figure 17.1. It is a diagram showing the order in which all activities post-Design Synthesis Exercise (DSE) are to be scheduled. Each phase is represented by a parent block such as "Assembly" or "Certify the UAV" and broken down into multiple steps or actions. These can either be all performed sequentially, in parallel or mixed. Steps taken in parallel are shown as originating directly from their parent block and placed one under another. For each of these branches, a sequence of steps can unfold. Each block is aimed to be technically specific to the project and relevant for each larger phase from the end of the DSE to the end of life.

17.4. Post-DSE Project Gantt Chart *Author(s): Kyle, Kaj*

To define the steps taken after this conceptual design phase, a project Gantt has been created, shown in Figure 17.2. This figure shows the next phases of the design with an entry into service in mid-September 2027.

The steps displayed in the Gantt chart are in accordance with the time budget set up in the baseline report [2]. Ensuring that the testing phase is finished in 6 months after the final design review.

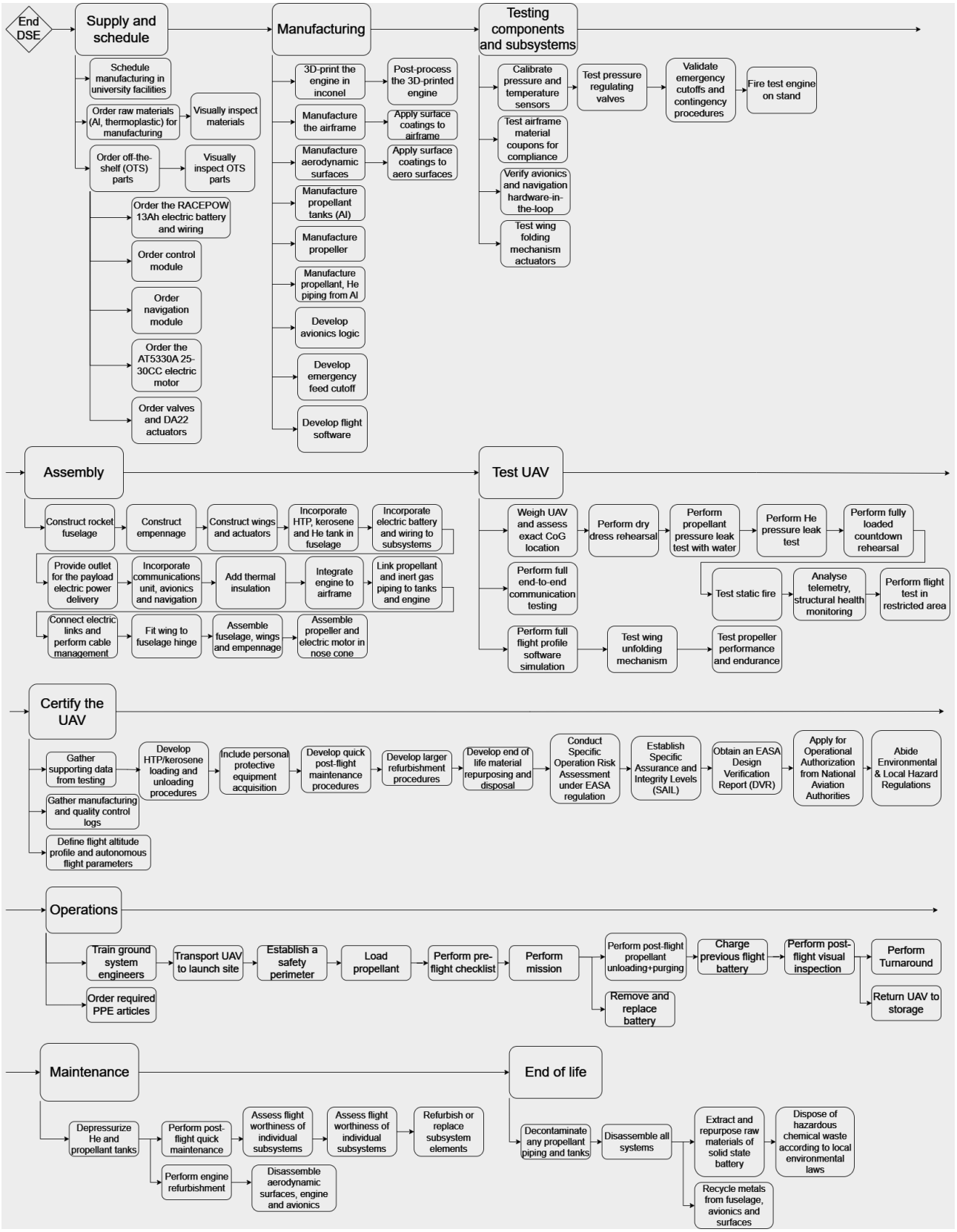

Figure 17.1: Project design and development logic

	ID	Name	Duration
1	**1**	**Class III Detailed Design**	**63 days**
2	1.1	Propulsion System	56 days
3	1.2	Aerodynamics & Structures with FEM and CFD	56 days
4	1.3	Avionics & Control	56 days
5	1.4	Launch Tower	34 days
6	1.5	Recovery Net	24 days
7	1.6	Detailed CAD Design	20 days
8	1.7	Design Review	5.5 days
9	**2**	**Procurement & Component Testing**	**35 days**
10	2.1	Procurement of Specialised Components	24 days
11	2.2	Component Testing	11 days
12	**3**	**Manufacturing & Integration**	**40 days**
13	3.1	Airframe Manufacturing	35 days
14	3.2	Propulsion System Manufacturing + Integration	40 days
15	3.3	Avionics Wiring and software integration	33.375 days
16	3.4	Recovery Net Manufacturing	33 days
17	3.5	Launch Tower Manufacturing	33 days
18	3.6	Ground systems manufacturing	29 days
19	3.7	Software Development	35 days
20	**4**	**Testing Campaign**	**59 days**
21	4.1	Subsystem Tests	14 days
22	4.2	System tests	14 days
23	4.3	Integrated System tests	14 days
24	4.4	Operations Testing	14 days
25	4.5	Design Correction	18 days
26	**5**	**Flight Testing**	**58 days**
27	5.1	Flight Readiness Review	10 days
28	5.2	Certification Flight Test	18 days
29	5.3	Type Certification Review	30 days
30	**6**	**Operations**	**61 days**
31	6.1	settng up ground training	22 days
32	6.2	setting up supply chain	22 days
33	6.3	Acceptance testing	22 days
34	6.4	Customer documentation	22 days
35	6.5	First Customer Deliveries	37 days
36	6.6	Entry Into Service	0 days

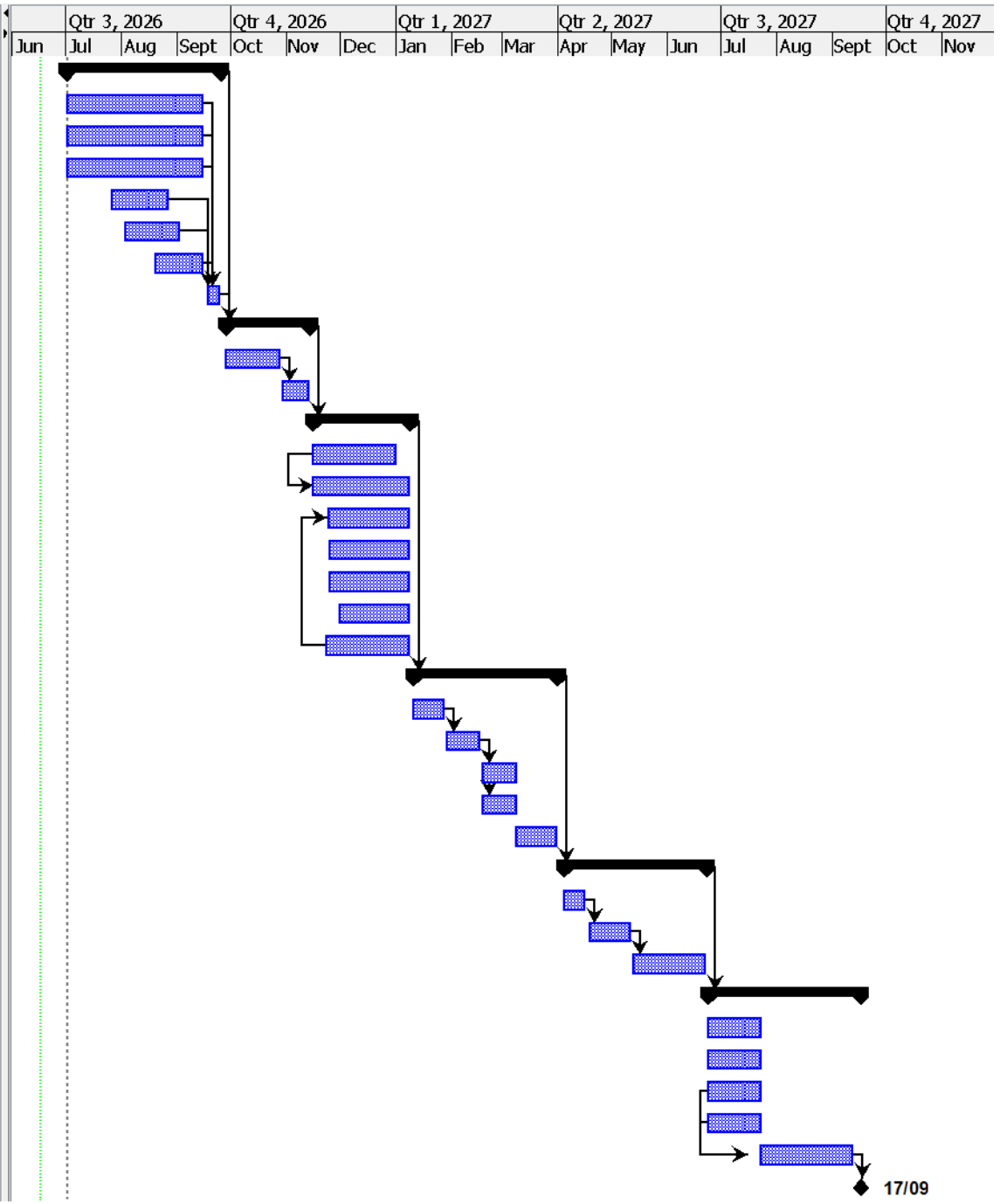

Figure 17.2: Project Gantt Chart

18 | Sustainable Development Strategy

To ensure sustainable development and design, it is important to define appropriate strategies. Building on the work of Armeli et al. [1], this chapter further specifies the steps for sustainable design. First, the sustainability strategies are defined in Section 18.1. Next, hydrogen peroxide safety procedures are outlined, followed by end-of-life disposal strategies in Section 18.3. Finally, Section 18.4 evaluates VAPOR's sustainable competitiveness against its competitors using a simplified Life Cycle Assessment (LCA).

18.1. Sustainable Strategies *Author(s): Ivan*

This section will describe the sustainable strategies put in place throughout the entire design of VAPOR. They were first defined by Armeli et al. [1] and are further described here. Each of these strategies is linked to the primary United Nations Sustainable Development Goal (SDG). These SDGs are intended to guide countries, companies and entities towards a more sustainable development [1].

Propulsion and Fuel Selection

- 98% Hydrogen peroxide shall be used as an oxidiser: Unlike conventional hydrocarbon combustion, hydrogen peroxide is considered cleaner because its main by-products are oxygen and water. (SDG 13: Climate action)
- Non-cryogenic fuel selection: Unlike cryogenic oxidisers, hydrogen peroxide can be stored as a liquid in ambient conditions, reducing the need for energy-intensive cooling systems. (SDG 7: Affordable and Clean Energy)
- Unlike other hypergolic oxidisers, hydrogen peroxide presents lower toxicity, improving the safety and environmental impact related to the handling. (SDG 3: Good Health and Well Being)

Material and Manufacturing Process

- At least 25% of structural materials shall be recyclable or bio-based. (SDG 12: Responsible Consumption and Production)
- At least 25% of structural materials (e.g., carbon composites) shall be sourced from recyclable sources. (SDG 12: Responsible Consumption and Production)

Operational Sustainability

- The UAV shall be used more than 10 times with minimal refurbishment: The UAV should be designed to optimise the amount of resources needed for refurbishment between flights. This includes designing parts for easy inspection. (SDG 12: Responsible Consumption and Production)
- The environmental impact per kg of payload delivered shall be calculated. (SDG 13: Climate action)
- Operational emissions per flight hours shall be quantified. (SDG 13: Climate action)

Design Strategy for Sustainability

- Design for disassembly: The design of the UAV should be optimised for the disassembly of components and parts. (SDG 12: Responsible Consumption and Production)
- Design for repair optimisation: Design considerations are taken for repair optimisation. (SDG 12: Responsible Consumption and Production)
- Design for reuse of high-value components: The reusability of high-value components should be considered from the early stages of the design to maximise the component lifetime. (SDG 12: Responsible Consumption and Production)
- Design considerations on bonding techniques: Design should avoid permanent bonding techniques, which will make the separation of materials impossible at later stages of its recyclable process. (SDG 12: Responsible Consumption and Production)
- Hydrogen peroxide component compatibility: Materials and designs should be assessed concerning their compatibility with hydrogen peroxide to minimise component replacement or refurbishment. (SDG 12: Responsible Consumption and Production)
- Design for material optimisation: The weight of the UAV and hence the amount of material used should be minimised. This includes the material incorporated into the final assembly as well as the material consumed during the production and manufacturing processes. (SDG 12: Responsible Consumption and Production)

[1] un.org [Date Accessed: June 11]

- Documentation of recyclable vs non-recyclable materials: Documentation regarding the component identification into parts/ components that can be reused, reused with refurbishment, recyclable, non-recyclable and scrapped. (SDG 12: Responsible Consumption and Production)
- Supplier sustainability: Suppliers should be chosen considering their material traceability, environmental documentation and overall sustainability practices. (SDG 12: Responsible Consumption and Production)
- Design for transportation efficiency: The UAV should be designed considering its environmental impact related to the transport, storage and deployment of it. (SDG 13: Climate action)

18.2. Hydrogen Peroxide Safety Procedures *Author(s): Kyle*

Due to the use of hydrogen peroxide, it is important to define the safety measures that need to be taken such that operators do not come to harm. Ventura and Durant [75] describe safety measures that need to be considered, and the procedures shall be defined from these. The following measures will be taken to ensure safe operations for personnel and also provide mitigation strategies in case of accidents.

- Any personnel handling hydrogen peroxide shall wear at least non-absorbing, water-resistant clothes. The sleeves shall cover the entire length of the arms and legs. This should also include a hood. The shoes shall also be non-absorbing and water-resistant, and fit inside the pants. Nitrile gloves shall also be worn by operators.
- During handling of hydrogen peroxide, the eyes shall be protected with chemical spray goggles. The face shall be protected with a face shield.
- Large amounts of water shall be available near the site of operation for deluging.
- Eyewash stations and showers shall be available near the site of operation.

18.3. End-of-Life Disposal *Author(s): Kyle*

In this section, the end-of-life procedures shall be defined as described by Armeli et al. [1].

18.3.1. Peroxide Tanks and Feed Lines

Since hydrogen peroxide is a highly reactive substance, it is important to define the disposal strategy of the tanks and the feed lines, which all contain traces of hydrogen peroxide. Terlizzi and Streim describe these considerations for safe peroxide handling [76] along with the safety guidelines by Rocket Laboratory Safety and Design Manual [77]. With these, the end-of-life strategy can be defined.

First, the tanks shall be emptied into compatible storage units. The peroxide in these units will be diluted and disposed of as specified by section 5.6.5.4 of the Rocket Laboratory Safety and Design Manual [77].

The next step is cleaning the tanks. This will be done in accordance with 5.6.4.5 from the Rocket Laboratory Safety and Design Manual [77]. First, the tanks and fuel lines are disassembled and cleaned using trichloroethylene. This will then be drained and rinsed with hot water. Subsequently, these parts will be put in a 1/15 normal sodium hydroxide solution. This can then be rinsed with deionised water, and the parts can now be decomposed and recycled for future use.

18.3.2. Solid State Battery

As described in Chapter 8, the battery that is used is a solid-state battery (SSB). Since this is a new technology, clear end-of-life procedures and guidelines have not been developed yet. However, recent studies have been performed on the recycling of SSBs compared to traditional Lithium-Ion Batteries (LIB) [78, 79]. Based on this, the end-of-life procedure shall be defined qualitatively.

Before defining the end-of-life procedure, the regulations need to be made clear. Since this solid-state battery uses LiPo (lithium polymer), Nickel, Cobalt, and Manganese, it shall be classified as a lithium-based battery. For lithium-based batteries, the European Commission has set the mandatory goal of 70 % recycling efficiency by 2030 [2]. In these same regulations, the material recovery goals for Cobalt and Nickel are 95 % by 2031 and 80 % for Lithium.

The first step in the end-of-life procedure is the pre-treatment. This consists of discharge and disassembly. The discharge can be done by connecting it to an external circuit, where the remaining energy can be used to avoid wasting energy. Then, the battery can be disassembled. This is done through removing the protective outer layer and all of its wiring and electronics. The next step is mechanical separation and processing.

[2] European Commission Battery Recycling Goals. [Date Accessed: June 15]

This involves separating the major components using shredding, crushing and sieving [79]. Furthermore, to separate the active materials, mild thermal treatment will be applied. This will result in "black mass", which is a mix of cathode and anode powders. This black mass can be separated by using hydrometallurgy, which is the next step.

Hydrometallurgy is the primary recycling step for recovering various chemicals from the solid-state battery. This method uses water-based chemical reactions to separate the various metals in the black mass [79]. For lithium-ion batteries (LIB), it allows a recovery rate higher than 90 % [79]. Research from Li et al. shows that recovery rates for Nickel, Cobalt, and Manganese are 96 %, 81 %, and 92 %, respectively, from waste ternary lithium-ion batteries [80].

After hydrometallurgy, a liquid containing the metals is obtained. This will be separated using hydrothermal regeneration. Here, the metals are placed in an aqueous solution for several hours. After this, some washing, filtering, and a brief heat-treatment are applied [79]. The recovered metals for this can now be reused in other applications.

While the recovery rates do not meet the goals of the European Commission yet, new technologies are being researched due to the high potential of solid-state batteries. The method described is not fixed and is open to the change of these new technologies.

18.3.3. Recycling of Structural Material, Off-The-Shelf Components, and Other Components

In this section, the recycling of all other components of VAPOR will be discussed. First is the airframe. The airframe will be made of aluminium and thermoplastic carbon fibre. Aluminium is one of the most recycled materials on Earth, making it a sustainable option [3]. After the operational lifetime, the airframe can be disassembled and all of the aluminium recycled. Moreover, due to the recyclability of aluminium, it is also possible to manufacture it out of recycled aluminium. However, part of the airframe will also be made of thermoplastic carbon fibre. The recycling of which has been proven to be a challenge [81]. Ateeq provides a review of the current recycling methods of carbon fibre. They show that pyrolysis remains the most promising for utilisation. However, not all of the strengths can be retained [4]. This means the use of recycled carbon fibre is limited to non-critical components or in other sectors.

The second component is the propulsion system. This will be made out of Inconel and steel. Steel can be recycled easily without any loss in quality. [5]. This is done through shredding and melting of the steel. So any components made of steel can be recycled and made from recycled steel. Inconel, however, is more complicated. This is due to contamination of the fuel burned during the launch phase and the high melting point of Inconel [6]. Solutions have also been identified. These are: Vacuum Induction Melting (VIM), Electron Beam Melting (EBM), and Plasma Arc Melting (PAM). Of these, EBM has been used more frequently. However, Gruber also shows that more material defects occur during EBM [82]. This material degradation means it can not be recycled fully and, at some point, will leave the recycling chain.

The third component is the hinge mechanism. This will use gas springs and bearings. The latter of which are made of steel and, as described earlier, can be recycled fully. The gas springs consist of nitride-plated steel struts and zinc-plated ends. Nitriding is a heat-treating process that hardens the metal. This makes it more suitable for components that experience heavy loads, such as the hinge mechanism [7]. However, since it is still steel, it can be recycled fully as described earlier. The nitride coating will fully evaporate during the melting process [83]. The zinc-plated ends have similar properties, where they can be recycled in the same way as steel. The zinc-plated steel, also called galvanised steel, can be recycled with other scrap. The zinc coating volatilises early in the recycling process [8].

The fourth component is the avionics. Firstly, the working of the components inside the avionics will be checked. They can be reused if they still work without the need for recycling. In case this is not possible, a similar approach to the recycling of the batteries is needed. This is needed due to all the chemical components inside. This does not have a 100% recovery rate. However, working actuators or other electrical components will be reused in the next generation of UAVs.

The fifth component is the propeller. The propeller will be made from carbon fibre. The recycling of which

[3] International Aluminium. [Date Accessed: June 15] [4] Patsnap. [Date Accessed: June 15] [5] Steel Recycling Process. [Date Accessed: June 15] [6] Questmetals. [Date Accessed: June 15] [7] Fractory. [Date Accessed: June 15] [8] Recycling Galvanised Steel. [Date Accessed: June 15]

will be similar to that described in the recycling of the carbon fibre in the airframe section.

The sixth component is the emergency parachute. This parachute will be made of nylon [9]. While it is difficult to recycle this, this parachute can also be used in other UAVs as long as it is structurally intact. Tonsi et al. describe the methods used to recycle nylon, with mechanical recycling as the most common one. However, it is not possible to retain their original properties. The recycled nylon can therefore only be used in non-critical components or in other sectors such as recreation [84].

The seventh component is the launch tower. While the design of this launch tower is out of the scope of this conceptual design, this component will be made from steel. As explained before, this is 100 % recyclable, and it can also be used throughout the operations of multiple UAVs.

The last component is the landing net. While the design of the landing net is out of the scope of this conceptual design, these nets are usually made of synthetic polymers such as Ultra-high molecular weight polyethylene (UHMWPE) [10]. This material is challenging to recycle due to its high melt viscosity. Cao et al. show that this material can be recycled while keeping the majority of its strengths through the use of pulse vibration moulding [85]. However, this net can be reused for multiple UAVs, making it a sustainable landing option.

18.4. Sustainable Competitiveness *Author(s): Kyle*

This last section compares VAPOR with competitor UAVs, divided into electric and air-breathing categories. For a fair comparison, the same manufacturing method is assumed for all UAVs, although manufacturing has a major impact on sustainability; VAPOR's sustainable approach is outlined in Chapter 16. Resource extraction is still considered. Due to limited publicly available data, the comparison is qualitative and conducted at a general level.

The main advantage of electric UAVs is that they have no carbon emissions during operations. However, the downside is that they employ a heavy battery containing many chemicals that need careful processing. The extraction process of these chemicals should also be taken into account. Furthermore, the market analysis performed in Chapter 2 shows the competitors. One of the closest competitors to the identified market gap is the DJI Matrice 350 RTK. The energy density of this UAV equals 200 Wh/kg[11]. The battery chosen for VAPOR in Table 8.2 has an energy density of 350 Wh/kg due to the use of the new solid-state technology. This higher energy density reduces the required battery mass, which lowers the mass of all these chemicals and makes it a more sustainable option. This means that overall, in the trade-off between VAPOR and the electric UAV counterpart, a significant portion of battery mass is traded off against CO_2 and CO emissions, which are kept minimal due to the use of hydrogen peroxide as oxidiser.

Air-breathing UAVs burn fuel throughout the entirety of their mission. This means that their emissions are high compared to VAPOR or their electric competitors. Their advantage, however, is that they do not need a battery for propulsion. This makes their battery mass considerably lower as it is only needed to power the avionics equipment [86]. This also means that end-of-life procedures are more sustainable since there is no heavy battery with chemicals that need careful procedures. In Table 18.1, a qualitative overview of the sustainability comparison can be seen. The electric UAV has been taken as a 100% reference point in terms of resource extraction and end-of-life, while the air-breathing UAV is the reference point of the emissions during mission.

Table 18.1: Qualitative Sustainability Comparison

Indicators	VAPOR	Electric UAVs	Air-breathing UAVs
Emission during mission	10 - 15 % [87]	0 %	100%
Resource Extraction	50 - 60%	100 %	10 - 20 % [88]
End-of-Life	50 - 60 %	100 %	10 - 20 % [88]

From Table 18.1, it is clearer how VAPOR strikes a middle ground on sustainability among its competitors. With the use of a solid-state battery and hydrogen peroxide, it can ensure it is sustainably competitive with its competitors, as was originally proposed as a project objective.

[9] Parachute. [Date Accessed: June 17] [10] Gourock. [Date Accessed: June 15] [11] dronesmadeeasy.com [Data Accessed: June 15]

19 | Requirements Compliance Matrix

Author(s): Noah, Duco, Marco, Kyle, Kaj

Table 19.1: Compliance matrix indicating whether each requirement is satisfied (✓) or not satisfied (✗).

ID	Requirement	Status	Verification Description
REQ-STK-SAR-01	Engine shall shutdown and switch to a recovery system in case of overpressure or flight anomaly.	✗	The design did not cover the design of a recovery system.
REQ-STK-SAR-02	Propellant containment and leak detection system shall meet UN/DOT storage safety standards.	✗	The design did not cover UN/-DOT compliance
REQ-STK-SAR-03	Mission success probability shall be ≥90% considering at least 10 flights.	✗	Mission reliability can only be tested in static fire tests
REQ-STK-SAR-04	The design shall address safe handling of hydrogen peroxide, including its operational safety.	✓	Section 18.2
REQ-STK-SUS-01	The design shall make use of reusable modular engine and tank assembly.	✓	Section 7.3
REQ-STK-SUS-02	Hydrogen peroxide shall be selected as a clean oxidizer with water and oxygen as main by-products.	✓	Section 18.1
REQ-STK-SUS-03	The design shall adhere to hydrogen peroxide sustainability standards, including reusability and environmental impact.	✓	Section 18.1
REQ-STK-SUS-04	At least 25% of structural materials shall be sourced from recyclable sources.	✓	Section 18.1
REQ-STK-SUS-05	A simplified LCA shall be performed comparing the proposed liquid bi-propellant UAV to an equivalent battery-electric UAV in terms of CO_2 equivalent emissions per mission, energy density and resource use, and material footprint.	✓	Section 18.4
REQ-STK-SUS-06	Operational emissions per flight hour shall be quantified.	✓	Section 7.3
REQ-STK-SUS-07	Environmental impact per kilogram payload delivered shall be calculated.	✗	Payload delivery is not considered the function of VAPOR
REQ-STK-SUS-08	At least 25% of structural materials shall be recyclable or bio-based.	✓	Chapter 16
REQ-STK-SUS-09	The propulsion module shall be reusable for at least 10 cycles.	✓	Section 7.5
REQ-STK-SUS-10	End-of-life disposal strategy for peroxide tanks shall be defined.	✓	Section 18.3
REQ-STK-SUS-11	End-of-life disposal strategy for batteries shall be defined.	✓	Section 18.3
REQ-STK-OPS-01	The UAV shall comply with EASA Specific Category operational framework.	✓	Section 15.3
REQ-STK-OPS-02	Ground handling procedures for hydrogen peroxide shall be defined.	✓	Section 18.2
REQ-STK-OPS-03	Refueling turnaround time shall be less than 30 minutes.	✓	Section 12.2
REQ-STK-OPS-04	Required ground crew shall be less than 3 operators.	✓	Section 15.2
REQ-STK-OPS-05	Launch and recovery footprint shall be less than 20 m × 20 m.	✓	Section 15.1
REQ-STK-OPS-06	The UAV shall adhere to International Civil Aviation Organisation (ICAO) and national UAV operation regulations for experimental prototype systems.	✓	Section 15.3
REQ-STK-OPS-07	The UAV shall be able to perform all mission phases under adverse environmental conditions.	✗	The mission can only perform after weather assessment.
REQ-STK-BUD-01	Prototype development budget shall be lower than €30,000 for an academic-scale prototype.	✓	Subsection 17.1.3
REQ-STK-BUD-02	Test campaign shall be completed within 6 months of design freeze.	✓	Section 17.4

ID	Requirement	Status	Verification Description
REQ-STK-BUD-03	The UAV shall be designed for at least 10 reuses with minimal refurbishment.	✓	Section 18.1
REQ-STK-BUD-04	Operation shall be within UAV safety envelope.	✓	Section 15.1
REQ-STK-CAP-01	UAV shall be able to climb to mission altitude faster than competitors.	✓	Chapter 2
REQ-STK-CAP-02	UAV shall have a total mission duration of at least 35 minutes.	✓	Section 12.2
REQ-STK-CAP-03	The UAV shall be able to perform surveillance over an area of at least 25 km^2.	✗	The payload design is out of the scope of the UAV design and is left to the buyer.
REQ-STK-CAP-04	The UAV surveillance oriented payload shall have a resolution of 1px per 5 centimetres at its mission altitude.	✗	The payload design is out of the scope of the UAV design and is left to the buyer.
REQ-STK-CAP-05	The UAV shall be able to deploy payload.	✓	Subsection 15.2.1
REQ-STK-CAP-06	The UAV shall produce noise under 150 dB.	✓	Subsection 9.5.1
REQ-STK-CAP-07	The UAV shall be capable of vertical take-off and landing (VTOL).	✓	Chapter 15
REQ-MIS-PRF-01	The thrust-to-weight ratio shall be ≥1.5 during take-off.	✓	Section 7.3
REQ-MIS-PRF-02	The UAV shall support a total mission duration of at least 35 minutes.	✓	Section 12.2
REQ-MIS-PRF-03	The range shall be at least 10 km.	✓	Section 12.2
REQ-MIS-PRF-04	The UAV shall operate exclusively within the Earth's atmosphere at altitudes between 100 m and 2500 m AGL.	✓	Section 12.2
REQ-MIS-PRF-05	The UAV shall be capable of sustained flight operations over terrain with elevations up to at least 4000 m above sea level.	✓	This was not part of the design and also not a critical customer requirement in the end
REQ-MIS-PRF-06	The UAV shall be able to climb from ground level to at least 2500 m AGL.	✓	Section 11.4
REQ-MIS-PRF-07	The cruise velocity shall be in the range of 60-160 km/h.	✓	Section 12.2
REQ-MIS-PRF-08	The UAV shall be powered by a compact, pressure-fed liquid bipropellant propulsion system.	✓	Section 7.1
REQ-MIS-PRF-09	The UAV shall be able to climb to target altitude in under one minute.	✓	Section 12.2
REQ-MIS-PRF-10	The UAV shall be able to perform all necessary manoeuvres and adjustments to successfully perform vertical landing.	✓	Subsection 15.2.2
REQ-MIS-PRF-11	The UAV shall not use more than 95% of fuel during the take-off and climb to altitude phases combined.	✗	The UAV burns until burnout.
REQ-MIS-PRF-12	The UAV shall be able to perform a coordinated turn with a bank angle of at least 30°.	✓	Midterm Report [1]
REQ-MIS-OPS-01	The UAV shall use kerosene as fuel and 98% hydrogen peroxide as oxidizer.	✓	Section 7.1
REQ-MIS-OPS-02	The UAV shall be capable of vertical take-off and landing (VTOL).	✓	Chapter 15
REQ-MIS-OPS-03	The UAV shall be capable of landing on any flat terrain type.	✗	The UAV can only land in a positioned net
REQ-MIS-OPS-04	The UAV shall be designed for reuse and recovery from anywhere with a flat area of 20 m × 20 m.	✓	Section 15.1
REQ-MIS-OPS-05	The UAV shall operate within EU-allocated frequency bands.	✓	Subsection 8.4.1

ID	Requirement	Status	Verification Description
REQ-MIS-OPS-06	Communication between the UAV and the ground station shall be ensured at all times.	✓	Table 8.3
REQ-MIS-OPS-07	The UAV shall identify the target landing site before entering the approach phase.	✓	Section 15.1
REQ-MIS-OPS-08	The UAV shall be designed for accessibility of critical components.	✓	Section 15.4
REQ-MIS-OPS-09	The UAV shall be able to operate efficiently at temperatures from −30°C to 50°C.	✓	Section 12.2
REQ-MIS-OPS-10	The UAV shall be able to perform vertical landing with cross-winds up to 20% of its stall speed.	✓	Section 15.1
REQ-MIS-SAR-01	The UAV shall include a return-to-home function.	✓	Chapter 8
REQ-MIS-SAR-02	The UAV shall include a procedure to safely shutdown the engine.	✓	Section 15.1
REQ-MIS-SAR-03	The UAV shall include a contingency procedure in case of critical failure.	✓	Section 15.3
REQ-MIS-SAR-04	The UAV shall comply with at least an IP55 rating standard.	✗	This was not part of the design
REQ-MIS-SAR-05	No single failure shall result in catastrophic loss of vehicle.	✓	Section 15.4
REQ-MIS-SAR-06	Hydrogen Peroxide decomposition events shall be contained without structural breach.	✗	The design does not cover this.
REQ-MIS-SAR-07	The UAV shall support manual override at all times.	✓	Section 15.1
REQ-MIS-SAR-08	All external interfaces shall resist corrosion from oxidizer exposure.	✓	Chapter 16
REQ-MIS-BUD-01	The entire UAV shall have a total take off mass lower than 34 kg.	✓	Section 14.2
REQ-MIS-BUD-02	The UAV shall be capable of carrying a minimum payload mass of 3 kg.	✓	Section 14.2
REQ-MIS-BUD-03	The UAV shall have a maximum fuel mass of 8 kg.	✓	Section 7.3
REQ-MIS-BUD-04	The UAV's propulsion system shall have a mass lower than 25 kg.	✓	Section 7.3
REQ-MIS-BUD-05	The electric power system shall include a battery for avionics and actuation.	✓	Chapter 8
REQ-MIS-BUD-06	The electric power system shall allocate a budget of 100 W for the payload.	✓	Chapter 8
REQ-MIS-BUD-07	The deployable payload shall at most be 3 L in volume.	✓	The payload volume available is higher than 3 L
REQ-SYS-PRP-01	The propulsion system shall provide a nominal thrust level of at least 500 N during powered flight phases such as take-off, climb, and manoeuvring.	✓	Section 7.3
REQ-SYS-PRP-02	The chamber pressure (p_C) at maximum thrust shall be between 2.5 and 3.5 MPa.	✗	A pressure lower that what specified in the requirements was needed to allow for sufficient regenerative cooling
REQ-SYS-PRP-03	The propellant shall be stored in pressurized tanks at a minimum of $1.15p_C$.	✓	Section 7.3
REQ-SYS-PRP-04	The pressurizer gas shall be stored at a pressure in the range 15-35 MPa.	✓	Section 7.3
REQ-SYS-PRP-05	The propulsion system shall be capable of generating a mass flow of at least 0.2 kg/s at full thrust.	✓	Section 7.3
REQ-SYS-PRP-06	The maximum nozzle exit diameter shall not exceed 12 cm.	✓	Section 7.3
REQ-SYS-PRP-07	The propulsion system shall be capable of safely re-igniting for a minimum of 3 burns per mission.	✗	The Strawman concept that was ultimately decided did not include re-ignition of main engine per mission.

ID	Requirement	Status	Verification Description
REQ-SYS-PRP-08	The propulsion system shall be able to safely throttle the thrust level in a range between 80% and 100% of the maximum thrust.	✗	The selected Strawman concept did not include throttling.
REQ-SYS-PRP-09	The oxidizer tank shall not exceed 5 L in volume.	✓	Section 7.2
REQ-SYS-PRP-10	The fuel tank shall not exceed 1.8 L in volume.	✓	Section 7.2
REQ-SYS-PRP-11	The pressurizer tank shall not exceed 2 L in volume.	✓	Section 7.2
REQ-SYS-PRP-12	The pressurizer and propellant tanks shall be able to operate in a temperature range −2 to 20°C.	✓	Section 7.2
REQ-SYS-PRP-13	The propulsion system shall have a minimum cumulative burn time greater than 20 s.	✓	Section 7.3
REQ-SYS-PRP-14	The temperature in the combustion chamber shall not exceed 3000 K.	✓	Section 7.3
REQ-SYS-PRP-15	The propulsion system shall work with an oxidiser-to-fuel ratio between 5.0 and 8.0.	✗	A O/F lower that what specified in the requirements was needed to allow for sufficient regenerative cooling
REQ-SYS-PRP-16	The propulsion system shall be capable of repeating take-off and landing cycles for at least 10 times.	✓	Section 7.5
REQ-SYS-PRP-17	The propulsion system shall have a redundant feeding system.	✗	The design did not cover this
REQ-SYS-PRP-18	The propulsion system shall ensure that the fuel and oxidiser are both kept at the liquid state before combustion during operations.	✓	Equation 7.2.2
REQ-SYS-PRP-19	Thermal interfaces between propulsion and airframe shall limit heat transfer to adjacent systems below TBD W.	✓	Equation 7.2.2
REQ-SYS-PRP-20	End of life disposal of propellant and pressurizer tanks shall be defined.	✓	Section 18.3
REQ-SYS-PRP-21	The propulsion system shall be able to generate nominal thrust within 0.5 s.	✗	The design did not cover this
REQ-SYS-AVN-01	The avionics system shall be able to calculate the UAV's position with an error of less than 10 m.	✓	Chapter 8
REQ-SYS-AVN-02	The avionics system shall be able to calculate the UAV's velocity with an error of less than 1 m/s.	✓	Chapter 8
REQ-SYS-AVN-03	The avionics system shall be able to calculate the UAV's attitude parameters with errors of less than 3°.	✓	Chapter 8
REQ-SYS-AVN-04	The avionics system shall be able to update input information with a refresh rate greater than 10 Hz.	✓	Chapter 8
REQ-SYS-AVN-05	The avionics system shall be able to monitor all other systems and detect potential anomalies.	✓	Chapter 8
REQ-SYS-AVN-06	The avionics system shall be equipped with sensors capable of calculating the outside total pressure with an accuracy of at least 3%.	✓	Chapter 8
REQ-SYS-AVN-07	The avionics system shall be equipped with sensors capable of calculating the outside static pressure with an accuracy of at least 1%.	✓	Chapter 8
REQ-SYS-AVN-08	The avionics system shall be equipped with sensors capable of calculating the outside total temperature with an accuracy of at least 2°C.	✓	Chapter 8
REQ-SYS-AVN-09	The avionics system shall be equipped with sensors capable of calculating the angle of attack with an accuracy of at least 0.5°.	✓	Chapter 8
REQ-SYS-AVN-10	The avionics system shall be capable of correctly processing internal and external sensor data.	✓	Chapter 8
REQ-SYS-AVN-11	All of the avionics system components shall have a reliability of at least 95% considering 10 missions.	✗	Tests have to be performed to validate this

ID	Requirement	Status	Verification Description
REQ-SYS-AVN-12	The avionics system shall be equipped with redundant sensors such that single-point failures will not cause mission failure.	✓	Chapter 8
REQ-SYS-AVN-13	The avionics system shall be equipped with an autopilot subsystem capable of performing obstacle avoidance.	✓	Chapter 8
REQ-SYS-AVN-14	The avionics system shall be equipped with a redundant communication subsystem.	✓	Section 8.1
REQ-SYS-AVN-15	The avionics system shall provide a minimum downlink speed of 1-3 Mbps.	✓	Table 8.3
REQ-SYS-AVN-16	The avionics system shall provide a minimum uplink speed of 1-5 Kbps.	✓	Subsection 8.4.1
REQ-SYS-AVN-17	The avionics system shall ensure a minimum link margin of 10 dB.	✓	Table 8.3
REQ-SYS-AVN-18	The avionics system shall ensure communication in frequencies of 868 MHz, 1.2 GHz or 2.4 GHz.	✓	Subsection 8.4.1
REQ-SYS-AVN-19	The avionics system shall visually determine the landing site before entering the approach phase with an accuracy of 10 m.	✗	The design did not cover this, but VAPOR can navigate to a GPS location
REQ-SYS-AVN-20	The avionics system shall be able to perform any potential trajectory and attitude corrections to comply with REQ-STK-OPS-05.	✓	Section 11.4
REQ-SYS-AVN-21	The avionics system shall detect and isolate propulsion anomalies within a rate of 10 Hz.	✗	The design did not cover this
REQ-SYS-CNT-01	The control system shall be capable of deflecting control surfaces up to ±15°.	✗	Maximum deflections were chosen to be ± 12° (Already conservative)
REQ-SYS-CNT-02	The control system shall be able to change the trajectory of the UAV with an accuracy of at least 5 m.	✓	Section 11.4
REQ-SYS-CNT-03	The control system shall be able to change the attitude of the UAV with an accuracy of at least 5°.	✓	Section 11.4
REQ-SYS-CNT-04	The control system shall be able to perform attitude manoeuvres for VTOL.	✓	Section 11.4
REQ-SYS-CNT-05	The control system shall have a response time to flight computer inputs not exceeding 100 ms.	✗	The design did not cover control timings
REQ-SYS-CNT-06	The control system shall be able to respond to atmospheric disturbances, including gust loads and crosswinds, ensuring stability and controllability.	✓	Section 11.3
REQ-SYS-CNT-07	The control system shall have a reliability higher than 90% considering 10 missions.	✗	The design did not cover this
REQ-SYS-CNT-08	The control system shall be equipped with redundancy paths in order to operate efficiently in case of single-point failure.	✗	The design did not cover this
REQ-SYS-CNT-09	The control system shall be able to safely control the UAV in case of engine failure.	✓	Subsection 12.1.3
REQ-SYS-ARF-01	The airframe system shall ensure longitudinal stability during unpowered mission phases.	✓	Subsection 11.1.2
REQ-SYS-ARF-02	The airframe system shall ensure lateral stability during unpowered mission phases.	✓	Subsection 11.1.2
REQ-SYS-ARF-03	The airframe system shall be able to remain stable under a shift in center of gravity of TBD cm during operations.	✓	Section 10.2
REQ-SYS-ARF-04	The airframe system shall be capable of generating a maximum lift of at least 400 N at all operational altitudes and velocities.	✓	Section 9.1
REQ-SYS-ARF-05	The airframe system shall have a glide ratio of at least 10.	✓	Section 12.2
REQ-SYS-ARF-06	The airframe system shall be capable of providing sufficient range, as described in REQ-MIS-PRF-03, in case of engine failure.	✓	Subsection 12.1.3

ID	Requirement	Status	Verification Description
REQ-SYS-ARF-07	The airframe system shall be capable of providing sufficient endurance, as described in REQ-MIS-PRF-02, in case of engine failure.	✓	Subsection 12.1.3
REQ-SYS-ARF-08	The airframe system shall be able to withstand loads of at least 2g without failure during take-off and landing.	✓	Chapter 9
REQ-SYS-ARF-09	The airframe system shall be able to withstand gust loads of at least 8 m/s.	✓	Subsection 9.6.2
REQ-SYS-ARF-10	The airframe system shall sustain a load factor of at least 1.5 during unpowered mission phases with no failure.	✓	Chapter 9
REQ-SYS-ARF-11	The airframe components shall not experience plastic deformation during operations.	✓	Section 9.3
REQ-SYS-ARF-12	The airframe components shall withstand the random vibration induced by the propulsion system	✓	Section 9.5
REQ-SYS-ARF-13	The airframe components shall resist corrosion from hydrogen peroxide handling.	✗	The design did not cover this
REQ-SYS-EPS-01	The electrical power system shall supply a total peak power of at least 1000 W.	✓	Chapter 13
REQ-SYS-EPS-02	The electrical power system shall supply a total energy of at least 300 Wh.	✓	Chapter 13
REQ-SYS-EPS-03	The electrical power system shall have an efficiency of at least 80%.	✗	It was not possible to achieve such efficiency Chapter 13
REQ-SYS-EPS-04	The electrical power system shall have redundant power paths in order to avoid single-point failure.	✗	The design did not cover this
REQ-SYS-EPS-05	The electrical power system shall prevent cascading failures.	✗	The design did not cover this
REQ-SYS-EPS-06	All components of the electrical power system shall not exceed a temperature of 60°C during operations.	✗	The design did not cover this
REQ-SYS-EPS-07	The electrical power system shall preserve 5% of power for landing operations.	✓	Chapter 8
REQ-SYS-EPS-08	The electrical power system shall not generate sparks around propellant tanks.	✗	The design did not cover this
REQ-SYS-EPS-09	The electrical power system shall be equipped with heat-resistant casings.	✗	The design did not cover this
REQ-SYS-EPS-10	The electrical power system shall provide information on SoC with a ±5% accuracy.	✗	The design did not cover this
REQ-SYS-EPS-11	End of life disposal of the EPS system shall be defined.	✓	Section 18.3

20 | Conclusion & Recommendations

Author(s): Kyle, Duco, Kaj
This chapter covers the conclusion & recommendations of this report.

20.1. Conclusion

This report aimed to justify the design decisions behind VAPOR, a hybrid electric and bi-propellant UAV for rapid surveillance missions. The need for such a vehicle emerged from a market analysis that revealed a clear gap in the rapid-surveillance segment, where current platforms fail to combine immediate deployment with long-endurance loitering. From this gap, the mission statement and mission functions were derived and subsequently translated into a highly specialised design.

Since conventional electric UAVs cannot deliver extreme climb performance without excessive mass, energy, or sustainability penalties, an innovative propulsion system was needed to achieve this mission. This is achieved by employing a hybrid propulsion system. A bi-propellant propulsion system allows for a rapid time-to-altitude, reaching a target altitude of 3,000 m in just 40 seconds. This rocket engine was designed from first principles: the propellant combination, injector type, combustion chamber material, catalyst bed, and nozzle geometry were all specifically designed to fit the mission profile. The resulting engine burns RP-1 with 98% high-test peroxide (HTP) at an Oxygen-to-Fuel ratio of 4, producing 500 N of thrust. The use of HTP, which decomposes cleanly to oxygen and water vapour, ensures the system remains a sustainable option. This system can be seen in Figure 20.1. Furthermore, to maintain altitude for surveillance once the boost phase is complete, a secondary propulsion system consisting of a lightweight, electrically-powered, carbon fibre propeller is engaged.

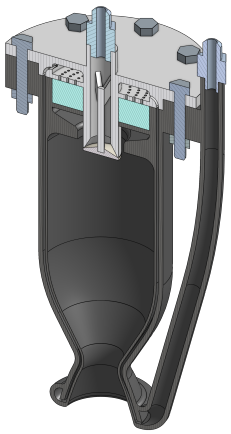

Figure 20.1: Rendering of the VAPOR main engine

The combination of a high-thrust bi-propellant system and an efficient electrical propeller allows for an ultra-fast climb with optimal endurance performance. To power the cruise motor and the advanced avionics suite, a solid-state battery is utilised, offering an energy density of 350 Wh/kg.
In addition to climb performance, maximising endurance was identified as a critical driver for VAPOR's aerodynamics. The aerodynamic efficiency has been obtained by using a slender, high aspect ratio, and cambered wing. However, due to the vertical launch profile, this configuration introduces severe aerodynamic instability during the boost phase. It was therefore decided to implement a folding wing mechanism. The wings are fully stowed during the vertical boost phase to enable stability and minimise drag, and deployed smoothly for cruise once the target altitude is reached. This design selection achieved a high lift-to-drag ratio of 16 during the cruise phase.

Finally, the vehicle's internal layout incorporates the payload required for diverse surveillance tasks. VAPOR is specifically designed to flexibly carry up to 7 kg of payload, such as dual-channel IR/optical cameras or hyperspectral scanners. The exact placement of the payload, alongside all other subsystems within the internal structure, is visualised in Figure 20.2.

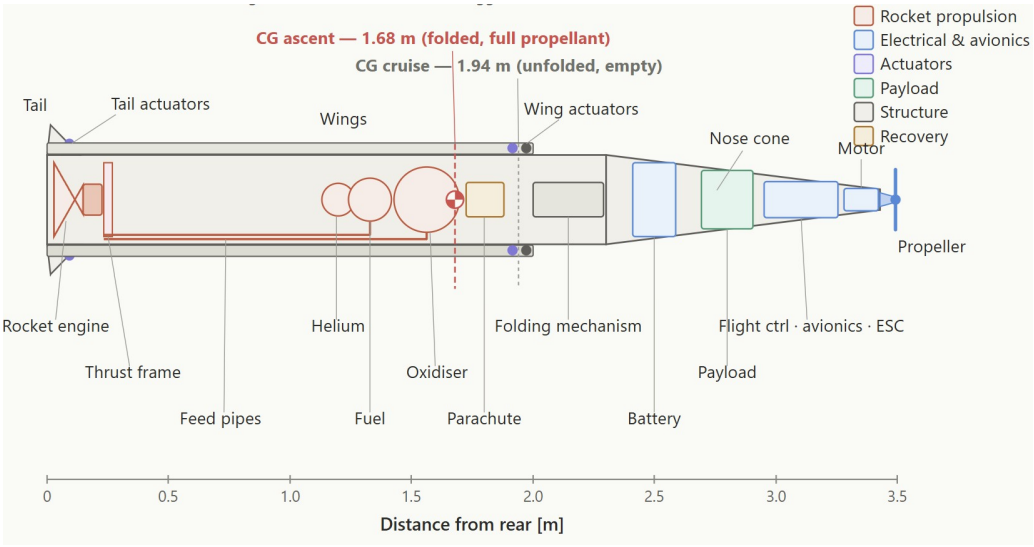

Figure 20.2: Internal Configuration Visualisation generated by Claude

With the design configuration shown in Figure 20.2, VAPOR achieves a cruise endurance of 68 minutes and covers an operational range of 85 km. This performance unlocks a unique value proposition for potential investors and end-users: VAPOR can arrive at an emergency scene up to 10 times faster than traditional fixed-wing or VTOL electric platforms, yet operates at a projected unit manufacturing cost of $45,000. This positions VAPOR as a highly disruptive, cost-effective asset for time-critical civil, industrial, and emergency response markets.
To provide a definitive summary of the vehicle's performance, the Key Performance Indicators can be seen in Table 20.1.

Table 20.1: VAPOR Key Performance Indicators

Performance Parameter	Achieved Value
Operational Altitude	3,000 m
Time-to-Altitude	40 s
Rocket Engine Thrust	500 N
Payload Capacity	7 kg
Glide Efficiency (L/D)	16
Operational Range	85 km
Endurance	68 min
Manufacturing Cost	$45,000

Furthermore, to ensure sustainable development, multiple sustainability strategies have been included in the design from day one. Materials have been selected with structural recyclability in mind; an airframe constructed primarily out of aerospace-grade aluminium combined with a solid-state battery improves overall end-of-life recyclability compared to carbon-composite alternatives. Secondly, advanced manufacturing methods have been chosen with sustainability as a determining factor, leveraging laser powder-bed fusion for low-buy-to-fly ratios, CNC machining, and friction stir welding. Comprehensive end-of-life strategies have been defined for each subsystem, with a strong focus on solid-state battery reclamation. Ultimately, VAPOR stands out as a sustainable competitor by striking an optimal trade-off balance, mitigating high battery manufacturing footprints through localised emissions elimination during its operational life.

20.2. Recommendations

While the conceptual design demonstrates immense potential, transitioning VAPOR to a detailed design phase requires addressing key assumptions, sensitivities, and inherent design risks. The following recommendations outline the essential analytical, computational, and experimental activities required to validate the design.
Firstly, a multidisciplinary design optimization (MDO) loop must be executed across all subsystems. This conceptual design relied on decoupled subsystem calculations; a coupled iteration loop is necessary to ensure convergence of the design. Secondly, advanced aerodynamic analysis using high-fidelity CFD software is recommended to replace the current low-fidelity aerodynamic methods. This analysis should model the fuselage effects and more accurately predict the viscous behaviour. This will also help provide a better picture of stability during the launch phase. This is to confirm whether the assumptions made during the stability analysis were valid, or whether further effort is required to ensure stability during the ascent phase. The control aspect also requires further development, particularly for roll control during the transfer phase, as it is inadequately modelled with the current approach. This will be better modelled using a 6 DOF sim-

ulation to accurately model the trajectory and confirm the feasibility of the transfer motion from the rocket phase to the control phase.
Finally, regarding thermal management, film cooling within the combustion chamber should be investigated alongside the current regenerative cooling method. This will mitigate the thermal decomposition and detonation risks associated with routing high-test peroxide (HTP) through cooling channels near extreme boundary layer temperatures. Also, more design effort is needed to develop the control scheme for the engine valves, ensuring proper engine controllability during take-off.
From a structural standpoint, the current assumption of a rigid airframe must be verified. Detailed FEM analysis is highly recommended to evaluate structural integrity under extreme dynamic pressure during the vertical rocket boost phase. These structural considerations must investigate fatigue loading from repeated wing deployment cycles and thermal deformations caused by the high-temperature gradient near the engine bay. Additionally, the folding wing mechanism represents a single point of failure; detailed kinematic and structural stress analyses are required to ensure it can withstand asymmetric gust loading during transition manoeuvres without jamming or structural failure. More mechanical design work is also needed on the wing's locking mechanism. The internal structure of the fuselage must be designed to mount the springs and solenoids. On the hinge, a locking mechanism must be fitted; the fuselage must also be adjusted to accommodate the pushrod exit. For the launching structure and net, further analysis should also be conducted on the frames supporting both and the load experienced by them. The airframe should also be modified to accommodate a smooth launch from the tower.
On the operational side of the project, further development is needed. This mainly consists of establishing procedures for loading and unloading the UAV; launch procedures should also be defined, and training programs must be established to safely train the crew to handle peroxide. The logistics side should also be further defined, mainly the transportation of the UAV, the net and the launching structure.
To systematically reduce technical risks, a comprehensive experimental testing roadmap must be executed:

- **Solid-State Battery Characterisation :** Thermal and electrical cell testing must be performed to validate its capabilities and discharge characteristics under the demands of the electronics and cruise systems within varying operational temperature envelopes.
- **Propulsion Hot-Fire Campaign:** A comprehensive hot-fire testing campaign of the bi-propellant rocket engine is critical. This testing must validate injector efficiency, catalyst bed decomposition stability, and reliable ignition/shutdown transients.
- **Wing Deployment Testing:** Hardware-in-the-Loop (HIL) testing of the mechanical wing actuators under simulated aerodynamic loads should be conducted to ensure mechanical deployment reliability.
- **Wind Tunnel Validation:** Scale-model wind tunnel testing must be conducted to validate the CFD and aerodynamic simulation results, specifically focusing on capturing the lift, drag, and moment coefficients during the wing deployment sequence and during cruise.
- **Recovery System Verification:** Prototype testing of the specialised landing net recovery system must be performed using dummy airframes. This will ensure that kinetic energy dissipation occurs safely without exceeding the structural g-load limits of the airframe or damaging the sensitive internal payload.
- **Integrated Flight Testing:** Ultimately, a full-scale flight test campaign must be executed to demonstrate end-to-end mission capabilities.

Finally, a quantitative life cycle assessment (LCA) must be conducted to formally validate the preliminary sustainability benefits claims and confirm VAPOR's environmental advantage over conventional platforms.

From a financial perspective, the current estimate serves as a preliminary baseline for the academic prototype rather than a comprehensive economic assessment of the final VAPOR system. The model currently captures direct component and material costs, omitting major economic drivers such as labour, manufacturing overhead, certification, operational maintenance, and scaling effects.

Consequently, the next design phase must incorporate a formal return-on-investment (ROI) analysis to evaluate the system's value relative to its total development and production costs. This analysis should weigh the expected revenue model, market demand, and unit production costs against operational lifetimes and existing market alternatives. Additionally, determining the payback period, break-even production volume, and sensitivity to fluctuations in material prices, labour rates, and manufacturing methods will be critical. Because the current prototype model relies on student-phase assumptions like unpaid labour, translating these figures into a commercial context requires a complete business case that rigorously evaluates long-term profitability, scalability, and financial feasibility.

From a commercial perspective, future iterations of the VAPOR Project must account for how investors might scale the conceptual design to target different market segments or operational use cases. Consequently, a comprehensive sensitivity and scalability analysis should be conducted to evaluate how variations in key design parameters—such as dimensions, payload capacity, endurance, and propulsion constraints affect both technical performance and financial viability.

This analysis will help identify which configuration changes yield the highest return. For instance, downsizing the platform could minimise upfront costs for short-range, low-risk missions, whereas scaling up could unlock demanding operations that require extended range and capacity.
Crucially, these technical modifications must be mapped directly to business metrics, including development overhead, manufacturing scalability, certification hurdles, and long-term maintenance costs. Quantifying how design decisions drive profitability and market adaptability will ultimately strengthen the project's business case and provide stakeholders with a reliable foundation for investment and commercialisation decisions.

Bibliography

[1] Armeli, M., Breeman, K., Ezcurra Masip, I., Larrondo Pérez-Izaguirre, M., Lievens, N., Lindhout, D., Plugaru, V., Vander Stichele, P., Voineag, V., and Zantboer, K., "Midterm report." May 2026.

[2] Armeli, M., Breeman, K., Ezcurra Masip, I., Larrondo Pérez-Izaguirre, M., Lievens, N., Lindhout, D., Plugaru, V., Vander Stichele, P., Voineag, V., and Zantboer, K., "Baseline report." May 2026.

[3] Guo, J., "Verification and Validation for the Attitude and Orbit Control System." `https://brightspace.tudelft.nl/d2l/le/content/782547/viewContent/4688357/View`. Accessed: May 21, 2026.

[4] Ponomarenko, A., "Rpa: Design tool for liquid rocket engine analysis," tech. rep., LPRE, Jan 2009. Technical report describing the Rocket Propulsion Analysis (RPA) software.

[5] Okninski, A., Kindracki, J., and Wolanski, P., "Multidisciplinary optimisation of bipropellant rocket engines using h2o2 as oxidiser," *Aerospace Science and Technology*, vol. 82-83, pp. 284–293, 2018.

[6] RP Software + Engineering UG, "Rocket Propulsion Analysis (RPA)," 2026. Accessed: May 18, 2026.

[7] NASA Glenn Research Center, "Chemical Equilibrium with Applications (CEA)," 2026. Accessed: June 5, 2026.

[8] Delft University of Technology, "Ideal rocket theory (part 1)," 2016. Lecture slides for Spacecraft Technology.

[9] Sutton, G., and Biblarz, O., *Rocket Propulsion Elements*. No. 9th in SoarTech Operations, Hoboken, New Jersey: John Wiley Sons, 2017.

[10] Special Metals Corporation, "Inconel alloy 718," tech. rep., Special Metals Corporation, n.d. Technical Bulletin.

[11] Bernier, M., "An experimental investigation of heat transfer to hydrogen peroxide in microtubes," master of science thesis, Massachusetts Institute of Technology, Cambridge, MA, Jun 2004.

[12] Outcalt, S. L., Laesecke, A., and Brumback, K. J., "Thermophysical properties measurements of rocket propellants rp-1 and rp-2," *Journal of Propulsion and Power*, vol. 25, no. 5, pp. 1032–1040, 2009.

[13] Abdulagatov, I.M. and Azizov, N.D., "Heat capacity of rocket propellant (rp-1 fuel) at high temperatures and high pressures," *Fuel*, vol. 90, no. 2, pp. 563–567, 2011.

[14] Fagherazzi, M., Santi, M., Barato, F., and Pizzarelli, M., "A simplified thermal analysis model for regeneratively cooled rocket engine thrust chambers and its calibration with experimental data," *Aerospace*, vol. 10, no. 5, 2023.

[15] Juan, A. B. and Platero, A. L., "Design of the regenerative cooling system for a 4 kn lox/ethanol student-built liquid rocket engine," in *Proceedings of the 10th European Conference for Aeronautics and Space Sciences (EUCASS)*, EUCASS Association, 2023. Aerospace Europe Conference 2023 – 10th EUCASS – 9th CEAS Conference.

[16] Ulas, A., and Boysan, E., "Numerical analysis of regenerative cooling in liquid propellant rocket engines," *Aerospace Science and Technology*, vol. 24, no. 1, pp. 187–197, 2013. VFE-2.

[17] Santoro, R. J., and Pal, S., "Experimental studies of the heat transfer to rbcc rocket nozzles for cfd application to design methodologies," final report, The Pennsylvania State University, Propulsion Engineering Research Center and Department of Mechanical Engineering, Feb 1999. Prepared for NASA Purchase Order H-29688D.

[18] Yang, J. and Naraghi, M. H., "A fin analogy model for thermal analysis of regeneratively cooled rocket engines," in *AIAA Propulsion and Energy 2020 Forum*, American Institute of Aeronautics and Astronautics, Aug. 2020.

[19] Tosun, I., "Evaluation of transfer coefficients: Engineering correlations," in *Modeling in Transport Phenomena: A Conceptual Approach*, ch. 4, pp. 59–115, Elsevier, 2nd ed., 2007.

[20] Gnielinski, V., "New equations for heat and mass transfer in turbulent pipe and channel flow," *International Chemical Engineering*, vol. 16, pp. 359–368, 1976.

[21] Cavazzuti, M., and Corticelli, M. A., "Convective heat transfer of turbulent decaying swirled flows in concentric annular pipes," *Applied Thermal Engineering*, vol. 120, pp. 517–529, 2017.

[22] Incropera, F. P., DeWitt, D. P., Bergman, T. L., and Lavine, A. S., *Convective Heat and Mass Transfer*. New York: John Wiley & Sons, 4th ed., 2002.

[23] Jyoti, B. V. S., "Personal communication regarding hydrogen peroxide operating temperature." Personal communication, 2026. Meeting with author, stated that the general sweet spot for 98% hydrogen peroxide operation is around 60°C.

[24] Uma Maheswaran, C. R. and Sekhar, S. C., "Fin efficiency of the newly developed compartmented coil of a single coil twin fan system," *ASHRAE Transactions*, 2004.

[25] Anderson, D. A., Tannehill, J. C., and Pletcher, R. H., *Computational Fluid Mechanics and Heat Transfer*. Washington, DC: Taylor & Francis, 2nd ed., 1997.

[26] Churchill, S. W. and Chu, H. H. S., "Correlating equations for laminar and turbulent free convection from a vertical plate," *International Journal of Heat and Mass Transfer*, vol. 18, no. 11, pp. 1323–1329, 1975.

[27] Smith, R., Inomata, H., and Peters, C., "Chapter 8 - heat transfer and finite-difference methods," in *Introduction to Supercritical Fluids* (R. Smith, H. Inomata, and C. Peters, eds.), vol. 4 of *Supercritical Fluid Science and Technology*, pp. 557–615, Elsevier, 2013.

[28] R. L. Morehead, M. J. Atwell, J. C. Melcher, and E. A. Hurlbert, *Cold Helium Pressurization for Liquid Oxygen / Liquid Methane Propulsion Systems: Fully-Integrated Initial Hot-Fire Test Results*.

[29] Cervone, A., "Personal communication on contraction ratio trends and film cooling modeling for a 500 N kerosene-HTP engine." Personal communication, 2026. Discussion noting that smaller engines tend to exhibit higher contraction ratios, and that film cooling is difficult to model accurately without combustion CFD simulations.

[30] Dassault Systèmes, "CATIA," 2026. Computer-aided design (CAD) software.

[31] Petrenko, V. V., Vimont, I. J., Gromov, S., Ryu, Y., Bock, M., Schmitt, J., Bauska, T. K., Hua, Q., and Brook, E. J., "Preindustrial-to-present-day changes in atmospheric carbon monoxide: agreement and gaps between ice archives and global model reconstructions," *Atmospheric Chemistry and Physics*, vol. 25, pp. 1105–1133, 2025.

[32] Montlaur, A., Trapote-Barreira, C., and Delgado, L., "Analytical models of flight fuel consumption and non-co2 emissions as a function of aircraft capacity," *Applied Sciences*, vol. 15, no. 17, 2025.

[33] Son, M., Radhakrishnan, K., Koo, J., Kwon, O. C., and Kim, H. D., "Design procedure of a movable pintle injector for liquid rocket engines," *Journal of Propulsion and Power*, vol. 33, no. 4, pp. 858–869, 2017.

[34] Harms, C., Fazeli, H., and Vanaken, J., "The characteristics of flow discharge coefficient of plain orifice geometries on pintle injector design," *International Journal of Fluid Mechanics Research*, vol. 48, 01 2021.

[35] Outcalt, S. L., Laesecke, A., and Brumback, K. J., "Thermophysical properties measurements of rocket propellants rp-1 and rp-2," *Journal of Propulsion and Power*, vol. 25, pp. 1032–1040, Sep 2009.

[36] Jung, S., Choi, S., Heo, S., and Kwon, S., "Scaling of catalyst bed for hydrogen peroxide monopropellant thrusters using catalytic decomposition modeling," *Acta Astronautica*, vol. 187, pp. 167–180, 2021.

[37] Huzel, D. K. and Huang, D. H., "Design of liquid propellant rocket engines," Tech. Rep. NASA SP-125, National Aeronautics and Space Administration, Washington, D.C., 1967. Office of Technology Utilization.

[38] van den Berg, P. M., Jyoti, B. V.S., and Hermsen, R. J.G., "Investigation of thermal behaviour of additively manufactured green bi-propellant thrusters in CubeSat applications using transient thermal modelling," in *Space Propulsion Conference*, 2020. Paper SP2020_00082.

[39] Zhou, C., Yu, N., Wang, S., Han, S., Gong, H., Cai, G., and Wang, J., "The influence of thrust chamber structure parameters on regenerative cooling effect with hydrogen peroxide as coolant in liquid rocket engines," *Aerospace*, vol. 10, no. 1, 2023.

[40] Hosseini, E., and Popovich, V.A., "A review of mechanical properties of additively manufactured inconel 718," *Additive Manufacturing*, vol. 30, p. 100877, 2019.

[41] Friis, H. T., "A note on a simple transmission formula," *Proceedings of the IRE*, vol. 34, pp. 254–256, May 1946.

[42] International Telecommunication Union, "A propagation prediction method for aeronautical mobile and radionavigation services using the VHF, UHF and SHF bands," Recommendation ITU-R P.528-5, ITU Radiocommunication Sector (ITU-R), Geneva, Switzerland, Sep 2021.

[43] International Telecommunication Union, "Calculation of free-space attenuation," Recommendation ITU-R P.525-5, ITU Radiocommunication Sector (ITU-R), Geneva, Switzerland, Nov 2024.

[44] Selig, M. S., Donovan, J. F., and Fraser, D. B., *Airfoils at Low Speeds*. No. 8 in SoarTech Operations, Virginia Beach, Virginia: SoarTech Publications, 1989.

[45] Martínez-Cagigal, V., "Multi-objective particle swarm optimization (MOPSO)," 2026. Accessed: June 5, 2026.

[46] Drela, M., "XFOIL: An Analysis and Design System for Low Reynolds Number Airfoils," in *Low Reynolds Number Aerodynamics* (Mueller, T. J., ed.), (Berlin, Heidelberg), pp. 1–12, Springer Berlin Heidelberg, 1989.

[47] Barrowman, J. S., "Calculating the center of pressure of a model rocket," Tech. Rep. TIR-33, Centuri Engineering Company, 1966. Technical Information Report; reprinted in High Power Rocketry, March 1998.

[48] Purser, P. E. and Campbell, J. P., "Experimental Verification of a Simplified Vee-Tail Theory and Analysis of Available Data on Complete Models with Vee Tails," Technical Report NACA-TR-823, National Advisory Committee for Aeronautics (NACA), Langley Field, VA, Nov 1944.

[49] Oliviero, F., "Weight Balance in AC design." `https://brightspace.tudelft.nl/d2l/le/content/782547/viewContent/4495962/View`. Accessed: May 19, 2026.

[50] Oliviero, F., "Requirement Analysis and Design principles for A/C stability control (Part 1)." `https://brightspace.tudelft.nl/d2l/le/content/782547/viewContent/4495954/View`. Accessed: May 19, 2026.

[51] Oliviero, F., "Requirement Analysis and Design principles for A/C stability control (Part 2)." `https://brightspace.tudelft.nl/d2l/le/content/782547/viewContent/4495955/View`. Accessed: May 19, 2026.

[52] Varriale, C., *Elements of Airplane Performance*. Delft, The Netherlands: TU Delft OPEN Publishing, 2025. Open access textbook.

[53] Delft University of Technology, "Aerospace design and systems engineering elements II (AE2111-II): Stability and control." Lecture notes, 2026. Course AE2111-III.

[54] "Acoustic loads generated by the propulsion system," NASA Space Vehicle Design Criteria Monograph NASA SP-8072, National Aeronautics and Space Administration, Washington, D.C., USA, Jun 1971.

[55] Varnier, J., "Experimental study and simulation of rocket engine freejet noise," *AIAA Journal*, vol. 39, no. 10, pp. 1851–1859, 2001.

[56] Haynes, J. T., and Kenny, J., "Modifications to the NASA SP-8072 distributed source method II for Ares I lift-off environment predictions," 2009.

[57] Gee, K. L., "A tale of two curves and their influence on rocket and supersonic jet noise research," *The Journal of the Acoustical Society of America*, vol. 149, pp. 2159–2162, Apr 2021.

[58] Plotkin, K. J., Sutherland, L., and Vu, B. T., "Liftoff acoustics predictions for the Ares I launch pad," in *Proceedings of the 15th AIAA/CEAS Aeroacoustics Conference*, 2009. AIAA Paper 2009-3163.

[59] European Parliament and Council, "Directive 2003/10/ec on the minimum health and safety requirements regarding the exposure of workers to the risks arising from physical agents (noise)." Official Journal of the European Union, 2003. L 42/38.

[60] NASA, "Structural vibration prediction," Tech. Rep. NASA/SP-8050, National Aeronautics and Space Administration, May 1970. Internal loads and stresses caused by space vehicle vibration resulting from induced or natural environments.

[61] Kulkarni, A. P., "Design methodology and optimization of kick stage main structures," Master's thesis, Delft University of Technology, Delft, Netherlands, 2023. Graduation Committee Members from ArianeGroup GmbH and Universität Bremen included.

[62] Sharpe, P. D., "Aerosandbox: A differentiable framework for aircraft design optimization," Master's the-

sis, Massachusetts Institute of Technology, 2021.

[63] Sharpe, P. D., *Accelerating Practical Engineering Design Optimization with Computational Graph Transformations*. PhD thesis, Massachusetts Institute of Technology, 2024.

[64] Mulder, J. A., van Staveren, W. H. J. J., van der Vaart, J. C., de Weerdt, E., de Visser, C. C., in 't Veld, A. C., and Mooij, E., *Flight Dynamics: Lecture Notes*. AE3202, Delft, Netherlands: Faculty of Aerospace Engineering, Delft University of Technology, 2013.

[65] Raymer, D. P., *Aircraft Design: A Conceptual Approach*. Washington D.C., USA: AIAA, 2nd ed., 1992.

[66] Ruijgrok, G. J. J., Voskuijl, M., and Varriale, C., *Elements of Airplane Performance*. Delft, The Netherlands: TU Delft OPEN Publishing, 3rd ed., 2025.

[67] Drela, M., "First-order DC electric motor model," tech. rep., MIT Aero & Astro, Feb 2007. QPROP documentation.

[68] Spakovszky, Z. S., "Performance of propellers." Thermodynamics and Propulsion (course notes), MIT Unified Engineering, Section 11.7. Accessed: June 1, 2026.

[69] Litherland, B. L. and Derlaga, J. M., "A performance analysis of folding conformal propeller blade designs," in *AIAA Aviation 2019 Forum*, (Dallas, Texas), American Institute of Aeronautics and Astronautics, Jun 2019. AIAA 2019-3676.

[70] Jeong, J., Shi, H., Lee, K., and Kang, B., "Improvement of electric propulsion system model for performance analysis of large-size multicopter UAVs," *Applied Sciences*, vol. 10, no. 22, p. 8080, 2020.

[71] Farid, S., and Moble, B., "Flight-validated electric powertrain efficiency models for small UASs," *Aerospace*, vol. 11, no. 1, p. 16, 2024.

[72] U.S. Government Accountability Office, "Cost estimating and assessment guide: Best practices for developing and managing program costs," Tech. Rep. GAO-20-195G, U.S. Government Accountability Office, 2020.

[73] National Aeronautics and Space Administration, *NASA Cost Estimating Handbook*. NASA, 2024.

[74] Brealey, R. A., Myers, S. C., and Marcus, A. J., *Fundamentals of Corporate Finance*. McGraw-Hill Education, 9th ed., 2017.

[75] Ventura, M. and Durant, D., "Field handling of hydrogen peroxide," in *40th AIAA/ASME/SAE/ASEE Joint Propulsion Conference and Exhibit*, American Institute of Aeronautics and Astronautics, 2004.

[76] Terlizzi, P. M. and Streim, H., "Liquid propellant handling, transfer, and storage," *Industrial & Engineering Chemistry*, vol. 48, no. 4, pp. 774–777, 1956.

[77] National Aeronautics and Space Administration, "Rocket lab safety manual," tech. rep., NASA, Nov 1959. Revised November 18, 1959.

[78] Ahuis, M., Doose, S., Vogt, D., Michalowski, P., Zellmer, S., and Kwade, A., "Recycling of solid-state batteries," *Nature Energy*, vol. 9, no. 4, pp. 373–385, 2024.

[79] Azhari, L., Bong, S., Ma, X., and Wang, Y., "Recycling for all solid-state lithium-ion batteries," *Matter*, vol. 3, pp. 1845–1861, dec 2020.

[80] Li, C., Dai, G., Liu, R., Wang, C., Wang, S., Ju, Y., Jiang, H., Jiao, S., and Duan, C., "Separation and recovery of nickel cobalt manganese lithium from waste ternary lithium-ion batteries," *Separation and Purification Technology*, vol. 306, p. 122559, 2023.

[81] Ateeq, M., "A state of art review on recycling and remanufacturing of the carbon fiber from carbon fiber polymer composite," *Composites Part C: Open Access*, vol. 12, p. 100412, 2023.

[82] Gruber, H., "Electron beam melting of alloy 718: Powder recycling and its effect on defect formation," Licentiate thesis IMS-2019-1, Chalmers University of Technology, Gothenburg, Sweden, 2019.

[83] Frączek, T., Michalski, J., Dudek, A., Kowalewska-Groszkowska, M., and Owczarek, J., "Phase transformations of iron nitrides during annealing in nitrogen and hydrogen atmosphere," *Coatings*, vol. 13, no. 11, 2023.

[84] Tonsi, G., Maesani, C., Alini, S., Ortenzi, M. A., and Pirola, C., "Nylon recycling processes: a brief overview," *Chemical Engineering Transactions*, vol. 100, pp. 727–732, 2023.

[85] Gao, S., Yan, W., Cheng, W., Yin, X., and Feng, Y., "High-value recycling of ultrahigh molecular weight polyethylene via pulse vibration molding," *Polymer*, vol. 334, p. 128725, 2025.

[86] Kurkin, A., Kryukov, E., Masleeva, O., Petukhov, Y., and Gusev, D., "Comparative life cycle assessment of electric and internal combustion engine vehicles," *Energies*, vol. 17, no. 11, 2024.

[87] Figliozzi, M. A., "Lifecycle modeling and assessment of unmanned aerial vehicles (drones) co2e emissions," *Transportation Research Part D: Transport and Environment*, vol. 57, pp. 251–261, 2017.

[88] Pollet, F., Budinger, M., Delbecq, S., Moschetta, J., and Planès, T., "Environmental life cycle assessments for the design exploration of electric uavs," in *Proceedings of the Aerospace Europe Conference 2023 – 10th EUCASS – 9th CEAS*, (Lausanne, Switzerland), EUCASS, Jul 2023.

A | Engineering Drawings

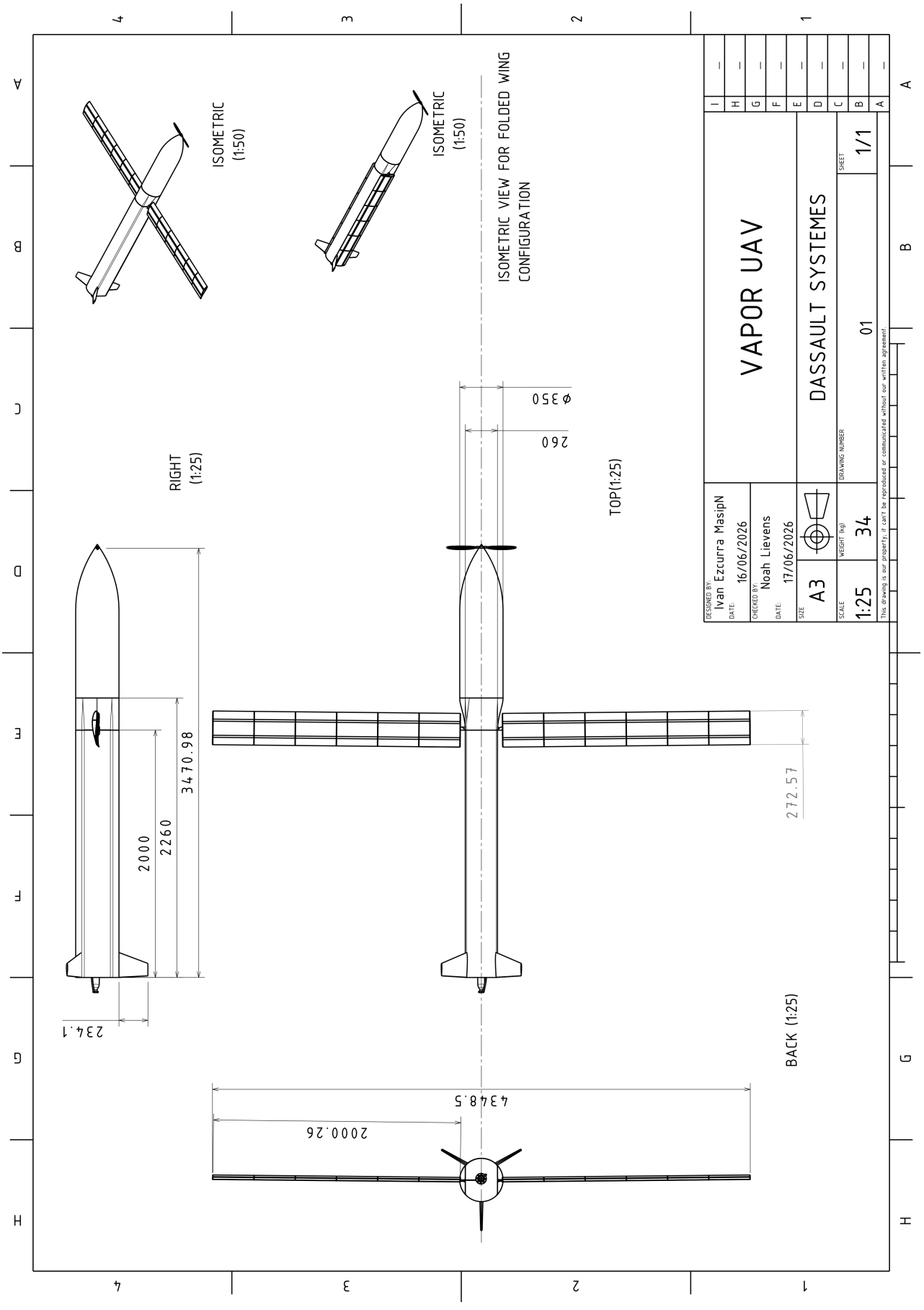

Figure A.1: Engineering Drawing Of The VAPOR UAV